# Development of Novel Microfluidic Technologies for use within the Pharmaceutical Industry

**A thesis submitted to the University of Manchester for the degree of Doctor of Philosophy in the Faculty of Engineering and Physical Sciences**

**2013**

**Francine Edwards**

**School of Chemical Engineering and Analytical Science**

## Contents

**Word count = 53,013**

# Abstract

University of Manchester
Francine Edwards
For the degree of Doctor of Philosophy
**Development of novel microfluidic technologies for use within the pharmaceutical industry**

The high throughput capabilities and low sample volume requirements of microfluidic technology make it an attractive prospect for the pharmaceutical industry. This thesis concerns the development of microfluidic devices to investigate two important challenges to the pharmaceutical industry: to interface microchannel systems with electrospray ionisation mass spectrometry, an extensively used technique in drug discovery and development, and to investigate drug precipitation and its prevention through formulation.

A microfluidic electrospray ionisation mass spectrometry interface was developed which could be placed within the source enclosure of a Waters ZQ mass spectrometer with little requirement for modification. The microfluidic interface showed a signal improvement of 38% over a capillary voltage of 4 - 4.75 kV when compared to the commercial probe which was operated at a desolvation gas flow rate of 120 L $hr^{-1}$. Under typical desolvation temperatures of 350 ºC, the commercial probe outperformed the microfluidic interface which was operated at a desolvation temperature of 60 ºC, however, only an 18% improvement in signal intensity was observed for a 290 ºC increase in temperature, and there is scope to increase the operating desolvation temperature of the microfluidic interface.

A novel droplet-based microfluidic light scattering detection system was developed to monitor drug precipitation of weakly basic poorly water soluble drugs. These drugs frequently exhibit poor bioavailability and variability due to precipitation in the GI tract. A pH-shift method was used to simulate gastric emptying conditions and generate a supersaturated state. Ketoconazole was used as the model drug in this study and was found to precipitate rapidly upon supersaturation. The extent of precipitation was shown to have a linear dependence on the degree of supersaturation for physiologically relevant supersaturations. This thesis also reports the first example of microfluidic screening of precipitation inhibitors. The inhibitory effect of two water soluble polymers, polyvinylpyrrolidone (PVP) and hydroxypropyl methylcellulose (HPMC) on ketoconazole precipitation was evaluated. HPMC was found to be a more potent precipitation inhibitor than PVP, with just 0.05 mM HPMC resulting in approximately a 75% decrease in ketoconazole precipitation, outperforming that of 1.7 mM PVP, which only decreased precipitation by approximately 60%. These findings corroborate results obtained from macroscale experiments employing dynamic light scattering detection. The onset time of precipitation for a range of ketoconazole supersaturations was measured using the scattered light intensity observed from the initial 22 seconds of ketoconazole precipitation. Onset times of between 0.24 – 2.45 seconds were determined for ketoconazole supersaturations of between 30 – 65.

## Declaration

No portion of the work referred to in the thesis has been submitted in support of an application for another degree or qualification of this or any other university or other institute of learning.

## Copyright Statement

# Acknowledgements

I would like to thank my supervisors: Professor Peter Fielden, Professor Nick Goddard, Dr Kin Tam and Dr Jonathan Booth for their guidance and support during this work.

I would also like to thank:
Brett Litten for the design and fabrication of the mass spectrometry microfluidic interface chips. Dr Stephan Mohr for the design and fabrication of the precipitation chips. Dr Sara Baldock for proofreading this thesis, and Dr Bernard Treves Brown for designing the video capture software and pump programs.

EPSRC and AstraZeneca for the funding that made this work possible.

# Publications

F. Edwards, C. Tsakmaka, S. Mohr, P. R. Fielden, N. J. Goddard, J. Booth and K. Y. Tam, ***Using droplet based microfluidic technology to study precipitation of a poorly water-soluble weakly basic drug upon a pH shift***, *Analyst*, 2013, **138**.

F. Edwards, J. Booth, P. Fielden, N. Goddard, K. Tam, **Microfluidic analysis of drug precipitation (poster presentation),** RSC Younger Members Symposium (YMS) 2012, University of Nottingham.

F. Edwards, P. Fielden, N. Goddard, K. Tam, J. Booth, **Microfluidic analysis of poorly water soluble drug precipitation in the presence of polymeric excipients (poster presentation),** Microfluidics 2012, The European Molecular Biology Laboratory (EMBL), Heidelberg.

# Abbreviations

| | |
|---|---|
| ADME | Absorption, Distribution, Metabolism and Excretion |
| AI | Atmospheric Ionisation |
| AVI | Audio Video Interleave |
| BCS | Biopharmaceutical Classification System |
| CCD | Charge-Coupled Device |
| CDER | Center for Drug Evaluation and Research |
| CE | Capillary Electrophoresis |
| CI | Centre Inlet |
| CNC | Computer Numerical Controlled |
| CRM | Charged Residue Model |
| DLS | Dynamic Light Scattering |
| DMSO | Dimethyl sulfoxide |
| DNA | Deoxyribonucleic Acid |
| DP | Drug precipitation |
| DRIE | Deep Reactive Ion Etching |
| EOF | Electroosmotic Flow |
| ES | Electrospray |
| ESI | Electrospray Ionization |
| ESI-MS | Electrospray Ionization Mass Spectrometry |
| FAB | Fast Atom Bombardment |
| FACS | Fluorescence Activated Cell Sorting |
| FaSSIF | Fasted State Simulated Intestinal Fluid |
| FDA | Food and Drug Administration |
| FeSSIF | Fed State Simulated Intestinal Fluid |
| FIB | Focused Ion Beam |
| HPLC | High Performance Liquid Chromatography |
| HPMC | Hydroxypropyl methylcellulose |
| HPMCAS | Hydroxypropyl methylcellulose acetate succinate |
| HSA | Human Serum Albumin |
| HTS | High Throughput Screening |
| i.d | Internal diameter |
| IEM | Ion Evaporation Model |
| LC | Liquid Chromatography |
| LED | Light Emitting Diode |
| LOD | Limit of Detection |

| | |
|---|---|
| LOQ | Limit of Quantification |
| MB | Magnetic beads |
| ME | Multiple Excipient |
| MEA | Multinozzle Emitter Array |
| MEMS | Microelectrical-Mechanical Systems |
| MS | Mass Spectrometry |
| µTAS | micro Total Analysis System |
| NCE | New Chemical Entity |
| NCEs | New Chemical Entities |
| NMR | Nuclear Magnetic Resonance |
| o.d | Outer diameter |
| OECD | Organization for Economic Cooperation & Development |
| OTCS | Octadecyltrichlorosilane |
| PC | Polycarbonate |
| PCB | Periodic Bond Chain |
| PCR | Polymerase Chain Reaction |
| PDMS | Polydimethylsiloxane |
| PEEK | Polyether ether ketone |
| PEG | Polyethylene glycol |
| PK-PD | Pharmacokinetic-Pharmacodynamic |
| PMMA | Poly(methyl methacrylate) |
| PNIPAM | Poly-N-isopropylacrylamide |
| POC | Point of Care |
| PTFE | Polytetrafluoroethylene |
| PVP | Polyvinylpyrrolidone |
| RF | Radio Frequency |
| RSD | Relative Standard Deviation |
| SARs | Structure Activity Relationships |
| SD | Standard Deviation |
| SEDDS | Self-emulsifying Drug Delivery System |
| SEM | Scanning Electron Microscopy |
| S/N | Signal-to-Noise |
| S-SEDDS | Supersaturable Self-emulsifying Drug Delivery System |
| SPE | Solid Phase Extraction |
| TC | Total Current |
| ThT | Thioflavin T |

| | |
|---|---|
| UV | Ultraviolet |
| UV-Vis | Ultraviolet-Visible |

## Thesis overview and research objectives

This thesis concerns the development of microfluidic devices for application in drug discovery and development. The benefits of microfluidic technology such as low sample consumption, fast reaction and analysis times and high throughput capability make it particularly desirable to the pharmaceutical industry. This thesis reports the development of two analytical devices, chapter two concerns the development of a microfluidic electrospray ionisation mass spectrometry platform, while chapters three through five detail the development of a microfluidic based setup used to detect drug precipitation using light scattering. A microfluidic platform capable of electrospray ionisation could potentially have numerous applications in the pharmaceutical industry as electrospray ionisation mass spectrometry is used extensively throughout drug discovery and development. Coupling microfluidics with mass spectrometry could lead to a reduction in the sample quantity as nanolitre droplets could be produced with ease on chip, these droplets could be manipulated on chip, reducing assay incubation times and eliminating the need to complex robotic steps for sample introduction. The second application would potentially provide a quick technique to determine drug behaviour under different pH conditions and in the presence of additives. Current techniques rely on long incubation times followed by sampling, filtration or centrifugation and off line detection; this process is not only time consuming but also does not provide an exact determination of the concentration at time of sampling as the drug can continue to precipitate out before concentration determination. The light scattering detection system presented in this thesis allows real-time measurement of the extent of precipitation of the drug while the low sample requirements of microfluidics means that incubation times are significantly reduced. A brief overview of each chapter is given below along with the research aims and objectives.

Chapter one will give a brief introduction into the theory of microfluidics, the drug discovery and development process and the role microfluidics could play in the pharmaceutical industry. Microfluidic devices will be reported that have been developed with the pharmaceutical industry in mind and the challenges of implementing microfluidic technology in the pharmaceutical industry will be discussed.

Chapter two concerns the development of a microfluidic mass spectrometry platform. The chapter contains an introduction to electrospray ionisation mass spectrometry and previous research into this area will be presented. Previous research focuses on three different microfluidic designs, chips capable of electrospray directly from the chip edge, from inserted electrospray emitters, and from integrated emitters. The work presented in this thesis concerns the development of a microfluidic MS platform with an inserted electrospray emitter, as it

eliminates the unstable electrospray associated with prolonged use of a chip capable of electrospray directly from the edge of the chip and allows electrical contact to be made directly to a stainless steel capillary, therefore eliminating the need to apply a conductive coating to the emitter which has been shown to have a finite operational time. The objective of this work was to develop a microfluidic platform with a mass spectrometric response comparable to or greater than that of the commercial probe, which could also be interfaced with the mass spectrometer with ease and preferably little or no modification to the mass spectrometer required.

Measuring the extent of drug precipitation under different conditions is critical in determining how the drug will behave *in vivo*, chapter three presents a microfluidic device that uses light scattering to monitor drug precipitation as the pH is shifted from an acidic pH reflecting that of the stomach to a pH typical of that observed in the intestines. The chapter contains an introduction to drug solubility, the issues associated with drug precipitation *in vivo*, nucleation theory and a brief introduction into light scattering theory. The aim of the experiments carried out in this chapter was to evaluate light scattering as a possible detection technique for drug precipitation and to develop a microfluidic analytical device which could determine the extent a weakly basic drug precipitates upon gastric emptying into the small intestine.

Chapter four concerns the use of microfluidics to evaluate the use of different additives which can affect the absorption of the drug *in vivo*. An overview of the drug formulation process will be given and the role of water soluble polymers as additives in drug formulations will be discussed. The microfluidic device presented in chapter three will be used to investigate two different water soluble polymers which are frequently used in drug formulation in the pharmaceutical industry. The effect of these polymers on ketoconazole precipitation will be determined and compared to results obtained from macroscale experiments and a similar study reported in the literature. A microfluidic device designed to increase the number of additives which can be examined in an experiment will be evaluated using different colour dyes and suggestions on how the design of the microfluidic device could be developed further will be discussed.

Chapter five investigates the use of microfluidics to determine precipitation kinetics. A brief introduction to nucleation theory will be presented. The benefits of using droplet-based microfluidics to monitor precipitation kinetics will be considered and two microfluidic devices capable of determination of precipitation kinetics which have been reported in the literature will be discussed. A microfluidic device based on the spiral design reported in chapters three and four will be presented and used to determine the onset time of drug precipitation. Both the effectiveness and limitations of the device will be discussed in detail.

# Chapter 1: Microfluidics and its applications within the pharmaceutical industry

## 1.1 Microfluidics

### 1.1.1 Introduction to microfluidics

Microfluidics concerns the behaviour and manipulation of fluids within microchannels. Diversification of MEMS (microelectrical-mechanical systems) led to the development of the field of microfluidics in the 1990s. As microfluidics is a developing field, its full potential is still far from being realised at present. The possible applications of microfluidics are numerous. In biotechnology, the fields of proteomics, genomics and cytology are already being influenced. The portability of microfluidic devices has led to their use as point of care (POC) devices in medicine to detect substances present in the body, and in the field for air and water analysis. It is predicted that microfluidic devices will also benefit drug discovery and development within the pharmaceutical industry. Synthesis of new chemical entities (NCEs) has been accomplished through the use of on-chip combinational chemistry, whilst the high throughput capabilities of microfluidic technology provide a possible route to test these NCEs.

The advantages of microfluidic systems are abundant. They include low sample consumption, fast analysis and reaction times, possibility of parallelization and high throughput, portability and integration. Integration is a major attraction. The ultimate goal of most microfluidic designs is to produce a multifunctional chip. A microchip which is capable of performing all the functions that the user requires is referred to as a 'Lab on a Chip' or micro total analysis system (μTAS), and was first envisioned by Manz *et al*.[1] Many laboratory functions can be incorporated on chip through the use of reservoirs, channels, mixers, as well as integrated valves, pumps and electrodes. Hence, sample preparation, reaction, separation, preconcentration and detection can all be accomplished on the same chip. Examples of these systems include chemical microreacters,[2] DNA amplifiers[3] and cytometers.[4]

Microscale properties differ considerably from those at the macroscale. Scaling laws can be used to predict these changes. Originally used by engineers to predict the implications of scaling up reactions, they give a measure of how properties of a system change as its dimensions are altered. They can be used in microfluidics to evaluate the potential

success of a microfluidic design, the table below gives an indication of how physical properties change with the size, $l$ of the system (table 1.1).

| Physical Quantity | Scaling Law |
|---|---|
| **Intermolecular Van der Waals force** | $l^{-7}$ |
| **Time** | $l^{0}$ |
| **Capillary force** | $l^{1}$ |
| **Distance** | $l^{1}$ |
| **Flow velocity** | $l^{1}$ |
| **Thermal power transferred by conduction** | $l^{1}$ |
| **Electrostatic force** | $l^{2}$ |
| **Diffusion time** | $l^{2}$ |
| **Volume** | $l^{3}$ |
| **Mass** | $l^{3}$ |
| **Force of gravity** | $l^{3}$ |
| **Magnetic force with an exterior field** | $l^{3}$ |
| **Magnetic force without an exterior field** | $l^{4}$ |
| **Centrifugal force** | $l^{4}$ |

**Table 1.1: Comparison of the scaling laws of physical quantities.[5]**

It can be seen that forces that dominate on the macroscale become less significant as the size of the system is decreased. On the microscale for instance, forces of gravity become negligible compared to capillary forces. Fluid flow on the macroscale is dominated by inertial effects, whereas on the microscale viscous forces are prevalent. There are two fluid regimes that define flow, turbulent and laminar. Turbulent flow is chaotic, whereas laminar flow is ordered and allows two fluids to run parallel to each other with minimal mixing. The Reynolds number (Re) (Equation 1.1) is a dimensionless quantity which provides the ratio of inertial to viscous forces acting on the fluid, hence determining whether the flow is laminar or turbulent in nature. Typically, if Reynolds numbers are less than 2000 the flow is laminar while turbulent flow occurs above this value, however this should only be used as a guide as the transition is believed to take place anywhere between 1500 and 2300. As the Reynolds number is dependent on channel dimensions, Reynolds numbers are inherently low in microfluidic devices and laminar flow dominates.

$$Re = \frac{v\, D_U}{\mu} \qquad [1.1]$$

Where $v$ is the characteristic velocity of the fluid (m $s^{-1}$), $D_U$ the hydraulic diameter of the channel (m), and $\mu$ is the kinematic viscosity of the fluid ($m^2$ $s^{-1}$).

The dominance of laminar flow in microfluidic systems result in mixing occurring through molecular diffusion. At the low microscale diffusion can be a sufficient mixing mechanism, however in high microscale systems the timescales required for diffusion can become inconvenient. Attempts have been made to improve mixing time, for example through the use of chaotic advection.[6]

Fluid movement in microfluidic systems typically occurs via pressure driven flow or electroosmotic flow (EOF). Pressure driven flow is an example of positive displacement pumping; the flow produced is non uniform in nature and assumes a pseudo parabolic profile. Electroosmosis is the movement of an ionisable fluid under an electric field. EOF occurs when the channels of the microfluidic system are charged under experimental conditions, resulting in a double layer of oppositely charged species in the fluid called the Stern layer. Redistribution of charges within the fluid results in a diffuse layer of charged ions. A plane of shear will be present between these two layers due to the difference in the properties and electrical imbalance of each. The electrical imbalance between the layers is called the zeta potential, ζ.

The charged fluid will undergo motion if an electric field is applied parallel to the channel. In contrast to pressure driven flow, electroosmotic flow generates a uniform, blunt profile, the bulk velocity of which can be given by the von Smoluchowski equation:

$$V_{EOF} = \frac{\varepsilon \zeta \mathrm{E}}{4 \pi \eta} = \mu_{EOF} E \qquad [1.2]$$

Where $V_{EOF}$ is the velocity of electroosmotic flow (cm $s^{-1}$), ε is the permittivity of the medium (F $m^{-1}$), ζ is the zeta potential (V), η is the viscosity of the medium (N s $m^{-2}$), $\mu_{EOF}$ is the electroosmotic mobility ($cm^2$ $V^{-1}$ $s^{-1}$) and $E$ is the applied electric field (V $cm^{-1}$).

## 1.1.2 Fabrication materials and techniques

Early chips were primarily produced from silicon as the manufacturing techniques required for this substrate were highly transferable from those used in the microelectronic industry. Glass also became a popular material as many of the techniques used for silicon were applicable to glass. As well as being a readily available, inexpensive material, the well characterised surface properties of glass popularised its use. More recently however microchips are polymer based, they are more suitable for mass production than glass or silicon and the diversity of polymers means that properties can be tailored to the system.

A number of metal microchips have also been produced, however the difficulty utilising electric fields in these systems and the fact that they are not chemically inert limit their use. The most popular microfabrication techniques are detailed below.

Lithographic techniques are largely used for glass and silicon microfluidic device fabrication. A pattern is transferred using electromagnetic radiation onto a substrate covered in a layer of photoresist. When the photoresist is developed the areas that were exposed to the radiation will behave differently than the areas that were shielded. Numerous techniques can now be used to produce the required design, such as wet or dry etching. This technique is expensive and labour intensive.

Polymer based techniques include computer numerical controlled (CNC) milling, photoablation, hot embossing, and injection moulding. CNC milling involves machining the chip design on the substrate using drills whereas photoablation uses laser pulses to break polymer bonds and produce channels. Hot embossing requires that the substrate is heated to just over its glass transition temperature and applied to a mould which has been heated separately, pressure applied between the two results in transfer of the design. Injection moulding is a related technique in which plastic granules are melted and injected into the mould. The moulds used are typically fabricated from metal.

Laminate fabrication methods are quite different from the methods described above. The microdevice is constructed from layers of material which have been laser or stamp cut to give the desired design once bonded together. Both polymer and glass substrates have been used. Polyethylene terephthalate, more commonly known as Mylar, is a frequently used material for this technique.

### 1.1.3 Multiphase microfluidics

Microfluidic research was originally based on continuous flow systems, however multiphase microfluidic systems are increasingly being reported. Multiphase microfluidics concerns aqueous phase droplets dispersed in an immiscible organic phase and has many advantages over continuous flow systems. The main benefit of droplets is that they serve as discrete packages, allowing the introduction of multiple species on the same chip. As they are typically surrounded by carrier fluid, they often do not come in contact with the channel walls, reducing possibility of contamination. Reagent consumption is also lower than that of continuous flow systems as the reagents are confined to small droplets, not the whole channel.

These discrete packages are referred to as either droplets or plugs/slugs. The former are generally spherical in nature as they have dimensions less than the channel dimensions. The latter terms are used interchangeably, plugs/slugs occur when the droplet diameter is greater than that of the channel resulting in their elongation within the channel. Droplets can be subjected to deformations when viscous effects begin to dominate over capillary effects. The ratio of these effects is given by a dimensionless number, termed the capillary number (Ca) and is given below. When the capillary number is low the droplets will be spherical, higher capillary numbers may result in deformations induced by viscous forces.

$$Ca = \frac{\eta_C \nu_C}{\gamma} \qquad [1.3]$$

Where $\eta_c$ is the viscosity of the continuous phase (kg $m^{-1}$ $s^{-1}$), $\nu_c$ is its velocity (m $s^{-1}$) and $\gamma$ the interfacial tension (kg $s^{-2}$).

### 1.1.3.1 Droplet generation

Droplets can be produced using microinjectors,[7] needles[8] and electric fields.[9] However, the most commonly used methods involve droplet generation in an immiscible carrier fluid using a T-junction[10-12] or flow focusing geometries.[13,14] The latter two droplet generation techniques will be discussed in more detail.

A schematic of droplet generation at a T-junction is shown in figure 1.1a. Two surface effects are competing at the T-junction; interfacial tension and inertial effects, the interfacial tension desires the interface to be as small as possible, whereas inertial effects wish to drag the interface downstream. The Weber number ($We$) gives the ratio of inertial effects to interfacial tension.

$$We = \frac{\rho \nu^2 l}{\sigma} \qquad [1.4]$$

Where $\rho$ is the density of the fluid (kg $m^{-3}$), $\nu$ is its velocity (m $s^{-1}$), $l$ is the characteristic length (m) i.e. droplet diameter, and $\sigma$ is the surface tension (N $m^{-1}$).

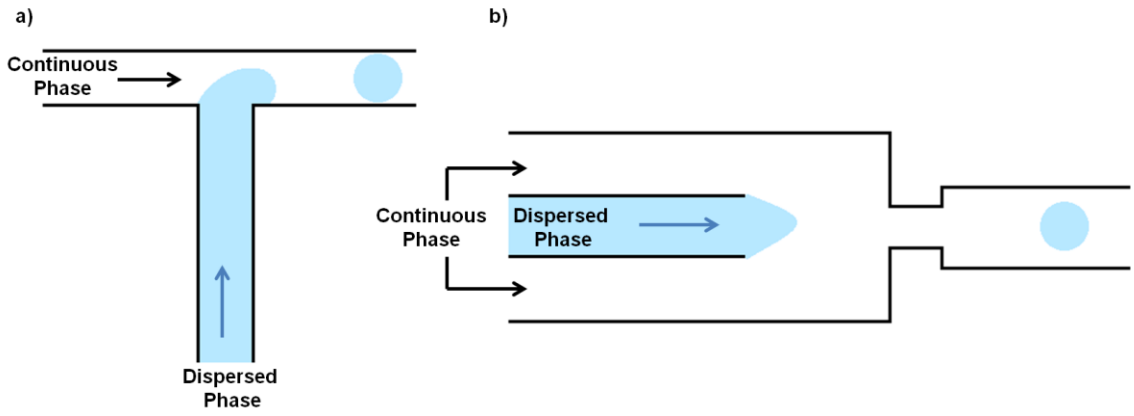


**Figure 1.1: Droplet generation in an immiscible carrier fluid at a T-junction (a) and using flow focusing geometry (b).**

Droplet production rate and droplet size are dependent on the relative flow rates of the continuous and disperse phases. An increase in continuous flow rate will result in a decrease in the diameter of droplets produced and an increase in production rate. The opposite is true when the disperse flow rate is increased, the resulting droplets will have a larger diameter but will be produced at a lower frequency. As the production rate is restricted by the required droplet size, integration of multiple T-junctions on chip has been investigated in order to mass produce droplets of a desirable size. In 2008 Nisisako *et al*. reported a chip with 128 T-junctions for mass production of droplets.[15]

The flow focusing geometry consists of a central channel for the disperse phase with continuous phase channels at either side (figure 1.1b). Where the channels converge, droplets are generated. The inner flow is driven into a narrow stream due to the viscous force applied by the outer flows. Generation of droplets will occur when this stream breaks up either in, or downstream, from the orifice. Reduced droplet sizes can be generated using this technique.

### 1.1.3.2 Droplet transportation

Electrowetting has been used to achieve droplet transportation across a surface containing an embedded electrode array. If the droplets are of sufficient size to cover the space between electrodes, application of an electric field to consecutive electrodes whilst turning off the voltage to the previous electrode will result in droplet movement. It should be noted however that this technique requires droplet contact with a surface which could lead to sample contamination.

Within microfluidic channels, droplets can be transported in numerous ways. Passive transport of droplets with the flow of the continuous phase is common, however droplet velocity cannot be altered in the system by simply changing the flow rate of the continuous phase as this will affect droplet generation. The velocity of droplets can be modified by altering the geometry of the channel, for example an increase in the width of the channel will naturally lead to a decrease in the flow velocity.

Dielectrophoresis concerns the movement of a particle by the application of an electric field. When a neutral particle is subjected to an electric field gradient, a force called the dielectrophoretic force appears, resulting in the movement of the particle towards a region of higher electric field. For positive movement of the particle, the carrier fluid must have a lower dielectric constant than the particle.

Thermocapillary forces can also be used to transport droplets. Typically embedded microheaters are used to generate a temperature gradient within the system leading to a difference in surface tension. The droplet will move towards the cooler region of the microfluidic device where the surface tension is greater.

### 1.1.3.3 Droplet manipulation

Link *et al.* present methods of generating, fusing, splitting and sorting droplets by electrostatics (figure 1.2).[16] During droplet generation an electric field is applied enabling control over droplet size and time of production, as well as charging the droplets so that further manipulation is possible. Droplet coalescence is achieved by oppositely charging the desired droplets for fusion. The attraction of these charges overcomes the surface tension, drainage forces and surfactant effects that hinder droplet fusion. The extensional force induced by the applied electric field can be used to split the droplet, but also serves as a method of recharging neutral droplets for further manipulation. The droplets can also be sorted into different channels based on their charge by application of an electric field on the desired channel. Electrostatics are not the only way to control droplets on chip, some other methods that have been employed are discussed below.

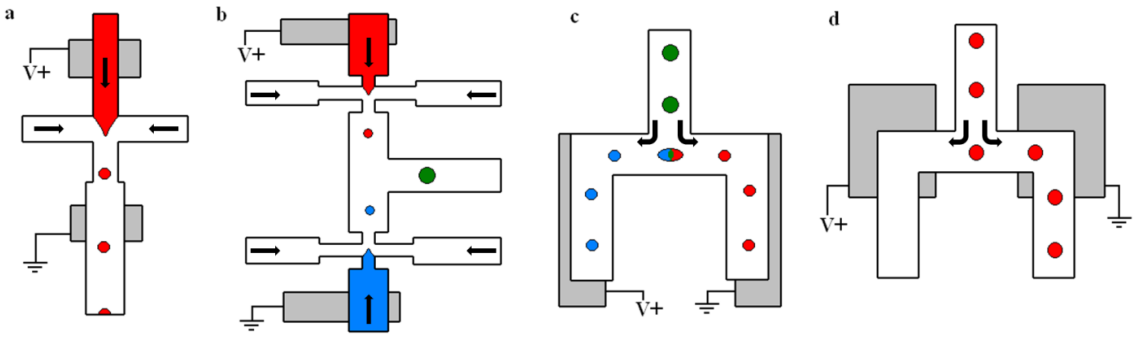


**Figure 1.2: Droplet manipulation using electrostatics. a) Droplet generation, b) Droplet fusion, c) Droplet fission and d) Droplet sorting. Red circles represent positively charged droplets, blue circles represent negatively charged droplets and green circles neutral droplets. The black arrows indicate the direction of flow. Adapted from Link *et al*.[16]**

Droplet fusion has been achieved by modifying the surface properties of the channel. Patterned poly(acrylic acid) has been photografted onto channel sections, the hydrophilic nature of which effectively traps the droplet, allowing fusion between the trapped droplet and a subsequent droplet.[17] Altering the channel geometry can also lead to droplet coalescence, as increasing the width of the channel results in a decrease in the velocity of the droplets and can result in their fusion.[18,19] The difference in velocity of different size droplets has also be used to fuse them.[6]

Droplet splitting can be accomplished through the introduction of a branching point into the channel.[6, 20] The volume proportions of the droplets after splitting can be controlled by altering the fluidic resistance of the branches,[21] and through the generation of a surface tension gradient by heating one channel after the branching point.[22]

Droplets can be sorted by size using an asymmetric junction,[23] however, it is of more use to sort droplets based on content. This has been achieved using electric fields, as detailed above, often in association with fluorescence activated cell sorting (FACS).[24, 25]

### 1.1.4 Detection techniques

The detection techniques for single phase microfluidics and multiphase microfluidics are the same. Detection on chip can be achieved using optical techniques such as fluorescence and luminescence, as well as electrochemical techniques such as capacitance and potentiometry. Integration of microfluidic devices with mass spectrometry has also been investigated, typically using electrospray as the ionisation source. The use of mass spectrometry as a form of detection has been a very recent accomplishment for multiphase microfluidics, as most designs require extraction of aqueous droplets from the

organic carrier fluid prior to mass spectrometric analysis due to carrier fluid incompatibility with electrospray ionization. Electrospray ionization mass spectrometry (ESI-MS) and its use as a detection technique for microfluidic systems will be discussed in chapter 2.

## 1.2 Drug discovery and miniaturisation

### 1.2.1 Background to drug discovery and development

Production of new drugs takes place in two stages, drug discovery and drug development. Drug discovery encompasses target selection, lead identification and lead optimisation, and the drug development process consists of clinical trails, manufacturing and product management (figure 1.3). Completion of these processes can take between 12-20 years.

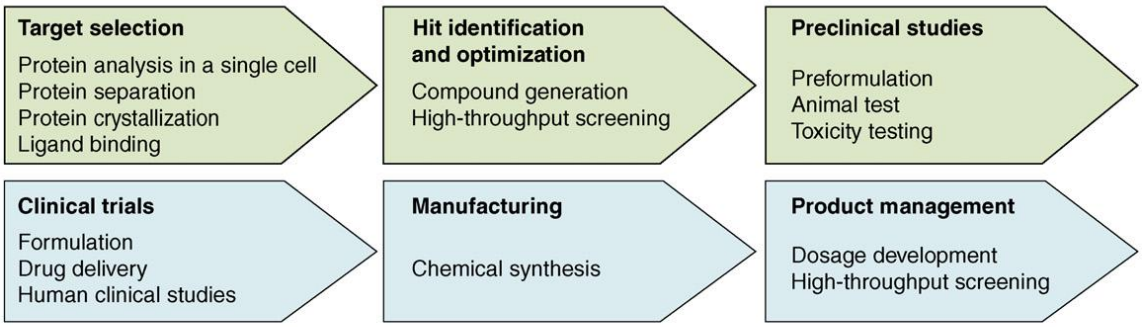


**Figure 1.3: The drug discovery and development process. Green arrows denote steps of drug discovery and blue arrows drug development.[26]**

Target identification involves the classification of the disease mechanism to be treated. The response of the system in the presence of potential drug compounds is measured and positive responses may become lead compounds for future development. The compounds analysed are the result of two different approaches, rational drug design and high throughput screening (HTS). The former requires an understanding of the biological target so that drugs can be tailored to the system. This normally requires knowledge of compounds that already fit into the target, typically natural compounds that are involved in the process or drug molecules with known activity towards the target. A more frequently used technique is high throughput screening, in which thousands of molecules are screened against the target. The large amount of compounds screened in drug discovery require that experimental procedures are high throughput, automated and require low reagent samples in order to keep processing time and costs at a minimum. Positive responses give an indication of molecular structures which may be therapeutic. Features of the structure which are favourable and those that are unfavourable are recorded and

referred to as structure activity relationships (SARs). SARs can be used to design molecules of high potency with desirable drug properties. The toxicology of the lead compounds will then be assessed, undergo preformulation, and their efficacy and safety evaluated using animal testing. Of the thousands of compounds screened, only a few compounds will progress to the development stage.

During the drug development stage the potential drug is formulated, additives will be added to improve bioavailability and the dosage will be considered. This is followed by clinical testing, initially on healthy volunteers to determined safety and dosage of the potential drug, followed by a small group of patients then a larger group of patients to determine safety and efficacy. The bioavailability, tolerated dose range and the therapeutic and side effects will be noted. The new chemical entity (NCE) will only be submitted for marketing approval if the results from clinical trials are favourable and regulations of the drug licensing authorities are met.

### 1.2.2 'Drug-like' properties and their determination

There is a high failure rate of NCEs in drug discovery and development due to the lack of 'drug-like' properties they exhibit. A study in the late 1980s suggested that nearly 40% of NCEs which had been withdrawn from further development were due to poor biopharmaceutical properties.[27]

Properties of fundamental importance are solubility, permeability, lipophilicity and ionization. From these properties it is possible to predict how the compound will behave in the body, as the drug's absorption, distribution, metabolism and excretion (ADME) can be predicted. Toxicology is also a crucial property with poor toxicology results contributing significantly to failure of NCEs. As poor physicochemical properties are the main source of failure in the drug development stage, it is crucial that these properties are determined as soon as possible. Development of NCEs with poor drug like properties can be time consuming and lead to escalating costs, as modifications to the compounds structure may be needed to improve the deficient property, or other properties may need to be improved to negate the deficiency.

The solubility of a substance is the quantity of that substance which will dissolve in a given amount of solvent at a given temperature. In drug discovery the solubility of a NCE will be determined by incubation of an excess of NCE in a buffer, typically under agitation. When

equilibrium has been reached the solids are removed by filtration or centrifugation and the concentration of NCE dissolved determined using HPLC or UV-Vis spectroscopy.

Permeability refers to the ease at which drugs are able to cross cell membranes. There are many *in silico* and *in vitro* methods that mimic membranes in the body. In early drug discovery, permeability measurements are similar to the shake flask method used for lipophilicity determination, except artificial membranes are used in a liposome/water system.

Lipophilicity is the affinity of a compound for a lipophilic environment. It is linked to the compounds solubility and permeability, for example if the lipophilicity of the NCE is too high then naturally it will be hydrophobic in nature and hence have low aqueous solubility, on the other hand if the lipophilicity is too low permeability will become an issue. Lipophilicity is typically determined from the partition of the NCE between two immiscible phases (water/1-octanol). The NCE is allowed to reach equilibrium, the phases are then separated and the concentration of NCE in each determined. The partition is expressed as a logarithm partition coefficient (logP), however logP only takes into account the partition of neutral species and is therefore not the best indicator of lipophilicity in *vivo* where many drugs will be ionised. As the proportion of drugs with an ionisable group has been estimated at 95%,[28] the distribution coefficient (logD) is often used to measure the lipophilicity of the NCE. LogD takes into account both neutral and charged species of the NCE and is dependent on the pH the measurement was taken, as the degree of ionisation of the NCE will change with pH. Measurement of logD allows the lipophilicity to be determined at physiologically relevant pH, i.e. pH 7.4, the pH of blood serum. This method is referred to as the 'shake flask' method, it is labour intensive and sensitive to impurities, therefore logP and logD values are frequently not measured but calculated using computational methods.

Whether the NCE is in an ionised state is an important consideration for drug absorption, as uncharged species exhibit greater membrane permeability. Typically $pK_a$ values are determined by potentiometric titration, however UV-Vis spectrometry, NMR spectroscopy, Liquid chromatography (LC) and capillary electrophoresis (CE) have also been used.[29]

Whether a NCE is likely to exhibit good drug like properties can be predicted by Lipinski's rule of five.[30] Lipinski *et al*. postulated that poor absorption was more likely when the

NCEs had more than five H-bond donors and ten H-bond acceptors, a molecular weight greater than 500 and a logP greater than 5.

### 1.2.3 Application of microfluidic technology to the drug discovery and development process

Improvement of the drug discovery process has focused on automation, increasing throughput and decreasing the quantity of NCE consumed. As a result, the application of microfluidics within drug discovery and development is very appealing. Pharmaceutical assays have the potential to be automated through the integration of multiple functionalities on a single chip, multiphase microfluidics could allow many NCEs to be studied at one time, and the small volume of microfluidic droplets means that sample consumption is minimal.

Miniaturisation within the pharmaceutical industry has already taken place in the form of microwell plates, the number of wells on each plate has increased over time from 96 to 384 to 1536. As the number of wells on the plate is inversely proportional to the volume of each well, these developments have resulted in reduced sample consumption. Further miniaturisation of microwell plates is limited by the volume of drug compounds that can be dispensed robotically. Microfluidic devices may be able to overcome this limitation through the used of droplet based systems. A number of both continuous flow and droplet based microfluidic devices which have potential applications within drug discovery and development are given below to emphasize the impact microfluidic technology could have in the future.

#### 1.2.3.1 Continuous flow microfluidic devices

Lee *et al.* presented a microfluidic device capable of investigating β –Amyloid aggregation.[31] Formation of cytotoxic β –Amyloid plaques are thought to play a major role in brain dysfunction in Alzheimer's disease. The device was used to investigate the effect of twelve small molecules and metal ions on β –Amyloid aggregation. The β –Amyloid monomer was attached to a microfluidic channel 100 µm x 100 µm in cross section, and a solution containing β –Amyloid monomers and the molecule/ion of interest continuously pumped through the channel. The channels were then treated with Thioflavin T (ThT) and formation of β –Amyloid investigated using a fluorescent microscope. Results presented in this study were comparable with macroscale studies.

### 1.2.3.2 Droplet based microfluidic devices

Droplet based systems can enable multiple NCEs to be studied like traditional well plate based methods, but offer the advantage of lower volume requirements (nanolitre and even picolitre volumes), and possibility of incubation without concern for evaporation.

Garcia-Egido *et al*. reported combinatorial synthesis of pyrazoles in microfluidic droplets and their subsequent on chip characterisation using UV detection.[32] Seven different 1,3-dicarbonyl reagents and three different hydrazines were introduced on chip using an autosampler, allowing generation of a 7x3 library of pyrazoles. The authors reported 99% conversion for 16 out of the 21 compounds generated, and those with less than 99% conversion benefited from longer reaction times on chip.

Lombardi and Dittrich examined absorption and distribution properties by using magnetic particles (coated with the target protein human serum albumin (HSA)) dispersed in microfluidic droplets to measure the binding constants of drug-protein interactions.[33] Droplets containing the magnetic beads and the drug of choice (warfarin in this case) were generated and the system allowed to reach equilibrium between bound and unbound drug. Separation of the unbound drug from the bound drug is achieved through application of a magnetic field droplet at T-junction (figure 1.4). The affinity of binding constant is determined from the ratio of bound drug to unbound drug.

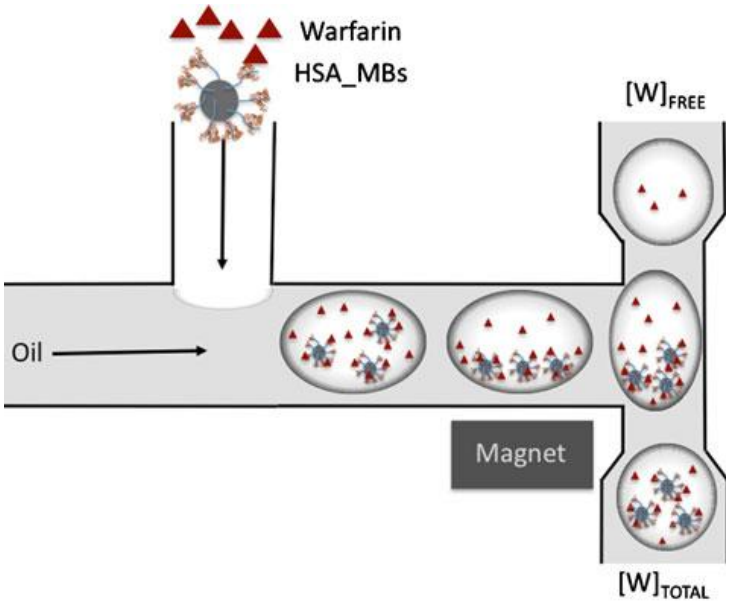


**Figure 1.4: Schematic of a microfluidic method to determine binding constants for drug-protein interactions. Microfluidic droplets containing human serum albumin (HSA) coated magnetic beads (MB) and a drug of interest (warfarin) are generated in an immiscible carrier stream, The system is allowed to reach equilibrium, unbound drug separated from bound drug through application of a magnetic field at a T-junction and the binding constant determined from their ratio.[33]**

Carlsson and Karlberg presented a method for partition coefficient determination.[34] Plugs of organic and aqueous phases are aspirated into a capillary and separated from other organic aqueous plugs by air bubbles. The plugs are pumped forwards and backwards through a UV-Vis electrophoresis detector until the signal obtained remained consistent. The partition coefficients were determined in just four minutes, required only 360 nL of sample and 210 nL of octanol phase and are in good agreement with the traditional shake flask method.

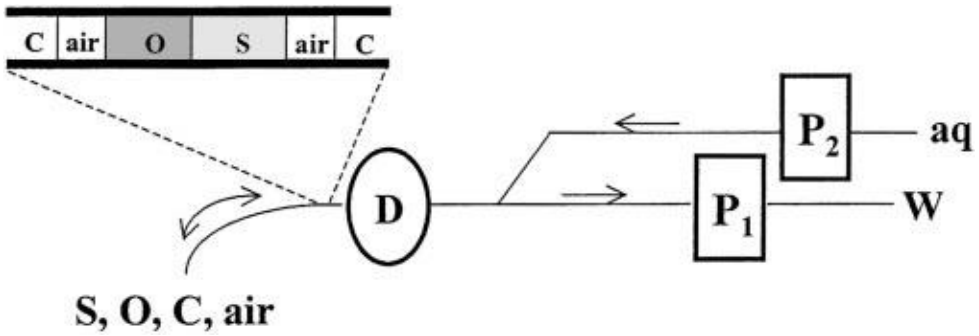


**Figure 1.5: Microfluidic setup used by Carlsson and Karlberg to determine partition coefficients.[34] Octanol (O) and sample (S) plugs are aspirated into a capillary. The plugs are separated from other octanol and sample plugs by air and a carrier solution (water) (C). These samples are pumped forwards and backwards through a capillary UV-Vis electrophoresis detector (D) by pumps P1 and P2 until signal remains constant i.e. the system has reached equilibrium.**

In 2008 Alimuddin *et al*. used a similar technique to determine partition coefficients.[35] The device consisted of a T-fitting in which the immiscible phases were mixed producing alternating droplets of octanol and water, and a separation channel containing a polytetrafluoroethylene (PTFE) membrane. The droplets were pumped into the separation channel and application of a pressure difference across the channel allowed separation of the octanol and water phases. Detection was carried out offline using HPLC. The partition coefficients obtained with this chip showed excellent correlation with values obtained from the traditional shake flask method. The large surface-to-volume ratio of the droplet allowed a contact time between phases of just six seconds prior to separation compared to the five minutes recommended by OECD guideline for testing chemicals.[36]

Brouzes *et al*. reported a microfluidic device capable of high throughput single cell screening (figure 1.6).[37] The cytotoxicity of mitomycin C on human monocytic U937 cells was determined by fluorescently coding droplets containing different concentrations of the drug. These droplets were then merged with droplets containing single cells and incubated off chip for 24 hours. The resulting droplets were reintroduced on chip and the

fluorescence measured to determine the effect of the drug on the cells and obtain coding information to determine droplet composition. This technology could be developed to transfer drug libraries into encoded droplets for high throughput assays.

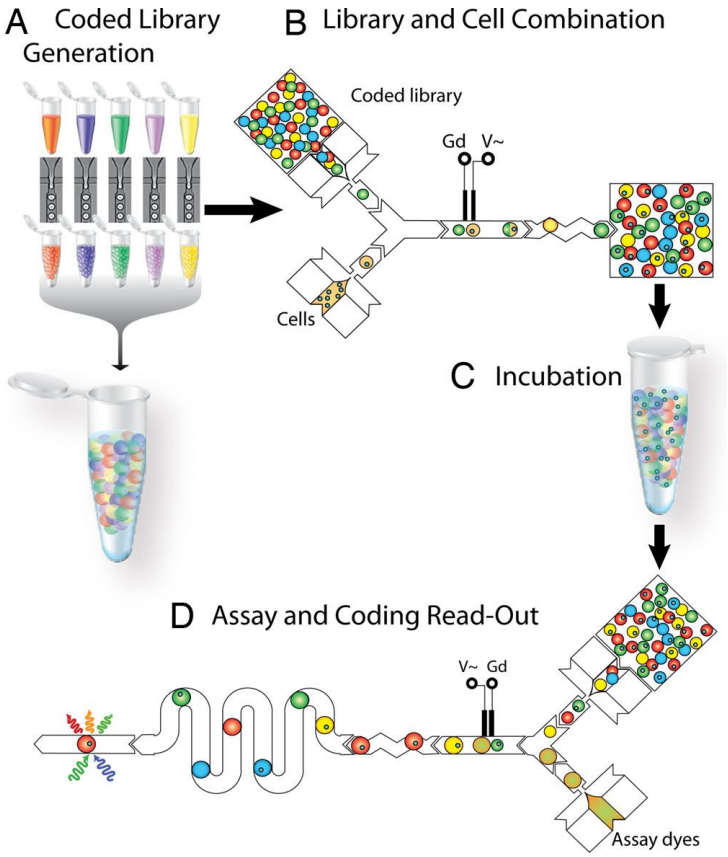


**Figure 1.6: A single cell cytotoxicity screen using microfluidic technology. A) droplets containing different concentrations of a drug are generated from a bulk solution and fluorescently coded so their concentration is discernable at the detection point. B) the coded droplet and single cell droplet are merged on chip. C) the droplets are incubated off chip for 24 hours. D) the droplets are reintroduced onto the chip and their fluorescence determined providing information on drug concentration and the effect of the drug on the cell.[37]**

### 1.2.3.3 'Organ-on-a-chip' devices

Devices which incorporate cells and produce organ function on chip are beyond the scope of this project, however a couple examples are reported below to highlight the capabilities of these devices and the role they may play in drug discovery.

Huh *et al*. developed a 'lung on a chip'.[38] The alveolar-capillary interface of the lung is produced on chip by construction a 10 μm think porous membrane between two microchannels, human alveolar epithelial cells are cultured on one side and human pulmonary microvascular endothelial cells on the other. The mechanical function of the

lung as air is inhaled/exhaled is also mimicked though application of a vacuum on channels either side of the membrane channel (figure 1.7). The authors used this device to examine epithelial and endothelial barrier function, and to determine the toxicology of nanoparticles and the effect of bacteria and inflammatory cytokines in the alveoli.

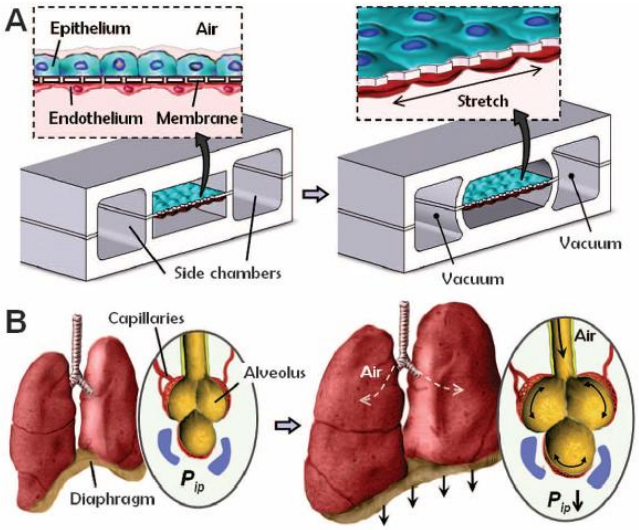


**Figure 1.7: The 'lung-on-a-chip' device developed by Huh *et al*.[38] (A) the microfluidic design incorporating a 10 μm think porous membrane between two microchannels with human alveolar epithelial cells cultured on one side and human pulmonary microvascular cells on the other. The effect of breathing on the alveoli is recreated by application of a vacuum to channels either side of the membrane channel, mimicking the expansion and relaxation of the alveolar-capillary interface during inhalation and exhalation respectively (B).**

Sung *et al*. presented a microfluidic device to determine pharmacokinetic-pharmacodynamic (PK-PD) properties of drugs.[39] The device imitates a multi-organ system through the use of multiple cell culture chambers connected via microfluidic channels. The effect of an anticancer drug on liver, tumour and marrow cells was determined using this device. The different cell culture chambers allow the effect of the drug on different cell lines to be investigated.

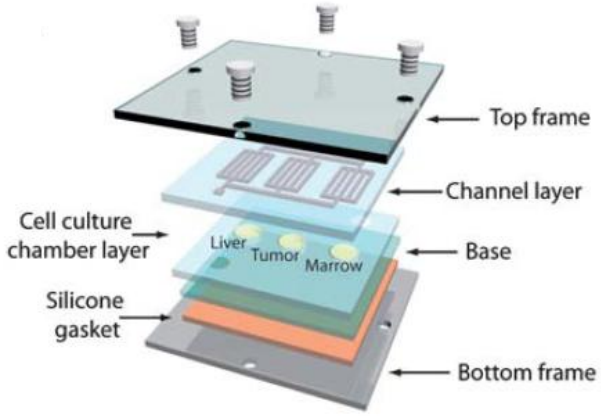


**Figure 1.8: A schematic of the microfluidic device developed by Sung *et al*. to investigate the pharmacokinetics-pharmacodynamic properties of an anticancer drug.[39] The design consists of a microfluidic channel layer and a cell culture layer sealed between two polycarbonate layers.**

Organs-on-chip have the potential to replace some animal testing, which apart from obvious ethical drawbacks, are time consuming, expensive and there exist concerns over the biological relevance of animal studies to humans. The cells on these chips could also be taken from the patient to develop personalised medicines.

### 1.2.3.4 Current impact of microfluidic technology within the pharmaceutical industry

To date, applications of microfluidic technology within drug discovery and development are limited. Possible reasons for this include the reliance of pharmaceutical companies on established techniques, there is a higher risk of failure by introducing new technology. Another factor is the recent large scale investment in robotic technology for automation in the pharmaceutical industry which means that technology designed to compliment this technology will be better received. Instrumentation companies are also indisposed to adopt this technology as detection typically occurs on chip, typically providing low cost alternatives to large instruments. Moreover, the operation of such devices still often require specialized skills, as there are still issues to overcome with microfluidic technology, such as air bubble formation in the channels and high throughput sample delivery.

# Chapter 2: Electrospray ionisation mass spectromtetry (ESI-MS) platforms

## 2.1 Chapter Overview

This chapter concerns the development of a microfluidic mass spectrometry platform. Electrospray ionisation was chosen as the desired ionisation technique as it is extensively used in drug discovery and development, and has been shown to be relatively easily coupled to microfluidic technology. This chapter will give an introduction to electrospray ionisation mass spectrometry and previous research into this area will be presented. Previous research focuses on three different microfluidic designs, chips capable of electrospray directly from the chip edge, from inserted electrospray emitters, and from integrated emitters. The work presented in this thesis concerns development of a microfluidic MS platform with an inserted electrospray emitter, as it eliminates the unstable electrospray associated with prolonged use of a chip capable of electrospray directly from the edge of the chip and allows electrical contact to be made directly to a stainless steel capillary, therefore eliminating the need to apply a conductive coating to emitter which has been shown to have a finite operational time. The objective of this work was to develop a microfluidic platform with a mass spectrometric response comparable to or greater than that of the commercial probe which could be interfaced with the mass spectrometer with ease and with preferably little or no modification to the mass spectrometer required.

## 2.2 Introduction to electrospray ionisation mass spectrometry

### 2.2.1 Electrospray ionization and its role within the pharmaceutical industry

Electrospray ionization (ESI) is an atmospheric ionisation (AI) technique, allowing both positive and negative gaseous ions to be produced from the liquid phase by application of an electric field. The integration of electrospray ionization and mass spectrometry has become a commonly used analytical technique in biological and biochemical research and within the pharmaceutical industry. It gained popularity in the 1990s due to its ability to analyse samples directly from liquid chromatography (LC). Other ionization techniques that generate gaseous ions from solution were available before the advent of electrospray ionization, such as fast atom bombardment (FAB). However FAB suffers from high

chemical background and is limited to compounds of less than 6,000 Da which are compatible with the liquid matrix.

Mass spectrometry impacts every sector of the drug discovery and development process, from assessing the indentity and purity of NCEs synthesized using combinational chemistry, to high throughput screening of compound libraries for activity, to determination of ADME properties and drug metabolite identification, to manufracturing and quality control. More specifically electrospray ionization mass spectrometry is used to indentify both NCEs and their metabolites, identify disease targets through proteome discovery, and characterise product related variants.[40] It is envisaged that integration of microfludics with this technology could increase throughput further.

## 2.2.2 History of electrospray

The application of an electric field to a solution as a possible method to produce a fine spray was known of well before it was investigated as an ionisation technique for mass spectrometry. In 1914, Zeleny undertook experiments that examined the electrical discharge of a liquid when subjected to an electrical potential.[41] Not only had it been investigated as early as this, it already had a number of practical applications before electrospray ionization mass spectrometry, examples include crop spraying, electrostatic painting, spray painting, fuel atomisation and electrostatic emulsification.[42]

## 2.2.3 Operational procedure and mechanism of ESI

The electrospray process is facilitated by the application of an electric field generally to a capillary tip, resulting in division of oppositely charged ions in the solution. The electric field ($E_c$) (V $m^{-1}$), exhibited at the capillary tip can be given by the following equation.[43]

$$E_C = \frac{2V_C}{r_C \ln\left(\frac{4d}{r_C}\right)} \qquad [2.1]$$

Where $r_c$ is the radius of the capillary (m), $d$ is the distance from the planar electrode (m), and $V_c$ is the given potential (V).

In 1986 Smith derived an equation to approximate the potential required for the onset of electrospray ($V_{ON}$). It should be noted however that stable electrospray requires a potential a few hundred volts more than the calculated voltage.[44]

$$V_{ON} = A_1 \left(\frac{2\,\gamma\, r_C\, \cos\theta}{\varepsilon_0}\right)^{\frac{1}{2}} \ln\left(\frac{4d}{r_C}\right) \qquad [2.2]$$

Where $V_{ON}$ is the required potential (V), $A_1$ is an empirical constant, $\gamma$ is the surface tension (N m$^{-1}$), $r_c$ is the capillary radius (m), $\varepsilon_0$ the permittivity of the vacuum (C N$^{-1}$ m$^{-2}$), and $\theta$ is the Taylor cone half angle.

When operating in the positive ion mode a voltage is applied to the capillary tip, resulting in accumulation of positive ions at the solution meniscus, the excess positive charge causes repulsion and expansion of the meniscus away from the capillary tip. A cone shaped meniscus is formed when the surface tension forces equal the electrostatic forces. This cone is known as the Taylor cone and named after Sir Geoffrey Taylor, who researched factors affecting stable cone formation such as surface tension of the liquid and magnitude of the applied electric field.[45] A jet or filament is produced from the cone when the surface tension is overcome by electrostatic forces, charged droplets are generated which will eventually become gaseous ions. These 'jets' had been reported as far back as 1896, when Rayleigh observed that 'the liquid is thrown out in fine jets, whose fineness, however, has a limit.'[46]

### 2.2.3.1 Electrospray as an electrolysis cell

The mechanism of the production of charged droplets from an electrospray ionization source was investigated by Kebarle *et al*.[47] The mechanism was known to be electrophoretic in nature, due to the separation of oppositely charged ions present in the solution, but this theory alone does not take into consideration charge conservation. When an electric field is applied, a partial separation of oppositely charged solvated ions occurs, leading to an excess positive charge at the capillary tip. Destabilisation due to the excess charge results in ejection of positively charged droplets from the capillary. For the electrophoretic charge separation mechanism to comply with charge balance requirements Kebarle reasons that the electrospray process must involve a conversion of ions to electrons. Hence the electrospray mechanism is essentially working as a special type of electrolysis cell, with oxidation occurring at the capillary tip and reduction at the counter electrode (figure 2.1).

To examine the oxidation reaction at the capillary tip, the authors used a metal capillary with a low reduction potential. A zinc capillary confirmed that an oxidation reaction does occur at the capillary as positively charged $Zn^{2+}$ ions were detected by the mass spectrometer. Similar results were found when using stainless steel as the capillary material when $Fe^{2+}$ ions were detected.

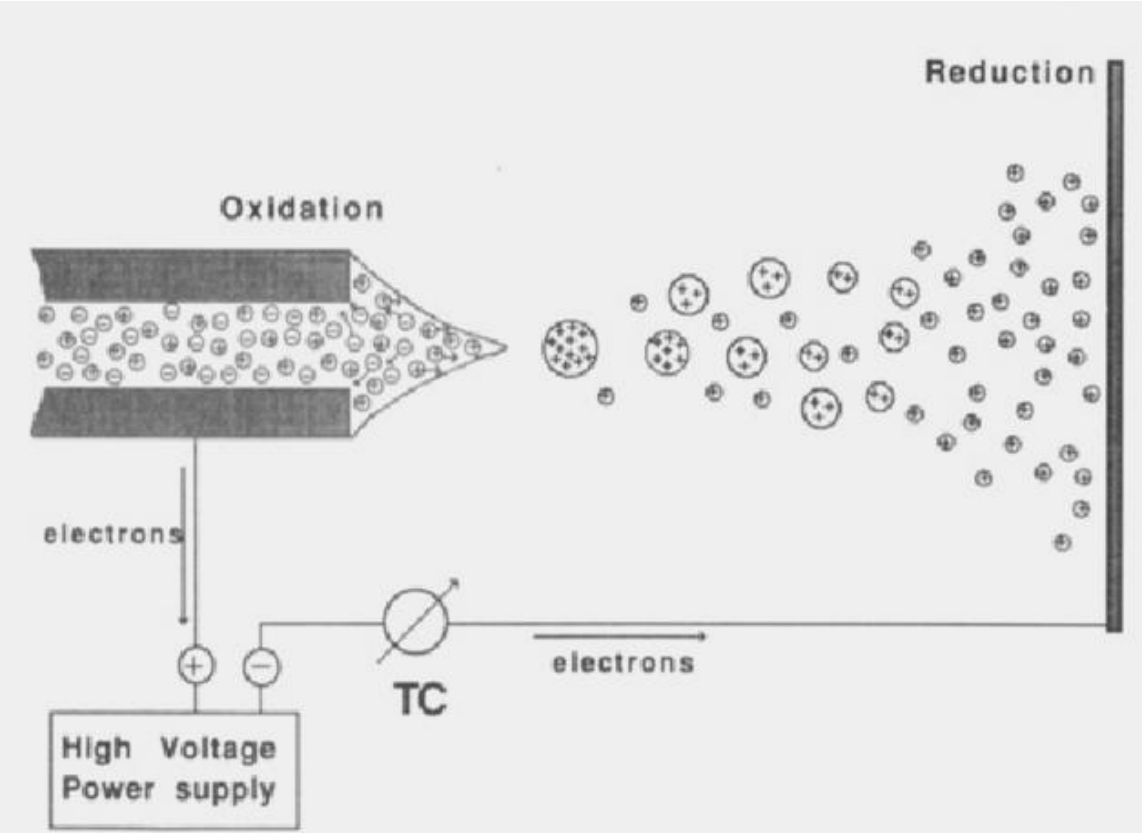


**Figure 2.1: Electrospray ionization as an electrochemical cell.[47] An application of an electric field to the ESI source results in concentration of positive ions at the meniscus of the solution. The destabilisation caused due to excess positive charge leads to formation of a cone, followed by ejection of a jet of droplets with an excess positive charge. Evaporation of these droplets increases coulombic repulsion between the positive charges. The droplets undergo fission to reduce this repulsion. As the droplets contain an excess positive charge, in order to comply with charge balance requirements, there must be a conversion of ions to electrons. Hence an oxidation reaction is occurring at the capillary and a reduction reaction at the counter electrode. TC is the total current.**

### 2.2.3.2 The charged residue model (CRM)

The possibility of integrating electrospray and mass spectrometry was first suggested in 1968 by Dole *et al*. who discovered that gaseous ions of macromolecules could be generated by electrospray ionization.[48] This had been a major challenge before

electrospray as other methods of ionization required heating which led to decomposition of these large molecules.

Dole produced gaseous ions of polyethylene with molecular masses of 411,000 Da from evaporating a dilute solution of polyethylene via electrospray in the presence of nitrogen to aid desolvation. In this investigation a theory on the mechanism of electrospray is put forward and still remains highly accepted. The charged residue model (CRM) states that droplets produced by electrospray will undergo evaporation, reducing droplet size and increasing the proximity of charges, hence increasing electrostatic repulsion within the droplet. After sufficient evaporation the droplets become unstable and are said to undergo coulombic explosion. The value at which this instability is reached is termed the Rayleigh limit and can be calculated from the following equation. This process is repeated until gaseous ions are all that remain.

$$Q = 8\pi\,(\varepsilon_0\,\gamma\,r^3)^{\frac{1}{2}} \qquad [2.3]$$

Where $Q$ is the droplet charge (C), $\varepsilon_0$ is the permittivity of vacuum (C $N^{-1}$ $m^{-2}$), $\gamma$ is the surface tension of the liquid (N $m^{-1}$), and $r$ is the droplet radius (m).

In 1994, Gomez and Tang provided evidence to support the CRM when they were the first to obtain photographic images of droplets undergoing fission, giving an insight into the fission process (figure 2.2).[49] From these images Gomez and Tang deduced that the charged droplets rapidly disperse due to coulombic repulsion. Both large droplets and satellite droplets were produced at the electrospray source, with coulombic repulsion resulting in the orientation of satellite droplets on the exterior and larger droplets in the interior of the electrospray plume. Gomez and Tang observed these droplets vibrating, forming oblate and prolate shapes sequentially. Fission occurred via the formation of a filament, from which a string of droplets were emitted. The report states that each droplet took 2% of the mass and 15% of the charge from the parent droplet. Droplet fission is reported below the Rayleigh limit; however this is justified by Gomez and Tang by the non spherical shapes of the droplets upon vibration.

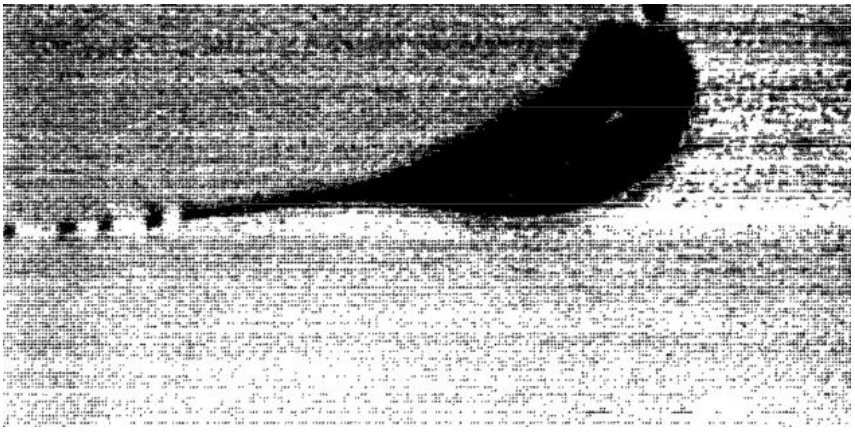

**Figure 2.2: Photograph of droplet fission taken by Gomez and Tang.[49]**

### 2.2.3.3 The ion evaporation model (IEM)

A second mechanism, known as the ion evaporation model (IEM) was proposed by Iribarne and Thomson in 1976. The charged residue model is not disregarded; indeed it is acknowledged that the charged droplets produced by electrospray undergo a series of desolvation and coulombic explosions. However, Iribarne and Thomson postulated that when the droplets reach a certain size a competing process is possible, in which ion evaporation can occur directly from the droplet surface.[50] When the required electrostatic energy is reached ion evaporation can occur, however evaporation must happen before the Rayleigh limit of instability is reached, otherwise coulombic fission will take place. The evaporation model is not only dependent on the size of the molecules electrosprayed, but also the concentration, as solutions which were too concentrated ($10^{-4}$ M), were evaporated to a dry salt before ion evaporation could occur.

Fenn provides supporting evidence for the IEM through the electrospray ionization of LiCl. Individual $Li^+$ ions are detected as with Iribarne and Thompson's experiments which the charge residue model cannot explain. The theory that the charge on the surface of a droplet can become so strong that an ion can be desorbed from its surface seems the most rational explanation.[51]

Both of these mechanisms are widely accepted. It is believed that the CRM occurs for large molecules, whereas the IEM results for small molecules.

### 2.2.3.4 Investigation into the droplet fission process

The size of the droplets produced by electrospray is dependent on the diameter of the filament or jet. During coulomb fission, another cone and filament is formed, and the

filament splits into a string of daughter droplets. In 2004 Kebarle *et al*.[52] examined the evaporation and coulomb fission of charged droplets and produced the scheme below (figure 2.3). This investigation showed that between each fission 40% of the droplet is evaporated, which corresponds to an increase of analyte concentration of 40%. These large increases in analyte concentration would probably lead to solid residues instead of reaching a size capable of producing gaseous ions, suggesting that most ions are produced via a jet of daughter droplets from the original droplet.

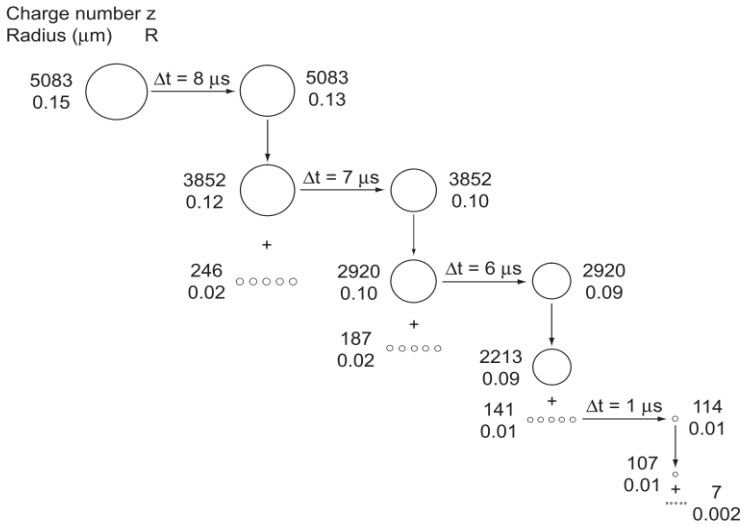


**Figure 2.3: Droplet fission scheme presented by Kebarle *et al*. The first droplet is a droplet produced by the electrospray source, this droplet will undergo evaporation and fission events to produce a series of smaller droplets. R gives the radius of the droplet and Z gives the charge on the droplet.[52]**

## 2.2.4 Integration of electrospray ionisation with mass spectrometry

The applicability of electrospray ionization to mass spectrometry was first demonstrated by Fenn *et al*. in 1984.[51] Gaseous ions were formed by electrospraying solutions into a bath gas and then expanding them in a vacuum, where their composition can be measured by mass spectrometry. Inspired by the work of Dole and motivated by a need to ionise non-volatile complex species without decomposition. Fenn strove to understand the mechanism of electrospray evaporation in order to rectify the limitations of mass spectrometry with regard to analysing non-volatile molecules without decomposition. It was also Fenn that demonstrated that electrospray could be used to produce both negative and positive ions.[53]

### 2.2.5 Practical ESI-MS

Gaseous ions, along with some charged droplets and solvent molecules are introduced into the mass spectrometer orifice. The heat of the cone or orifice capillary causes thermal declustering, removing any solvent molecules that are still present. The ions then enter a chamber at partial vacuum which has an electrical potential difference between its entrance and exit. This difference accelerates the ions and induces collision activation, further cleaning the sample. From this chamber they enter a high vacuum chamber which contains the mass spectrometer.[43]

Solvents used in electrospray are typically polar. Methanol and acetonitrile are popular choices and can be used either pure or with various amounts of water. However, even toluene which has low electrolyte solubility has been used, as only small concentrations of analyte are required for detection due to the sensitive nature of mass spectrometry. Liquids with higher surface tension such as water are harder to electrospray and using pure water can result in electrical discharge, leading to poor quality spectra and protonated solvent clusters peaks. Formic acid is normally added to the electrospray solvent when operating in positive ion mode to increase protonation, and $NH_2OH$ is added for negative ion mode to aid deprotonation.

Electrospray at atmospheric pressure is not only convenient, but is actually beneficial as the oxygen molecules in air readily capture electrons due to their high electron affinity. Electrical breakdown can be reduced by the presence of gases with high electron affinities. Trace amounts of $SF_6$ have been used for this purpose and have been observed to prevent discharge even when using pure water as a solvent. Their use has been known to result in detection of $F^-$ ions in the mass spectrum.[54] Pneumatic nebulisation has also been used to prevent electrical discharge and increase desolvation of charged droplets.[55]

## 2.3 Miniaturisation of electrospray ionisation

In 1994 Emmett and Caprioli developed microspray, an electrospray ionization source with an operating flow rate between 0.3 and 0.8 μL $min^{-1}$.[56] The needle was fabricated from a fused silica capillary, tapered to 50 μm by HF etching. An alternate capillary capable of microspray and packed with C18 for desalting and preconcentration prior to analysis was also reported.

In the same year nanospray was developed by Wilm and Mann,[57,58] a micropipette puller was used to form a borosilicate glass capillary with an internal tip diameter of between 1-3

μm. The tip was coated with gold for conductance. This ion source was able to produce droplets with diameters of 200 nm upon electrospray and was termed nanospray as it had operational flow rates in the nm $min^{-1}$ range.

Just a year later in 1995 Valaskovic *et al*. decreased the flow rates even further and reported picospray which required as little as 0.2 nL of sample. The needle used had an i.d of 1-5 μm, produced from laser heating and pulling 5-20 μm fused-silica capillaries followed by etching and a sputter coating of gold. The lower flow rates achieved were a result of reduced i.d of the capillary and not the i.d of the capillary tip.[59]

There are various advantages of miniaturized electrospray over conventional electrospray; the spray produced is much more stable and can be operated unassisted by sheath flows, pneumatic nebulisation or pumps. The sample quantities required are reduced while measurement times are increased. As the droplets produced by the ion source are much smaller than those produced from conventional electrospray less desolvation time is required. This enables closer positioning of the ESI source to the mass spectrometer orifice, allowing sampling of a greater proportion of the ES plume. Small droplet size also prevents clustering, as at this scale the droplets typically only contain one analyte.

## 2.3.1 Single phase ESI-MS analysis

### 2.3.1.1 Electrospray from the microchip edge

The first examples of microchip ESI-MS analysis concerned electrospraying directly from a microfluidic channel. In 1997 Ramsey and Ramsey observed a stable electrospray from the edge of a microfluidic chip.[60] Flow rates of 90 nL $min^{-1}$ were generated electroosmotically and electrical potential was applied to the sample reservoirs. A benefit of Ramsey's simplistic design was that fabrication of a tip or capillary at the channel exit and application of a conductive coating were not required.

In the same year Karger *et al*. produced a glass chip capable of sequential MS analysis.[61] The design consisted of multiple channels, each with an individual sample reservoir and exit. Electrical potential was applied to the sample reservoirs as above and a pressure driven flow rate of 100-200 nL $min^{-1}$ was required for stable electrospray. The chip was placed on a xyz translational stage so that each exit could be aligned with the mass spectrometer orifice consecutively.

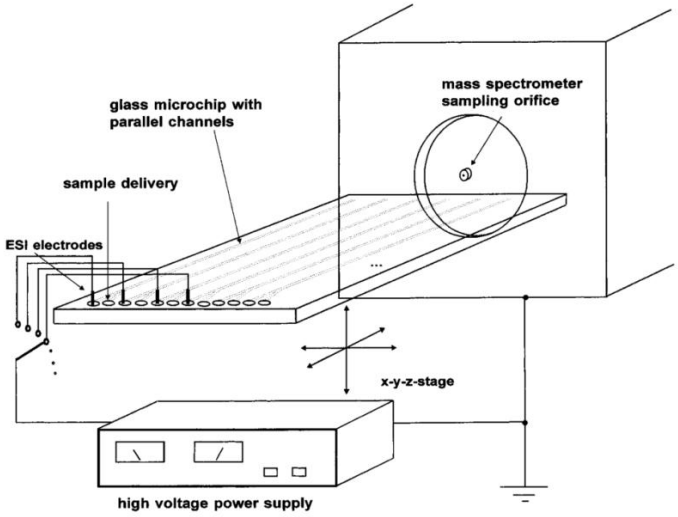


**Figure 2.4: Glass chip produced by Karger *et al*. capable of electrospraying multiple samples from the chip edge.[61] The microchip consists of nine parallel channels, each containing two wells. Well one contained buffer and a platinum electrode to which a voltage was applied. Well two contained the sample, connected to a syringe pump operated at 100-200 nL min$^{-1}$. Each channel was operated sequentially by application of the voltage, activating the sample flow and positioning the channel exit with the mass spectrometer orifice.**

Due to the hydrophilic nature of glass a hydrophobic coating was required to prevent wetting at the chip edge. N-octyltriacetoxysilane or Imunopen have been used to coat the edge of the chip, but have been found to have an electrospray lifetime of only 30 minutes. Wetting was the main problem associated with these chips. Various coatings were applied to the edge from which electrospray occurred, but each coating had a finite electrospray lifetime and therefore were not suitable for prolonged use. Investigation into a more stable solution was undertaken and a more refined Taylor cone was observed when the exit was closed with a porous PTFE membrane.[62] Dead volume at the electrospray exit due to droplet formation was eliminated by Zhang *et al*. through integrating pneumatic nebulisation onto the microchip.[63]

### 2.3.1.2 Electrospray from inserted emitters

The next generation of ESI microchips employed capillary emitters inserted into the microfluidic chip. In 1997, Figeys *et al*. presented a microfluidic chip with a microspray interface connected to the chip via a 12 cm capillary that served as an electroosmotic pump (figure 2.5).[64] Analysis of numerous peptide samples was possible using this design as the reservoirs on chip could be accessed sequentially with minimal cross contamination. A limit of detection (LOD) of 2 fmol μL$^{-1}$ was obtainable when coupling this device to an ion trap mass spectrometer. Extraction of small molecules and polymers

from the epoxy glue used for the capillary connection may have prevented a lower LOD being achieved. Contamination was particularly a problem when low molecular mass epoxy was used. A higher molecular weight epoxy resulted in a reduction in leaching of compounds from the glue.

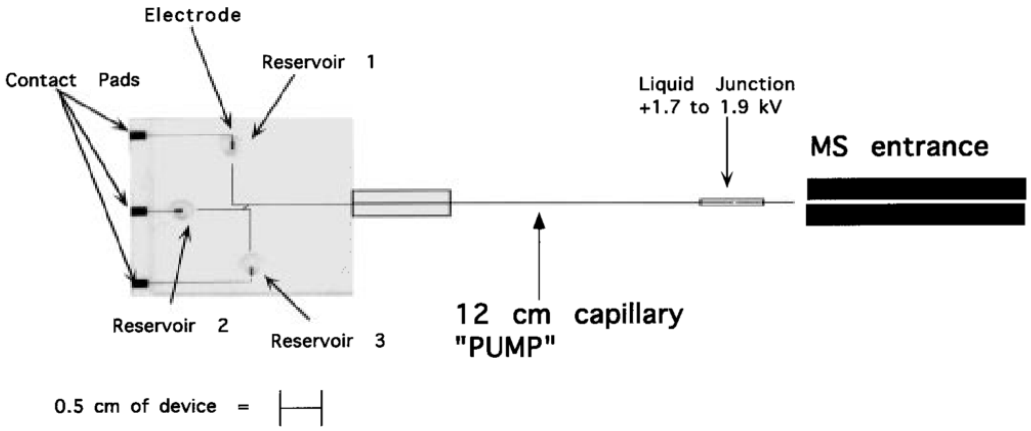


**Figure 2.5: Microfluidic chip produced by Figeys *et al*. incorporating an inserted capillary for electrospray.[64] The device has three reservoirs containing gold electrodes, each reservoir is connected to stainless steel tubing via a 12 cm fused silica capillary, another capillary (3 cm long, 50 µm i.d) is inserted in the other side of the stainless steel tubing. The power supply to the mass spectrometer is connected to the stainless steel tubing and a voltage of between +1.7 – 1.9 kV is applied to generate an electrospray. Samples are introduced by application of a negative voltage to the reservoir electrode and a positive voltage to the stainless steel tubing.**

Harrison *et al*. reported a similar design.[65] Electrospray occurred via a tapered fused silica capillary connected to the microfluidic channel. The main objective of this investigation was to create a low dead volume connection with the aim that separation could be accomplished on chip without resulting in band broadening due to dead volume in the ESI-MS interface connection. Figey *et al*. did not report the dead volume of their connection, the use of the fused silica capillary for separation instead of the chip suggests that on chip separation may have proved a problem. The connection for the fused silica capillary was created by drilling 200 µm diameter holes into the edge of the chip with tungsten carbide drills. Two different connections were investigated: a connection with a conical shaped bottom using a standard pointed drill, and a connection with a flat bottom created using a flat headed drill subsequent to drilling with the standard pointed drill. The dead volume of each connection was evaluated. The conical connection had a dead volume of 0.7 nL, and exhibited considerable band broadening, whereas the flat connection showed minimal dead volume and band broadening was removed.

In 2003 Tachibana *et al*. produced a removable microchip based ESI-MS interface to separate and detect drugs and peptides.[66] 360 µm o.d, 50 µm and 20 µm i.d fused silica capillaries tapered to 15 µm and 10 µm i.d respectively were attached to the microchip via a poly(ether ether ketone) PEEK screw inserted into a 370 µm guide hole at the microchannel exit. As no adhesive was required to fix the capillary in the guide hole the spray nozzle could be easily replaced. A stable electrospray was achieved by applying a voltage of 3 kV to platinum electrodes in the liquid junction reservoirs. It was noted that the flow rate within the microfluidic channel was affected by the generation of negative pressure at the electrospray tip, limiting the microchip's success as a separation device as this negative pressure resulted in band broadening.

Inserting capillary emitters into the microchannel exit eliminated the problems associated with wetting, however these chip were laborious to produce as the capillaries had to be inserted by hand making mass production of disposable chips unfeasible. Gluing capillaries into the chip created multiple problems, high dead volume and difficultly aligning the capillaries with the channel were not the only challenges faced. Compounds from the glue were reported to contaminate the spectra,[64] glue swelling occurred with prolonged use,[65] and the gluing process occasionally resulted in channel blockage.[67]

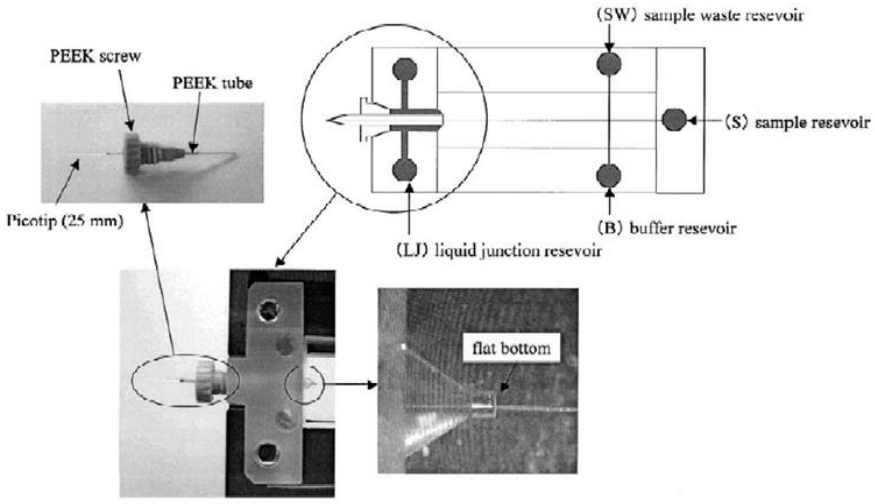


**Figure 2.6: A removable electrospray interface presented by Tachibana *et al*.[66] The microfluidic chip consists of three reservoirs and two liquid junction reservoirs, each containing a platinum electrode. A separation channel 22.9 mm long is connected to the removable electrospray interface, which is inserted into the chip via a PEEK screw and lies flush with the channel due the use of flat bottomed guide hole to minimise dead volume. Two electrospray tips were evaluated, 360 µm o.d, 50 µm and 20 µm i.d fused silica capillaries tapered to 15 µm and 10 µm i.d respectively.**

More recent examples available of electrospray from inserted emitters focus on separation or protein digestion in treated channels coupled with either metal capillaries[68] or fused

silica capillaries.[69-72] A microdevice of note was reported by Chen *et al*. which was capable of performing cell based drug assays. This device emphasises the impact microfluidics could have within the pharmaceutical industry.[73] The device has four functionalities: drug and cell medium injection to generate concentration gradients, bioreactor containing cells to analysis cell apoptosis, micro solid phase extraction (SPE) column for desalting and purification of metabolism products and an ESI emitter for direct interfacing with MS. Cell culture is achieved within the microfluidic device by direct infusion, seeding and incubation overnight in a 5% $CO_2$-humidified atmosphere, at 37 ºC while nutrient and oxygen was delivered via a constantly infusing cell medium. Test compounds are exposed to the cells at different drug concentrations by infusing the drug solution and the cell medium to varying extents. After exposure the cell viability is determined using fluorescent probes. The resulting metabolism products are analysed using MS using an ESI emitter connected to the chip after undergoing on chip purification and desalting.

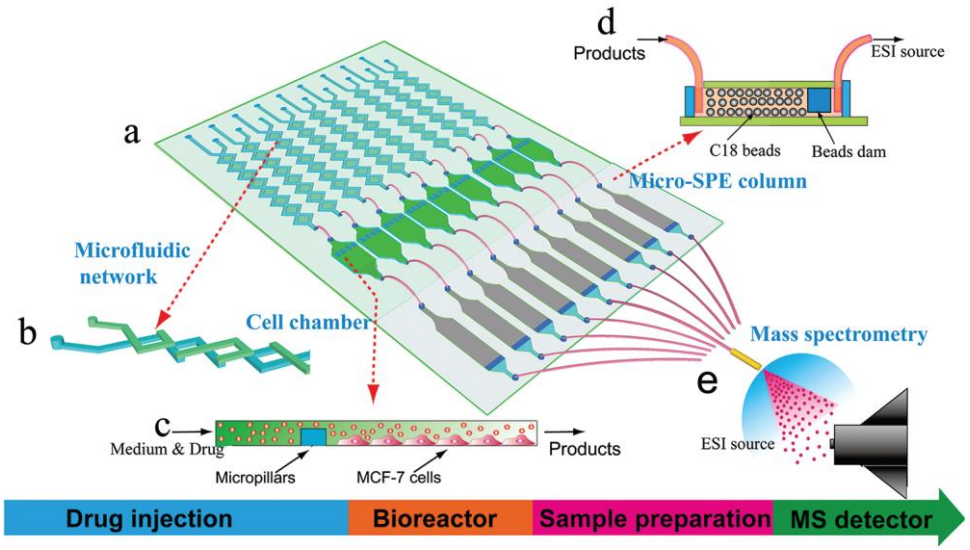


**Figure 2.7: (a) Cell based drug assay microfluidic ESI-MS chip presented by Chen *et al*.[73] The device consists of a microfluidic network for drug and cell medium injection to generate drug concentration gradients (b), a cell chamber in which the assay is performed and cell apoptosis is analysed (c), a micro SPE column for sample desalting and purification (d), and an ESI emitter for MS determination of cell metabolism products (e).**

### 2.3.1.3 Electrospray from integrated emitters

To overcome problems associated with dead volume and produce chips more applicable to mass production, emitters are increasingly being integrated into the chip design. In 2000 Schultz *et al*. used deep reactive ion etching (DRIE) to produce a microdevice with an integrated nozzle.[74] Nozzles with outer diameters between 15 - 100 µm were created on the top side of a silicon substrate using this method, the channel extends through the substrate to a reservoir located on the opposite face of the chip. The sample is introduced

through a movable fluid delivery probe containing a stainless steel tube connected to a fused silica capillary. Electrical voltage is applied to the stainless steel tube and the flow rate is controlled by application of pressure to the reservoir. These nozzles were compared to commercially available 15 µm i.d pulled capillaries and found to produce both a more intense signal (1.5 – 3 times increase in sensitivity), as well as a more stable electrospray (RSD 2-4% compared to 4-10% with the commercial capillary).

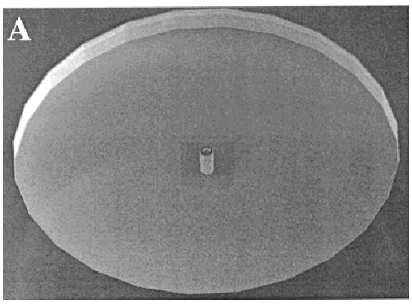


**Figure 2.8: An integrated electrospray nozzle developed by Schultz *et al*.[74] The nozzle was fabricated by deep reactive ion etching (DRIE) on a monolithic silicon substrate. The nozzle has an internal diameter of 10 µm and an external diameter of 20 µm. A reservoir is etched into the opposite side of the silicon substrate and sample injection achieved through a stainless steel tube at low flow rate of between 50 – 300 nL $min^{-1}$. Electrospray voltages of between 800 – 1500 V are applied to the same stainless steel tube.**

Svedberg *et al*. fabricated tips directly to injection moulded poly (methyl methacrylate) (PMMA) and polycarbonate (PC) microchips by either hand polishing or machine milling (figure 2,9).[75] Three tip shapes were evaluated and a low limit of detected reported (less than 0.5 fmol when analysing peptides). Unlike the integrated capillary discussed above, the electrical voltage was applied directly to the tip using either gold or graphite coating. Stable electrospray was obtained from all tips however, the conical tips required lower electrospray ionisation voltages than the tip with flat edges. The sputtered gold coating was found to be unstable and showed signal deterioration after just 30 seconds of electrospraying. The authors also reported that the electrospray outlets were coated with a thin film of polymer resulting in small outlet dimensions, although the authors state that electrospray was still possible from these chips this issue with need to be addressed if the design is developed as it could lead to outlet blockage or unstable electrospray.

Kelly *et al*. reported a 100 µm thick polydimethylsiloxane (PDMS) emitter cut to a 45º angle, which was capable of handling low flow rates (10 nL $min^{-1}$) and showed stability over 36 hours of operation over 6 days.[76] The device exhibited better sensitivity than a thicker PDMS emitter presented previously.[77] Investigation into more compact electrospray design has resulted in fabrication of nanofluidic ESI emitters (figure 2.10).

Dijkstra *et al*. coupled microfluidic channels to nanoslit emitters.[78] The emitters, fabricated using nanolithography techniques, had dimensions of 4 µm x 200 nm. Arscott and Troadec used focused ion beam (FIB) etching to fabricate a nanofluidic capillary slot with dimensions of 21 nm x 300 nm with a tip width of 75 nm.[79]

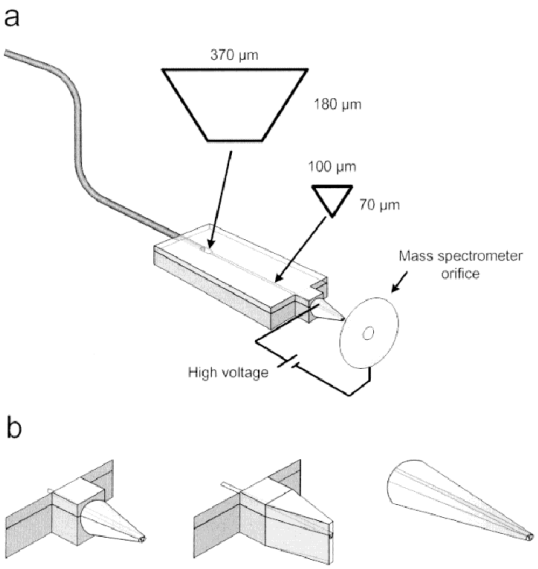


**Figure 2.9: Integrated electrospray emitter developed by Svedberg *et al*. a) polymer microdevice fabricated using injection moulding with an integrated emitter fabricated directly from the edge of the device using either machine milling or manual polishing. b) Different emitter geometries evaluated, on the right is a 3D machine milled emitter, centre 2D machine milled emitter, and left a 3D hand polished emitter. The emitters were coated with either sputtered gold, polymer embedded gold particles or graphite particles.[75]**

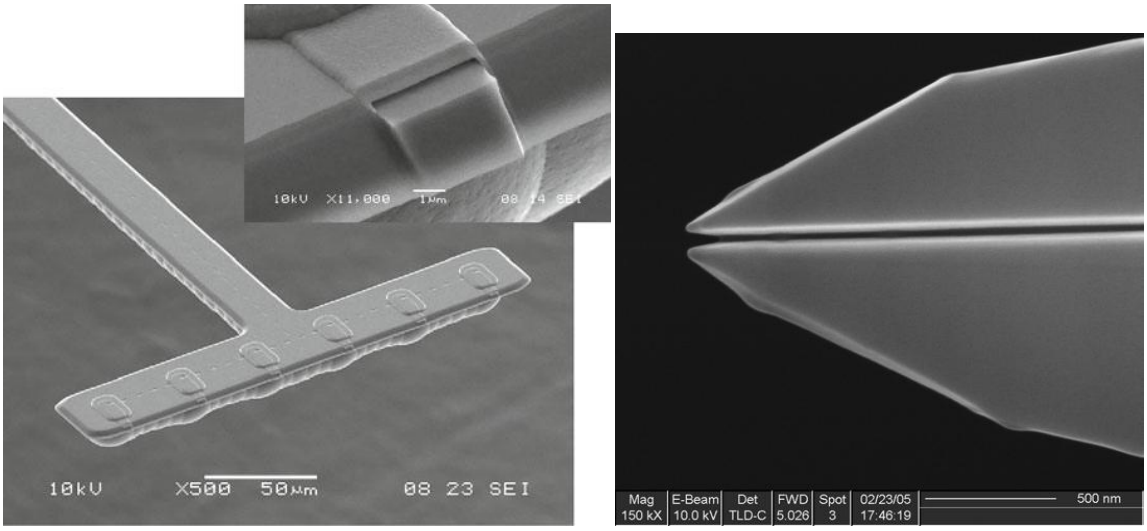


**Figure 2.10: Nanofluidic electrospray emitters. Right: a microfluidic probe containing six nanoslit electrospray emitters presented by Dijkstra *et al*., inset a close up of one of the nanoslit emitters (4 µm x 200 nm in dimension).[78] Left: Image of the nanofluidic capillary slot presented by Arscott and Troadec. The slot is 21 x 300 nm in dimensions, extending to a tip width of 75 nm.[79]**

## 2.3.2 Multiphase microfluidic ESI-MS analysis

Recently attempts have been made to integrate multiphase microfluidics with mass spectrometry. In 2009 Fidalgo *et al*. presented the first example of mass spectrometric analysis of droplets.[80] Prior to this development, detection for multiphase microdevices was limited to electrochemical and optical methods. The main difficulty in interfacing droplets with mass spectrometry is that the aqueous droplets are formed in an immiscible carrier fluid, typically fluorocarbon or mineral oils. These oils are incompatible with electrospray ionization, hence extraction of the aqueous droplets from the organic carrier fluid is required before the droplet contents can be analysed. Fidalgo accomplished this by embedding electrodes either side of a microfluidic channel containing parallel flowing organic and aqueous flows (figure 2.11). Application of a voltage between these electrodes resulted in extraction of an aqueous droplet from the organic flow into the aqueous channel. In this example the aqueous stream is transported to a silica capillary emitter inserted into a stainless steel sheath via PEEK tubing. The embedded electrodes make this design very versatile as specific droplets can be extracted. Selective droplet sorting is carried out on chip via fluorescence in order to determine the droplets of interest. There was some variation in the peak height of the analyte observed using this method. The authors reason that this inconsistency is a result of the emitter geometry, presence of carrier oil after extraction and limited scan rate of the mass spectrometer.

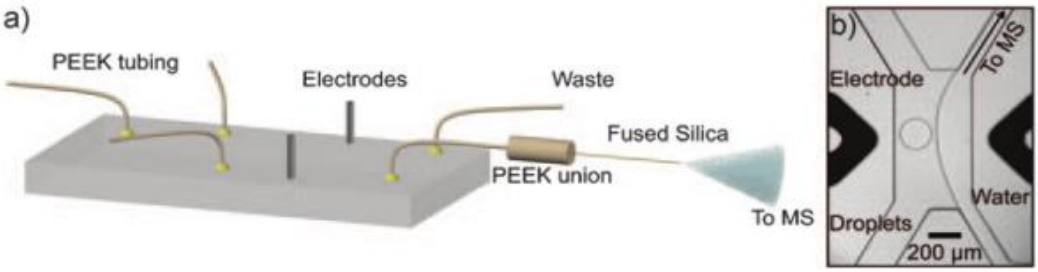


**Figure 2.11: a) Schematic of the droplet based ESI-MS interface. The PDMS device is fabricated using soft lithography, a silica capillary (75 µm i.d, 375 µm o.d) within a stainless steel tube serving as the electrospray emitter is connected to the microdevice via PEEK tubing. b) The droplet extraction process is achieved through the use of two embedded electrodes (shown in black) either side of the droplet extraction section. The channel on the left contains aqueous droplets within an organic flow, and the channel to the right contains an aqueous flow. Upon application of an electric field the droplet will coalesce with the aqueous stream and its contents determined using mass spectrometry.[80]**

Shortly after this work was reported, Kelly *et al*. presented an alternative method of droplet extraction (figure 2.12).[81] The chip design allowed automatic extraction of aqueous droplets into an aqueous carrier fluid through several apertures that partition the aqueous and organic streams. The aperture interface consists of a number of columns, 1.5 µm in diameter, separated by distances of 3 µm. Droplets are primarily transferred through the

first or second apertures, the presence of additional apertures serve to buffer the pressure differences between the two streams. The interfacial tension at the interface results in the exclusive transfer of aqueous droplets.

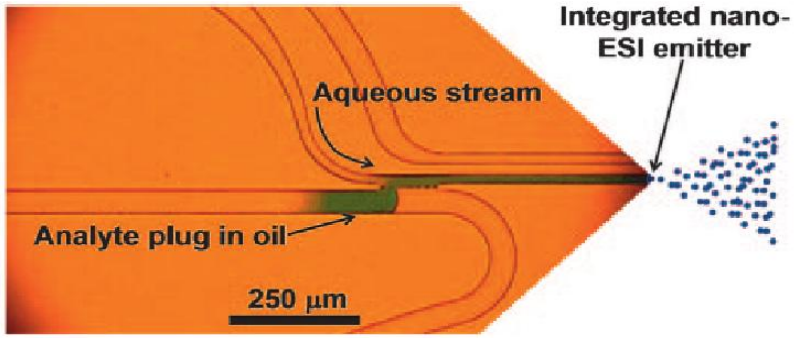


**Figure 2.12: Droplet based ESI-MS interface with droplet extraction occurring through several apertures between the organic and aqueous phases.[81] Droplet generation occurs (not shown here) upstream using flow focusing. When the droplet reaches the extraction interface, which consists of 6 cylindrical pillars (shown as black dots), 15 μm in diameter with a separation of 3 μm, the droplet merges with the aqueous stream. The voltage (3 kV) to enable electrospray is applied to stainless steel needle of the syringe providing the aqueous stream.**

The rate of the oil phase was set to more than twice the rate of the aqueous phase. This resulted in a pressure spike in the aqueous stream upon extraction of droplets and minimised diffusion of the droplet. When the distance between the extraction interface and the capillary emitter was 1 mm there was no diffusion, however as this distance was increased to 6 mm diffusion of the leu-enkaphalin analyte from the droplets into the met-enkaphalin spiked aqueous stream was observed.

In 2010 Zhu and Fang achieved droplet extraction through the use of a 'hydrophilic tongue' design (figure 2.13).[82] Droplet extraction occurs through a combination of droplet wetting on the 'hydrophilic tongue' and controlling the back pressure in the segmented flow channel by altering the height of the waste reservoir. When the waste reservoir is positioned much higher than the chip the pressure in the segmented flow channel (60 μm deep) exceeds the pressure in the smaller carrier flow channel (15 μm deep) resulting in extraction of the droplet into the carrier flow. Dilution of the sample occurs in the carrier flow, however the authors reason that this is not detrimental to the MS signal as mixing allows the matrix of the sample to be altered, improving its MS compatibility.

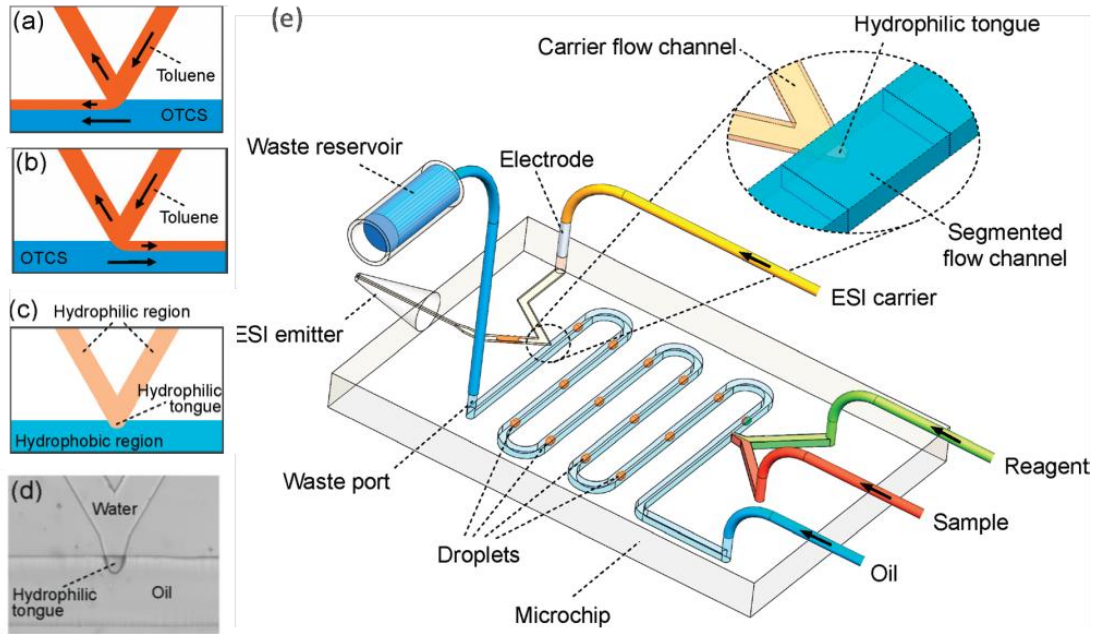


**Figure 2.13: Microfluidic chip developed by Zhu and Fang, incorporating droplet extraction via a 'hydrophilic tongue' design.[82] (a) and (b) give the surface modifying steps implemented to achieve the 'hydrophilic tongue' (a) toluene is pumped through the aqueous channel at 2 µL $min^{-1}$, while 2% v/v octadecyltrichlorosilane (OTCS) in toluene is pumped through the segmented flow channel, (b) the flow direction of the OTCS solution is reversed. (c) Shows the surface properties of the channels after modification, (d) a charge-coupled device (CCD) image showing the 'hydrophilic tongue', and (e) the overall design of the microfluidic device.**

Cartridge based ESI-MS interfaces have also been reported. Kennedy *et al*. developed a cartridge based ESI source which could be used to perform assays (figure 2.14).[83] Droplets containing test compounds separated with perfluorodecalin were aspirated into a cartridge. The different compounds were pumped through successive PDMS tees which facilitated, in this example, the addition of enzyme, substrate and a quenchant. Both the organic and aqueous phases flowed through the emitter, however the organic phase was removed by a Teflon tube placed near the tip. This simple design is capable of high throughput with 96 droplets loaded within 10 minutes and reagent addition occurring at a rate of 1.4 samples per second. The authors reported some cross contamination between samples, however this was rectified by running the experiments in quadruplicate and discarding the first droplet of each run, which equates to a loss of only 8 nL of test compound. This wastage could be eliminated by aspirating a buffer droplet between each test compound to remove any residue in the capillary.

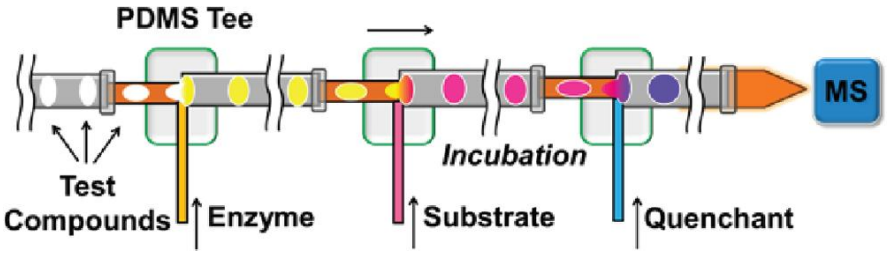


**Figure 2.14: Cartridge based ESI-MS interface reported by Kennedy *et al*.[83] A cathepsin B inhibitor screen was achieved by aspirating 25 test compounds separated by fluorinated oil from a well plate into a capillary. The droplets formed are then pumped through a succession of PDMS tees facilitating the addition of enzyme, substrate and quenchant. The resultant droplets are feed into an ESI emitter and detection achieved using MS. Only the droplets are analysed, the organic phase is removed at the electrospray emitter by a Teflon tube placed near the tip.**

### 2.3.3 High throughput potential of miniaturised ESI-MS

One of the first chips capable of sequential mass spectrometric analysis was discussed earlier (figure 2.4).[61] Since this time ESI microfluidic devices with increasing throughput potential have been reported. For example Figeys produced a microfluidic device containing 9 reservoirs connected via microfluidic channels to a common transfer capillary and microESI source.[84] This design was more sophisticated than the design presented by Karger, as computer controlled high voltage relays connected to each reservoir facilitated electroosmotic flow and allowed sequential automated analysis. De Biasi used a multiplexed electrospray interface to integrate on chip LC with MS.[85] It was estimated that this approach would take just one hour to analyse a 96 well microtitre plate. Tan incorporated 8 porous columns on chip using in situ polymerization.[86] These columns were capable of SPE, a commonly used sample clean up and preconcentration step before electrospray mass spectrometry. Although this chip could only serially analyse 8 samples, Tan suggests that this design could be scaled up to include 96 or even 384 columns to increase throughput.

Harrison produced a chip capable of separation and high throughput analysis by coupling a microfluidic chip to an autosampler tray by way of a 1 m capillary (figure 2.15).[87] Thirty samples per hour were analysed using this design. The different resistance of the channels on chip allow sample introduction. The channel between wells C and D is large, facilitating sample injection as well as serving as a temporary reservoir for alternating buffer and analyte plugs produced from the autosampler tray. A 30 second electrokinetic injection of 3-5 nL plugs was achieved by synchronising the sample injection time and the transfer time in the capillary, however this injection process presented some problems. There was some sample diffusion into the separation channel as a constant voltage had

to be applied to allow continuous operation, maximum throughput and prevention of droplet formation at the nanoelectrospray tip.

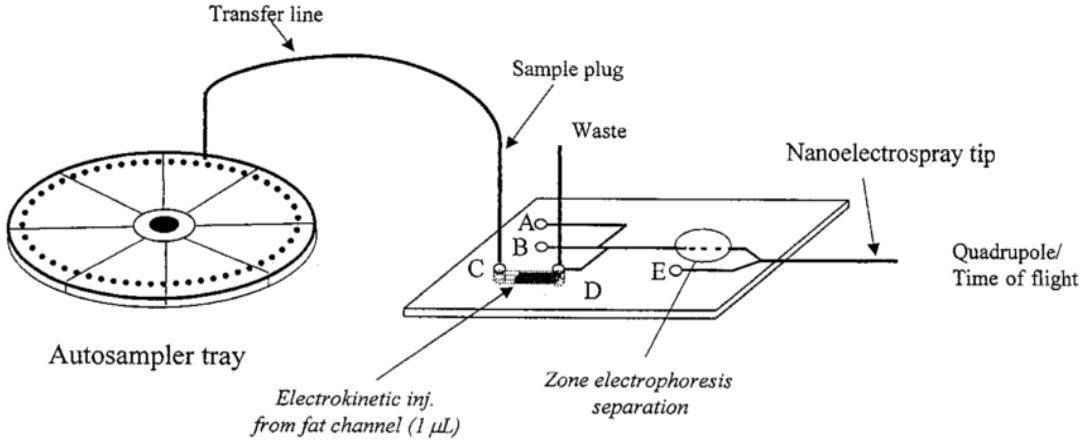


**Figure 2.15: Microfluidic chip capable of high throughput analysis by sample introduction from an autosampler tray.[87] The microdevice consists of four wells. Well A is for waste, well B contains buffer and wells C and D are separated by a large channel which allows sample introduction. Samples are introduced from an autosampler tray connected to the device by a 1 m long capillary. A gold coated emitter tapered to 15 μm i.d is glued into a flat bottomed hole drilled into the device. Application of a negative voltage (-2.5 kV) to well D while well A is grounded allows sample introduction into the separation channel, after introduction a negative voltage (-2.5 kV) is applied to well B initiating zone electrophoresis separation.**

Karger *et al*. also produced a design that utilized an autosampler (figure 2.16a). Sample introduction was achieved directly from a 96 well microtitre plate.[88] The concept of using a 96 well plate is particularly appropriate as many assays in the pharmaceutical industry are carried out within well plates. The well plate is positioned vertically on a xyz translational stage and the volume contained in its v shaped wells is so small that no cover is required as surface tension is enough to keep the samples in the wells. A computer controlled electropneumatic distributor transfers the samples to the microchip in just 2 seconds and washes the channels of the microdevice between analyses in just 3 seconds. Residence time on chip varied but was typically in the region of 30 seconds.

Karger produced another microchip based on a 96 well microtitre plate (figure 2.16b).[67] Each sample well was pressure activated by pumping nitrogen into the gas distribution channel corresponding to the required well. The sample is transported to the electrospray tip, where the electrospray voltage is applied to an embedded electrode. The chip is capable of analysing 96 samples in just 8 minutes. Chip fabrication is quite labour intensive, as each of the 96 electrospray tips had to be glued into place. In this instance 7 of the electrospray tips were not functional due to blockage during the gluing process, and

as this device is designed to be disposable, the fabrication process could be very time consuming and labour intensive.

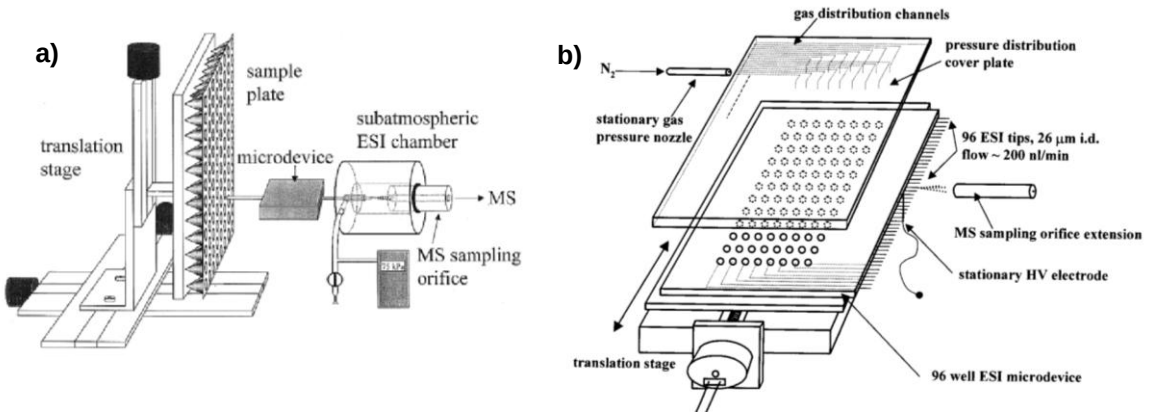


**Figure 2.16: Two microdevices based on 96 well plates. a) The first design samples directly from a well plate using a computer activated electropneumatic distributor. The microdevice contains a separation channel connected to an ESI emitter (25 µm i.d, 375 µm o.d) inserted into a guide hole in the device. The device was sandwiched between two electrodes, which supplied the ESI voltage (2 kV) and the gas pressure (~78 kPa). [88] b) The second design incorporates a well plate design into the chip and activates each well successively via pressurized nitrogen. Each well has a separate microchannel and ESI emitter (26 µm i.d, 140 µm o.d). The ESI voltage (2.5 – 7 kV) is applied via a stationary electrode under the device.[67]**

Mao *et al*. developed a silicon based multinozzle emitter array (MEA) microchip (figure 2.17).[89] The 3 inch circular chip boasts 96 emitters, each with 10 electrospray nozzles facilitating simultaneous multiple electrospray. Multiple electrospray nozzles should in theory led to enhanced MS sensitivity, as Tang *et al*. showed that the total spray current was approximately proportional to the number of emitters.[90] The authors reported an increase in MS sensitivity (~10%) when compared to commercially available capillaries. A similar design was reported by Sainiemi *et al*. consisting of a circular silicon wafer with 60 electrospray sources around the circumference.[91] The samples are introduced by direct pipetting into a sample well on the uncovered surface. The device has a throughput of 60 samples in 8 minutes, however the open design means sample analysis would need to be achieved before solvent evaporation occurs. The authors state that samples could be left to dry on the device and stored for later analysis, however this results in the need for an additional pipetting step.

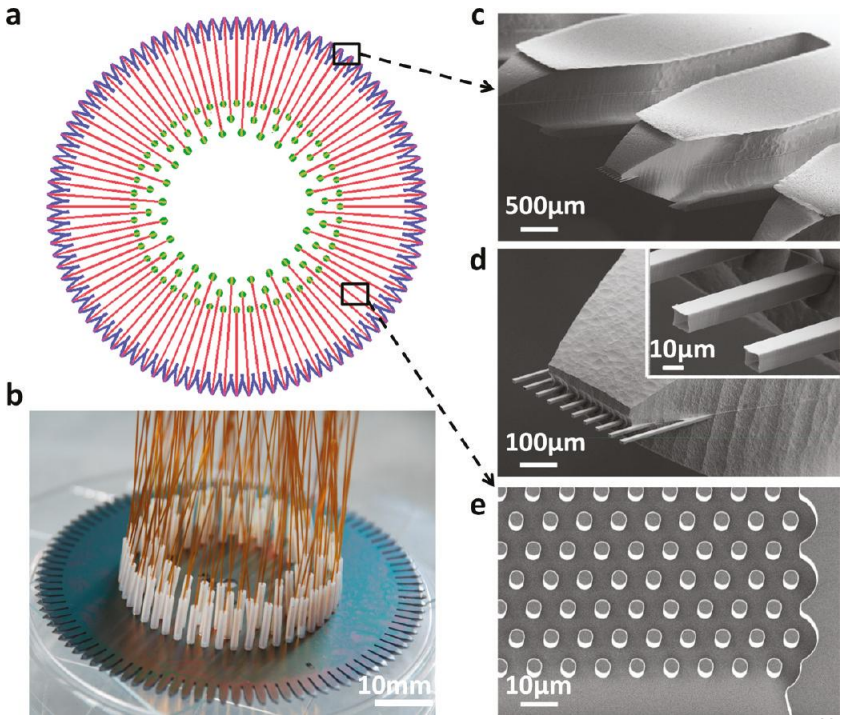


**Figure 2.17: The multinozzle emitter array (MEA) chip presented by Mao *et al*.[89] a) Schematic of the microdevice, green denotes sample inlets, red microchannels to the 10 nozzle emitter arrays on the 96 sharpened emitters shown in blue. b) Photograph of the device with 96 capillaries attached for sample introduction. SEM images of the multinozzle emitters (c), the ten nozzle array on each of the 96 emitters (d), and micropillar array which can be fabricated into the microchannels and selectively coated for separation or to investigate digestion (e).**

## 2.3.4 Commercial microfluidic ESI-MS platforms

Advion BioSciences developed the TriVersa NanoMate®, a microdevice capable of ESI. The silicon based device consists of 400 nanoelectrospray nozzles of different internal diameters so different flow rates (20 – 300 nL $min^{-1}$) can be used. The sample is aspirated from a traditional well plate and inserted into the back of the ESI microchip, a voltage is applied to the pipette containing the sample resulting in electrospray. The design is also compatible with HPLC, as after separation, part of the sample can be analysed using MS while the other part is deposited into a well plate. The TriVersa Nanomate system has been used in the literature to analyse protein digests[92], carbohydrates[93] and surface samples, for example, blood spots after liquid extraction.[94]

## 2.4. Development of miniaturised ESI platforms

The objective of this work was to develop a microfluidic platform with a mass spectrometric response comparable or greater than the commercial probe which could be easily interfaced with the mass spectrometer with ease and preferable little or no modification to the mass spectrometer required. It is anticipated that the microfluidic platform could be slotted into place within the mass spectrometer and will be able to be connected to other microfluidic devices designed to perform different assays.

### 2.4.1 Methods and Materials

#### 2.4.1.1 Chemicals

Warfarin was obtained from SigmaAldrich (Gillingham, UK). Acetonitrile, methanol and formic acid were obtained from Fisher Scientific (Loughborough, UK). All Materials were used as received.

#### 2.4.1.2 Microfabricaion[1]

##### 2.4.1.2.1 ESI chip 1 fabrication

A schematic of ESI chip 1 is shown in figure 2.18a. A microfluidic channel 300 x 300 µm in cross section and 37 mm in length (10 mm straight channel, 12 mm straight channel at 90º to the 10mm channel, followed by a 15 mm long curved channel) was milled into a 3 mm thick piece of PMMA using a M35 Computer Numerical Control (CNC) milling machine (Datron Technologies Ltd, Milton Keynes, UK). A 1.398 mm diameter hole was drilled for the fluidic connection at the end of the 10 mm straight channel and a 0.650 mm hole was drilled at the end of the curved channel for an electrospray capillary. On the opposite face (top face) of the substrate a 1.375 mm diameter circle with a 2.5 mm long, 1.3 mm wide rectangular extension was milled to a depth of 1 mm. The chip was reduced to a rectangle, 30 mm wide and 60 mm in length by cutting away unused material surrounding the channel. A stainless steel capillary (250 µm i.d, 645 µm o.d, and approximately 10 mm in length) was inserted into the hole drilled for the capillary. A wire was placed into the rectangular extension of the circular recess surrounding the capillary, and the whole recess filled with silver loaded epoxy adhesive (RS Components Ltd.

[1] Fabrication of ESI chips carried out by Brett Litten (AstraZeneca)

Corby, UK), fixing the wire in place and providing electrical contact to the capillary. The epoxy was cured at 80-100 °C for 30 minutes. The wire was attached to the substrate using a nut and bolt and electrospray voltage provided by modifying the probe cable of the mass spectrometer. The channel on the underside of the chip was sealed using a PCR seal (Corning Inc. New York, USA).

### 2.4.1.2.2 ESI chip 2 fabrication

A schematic of ESI chip 2 is shown in figure 2.18b. ESI chip 2 was fabricated following a nearly identical fabrication method as that used for ESI chip 1, the only difference was the microfluidic channel was 32 mm in length. The channel consisted of a 5 mm straight channel, followed by a 12 mm straight channel at 90º to the first channel, followed by a 15 mm long curved channel. This resulted in the chip being reduced to a rectangle 20 mm wide and 60 mm in length.

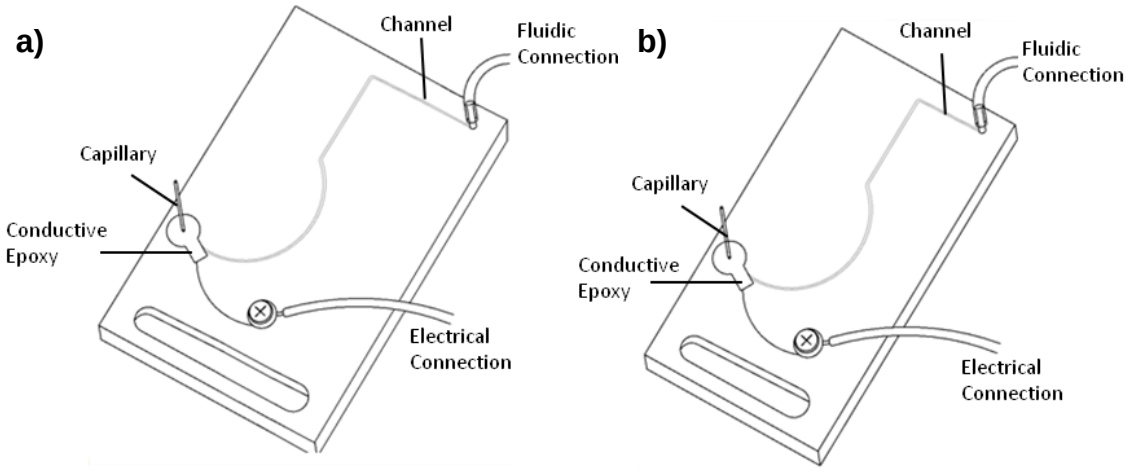


**Figure 2.18: Schematic of ESI Chip 1 and 2. The ESI chips 1 and 2 consist of a microfluidic channel (300 x 300 µm in cross section) leading to a stainless steel capillary (250 µm i.d, 645 µm o.d, 10 mm in length). Voltage is applied to the capillary via a wire embedded in conductive epoxy which surrounds the capillary. a) ESI chip 1 consists of a 37 mm long microfluidic channel and has dimensions of 30 mm x 60 mm. b) ESI chip 2 consists of a 32 mm long microfluidic channel and has dimensions of 20 mm x 60 mm.**

### 2.4.1.2.3 ESI chip 3 fabrication

A schematic of ESI chip 3 is shown in figure 2.19. A microfluidic channel 300 x 300 µm in cross section and 32 mm in length (5 mm straight channel, 12 mm straight channel at 90º to the 10mm channel, followed by a 15 mm long curved channel) was milled into a 3 mm thick piece of PMMA using a M35 Computer Numerical Control (CNC) milling machine (Datron Technologies Ltd, Milton Keynes, UK). On the reverse side, the substrate was

reduced to 1 mm in depth where the curved channel ended, by milling a 5 mm diameter, 2mm deep circle, allowing the drill to clear the substrate when drilling the capillary hole and to serve as a mount for the silver loaded epoxy resin. A 0.225 mm hole for the capillary and a 1.398 mm diameter hole for the liquid connection were drilled through the substrate. The chip was reduced to rectangle 20 mm wide and 60 mm in length by cutting away unused material surrounding the channel. A standard waters Z probe capillary (Waters Corp, Milford, USA) (100 µm i.d, 220 µm o.d) cut to approximately 10 mm in length was inserted into the capillary hole and surrounded by silver loaded epoxy resin (RS Components Ltd. Corby, UK), a wire was sunk into the epoxy to provide electrical connection and the epoxy cured at 80-100 °C for 30 minutes. The wire was attached to the modified probe cable and fixed to the substrate using a nut and bolt as above. The channel on the underside was sealed using optical sealing tape (Corning Inc. New York, USA).

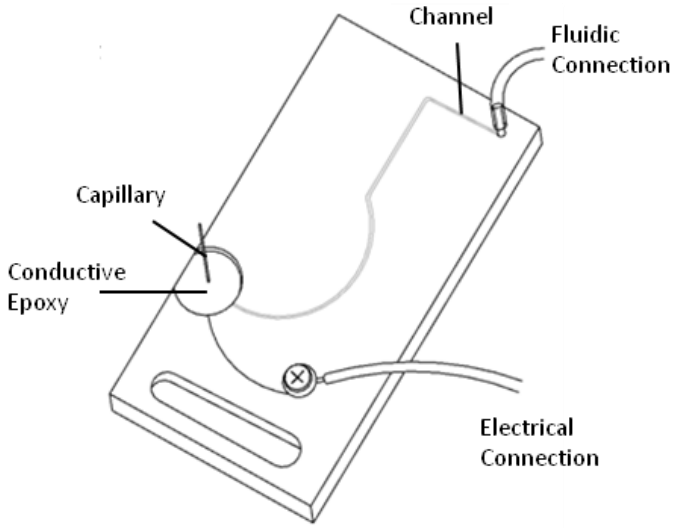


**Figure 2.19: Schematic of ESI Chip 3. The ESI chip consists of a 32 mm long microfluidic channel (300 x 300 µm in cross section) leading to a stainless steel capillary (100 µm i.d, 220 µm o.d, 10 mm in length). Voltage is applied to the capillary via a wire embedded in conductive epoxy which surrounds the capillary. The chip has dimensions of 20 mm x 60 mm.**

### 2.4.1.3 Mass spectrometry setup

A Waters ZQ mass spectrometer (Waters Corp, Milford, USA) was used to evaluate the mass spectrometric response from the microfluidic chips. The setup is shown in figure 2.20. Several modifications were made to the mass spectrometer to allow the ESI chips to be positioned within the source enclosure without overriding any safety protocols of the MS. The glass window of the source enclosure was replaced with Perspex. Fluidic and

electrical connection with the chip was made via numerous holes drilled down the right side of the replacement window. The modified window allowed the source cover to be closed during operation protecting the user from any electrical hazards and utilising the MS safety procedures if the source were to be opened during operation. A custom made bracket containing numerous slots to affix the chip, was attached to the ion block directly on top of the cone gas spring clip, via the screws used to attach the latter. Positioning of the ESI chips was achieved through the use the slots machined in the bracket and chips. Slots in the bracket to affix the chip allowed z translation, the chip slot allowed x translation and bracket slots to attach the bracket to the gas spring clip allowed a small amount of y translation. This allowed optimisation of the chip position with regard to the MS orifice. Electrical connection with the ESI chips was made through an additional probe cable which had been modified to interface with the chips. The modified probe cable made electrical contact with the chips though the modified source window and was grounded by attaching the ground wire to the casing of the source enclosure. Modifying the probe cable allowed the capillary voltage to be controlled using the MassLynx software used to run the mass spectrometer. Comparison of the ESI chips and the MS probe was achieved by switching the modified probe cable with the original probe cable.

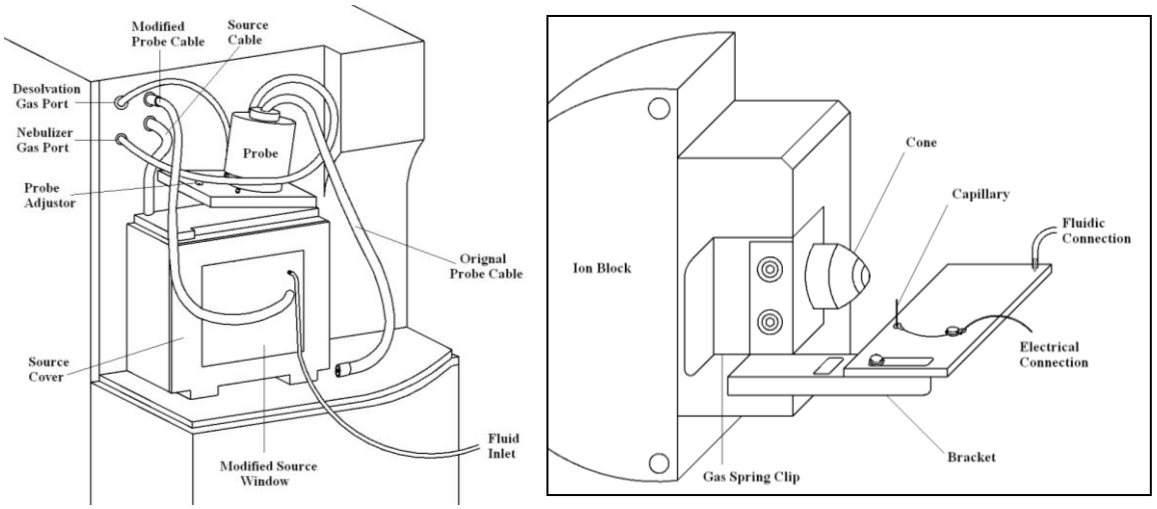


**Figure 2.20: The mass spectrometry setup. a) Outer MS setup. A modified probe cable is plugged into the mass spectrometer and electrical connection with the ESI chip provided through a hole drilled through a replacement source window made of Perspex. Fluidic connection is also made through a hole drilled in the Perspex source window. The original probe cable is unplugged but remains to allow comparison between the ESI chips and the original probe. b) Setup within the source enclosure. A custom made bracket was attached the ion block via screws used to attach the cone gas spring clip. The ESI chip was attached to the bracket through slots machined into the ESI chip and the bracket. These slots allowed movement of the ESI chip in the x and z axes, while movement in the y axis was achievable to a small extent by altering the attachment position of the bracket to the ion block.**

### 2.4.1.4 ESI-MS operating procedure

ESI-MS analysis was undertaken in positive ion mode. Scans were taken over the full scan range, readings were taken over one minute at a scan rate of 2 $s^{-1}$. The mass spectrometry conditions used in the evaluation of the electrospray chips are given in table 2.1, any variation from these conditions will be stated where appropriate.

| Electrospray Conditions | |
|---|---|
| Cone Voltage (V) | 25 |
| Extractor Voltage (V) | 3 |
| RF Lens (V) | 1 |
| | |
| Source Temperature (°C) | 120 |
| Desolvation Temperature (°C) | 60 |

**Table 2.1: The electrospray conditions used in this study. The cone voltage aids introduction of ions into the first vacuum region, extractor voltage directs the ions toward the hexapole radio frequency (RF) lens and RF lens voltage focuses the ions to the quadrupole centre. Source temperature and desolvation temperature control the desolvation of the solution. All conditions used above are typical of those outlined by Waters.**

### 2.4.1.4.1 ESI chip comparisons

A solution of warfarin in acetonitrile ($3.24x10^{-8}$ M) was diluted using 50:50 0.1% v/v formic methanol: 0.1% v/v formic water. The following solutions were made up 1:10, 1:100, 1:1000 and 1:10,000, corresponding to concentrations of $3.24x10^{-9}$ M, $3.24x10^{-10}$ M, $3.24x10^{-11}$ M, $3.24x10^{-12}$ M respectively. The mass spectrometer was put in operating mode and a 5 kV charge applied to the capillary. Solutions of warfarin were infused into the mass spectrometer, at a flow rate of at 11.9 µL $min^{-1}$, using the mass spectrometer syringe pump for ESI chip 1 and a syringe pump (RAZEL scientific instruments, St Albans, USA) for ESI chips 2 and 3.

### 2.4.1.4.2 ESI chip 3 optimisation

A $3.24x10^{-10}$ M solution of warfarin was made up in various solvent compositions. 50:50, 60:40, 70:30, 80:20 and 90:10 of 0.1% v/v formic methanol : 0.1% v/v formic water. These solutions were infused into the mass spectrometer at a flow rate of 11.9 µL $min^{-1}$ using a syringe pump (RAZEL scientific instruments, St Albans, USA). The experiment was repeated at flow rates of 12.7 µL $min^{-1}$ and 13.6 µL $min^{-1}$.

### 2.4.1.4.3 Comparison of ESI chip 3 with the commercial probe

A $3.24x10^{-10}$ M solution of warfarin made up in an electrospray solvent composition of 65:35 0.1% v/v formic methanol: 0.1% v/v formic water was used to compare ESI chip 3 and the commercial MS probe. The warfarin solution was infused into ESI chip 3 at a flow rate of 12.7 µL $min^{-1}$ using a syringe pump (RAZEL scientific instruments). The response of the mass spectrometer was investigated over a range of capillary voltages (3.75, 4, 4.25, 4.5, 4.75 and 5 kV). The commercial mass spectrometer probe, set at an angle of 6º, was reconnected and the 1:100 ($3.24x10^{-10}$ M) solution of warfarin infused to the probe at a flow rate of 12.7 µL $min^{-1}$ using a syringe pump (RAZEL scientific instruments, St Albans, USA). The response of the mass spectrometer was investigated over a range of capillary voltages (3.0, 3.5, 4, 4.25, 4.5, 4.75 and 5 kV) applied to the probe capillary.

The effect of desolvation gas was investigated. The flow rate of desolvation gas was sequentially set at 60, 90, 120, 150 and 180 L $hr^{-1}$. For each setting the probe capillary voltage was increased from 4 to 5 kV in 0.25 kV increments. A $3.24x10^{-10}$ M solution of warfarin made up in 65:35 0.1% v/v formic methanol: 0.1% v/v formic water was introduced at a flow rate of 12.7 µL $min^{-1}$.

To evaluate the effect of desolvation temperature on signal intensity the desolvation gas flow rate was deactivated and the desolvation temperature was increased from 60 ºC to 350 ºC. The ESI chip was removed from the source enclosure as it is incompatible with such high temperatures. A $3.24x10^{-10}$ M solution of warfarin made up in 65:35 0.1% v/v formic methanol: 0.1% v/v formic water was introduced at a flow rate of 12.7 µL $min^{-1}$. Measurements were taken over a probe capillary voltage range of 2.75 to 5 kV in increments of 0.25 kV.

The effect of the angle of the probe was investigated. The capillary voltage was set at 5 kV and the desolvation temperature set at 60 ºC. The angle of the probe capillary with respect to the sample cone was varied between 5° and 14° in 1° increments using the probe adjuster. A $3.24x10^{-10}$ M solution of warfarin made up in 65:35 0.1% v/v formic methanol: 0.1% v/v formic water was introduced at a flow rate of 12.7 µL $min^{-1}$. The chip was removed from the mass spectrometer source and the experiment repeated.

## 2.4.2 Results and discussion

### 2.4.2.1 Overview

Three microfluidic chips capable of electrospray have been fabricated and their mass spectrometric response evaluated using different concentrations of warfarin. Diagrams of the ESI chips including details of chip, channel and capillary dimensions are given in figure 2.18 and 2.19. A comparison of the final chip design (ESI chip 3) and the commercial MS probe was made, evaluating the effect of operational parameters such as capillary voltage, desolvation temperature and desolvation gas.

### 2.4.2.2 Justification of chip design and operational parameters

The microfluidic chip was designed so that a droplet extraction functionality could be added at a later date by adding an additional channel which would run parallel with the current microfluidic channel and merge at the point the current channel arcs. It was anticipated that electrodes would be placed either side of where the two channels merge to facilitate the movement of droplets from the organic stream to the aqueous stream, in a similar manner to that shown in figure 2.11. Previous research focuses on three different microfluidic designs, chips capable of electrospray directly from the chip edge, from inserted electrospray emitters, and from integrated emitters. The work presented in this chapter concerns a microfluidic MS platform with an inserted electrospray emitter, as it eliminates the unstable electrospray associated with prolonged use of a chip capable of electrospray directly from the edge of the chip and allows electrical contact to be made directly to a stainless steel capillary, therefore eliminating the need to apply a conductive coating to emitter which has been shown to have a finite operational time. Channel dimensions were chosen to allow large enough droplets to be produced to elicit an adequate mass spectrometric response while still maintaining low sample requirements. The flow rates used in the following experiments were chosen using a trial-and-error approach to determine at which flow rate a stable electrospray was produced. If the flow rate was too low sputtering of the electrospray was observed while if the flow rate was too high the voltage applied to the capillary was insufficient to vaporise the sample and droplets accumulated at the capillary tip. The anticoagulant drug Warfarin was used as the model drug as it was readily available, and it has a well know and good ESI-MS response.

### 2.4.2.3 ESI chip 1 and 2 comparison

Figure 2.21 shows a comparison of ESI chips 1 and 2 as a function of warfarin concentration. ESI chip 1 exhibited a low stability and no response to large changes in warfarin concentration was observed. The lack of response to changes in concentration is attributed to instability of the mass spectrometer syringe pump at low flow rates. Sputtering of the electrospray at the capillary was frequently visible and resulted in a sporadic signal. It was also evident that the dimensions of ESI chip 1 were too large for the chip to be easily manoeuvred within the source enclosure, hindering optimisation of the chip position with respect to the sampling cone.

The design of ESI chip 2 resulted in a reduction in chip width by 1 cm compared to ESI chip 1. The modification addressed the problem of manoeuvrability within the source enclosure. The new size allowed positioning of the ESI chip further away from the sampling cone. A good MS response was observed when the chip was placed 10 mm or more away from the sampling cone, an optimum signal was produced when the capillary of the ESI chip was placed directly under the original probe capillary. It is evident that the poor response observed for ESI chip 1 was partially due to its close proximity with the sampling cone, the distance between the capillary and cone must not have been sufficient for solvent evaporation to occur prior to sampling. Placement of the chip further away solves this problem and eliminates any possibility of arcing between the capillary and the sample cone. Solution introduction to ESI chip 2 was achieved using a different syringe pump (RAZEL scientific instruments, St Albans, USA), which appeared to generate a more stable flow, as the sputtering observed when using the MS pump with ESI chip 1 was not visible.

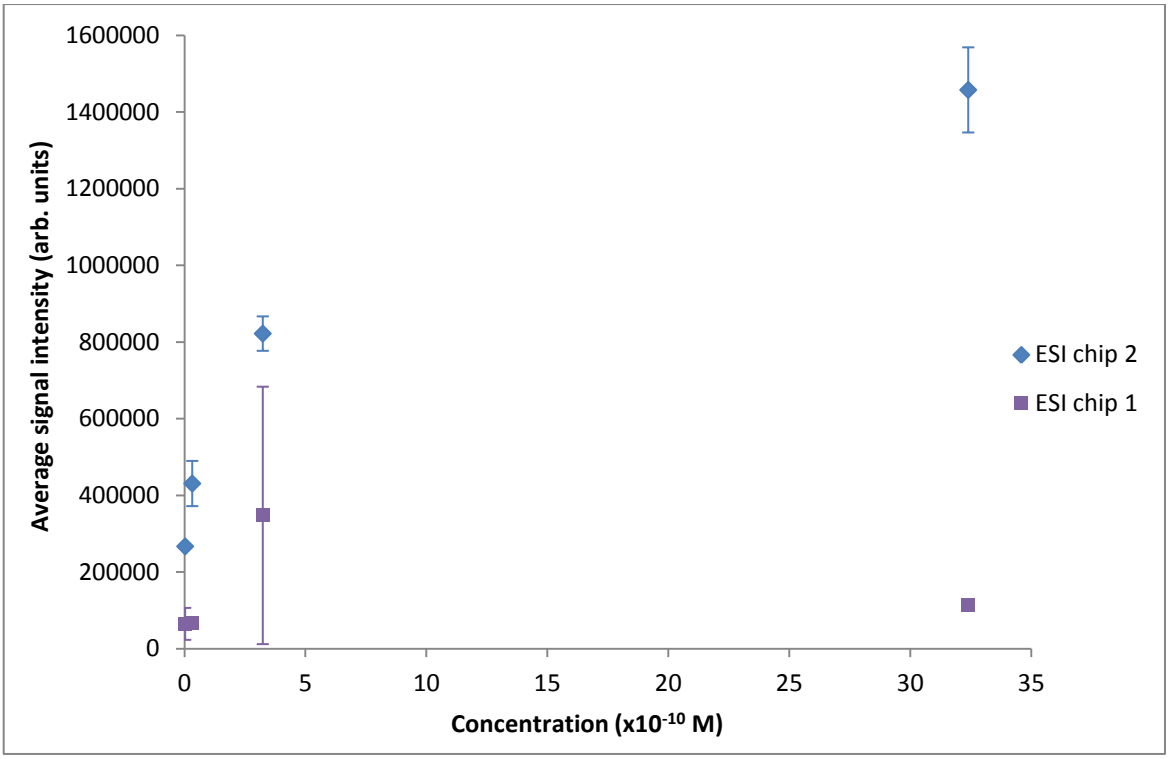


**Figure 2.21: Comparison of the mass spectrometric response of ESI chips 1 and 2 as a function of warfarin concentration. Measurements were taken in positive ion mode, at a capillary voltage of 5 kV and sample flow rate of 11.9 µL $min^{-1}$. Scans were taken over one minute at a scan rate of 2 $s^{-1}$. The error bars show the standard deviation (n=3).**

As shown in figure 2.21 ESI chip 2 had both improved sensitivity and stability over ESI chip 1. The stability of the signal was not reliable enough for routine use however, as every three to four seconds the signal vanished momentarily. A better response to changes in warfarin concentration was observed for ESI chip 2, however the response is not very linear in nature, a requirement which will need to be met if the response from the ESI chip is to be used to quantify samples. Further optimisation of ESI chip 2 was attempted, for example different capillary voltages, flow rates and solvent compositions were evaluated. The results obtained from these experiments were however inconclusive. It was evident that issues concerning the stability of the signal had to be addressed before optimisation could occur. High capillary voltages were required for ESI chips 1 and 2, with 5 kV providing the most intense signal and anything less than 4.75 kV insufficient to produce a signal. The high capillary voltages required may be due to the large dimensions of the ESI chip capillary, which with an internal diameter of 250 µm, is 2.5 times larger than the probe capillary, which has an optimal capillary voltage of between 2 and 4 kV (Waters Micromass ZQ operator's guide) when operating in positive ion mode. The large external diameter of the capillary (645 µm) will also result in greater wetting of the sample on the capillary tip, compared to the original probe capillary which has an external

diameter of 220 µm. As the volume on the surface of the capillary increases, the ease at which electrospray occurs will diminish, resulting in the requirement of a larger capillary voltage to facilitate electrospray. It should also be noted that upon closer examination of the capillary of ESI chip 2, it was apparent that the cut of the capillary was slightly uneven and could be contributing to the variable signal.

### 2.4.2.4 ESI chip 2 and 3 comparison

In order to form a direct comparison with the MS probe, the capillary used in ESI chip 3 was a Waters capillary cut down to 10 mm. The same capillary used in the mass spectrometer probe. The design of the overall chip remained the same, as the dimensions of ESI chip 2 were considered adequate for position optimisation. ESI chip 3 was evaluated in the same manner as ESI chips 1 and 2, a comparison of the MS response of ESI chips 2 and 3 are given in figure 2.22. The results suggest that ESI chip 3 is more sensitive than chip 2, with a greater MS signal generated from three of the four warfarin concentrations infused. The large standard deviation (RSD 25.7%) at a warfarin concentration of $3.24x10^{-10}$ M suggests there is a large degree of error associated with these results, A possible source of error could be that the results for ESI chip 3 were obtained over different days, however if this is the case a more robust design will need to be employed as day to day variations are undesirable when no changes were knowingly made to the conditions or configuration of the chip, however the position of the chip was prone to movement upon closure of the source cover, which could affect the MS response. The increase in MS signal intensity is most likely due to the reduced i.d of the capillary as smaller electrospray droplets will be produced by the smaller capillary, these droplets will have a higher surface-to-volume ratio increasing ionization efficiency. Another benefit of a smaller capillary is that the electric field at the capillary tip will be higher as electric field is inversely proportional to the radius (external) of the capillary (Equation 2.1, section 2.2.3).

There is only a minimal change in signal intensity after the solution undergoes a tenfold dilution as the solution becomes very dilute for all three chips. This suggests that the limit of detection may have been reached and the response obtained could be primarily noise. Further experiments will need to be carried out to investigate.

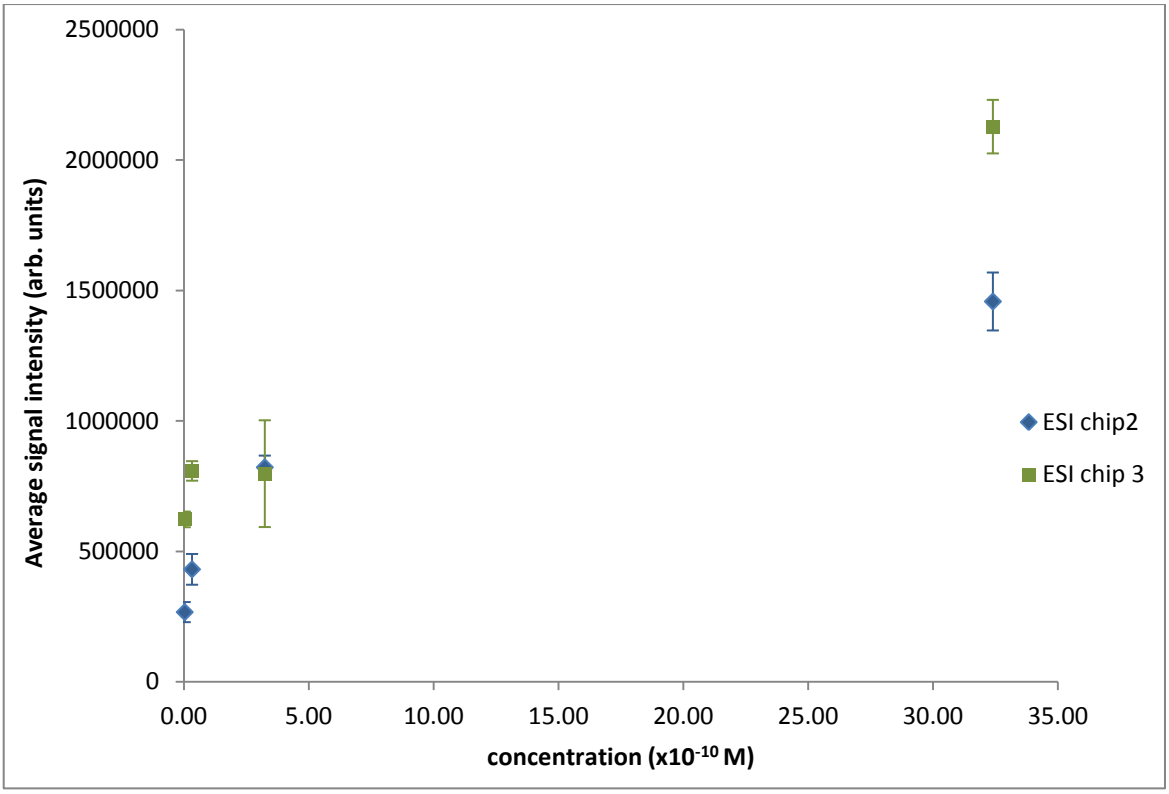


**Figure 2.22: Comparison of the mass spectrometric response of ESI chips 2 and 3 as a function of warfarin concentration. Measurements were taken in positive ion mode, at a capillary voltage of 5 kV and sample flow rate of 11.9 µL $min^{-1}$. Scans were taken over one minute at a scan rate of 2 $s^{-1}$. The error bars show the standard deviation (n=3).**

### 2.4.2.5 Optimisation of ESI chip 3

Although the nonlinearity of the results are still concerning, ESI chip 3 allowed further optimisation of the parameters which affect MS response. The effect of capillary voltage, flow rate, and solvent composition were evaluated, as optimisation of these parameters could lead to a more stable signal. An attempt was made to optimise the position of the chip relative to the mass spectrometer orifice, but as accurate measurements inside the source enclosure were unrealistic due to the confined conditions and the chip position was frequently altered slightly when the source cover was closed, it was challenging to pinpoint the position of the chip and ensure that it remained in that position after the source cover was closed. It was found that a good MS response was produced when the chip capillary was placed directly underneath the original probe as with ESI chip 2. This result is not surprising as the probe and chip capillaries are of the same internal and external diameter and therefore should require the same distance for desolvation to occur.

### 2.4.2.5.1 Effect of solvent composition on MS response

The electrospray solvent composition was evaluated using ESI chip 3. Initial experiments were carried out in a 50:50 0.1% v/v formic methanol to 01.% v/v formic water, increasing the content of methanol present in the solvent will result in a lower solvent surface tension, as methanol has a lower surface tension than water (methanol 22.07 mN $m^{-1}$, water 71.99 mN $m^{-1}$ at 25 $^{o}C$[95]), hence electrospray should occur more readily and possibly allow a lower capillary voltage to be used. A higher methanol content will also result in a more volatile electrospray solvent which will increase the ease at which desolvation occurs. As shown in figure 2.23 there is a strong dependence of signal intensity on solvent composition, The signal intensity increases as the methanol content of the solvent increases from 50% to 70%, where the intensity peaks. At <70% methanol content however the signal intensity decreases. Similar results have been reported.[96, 97] Zhou *et al*. reported that signal intensity reached a maximum at approximately 80% methanol content. Similar results were found for all four compounds evaluated suggesting that the result was not due to an attribute of the analyte, but the solvent composition was having an impact on the ion concentration generated. The authors suggest at high methanol content, ion suppression could be occurring in the solution or gas phase via proton transfer from the analyte ions to neutral solvent molecules, due to the increased proton affinity of methanol compared to water (methanol 761 kJ $mol^{-1}$, water 697 kJ $mol^{-1}$ [98]).[97] The results in figure 2.23 suggest that an optimal composition is in the region of 60:40 to 70:30 methanol to water, therefore an electrospray solvent of 65:35 0.1% v/v formic methanol to 0.1% v/v formic water will be used in the following experiments.

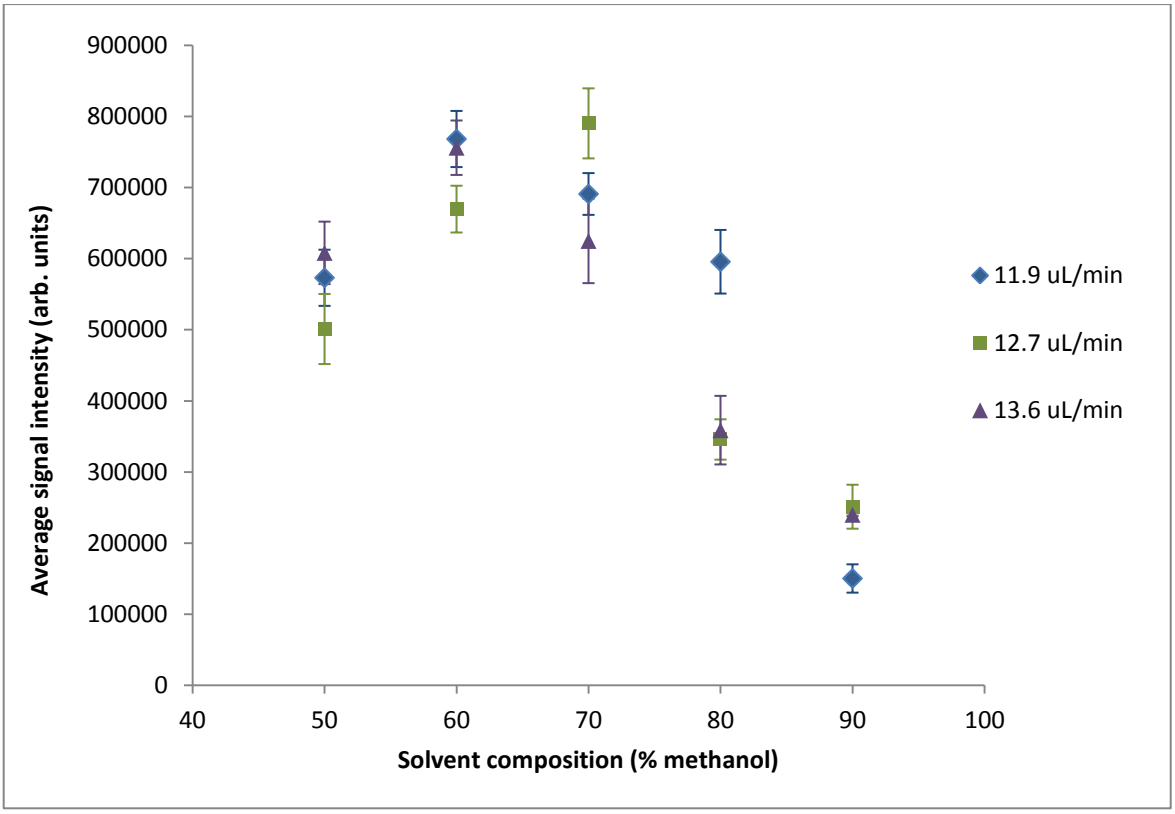


**Figure 2.23: Mass spectrometric response of ESI chip 3 as a function of solvent composition when electrospraying a 3.24x10$^{-10}$ M solution of warfarin made up in an electrospray solvent consisting of various ratios of 0.1% v/v formic methanol to 0.1% v/v formic water. Measurements were taken in positive ion mode, at a capillary voltage of 5 kV and sample flow rates of 11.9, 12.7 and 13.6 µL min$^{-1}$. Scans were taken over one minute at a scan rate of 2 s$^{-1}$. The error bars show the standard deviation (n=3).**

## 2.4.2.5.2 Effect of flow rate on MS response

The effect of flow rate was evaluated alongside solvent composition (figure 2.23). There appears to be little dependence of signal intensity on the flow rate. Flow rates of 11.9 and 13.6 µL min$^{-1}$ peaked at 60% methanol content whereas an intermediate flow rate of 12.7 µL min$^{-1}$ peaked at 70% methanol content. This may be because a sufficiently wide range of flow rates was not investigated, however the low dependence on flow rate is somewhat expected. It has been found experimentally that for medium to high flow rates (greater than 100 nL min$^{-1}$), the flow rate has little affect on the signal intensity due to a decrease in the ionisation efficiency at higher flow rates.[99]

## 2.4.2.6 Comparison of MS interface with the commercial probe

A comparison of ESI chip 3 with the commercial probe was undertaken to determine how the microfluidic platform compared to the system currently in place. The electrospray conditions for both the microchip and the MS probe were comparable, the same capillary

was used for each device and the distance of the capillary to the sampling orifice was similar. A comparison under these conditions should therefore give an indication of the viability of the microfluidic based ESI-MS platform. As shown in figure 2.24 ESI chip 3 produced a more intense MS response than the probe under the same conditions. Each device produced its most intense signal upon application of a 5 kV capillary voltage, however the signal produced by the microchip was nearly 60% greater than the response from the commercial probe. The probe performed over the capillary voltage range investigated (3 – 5 kV), whereas no MS signal was obtainable for the microchip when the voltage applied to the capillary was less than 3.75 kV.

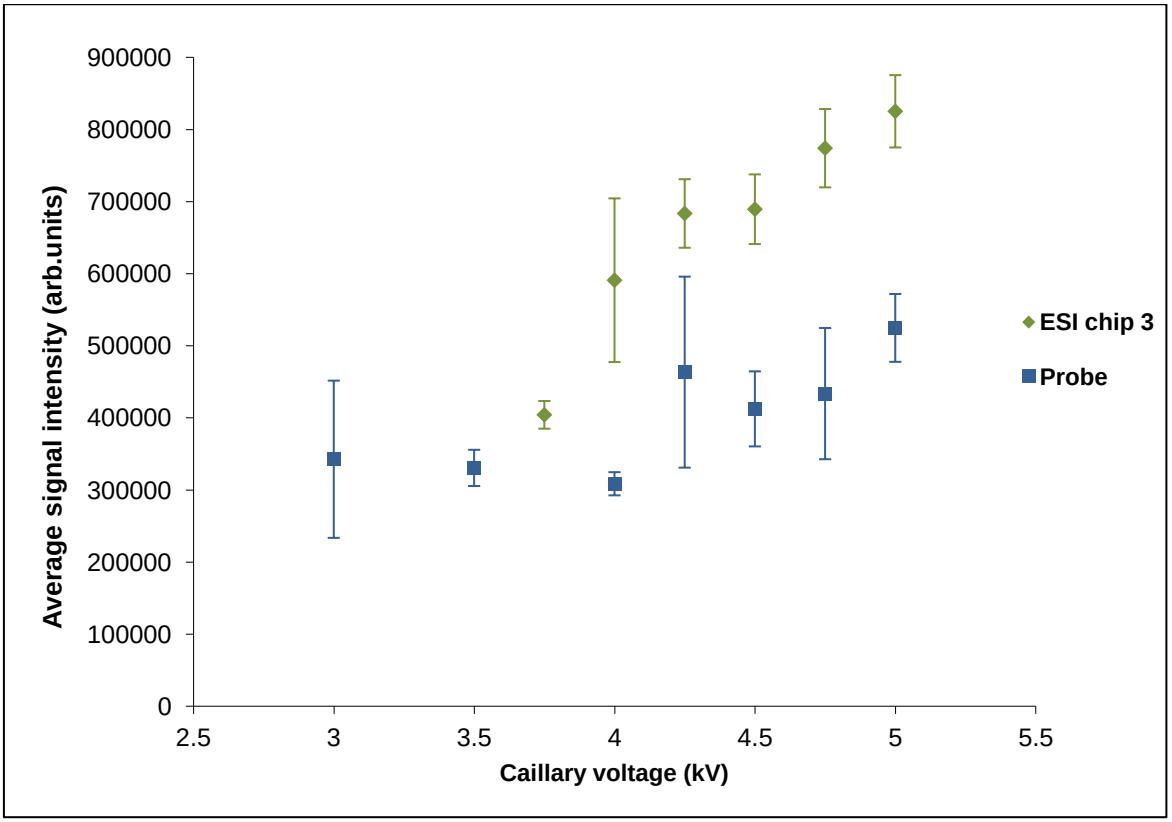


**Figure 2.24: Comparison of the mass spectrometric response of ESI chip 3 and the commercial MS probe as a function of capillary voltage. Measurements were taken using a warfarin concentration of $3.24 \times 10^{-10}$ M made up in a 65:35 0.1% v/v formic methanol: 0.1% v/v formic water electrospray solvent. The MS was operated in positive ion mode and solutions were introduced at a flow rate of 12.7 µL $min^{-1}$. Scans were taken over one minute at a scan rate of 2 $s^{-1}$. The error bars show the standard deviation (n=3).**

This is not to say that the ESI chip outperforms the MS probe. The probe is generally not operated under these conditions, both a high desolvation temperature and desolvation gas are typically employed to aid desolvation, the effect of each of these will be investigated in order to make an accurate comparison with the MS probe.

### 2.4.2.6.1 Effect of desolvation gas

The effect of desolvation gas was investigated. The optimum desolvation gas flow rate is dependent on both the mobile phase composition and flow rate. Operational desolvation gas flow rates are typically greater than 100 L $hr^{-1}$. A wide range of desolvation gas flow rates (60-180 L $hr^{-1}$) were examined, as the analyte solution flow rate used in these experiments is moderately low. Stable electrospray can occur at flow rates of up to 200 µL $hr^{-1}$ in the presence of desolvation gas.[100] The results from the MS probe operating with desolvation gas flow rates of 60 and 120 L $hr^{-1}$ are shown in figure 2.25.

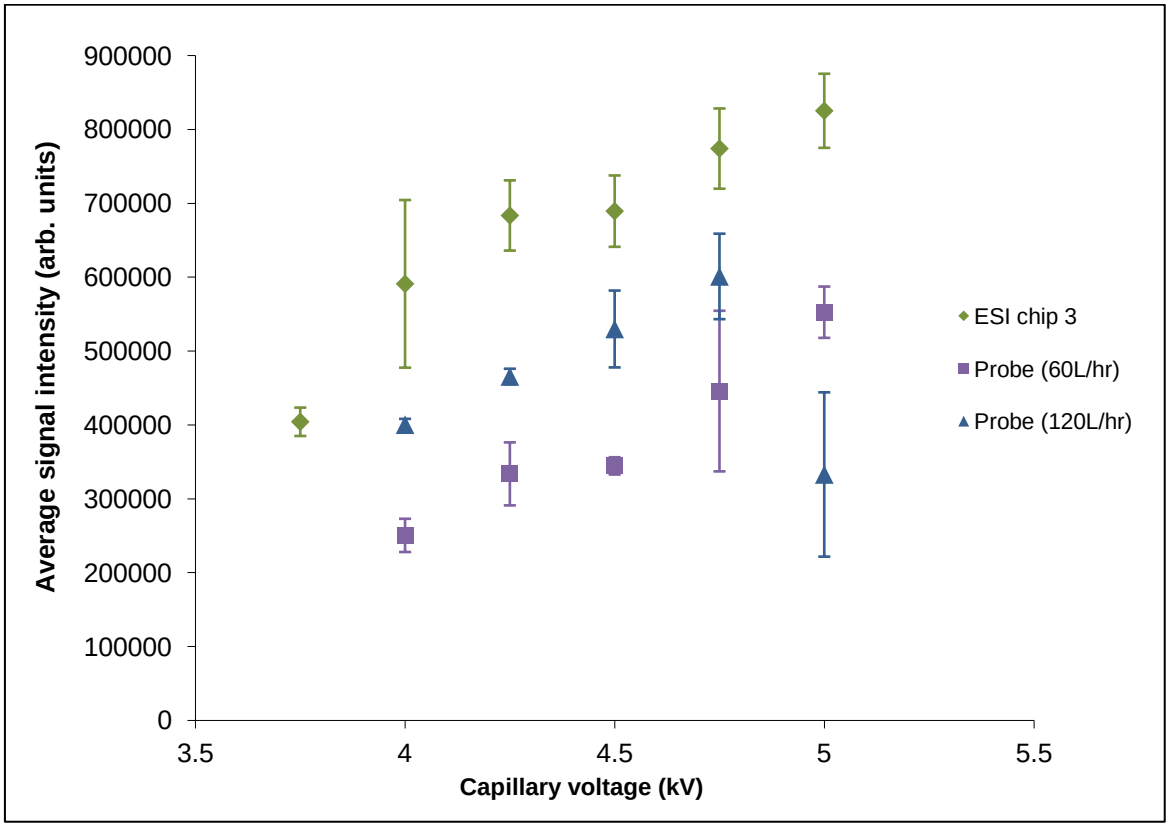


**Figure 2.25: Comparison of the mass spectrometric response of ESI chip 3 with the commercial MS probe, operating at desolvation gas flow rates of 60 and 120 L $hr^{-1}$, as a function of capillary voltage. Measurements were taken using a warfarin concentration of $3.24x10^{-10}$ M made up in a 65:35 0.1% v/v formic methanol: 0.1% v/v formic water electrospray solvent. The MS was operated in positive ion mode and solutions were introduced at a flow rate of 12.7 µL $min^{-1}$. Scans were taken over one minute at a scan rate of 2 $s^{-1}$. The error bars show the standard deviation (n=3).**

The results suggest that the chip produces a more intense signal than the probe in the presence of desolvation gas. The graph shows a greater intensity signal is produced when the desolvation gas flow is increased from 60 to 120 L $hr^{-1}$. It should be noted that similar results were obtained from the probe without desolvation gas and the probe with desolvation gas at 60 L $hr^{-1}$, suggesting desolvation gas at a flow rate this low has no

impact on the performance of the probe. There was an improvement at 120 L $hr^{-1}$, on average the signal was 47% more intense across a capillary voltage range of 4 - 4.75 kV when compared to a desolvation gas flow rate of 60 L $hr^{-1}$, however the signal intensity was still 38% lower than the response from the microchip over the same capillary voltage range. When flow rates were examined above 120 L $hr^{-1}$ there was little improvement in signal intensity. The use of desolvation gas may allow the applied capillary voltage to be reduced however, as at desolvation gas flow rates greater than or equal to 90 L $hr^{-1}$ the signal reaches a maximum around 4.75 kV and drops off at 5 kV. These results suggest that at these flow rates desolvation gas may be beneficial but not a necessary requirement to stabilise the electrospray.

It should be noted that the above comparison was made when the desolvation temperature was at 60 °C, the same temperature under which the ESI chips were evaluated. The PMMA microchip can operate under slightly higher temperatures than this, however it will be unstable at temperatures typically used for the commercial probe, as PMMA has a glass transition temperature of 105 ºC.[101] The MS probe on the other hand can operate at desolvation temperatures of up to 450 ºC. The effect of increasing the desolvation temperature was therefore investigated.

### 2.4.2.6.2 Effect of desolvation temperature

A comparison of the probe at a desolvation temperature of 350 ºC and the chip operating at 60°C was made and the results are shown in figure 2.26. Although the signal obtained from the probe is slightly irregular a basic trend can be seen. The signal peaks when the capillary voltage reaches 3.75 kV, there is an unexpected rise at 4.75 kV however as the increase in signal is only small this irregularity could be attributed to the variability of the signal. The signal intensity from the chip slowly increased up to 5 kV, as this is the highest voltage obtainable in the current system, this capillary voltage is taken as the optimum and used for the comparison. The signal intensity produced by the MS probe operating at a desolvation temperature of 350 °C and a capillary voltage of 3.75 kV is approximately 18% greater than the signal intensity generated by the microfluidic platform operating a desolvation temperature of 60 ºC and a capillary voltage of 5 kV.

Desolvation gas and desolvation temperature were evaluated separately to determine their individual effect. Although the chip cannot withstand desolvation temperatures of 350 °C without changing the material it's fabricated from, on chip nebulisation is a possibility and has been reported.[63,102,103] The results concerning desolvation gas and

desolvation temperature are encouraging. Although there was an improvement in signal intensity at a desolvation flow rate of 120 L $hr^{-1}$ the intensity was still 38% less than the response of ESI chip 3 without desolvation gas, hence complicated designs to incorporate nebulisation on chip may not be required. Increasing the desolvation temperature does improve the signal intensity, however, there is only an 18% increase in signal intensity for a 290 °C increase in desolvation temperature. It should be noted that in order to form a proper comparison with the MS probe these parameters will need to be examined simultaneously.

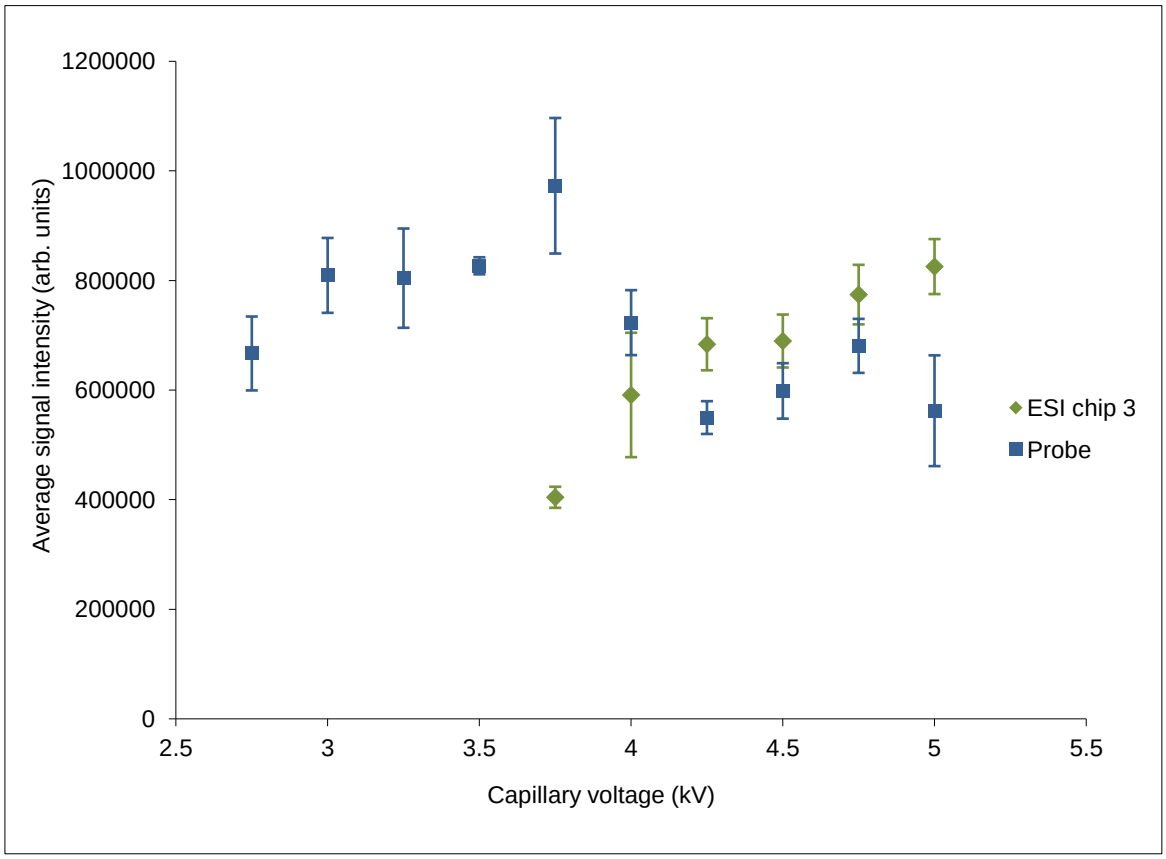


**Figure 2.26: Comparison of the mass spectrometric response of ESI chip 3 at a desolvation temperature of 60 ºC with the commercial MS probe at a desolvation temperature of 350 °C, as a function of capillary voltage. Measurements were taken using a warfarin concentration of $3.24x10^{-10}$ M made up in a 65:35 0.1% v/v formic methanol: 0.1% v/v formic water electrospray solvent. The MS was operated in positive ion mode and solutions were introduced at a flow rate of 12.7 µL $min^{-1}$. Scans were taken over one minute at a scan rate of 2 $s^{-1}$. The error bars show the standard deviation (n=3).**

## 2.4.2.6.3 Effect of capillary angle

As the probe and microchip capillaries have identical internal diameters and are placed in similar positions, it is conceivable that optimisation of the probe position may give an indication of the optimum chip position. The effect of the angle of the capillary on the

signal intensity was evaluated. The angle of the probe capillary can be easily altered using the probe adjuster on the top of the source enclosure. Although the bracket to which the ESI chip is attached does not allow the angle of the chip to be altered, it is a feature which could be incorporated into future designs. Figure 2.26 shows the effect of the capillary angle on the signal intensity. The most intense signal was produced when the angle of the capillary was set to 6°, there was a decrease in signal intensity at angles above 6º. To ensure that the presence of the chip within the source enclosure did not affect the performance of the probe, the chip was removed from the mass spectrometer and the experiment repeated. There is a slightly improvement when operating the mass spectrometer without the electrospray chip, at a capillary angle of 6º there was an improvement in signal intensity by 34%, however it should be noted that this value has a high RSD (25.68%). There was an average improvement in signal intensity of approximately 18% across the capillary voltage range.

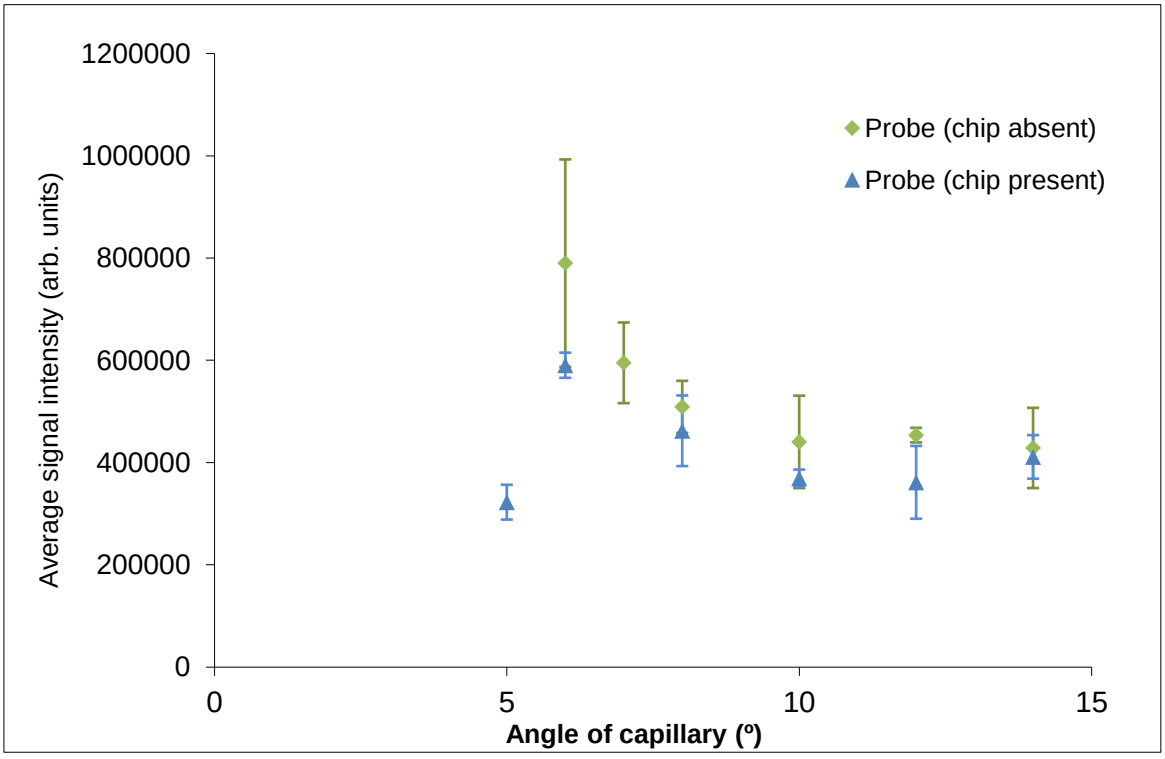


**Figure 2.26: Mass spectrometric response of the commercial MS probe as a function of capillary angle. Separate experiments were conducted with and without the chip present to determine if the presence of the chip had a detrimental effect on the MS response. Measurements were taken using a warfarin concentration of $3.24 \times 10^{-10}$ M made up in a 65:35 0.1% v/v formic methanol: 0.1% v/v formic water electrospray solvent. The MS was operated in positive ion mode and solutions were introduced at a flow rate of 12.7 µL $min^{-1}$. Scans were taken over one minute at a scan rate of 2 $s^{-1}$. The error bars show the standard deviation (n=3).**

## 2.5 Conclusions and future work

This report details experimental work that has been undertaken to develop a microfluidic platform capable of electrospray ionization. The most recent microfluidic chip has shown improvement when compared to previous chips (ESI chips 1 and 2) and has allowed some optimization to be carried out and a greater understanding of the system obtained. However there are still some areas of concern that will need to be addressed, such as determining of the optimum position of the chip within the mass spectrometer and obtaining a linear response to changes in concentration.

The concentration dependence of ESI chip 3 should be re-evaluated. The signal-to-noise ratio (S/N) must be determined for each concentration to determine whether the non-linearity of the graph is due to noise at lower concentrations. This will give information on both the LOD and limit of quantification (LOQ) of the microfluidic platform, and will allow comparison with the reported sensitivity of the Waters ZQ mass spectrometer.

At present the ESI microfluidic devices presented in this thesis offer no advantage over microfluidic ESI platforms presented in the literature when considering mass spectrometric response and high throughput capabilities, however the aim of this research was to develop a interface which could be connected to the mass spectrometer when need as it was considered that this design would be more readily accepted by the pharmaceutical industry. The work presented constitutes necessary preliminary investigations into development of an interface which can be directly interfaced with a mass spectrometer with ease and requiring as minimal modification to the mass spectrometer as possible. Development of a more accessible and manoeuvrable chip will need to be undertaken. It is suggested that utilizing the existing probe casing would achieve both of these goals. The chip could be placed in position through the top of the source enclosure and would be more manoeuvrable, in that the probe adjuster could be used to change the angle of the chip capillary with respect to the sample cone. This should solve the problem of position optimization as the position of the chip would be definable and movement of the chip when closing the source enclosure would be eliminated. Utilising the probe casing would also allow integration with other mass spectrometers without the need to modify the source cover. The MS signal could be further improved by using a polymer which is more resistant to high temperatures, such as PEEK.

The next step would then be to integrate multiphase microfluidics within the mass spectrometry platform. Experiments could be undertaken in the lab prior to integration with

the mass spectrometer to determine the optimum flow rates to produce a stable interface between the organic and aqueous flows. If droplet extraction is achieved through application of a voltage to embedded electrodes, the effect of applying different voltages should be investigated to establish conditions most suitable for droplet extraction. When the conditions have been refined, droplet extraction could be incorporated onto the mass spectrometry microfluidic platform and the response determined. S/N, LOD and LOQ can then be ascertained and compared with the commercial probe and other mass spectrometry platforms that have been reported.

# Chapter 3: Microfluidic technology and drug precipitation

## 3.1 Chapter overview

This chapter will give an introduction into the factors which affect drug solubility, how it is determined in the pharmaceutical industry and the precipitation process. Recent developments in the literature investigating precipitation within microfluidic devices will be presented, and the development of a microfluidic device capable of monitoring drug precipitation will be reported. The microfluidic setup will use light scattering detection to measure the precipitation of a poorly water soluble drug, ketoconazole, upon a pH shift, where the drug, dissolved in an acidic solution reflecting the pH of the stomach, is mixed with sodium phosphate to generate a buffer at intestinal pH of 6.5 and 7.0.

### 3.1.1 The model drug: ketoconazole

Ketoconazole is a systemic antifungal drug, which is formulated as a 200 mg tablet for oral administration.[130] It was chosen as the model drug for this study as it is given a group II classification in the BCS, indicating high permeability but low aqueous solubility, and is a weak base. Ketoconazole has pKa values of 2.9 and 6.5 corresponding to the respective ionisations of the piperazine and imidazole groups (see figure 3.1, for ketoconazole structure).[131] As a weak base it exhibits lower solubility in the intestines than in the stomach where it will be ionised, as a result rapid precipitation can occur upon gastric emptying, resulting in low and variable oral bioavailability.[132] For this reason it was anticipated that ketoconazole would be an ideal drug to study using the pH shift method as this method reflects the change in pH upon gastric emptying.

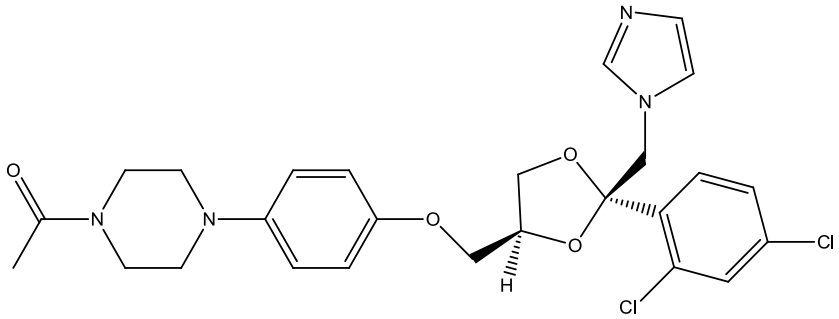


**Figure 3.1: Structure of ketoconazole.**

## 3.2 Drug solubility

A drug must have a high enough aqueous solubility to dissolve and be transported to the cellular membrane, but must also be lipophilic enough to cross the membrane. For this

reason, both solubility and permeability properties are fundamental considerations in whether NCEs will be effective drugs. The biopharmaceutical classification system (BCS) was designed to classify NCEs into four categories based on their permeability and solubility properties (figure 3.2).[104] Current FDA guidance states that a drug is considered highly soluble if its highest strength dose is soluble in 250 mL or less of aqueous media across a pH range of 1.0 – 7.5, if this is not the case the drug is considered poorly soluble. A compound is considered to be highly permeable when the extent of its intestinal absorption is greater than or equal to 90%, if absorption is less than this the compound is considered to be poorly permeable.[105]

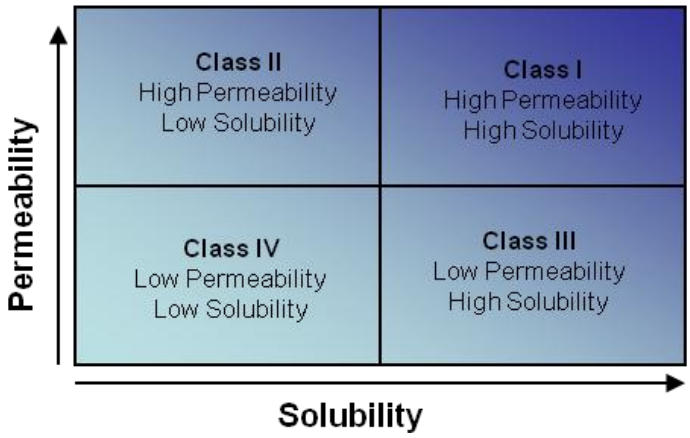


**Figure 3.2: The Biopharmaceutical Classification System (BCS) as described by Amidon *et al*.[104] The BSC classifies NCEs by their solubility and permeability properties in order to predict the intestinal absorption of orally administered drugs.**

The BCS classifies poorly soluble compounds into class II and class IV, those with high permeability and those with low permeability respectively. Low aqueous solubility of drugs can lead to precipitation *in vivo,* reducing the aqueous phase concentration of the drug and resulting in poor absorption and variable bioavailability. The importance of understanding how the solubility of the drug will change under the varying conditions of the gastrointestinal tract is therefore evident if improvements to drug absorption and bioavailability are to be attempted. The trend towards use of lower solubility compounds in drug discovery and development has been attributed to the introduction of combinatorial chemistry and HTS. Ku suggests that these techniques are the most likely cause of the decrease in the number of class I compounds from ~40% to 10 – 20%, and the increase in the number of class II compounds from ~30% to 50 - 60%, recently entering development.[106] For this reason, techniques which are able to predict the behaviour of poorly soluble compounds under biologically relevant conditions are of fundamental importance.

### 3.2.1 Factors which affect solubility

Poor aqueous solubility is typically caused by strong intermolecular interactions which are energetically costly to overcome. In order for a substance to be dissolved, both solvent-solvent interactions and solute-solute interactions need to be overcome. The solubility of a substance will depend on the nature of both the solvent and solute. As a general rule, like dissolves like, nonpolar substances are typically more soluble in nonpolar solvents, and ionic and polar substances in polar solvents. As a result, the pH of the solution can affect the solubility of a drug, for example acidic or basic drugs can be present in their unionised/ionised forms depending on the pH of their environment. Ionised molecules typically have a higher aqueous solubility than their unionized counterparts, as water is a polar solvent and will favour polar solute dissolution. Acidic drugs will have improved solubility at high pH and basic drugs at low pH, as they will be ionised under these conditions. Although ionised drugs will exhibit greater solubility this will not necessary lead to improved drug absorption, as it is unionised drugs which are more readily transported across biological membranes.

The effect of temperature on the solubility depends on whether the dissolution is endothermic or exothermic in nature. Most dissolution reactions are endothermic and an increase in temperature will lead to greater solubility of the solute, for an exothermic reaction the reverse is true. However, as most drugs are administered at room temperature and physiological temperature is 37 ºC, changes in temperature cannot be used to improve drug solubility.

The size of the drug particles will affect the rate at which drug dissolution occurs, as particle size and surface area are inversely proportional to one another, decreasing the drug particle size will lead to an increase in dissolution rate, as the surface area of the drug in contact with the solvent will increase. The crystal structure of the drug is also important as polymorphs (molecules which can assume two or more crystalline structures) can have different dissolution and solubility properties. Whether the drug is in a crystalline or amorphous state will also affect the solubility of the drug. Amorphous drugs typically exhibit faster dissolution rates and higher solubilities than their crystalline counterparts.

### 3.2.2 Solubility determination

There are two types of solubility which can be measured: kinetic solubility and thermodynamic solubility. Kinetic solubility is measured immediately after a sample is added to a solution, whereas thermodynamic solubility involves incubation of the sample

for between 12 and 24 hours. For kinetic solubility determination, the NCE is initially dissolved in dimethylsulfoxide (DMSO), which is a polar aprotic solvent that is miscible in a wide range of organic solutions and water, and can be used to dissolve both polar and non-polar compounds. The DMSO solution containing the NCE is then diluted with an aqueous solution. When its solubility is reached any excess drug will precipitate out and the solubility can be measured in a number of ways. Current high throughput methods to determine the kinetic solubility include turbidimetric, nephelometric and UV absorption techniques.[107, 108] As equilibrium is not reached when determining the kinetic solubility it cannot be interchanged with the thermodynamic solubility. For thermodynamic solubility determination, a small quantity of the NCE is placed into a well plate and an aqueous solution is added. After incubation of the plate, the solution is filtered and the solubility can be determined using a UV plate reader or chemiluminescent nitrogen detector.[109, 110] As an equilibrium is reached using this method, it is considered the true solubility of the compound, whereas the kinetic solubility is typically an overestimate. Kinetic measurements of drug solubility are important in early drug discovery, while the thermodynamic solubility tends to be determined in lead optimisation, due to the time consuming nature of thermodynamic solubility determination.

Thermodynamic solubility can also be represented as intrinsic and apparent solubility. The intrinsic solubility ($C_0$) is the solubility when the compound is present in its unionised form, whereas the apparent solubility (C) refers to the solubility at a pH where the compound is present in its ionised form. The apparent solubility is a function of the intrinsic solubility, pH and $pK_a$. The relationship between apparent solubility and intrinsic solubility is based on the Henderson-Hasselbalch equation. The relationships for monoacidic and monobasic compounds are given in equations 3.1 and 3.2 respectively.[111]

$$C = C_0\left[1 + 10^{(pH - pk_a)}\right] \quad [3.1]$$

$$C = C_0\left[1 + 10^{(pk_a - pH)}\right] \quad [3.2]$$

### 3.2.3 Physiologically relevant media

The presence of lecithin and bile salts in the intestine can increase the solubility of the drug through micelle formation. *In vitro* methods to determine the solubility under these conditions are achieved by adding these species to the buffered solution. Table 3.1 shows the composition of fasted state simulated intestinal fluid (FaSSIF) and fed state simulated

intestinal fluid (FeSSIF). These simulated fluids give a better indication of drug dissolution and solubility *in vivo*.

| Fasted state simulated intestinal fluid (FaSSIF) | | Fed state simulated intestinal fluid (FeSSIF) | |
|---|---|---|---|
| **$KH_2PO_4$** | 0.029 M | **Acetic acid** | 0.144 M |
| **Sodium taurocholate** | 5 mM | **Sodium taurocholate** | 15 mM |
| **Lecithin** | 1.5 mM | **Lecithin** | 4 mM |
| **KCl** | 0.22 M | **KCl** | 0.19 M |
| **pH** | **6.8** | **pH** | **5** |

**Table 3.1: Composition of physiologically relevant media used to simulate fasted state (FaSSIF) and fed state (FeSSIF) intestinal fluid. The solutions are made up in distilled water and pH adjusted using sodium hydroxide or hydrochloric acid.[112]**

## 3.2.4 Drug precipitation

### 3.2.4.1 Supersaturation and its role in precipitation

A solution in thermodynamic equilibrium with a solid phase is said to be saturated. Various techniques can be employed to result in the mass of dissolved solute exceeding the equilibrium saturation of the system. The resulting solution is classified as supersaturated. Supersaturation is a requirement for all precipitation events, as it is the driving force for nucleation and crystal growth, however, just because a solution is supersaturated does not necessarily mean that precipitation will occur. Precipitation from a supersaturated solution is thermodynamically favoured as it leads to a decrease in the Gibbs free energy of the system, however an activation barrier still needs to be overcome before the process can occur. If the activation energy required is too high then the solution will remain supersaturated. The terms ‘labile’ and ‘metastable’ were introduced by Oswald in 1897 to define supersaturated solutions from which spontaneous precipitation would occur (labile) and would not occur (metastable).[113] This led to the generation of the solubility-supersolubility diagram by Miers and Isaac in 1907.[114]

An example of a solubility-supersolubility diagram is shown in figure 3.3. The solubility curve is given as a solid line and represents the transition between the stable unsaturated zone in which precipitation is impossible and the metastable zone, where the solution has become supersaturated but spontaneous crystallization is improbable due to a high activation energy. Precipitation can occur in the metastable region if a crystal seed is

present. The dashed line represents the supersolubility curve, its position is not clearly defined as it is affected by numerous factors, such as the rate at which supersaturation is generated, existence of impurities in the system and the presence and intensity of agitation. Spontaneous crystallisation in the labile zone is likely, but not certain.

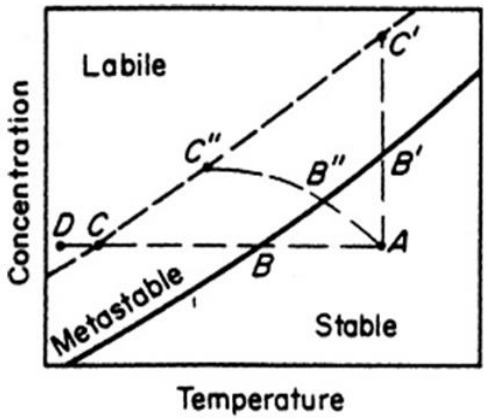


**Figure 3.3: A solubility-supersolubility diagram. The solid black line represents the solubility of the solute. The dashed line is the supersolubility line representing the transition between the metastable region, in which the solution is supersaturated but precipitation is improbable, and the labile region, in which spontaneous precipitation is probable. Line ABCD represents cooling of the solution without loss of solvent, line AB'C' represents evaporation of the solvent, and line AB"C" is a combination of the two. All three trajectories will probably result in precipitation if the labile region is reached.[113]**

## 3.2.4.2 Generating a supersaturated state

There are a number of ways to induce supersaturation within a solution. An overview of these methods is given below.

*1. Temperature*

Reducing the temperature will lead to a decrease in the solubility of the solute resulting in supersaturation. This trajectory is given by line ABC on the solubility-supersolubility diagram (figure 3.3).

*2. Solvent evaporation*

Loss of solvent will lead to an increase in the concentration of the solute. If evaporation occurs to the extent that the concentration exceeds the saturation level, supersaturation will result. Penetration into the labile region seldom occurs as increased solute concentration at the evaporation surface leads to crystal formation. The crystals formed at the surface fall back into the bulk solution and act as seeds.

*3. Antisolvent*

When a solution is mixed with a solvent in which the solute is less soluble (an antisolvent) then the solubility of the solute in the mixed solution is reduced, resulting in a supersaturated system. This technique is frequently employed in the pharmaceutical industry and is termed 'salting out'.

*4. Reaction*

When the resulting product of two or more reactants is formed in quantities which exceed the solubility of the mixed solutions then a supersaturated solution is formed.

*5. pH*

Changing the pH of a solution to a pH in which the solute is less soluble can result in the formation of a supersaturated state. It will be used in this study to mimic gastric emptying of a weakly basic drug, i.e. transition from acidic stomach conditions (pH 1.0 - 2.0) to intestinal conditions (pH 6.0 - 8.0).

### 3.2.4.3 Expressions of supersaturation

Supersaturation can be defined in numerous ways. It can be expressed as the difference in chemical potential ($\Delta\mu$, expressed in Joules) between the molecule in the solution ($\mu_s$) and in the crystal phase ($\mu_c$) (Equation 3.3).[115] The solution is unsaturated when $\Delta\mu < 0$, saturated when $\Delta\mu = 0$, and supersaturated when $\Delta\mu > 0$.

$$\Delta\mu = \mu_s - \mu_c \qquad [3.3]$$

The chemical potential of a supersaturated solution is greater than the saturated solution resulting in formation of a thermodynamically unstable solution when supersaturation is reached. The system will want to return to a lower chemical potential through precipitation. Substituting thermodynamic equations for $\mu_s$ and $\mu_c$ into the above equation gives $\Delta\mu$ in the form:[115]

$$\Delta\mu = k_B T \ln S \qquad [3.4]$$

Where $k_B$ is the Boltzmann constant ($1.3805 \times 10^{-23}$ J $K^{-1}$), $T$ is the absolute temperature (K), and $S$ is the supersaturation ratio, which in general can be simplified to:[115]

$$S=C/C_e \quad [3.5]$$

Where $C$ is the concentration and $C_e$ is the solubility. When S<1 the solution is unsaturated, S=1 the solution is saturated and S>1 the solution is supersaturated.

Supersaturation can also be characterised as the relative supersaturation σ (equation 3.6).[115]

$$\sigma = S - 1 \quad [3.6]$$

### 3.2.4.4 The precipitation process

To address the problem of inadequate absorption of poorly water soluble drugs, it is essential to understand the precipitation/crystallisation process in order to determine how absorption of these compounds can be improved. Crystallisation typically refers to a process which generates crystalline material, whereas precipitation can result in the formation of both crystalline and amorphous solids, therefore the term precipitation will be used hereafter. Precipitation can be divided into two processes: nucleation and crystal growth. For crystal growth to occur nucleation must have taken place, however the processes are not mutually exclusive, although nucleation must occur first it does not cease when crystal growth begins. Nucleation and crystal growth can occur simultaneously, however there are certain conditions which are favourable to each process. A brief introduction to each process is given below.

#### 3.2.4.4.1 Nucleation

Nucleation is the first step of precipitation and refers to the aggregation of solute molecules. Fluctuating aggregation and disaggregation of solute molecules is a common property of most solutions. These aggregations are typically not visible and must reach a critical size, termed the critical radius ($r_c$), if crystal formation is to occur. The nucleus size can be defined by the number, *n,* of solute molecules it contains, with the critical nucleus size denoted as $n_c$. Clusters of size $n<n_c$ are referred to as subnuclei, clusters of $n=n_c$ are termed critical nuclei and clusters of $n>n_c$ are supernuclei. Spontaneous growth into macroscopic crystals can only occur for supernuclei.

Nucleation can be classified as either primary or secondary nucleation. Primary nucleation concerns nucleation which takes place in a system where no other crystalline material is present. Secondary nucleation is seeded by the presence or addition of crystals and is the method typically employed in industrial settings in order to control crystal size and size distribution. Primary nucleation can be further divided into homogenous and heterogeneous nucleation. Homogenous nucleation results from successive bimolecular additions, its occurrence is rare as most systems will contain impurities of some description. Heterogeneous nucleation is seeded by impurities or a surface in the system.

Formation of crystals requires energy, more specifically, the free energy of formation ($\Delta G$). $\Delta G$ is equal to the sum of the surface excess free energy, $\Delta G_S$, and the volume excess free energy, $\Delta G_V$, (Equation 3.7).[113]

$$\begin{aligned} \Delta G &= \Delta G_S + \Delta G_V \\ &= 4\pi r^2 \gamma + \frac{4}{3} \pi r^3 \Delta G_v \end{aligned} \qquad [3.7]$$

Where $r$ is the particle radius (m), $\gamma$ is the interfacial tension (J $m^{-2}$), and $\Delta G_v$ is the free energy change of the transformation per unit volume. The surface excess free energy refers to the excess free energy between the surface of the particle and the bulk of the particle. The volume excess free energy is the free energy between a large particle and the solute. $\Delta G_S$ is a positive term and $\Delta G_V$ is a negative term, the competition between these two forces result in $\Delta G$ passing through a maximum (figure 3.4), when the nucleus reaches a critical radius, $r_c$, (Equation 3.8),[113] corresponding to a critical free energy of formation, $\Delta G_{crit}$, i.e. activation energy of nucleation (Equation 3.9).[113]

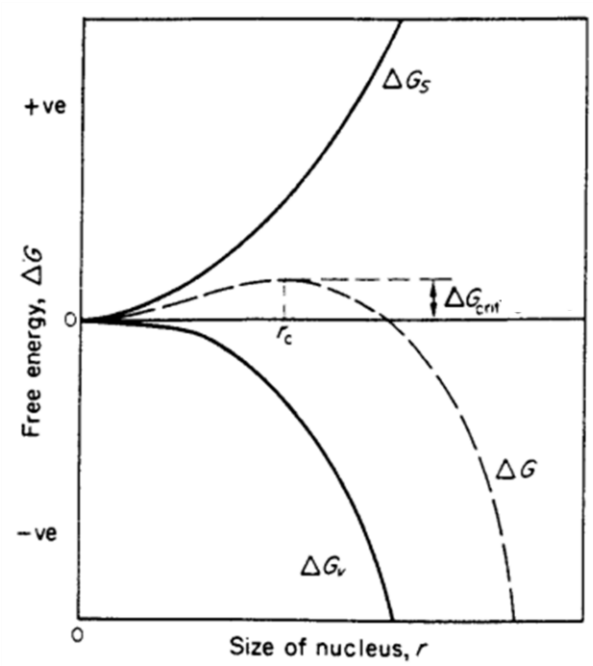


**Figure 3.4: A free energy diagram to show the presence of a critical radius ($r_c$), at a critical Gibbs free energy ($\Delta G_{crit}$).[113] $\Delta G$ is the Gibbs free energy of formation, $\Delta G_S$ is the surface excess free energy and $\Delta G_V$ is the volume excess free energy.**

$$r_c = \frac{2v\gamma}{k_B T ln S} \quad [3.8]$$

$$\Delta G_{crit} = \frac{16\pi v^2 \gamma^3}{3(k_B T ln S)^2} \quad [3.9]$$

Where $v$ is the volume of the particle ($m^3$), γ is the interfacial tension (J $m^{-2}$), $k_B$ is the Boltzmann constant, T is the temperature (K) and S is the supersaturation. From equation 3.9, it is clear that the Gibbs free energy required for nucleation will decrease with increasing supersaturation and temperature, and decreasing interfacial energy. As the Gibbs free energy of formation decreases the nucleation rate will increase, therefore high levels of supersaturation and temperature, and low values of interfacial energy will favour nucleation.

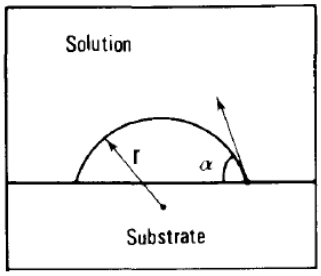


**Figure 3.5: Formation of a crystal on a substrate. The nucleus is cap shaped with a radius of *r* and has a contact angle of $\alpha$.**[116]

The Gibbs free energy of formation for heterogeneous nucleation ($\Delta G^*_{crit}$) is lower than that for homogenous nucleation as the nucleus forms on a substrate, and is therefore not spherical (figure 3.5). The critical Gibbs free energy of formation for heterogeneous nucleation is a function of the contact angle α and can be given by the following equation.[116]

$$\Delta \boldsymbol{G}^*_{\boldsymbol{crit}} = \Delta \boldsymbol{G}_{\boldsymbol{crit}} (\frac{\mathbf{1}}{\mathbf{2}} - \frac{\mathbf{3}}{\mathbf{4}} \mathbf{cos}\, \boldsymbol{\alpha} + \frac{\mathbf{1}}{\mathbf{4}}\, \boldsymbol{cos}^{\mathbf{3}} \boldsymbol{\alpha}) \qquad [3.10]$$

Impurities can affect the nucleation rate thermodynamically or kinetically. Addition of or presence of impurities can lower the interfacial tension and lead to an increase in nucleation rate, this effect is thermodynamic. Impurities can affect the nucleation rate kinetically by absorbing onto the crystal surface and impairing crystal growth above critical nucleus size. This effect is more pronounced at lower supersaturation where there are fewer solute molecules blocking the absorption of the impurity.

## 3.2.4.4.2 Crystal growth

When a nucleus reaches supernuclei size, it will begin to grow into a visible crystal. Crystal growth can be simplified into two main steps (1) diffusion of solute molecules to the crystal interface and (2) integration into the crystal structure. The growth of a crystal can be described by periodic bond chain (PBC) theory, which assumes that crystal growth occurs through formation of strong bonds between growth units, forming a chain of repeating units throughout the crystal structure.[117] According to PBC theory, three different types of face growth can occur: flat face, stepped face, and kinked face (figure 3.6). Flat faces grow parallel to the crystal by a 2D nucleation mechanism or spiral mechanism. Kinked faces grow through inclusion of individual solute molecules within the kink sites. The mechanism of growth of kinked faces is faster than that of flat faces. Stepped face addition of solute molecules occurs at the stepped sites and is intermediate in growth rate

between flat and kinked growth rates. The large growth rates of stepped and kinked faces often result in their disappearance from the final crystal structure, as faster growth tends to be less stable in nature. Each crystal will have different growth mechanisms and rates which are dependent on numerous factors, such as structure and defects of the crystal, degree of supersaturation and presence of impurities. Due to the decrease in supersaturation as a result of precipitation, Ostwald ripening of the particles may be observed. Ostwald ripening is a thermodynamically driven process first described by Wilhelm Ostwald in 1896. It states that small less thermodynamically stable particles will dissolve in favour of growth of larger more thermodynamically stable particles. This behaviour is thought to be a result of the solid phase in the system achieving a minimum total surface energy.[113]

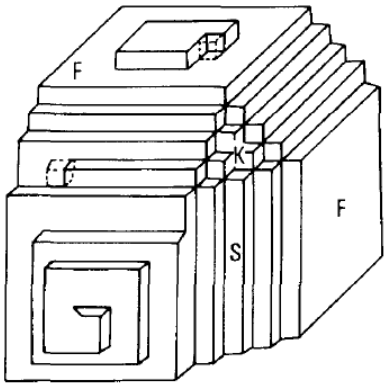


**Figure 3.6: Schematic illustrating different crystal growth sites: flat (F), stepped (S) and kinked (K).[116]**

Impurities such as ions, molecules, particles of dust, can enhance or suppress growth. They also have the ability to change the crystal habit through face selectivity. If the impurities are soluble they may change the equilibrium solubility of the system or even chemically react with the solute. It is almost impossible to predict the effect impurities will have on crystal growth.

## 3.3 Using microfluidic technology to monitor precipitation

Recently microfluidic technology has been used to monitor the precipitation process. The benefits of scaling down the volume in which precipitation occurs was first exhibited by Vonnegut *et al*. when the classical droplets method was developed.[118] This method involves the generation of numerous small droplets that serve as independent crystallizers. If the number of droplets greatly exceeds the number of impurities present then homogenous nucleation events can be observed, and if the droplets are of a sufficiently small size then the probability of observing a crystal can be related to the

nucleation rate. The disadvantage of this method is that it is known to suffer from variability due to droplet volume polydispersity.[119] This problem can be overcome using microfluidics where monodisperse droplets can be produced with ease.

Salmon *et al*. has presented a microfluidic device based on the classical droplets method. The authors used the probability of finding a crystal in each droplet to determine the nucleation rate of precipitation.[120] This device will be discussed in further detail in chapter 5.

Microchips capable of studying different solubilities of potassium nitrite polymorphs were reported by Salmon *et al*.[120, 121] The droplets were generated in silicone oil and stored in a serpentine channel. Detection of crystals within the droplets was achieved using a CCD camera and stereomicroscope under cross polarizers. During storage the temperature was first decreased until all droplets (up to 300, 100 nL droplets) contained a crystal. The temperature was then ramped up and the dissolution of crystals monitored, giving information on the number of polymorphs and their solubility.

Microfluidic technology enables various conditions which affect precipitation to be manipulated,[122] even reversibly is some cases.[123] Generation of monodisperse droplets in microfluidic channels allows numerous independent crystallization experiments to be carried out on chip without concern for cross contamination. Salmon *et al*. presented a chip in which hundreds of microfluidic droplets of varying concentration are stored on a chip under the application of a temperature gradient to investigate solubility diagrams (figure 3.7).[122] The authors report that a solubility diagram can be produced in less than an hour with only 250 µL of sample using this method. Droplets of different concentration are infused into ten parallel channels, with each channel containing a single concentration. The temperature is decreased until all droplets contain a crystal. A temperature gradient is then applied parallel to the channels, so that each droplet of the same concentration is at a different temperature (figure 3.7a). Crystals with a solubility temperature lower than the applied temperature will dissolve, allowing estimation of the solubility limit of the compound evaluated, from the separation of the droplets containing crystals and those that do not (figure 3.7c).

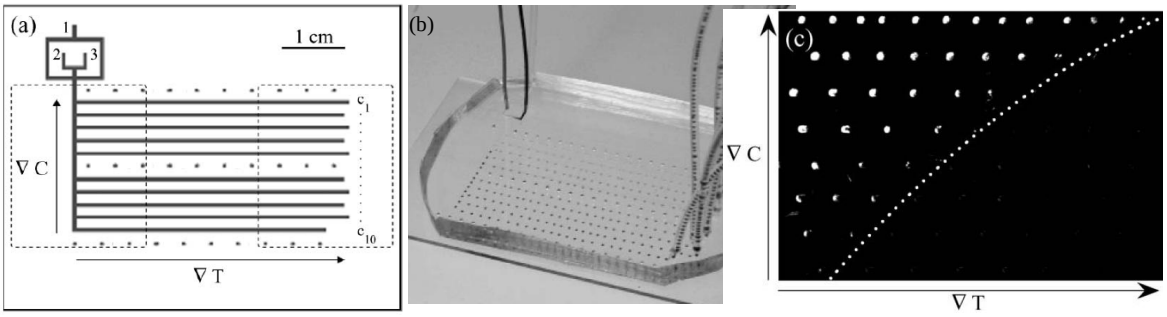


**Figure 3.7: The microfluidic device presented by Salmon *et al*. for the measurement of solubility diagrams.[122] a) Shows a schematic of the microfluidic device. Silicon oil is infused through inlet 1 and aqueous solutions through inlets 2 and 3. A temperature gradient is applied via two Peltier modules, the positions of which are indicated by dotted rectangles. The applied temperature is measured in the positions indicated by dotted lines. b) Is a photograph of the PDMS device sealed with a glass slide. Dye has been injected into the device to emphasise the concentration gradient. c) Shows the visualisation of the solubility curve, with the dotted line the estimated solubility limit.**

Microfluidics have been used to optimise protein crystallisation conditions.[123] Using a small quantity of protein (10 µg), Shim *et al.* were able to investigate optimum protein crystallisation conditions by decoupling the nucleation and crystal growth stages. This was achieved using a thin PDMS membrane (15 µm thick) to reversibly change the saturation within the droplet (figure 3.8). Aqueous droplets are introduced into wells adjacent to the channel using surface tension forces. The membrane, which is permeable to water but not salt and protein joins the droplet storage wells to a reservoir. Flowing dry air or a salt solution through the reservoir will result in permeation of water from the droplet to the reservoir, the concentration of protein and salt within the droplet will increase leading to the high supersaturations required for protein nucleation. Once crystals have been produced, a water solution can be introduced into the reservoir, resulting in permeation of water from the reservoir to the droplet, decreasing the supersaturation within the droplet. The lower supersaturation will favour crystal growth causing small crystals within the droplet to dissolve while larger crystals grow. The microdevice contains 100 wells so in theory 100 different protein/salt concentration combinations could be examined at one time.

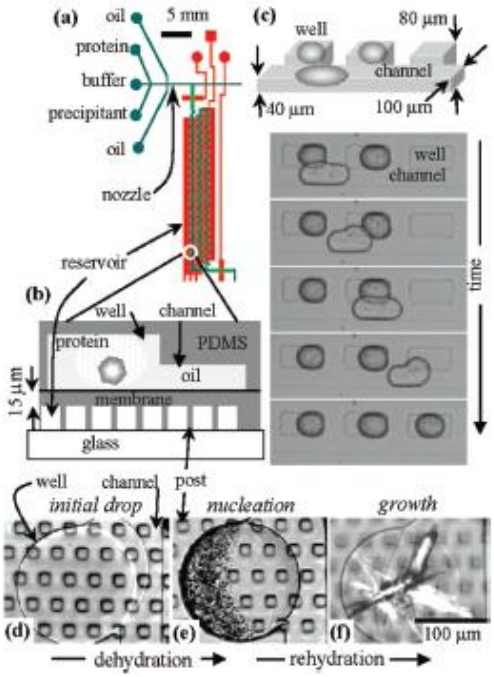


**Figure 3.8: The microfluidic device reported by Shim *et al*. to optimise protein crystallisation conditions by decoupling nucleation and crystal growth.[123] a) Shows a schematic of the microfluidic device. Droplets containing protein and precipitant are produced using flow focusing and are stored on chip in wells adjacent to the microfluidic channel (shown in green), directly on top of a reservoir (shown in red), separated by a PDMS membrane. b) Shows a close up of the channel, membrane and reservoir configuration. c) Details of droplet introduction into the storage wells, droplets will flow past any filled wells and be deposited in the next empty well. The crystallisation process is show in images d-f d) is the initial droplet, e) droplet after dehydration which induces nucleation and f) the crystal grown after the droplet is hydrated again.**

Zheng *et al*. also used microfluidics to study protein crystallisation.[124] Nanolitre sized droplets containing various amounts of protein, precipitant and additive were produced at a T-junction. The droplets were then incubated on chip and monitored for crystal formation. Two protein crystallisation techniques were employed: the microbatch technique which involved incubation being carried out with the PDMS chip submerged in water to prevent evaporation, and the vapour diffusion technique which allowed solvent evaporation, increasing the concentration of species within the droplet and inducing nucleation of crystals. Hansen *et al*. used an elastomer based chip to crystallise proteins.[125] The device is capable of performing 144 crystallisation screens, with each screen requiring only 10 nL of protein sample. The microdevice contains 144 crystallisation compartments, which consist of two chambers separated by a valve. Each chamber is primed with fluid by pressurising the gas in front of the fluid, which causes the gas to diffuse into the elastomer. When the chambers are primed, the valve is opened and the contents of the chambers mix via diffusion resulting in crystallisation if the correct crystallisation conditions are met.

### 3.3.1 Detection techniques

Microfluidic technology also offers the advantage of real time monitoring of the precipitation process. One of the major disadvantages of using macroscale methods to monitor solubility/precipitation is that concentration determination is typically accomplished by either UV-Vis spectroscopy or HPLC. The time taken between sampling and concentration determination can be lengthy, and therefore not give an accurate indication of the concentration at the time of sampling, as precipitation can continue to occur. The devices presented above use a microscope typically operated under crossed polarizers to visualise crystals which are formed during droplet storage. This thesis reports the use of on chip light scattering detection to monitor precipitation. Light scattering detection allows the extent of precipitation to be determined on-chip, from droplets moving at high speeds and is an easy and cost efficient detection system to use on this scale. Light scattering detection also offers the potential to determine the particle size of the precipitate if multiple detectors are used at different detection angles. As light scattering detection will be used in the following experiments a brief introduction to relevant light scattering regimes is given below.

#### 3.3.1.1 Introduction to light scattering detection

Light scattering can be defined as the deflection of a beam of light by a particle, and can give important information on particle size and structure as well as the motion of the particle, if the particle is moving. Scattering can be described as elastic or inelastic. No energy is lost in the case of elastic light scattering, i.e. the wavelength of the light will remain the same, whereas energy is exchanged during inelastic light scattering, resulting in a change in the wavelength of the light.

#### 3.3.1.2 Types of light scattering

There are many types of light scattering regimes. The light scattering regime observed is typically dependent on the wavelength of light, the size and shape of the particles, and the refractive index of the particle. A brief introduction will be given to Rayleigh scattering and Mie scattering, as these regimes are most relevant to this study.

##### 3.3.1.2.1 Rayleigh scattering

Rayleigh scattering, which is named after Lord Rayleigh, is the elastic scattering of light by particles of dimensions less than the wavelength of incident light. Rayleigh scattering

results for small particles that are optically soft i.e. have a refractive index close to 1. It should be noted, that when the particle is suspended in a solution the refractive index of the solution will need to be taken into account, as particles which have a refractive index in air greater than that required for rayleigh scattering, may exhibit Rayleigh scattering in solution. The relative refractive index ($n_r$) is given by equation 3.11,[126] where $n_1$ is the refractive index of media 1 and $n_2$ is the refractive index of media 2.

$$n_r = \frac{n_1}{n_2} \qquad [3.11]$$

The parameter, $x$, which is given by the ratio of the radius of the particle (r) and the wavelength of light in the media surrounding the particle ($\lambda$) (equation 3.12),[126] is an indication of which scattering regime will be observed. Rayleigh scattering occurs when $x \ll 1$, when $x > 1$ Mie scattering occurs.

$$x = \frac{2\,\pi\, r}{\lambda} \qquad [3.12]$$

$$where\ \lambda = \frac{\lambda_0}{n_{media}} \qquad [3.13]$$

Where $\lambda_0$ is the wavelength in a vacuum and $n_{media}$ is the refractive index of the media. The amount of light scattered by a particle from an unpolarised light source is given by equation 3.14.[127] The intensity, $I$, of light scattered is inversely proportional to the fourth power of the wavelength; it is for this reason that shorter wavelengths are scattered more than longer wavelengths. It also has a strong dependence on the size of the particle, as the intensity is proportional to the sixth power of the radius of the particle.

$$I = I_0 \frac{1+cos^2\,\theta}{2\,R^2} \left(\frac{2\,\pi}{\lambda}\right)^4 \left(\frac{n^2-1}{n^2+2}\right)^2 r^6 \qquad [3.14]$$

Where $I_0$ is the incident intensity of the beam of light, $\theta$ is the scattering angle, $R$ is the distance to the particle, $n$ is the refractive index and r is the radius of the particle.

Rayleigh scattering is a result of the polarisability of the particle. The oscillating electric field of a light wave causes an oscillating dipole within the particle. The more polarisable the particle, the larger the induced dipole will be, resulting in a greater intensity of

scattered light being observed. Figure 3.9 shows Rayleigh light scattering of a small particle; the forward light scattering is equivalent to the backward light scattering.

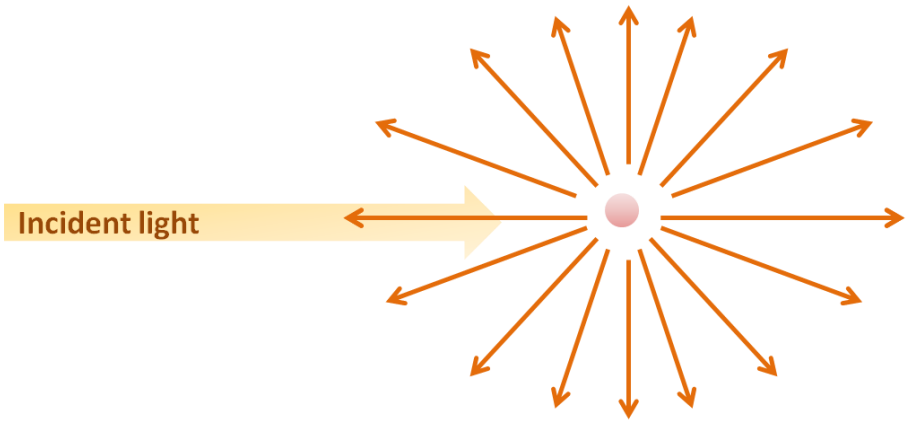


**Figure 3.9: Rayleigh light scattering profile**

### 3.3.1.2.2 Mie scattering

Mie scattering is the elastic scattering of light by spherical particles with dimensions larger or comparable to the wavelength of incident light. The intensity of scattered light is dependent on particles size but not strongly dependent on wavelength. Mie scattering is not uniform in nature, more light is scattered in the forward direction than in the backward direction (figure 3.10). As the particle size increases the amount of forward scattering light will increase.

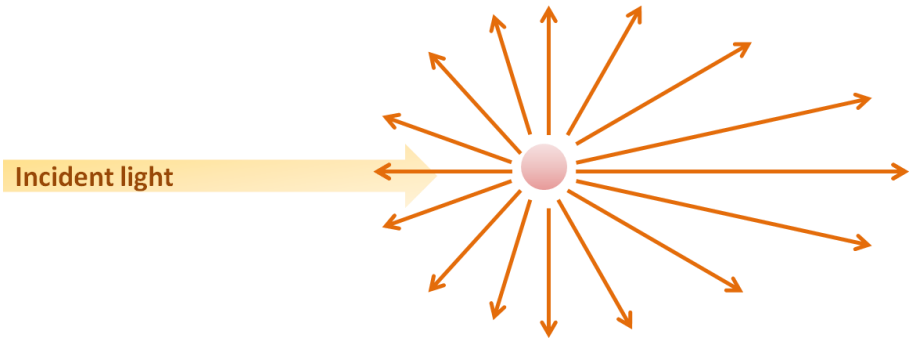


**Figure 3.10: Mie light scattering profile**

Analysis of Mie scattering is complex and involves solving the Maxwell equations, which is beyond the scope of this project. For a comprehensive discussion of both Rayleigh and Mie scattering, see references 128 and 129.

## 3.4 Development of a droplet based microfluidic device capable of monitoring drug precipitation upon a pH-shift

### 3.4.1 Overview

A droplet based microfluidic device has been developed which is capable of monitoring the precipitation of a poorly water soluble, weakly basic drug upon a pH shift. The model drug used in this investigation is ketoconazole. As a weakly basic drug, ketoconazole has greater solubility in acidic environments, i.e. in the stomach (pH 1.5 - 2.0), where ionisation will occur. Upon gastric emptying into the small intestine (pH 5.0 – 8.0), the solubility of the drug will decrease and precipitation may result. In this investigation the drug is initially dissolved in acidic media (pH 1.5). During droplet formation in the microfluidic device, this solution will be mixed with a basic solution so as to form a buffer solution of pH reflecting that of the small intestine. This pH shift will simulate the change in pH upon gastric emptying into the small intestine. Drug precipitation under these conditions will be monitored using a laser scattering technique.

### 3.4.2 Methods and Materials

#### 3.4.2.1 Chemicals

Latex bead solutions were obtained from SigmaAldrich (460, 600, 800 nm diameter), Varian (Agilent Technologies, Stockport, UK) (1000 nm) and Polysciences Inc. (Eppelheim, Germany) (384 nm). Ketoconazole was obtained from Fisher Scientific, and trisodium phosphate from Acros Organics (Fisher Scientific, Loughborough, UK). Perfluorodecalin was obtained from Fluorochem (Hadfield, UK). Amaranth and cresol red were obtained from SigmaAldirch. All materials were used as received.

#### 3.4.2.2 Determination of ketoconazole solubility[2]

A known mass of ketoconazole was added to 0.1 M pH 7.4 aqueous phosphate buffer and pH 6.5 fasted state simulated intestinal fluid (FaSSIF)[112] to attain a concentration of 1 mg $mL^{-1}$. The solutions were stirred using parylene coated discs (5.3 mm) and a magnetic stirrer (model VP710E, V&P Scientific, San Diego, USA) for 24 hours. The pH 7.4 buffer experiment was stirred at room temperature and the FaSSIF experiment at 37 $^{\circ}$C. The

[2] Solubility determination preformed by the screening and profile group (Alderley Park, AstraZeneca)

resulting mixture was centrifuged (Jouan Kr 4i Centrifuge, Thermo Scientific) twice at 3800 rpm to remove any solid material. The supernatant was analysed with a HPLC (Waters 2790, Waters Ltd.) coupled to an UV diode array detector (Waters 996, Waters Ltd.). Ketoconazole solubility was determined by comparing the peak area with that of a standard solution of known concentration.

### 3.4.2.3 Fabrication of the microchip[3]

The chip design is shown in figure 3.11. A rectangular cross-section spiral channel 730 µm wide, 700 µm deep and 828.4 mm in length, including a T-junction 400 x 400 µm in cross section, was milled into a PMMA substrate using a CAT3D-M6 computer numerical control (CNC) milling machine (Datron Technologies Ltd.). Three inlet holes (one organic and two aqueous) and one outlet hole were drilled through the substrate, all holes drilled were 1.398 mm in diameter. The microfluidic device was sealed using a PCR seal (Corning Inc.) and a hydrophobic coating applied to the channels by infusing a surface modifying fluorinated polymer in a hydrofluoroether solvent (Certonal FC732, Acota Ltd, Shrewsbury, UK). The fluorinated polymer was left in the chip for an hour being removed and the chip allowed to dry.

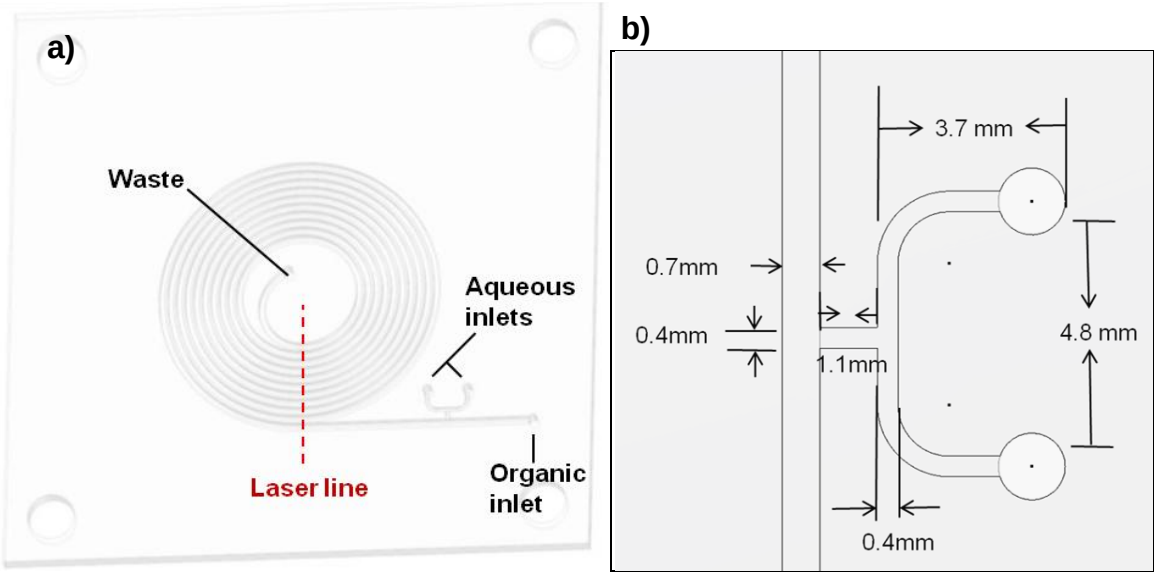


**Figure 3.11: a) The microfluidic chip design. The area illuminated by the laser line generator is indicated by the red dashed line, b) the dimensions of the aqueous inlets.**

### 3.4.2.4 Experimental setup

The experimental setup is shown in Figure 3.12. Successive areas of the spiral channel were illuminated (figure 3.9a) using a laser line generator (RS Components Ltd., Corby,

[3] Fabrication carried out by Dr Stephan Mohr (University of Manchester)

UK) (3 mW) with a wavelength of 635 nm. Organic and aqueous flows were infused using Kloehn pumps (Kloehn Inc., Las Vegas, USA) controlled using a LabVIEW (National Instruments, Austin, USA) program designed in house by Dr Bernard Treves Brown. The amount of light scattered by the aqueous phase was recorded with a camera (PixeLINK PL-A741, Ottawa, Canada) using ViMicro Cam software (ViMicro Corporation, Beijing, China).

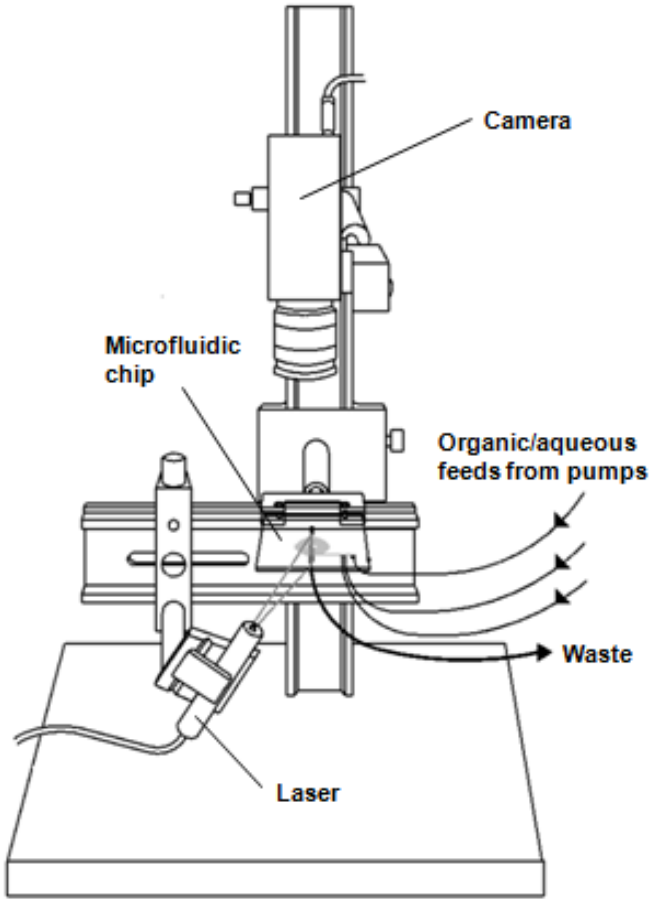


**Figure 3.12: The experimental setup used to monitor drug precipitation. The microfluidic chip was affixed directly below a camera (PixeLINK PL-A741). A laser line generator (3 mW, 635 nm) was positioned so as to illuminate successive areas of the channel (area illuminated is shown in figure 3.11a). Organic and aqueous flows were generated using Kloehn pumps controlled by a LabVIEW program.**

### 3.4.2.5 Determination of the time taken for the droplet to reach each detection point

The intensity is measured at 11 positions on chip (figure 3.13). The speed of the droplet was determined to establish the time taken for the droplet to reach each position on chip. Droplet speed was calculated by measuring the time it took for a droplet to travel a known distance i.e. between position 1 and position 2 (110.4 mm). At a total flow rate of 60 µL

$min^{-1}$ (organic 40 µL $min^{-1}$, aqueous 20 µL $min^{-1}$) the average time the droplet took to travel 110.4 mm was 57.35 seconds with a standard deviation of 0.23 (n=3), corresponding to a speed of 1.925 mm $s^{-1}$. The speed was then used to calculate the time the droplet would reach positions 3-11. The time for the droplet to travel from position 0 to position 1 was determined as above and could not be calculated from the speed of the droplet, as mixing occurred prior to droplet detachment and the time taken for the droplet to detach needed to be taken into account. Therefore the average time taken from the beginning of droplet formation to the droplet reaching position 1 was determined to be 10.58 seconds with a standard deviation of 0.16 (n=3). A table of the calculated timings are given in table 3.2.

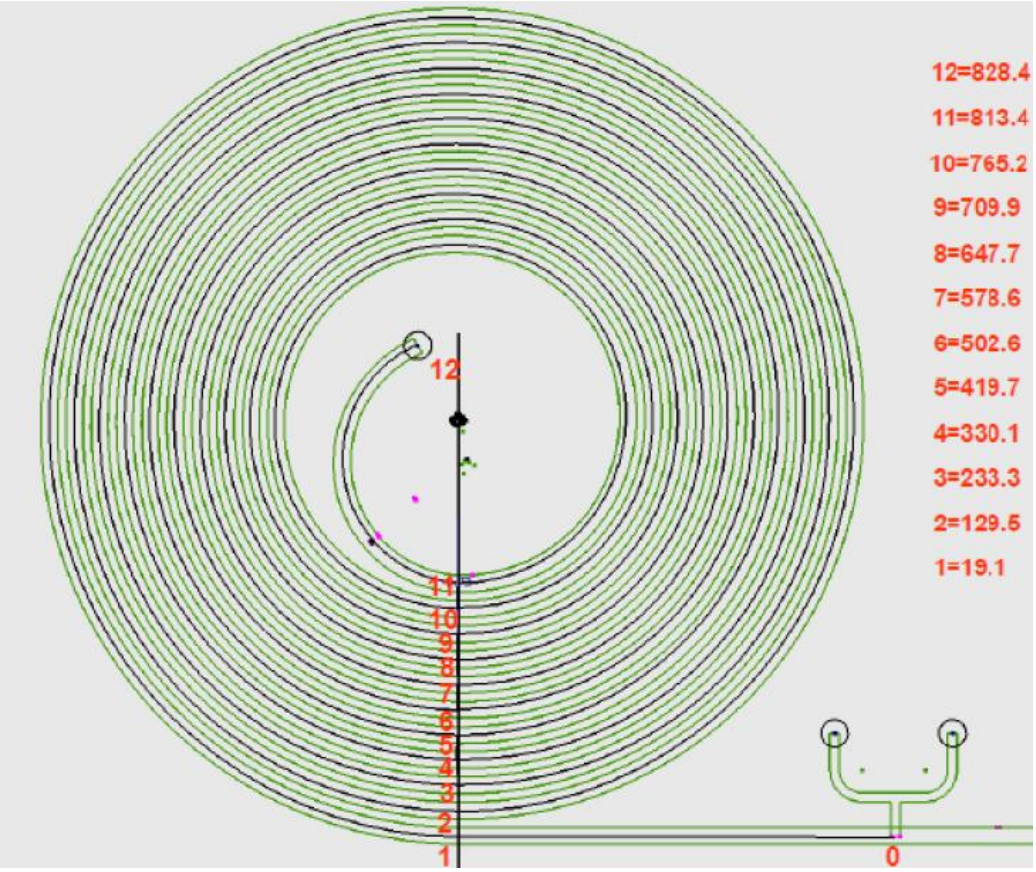


**Figure 3.13: Schematic of chip 1. The eleven positions at which the intensity of scattered light is measured are denoted (1-11). The distance from the T-junction (0, droplet generation) to each position are given (in mm) to the right of the spiral.**

| Position | Time (mins) |
|---|---|
| **1** | 0.18 |
| **2** | 1.13 |
| **3** | 2.03 |
| **4** | 2.87 |
| **5** | 3.64 |
| **6** | 4.36 |
| **7** | 5.02 |
| **8** | 5.62 |
| **9** | 6.16 |
| **10** | 6.64 |
| **11** | 7.05 |

**Table 3.2: Time taken for the droplet to reach each position on the microfluidic chip at a total flow rate of 60 µl $min^{-1}$ (organic 40 µL $min^{-1}$, aqueous 20 µL $min^{-1}$).**

### 3.4.2.6 Determination of the amount of light scattered by the precipitation in the droplet

The intensity of light scattered by precipitation in the droplets is determined from videos recorded during the experiment. The videos are then analysed using an AVI reader computer program designed in house by Prof. Nick Goddard. The AVI reader measures the intensity of light scattered by the droplet by averaging the greyscale in each selected frame of the recorded video. The video is loaded up and regions of interest (areas where the laser illuminates the channel) are manually selected (figure 3.14). Details of the areas selected are automatically inserted into the spreadsheet labelled calculated values. These positions can then be saved and reopened enabling consistency between analyses. The frame range to be analysed is selected and the extract range button activates the analysis.

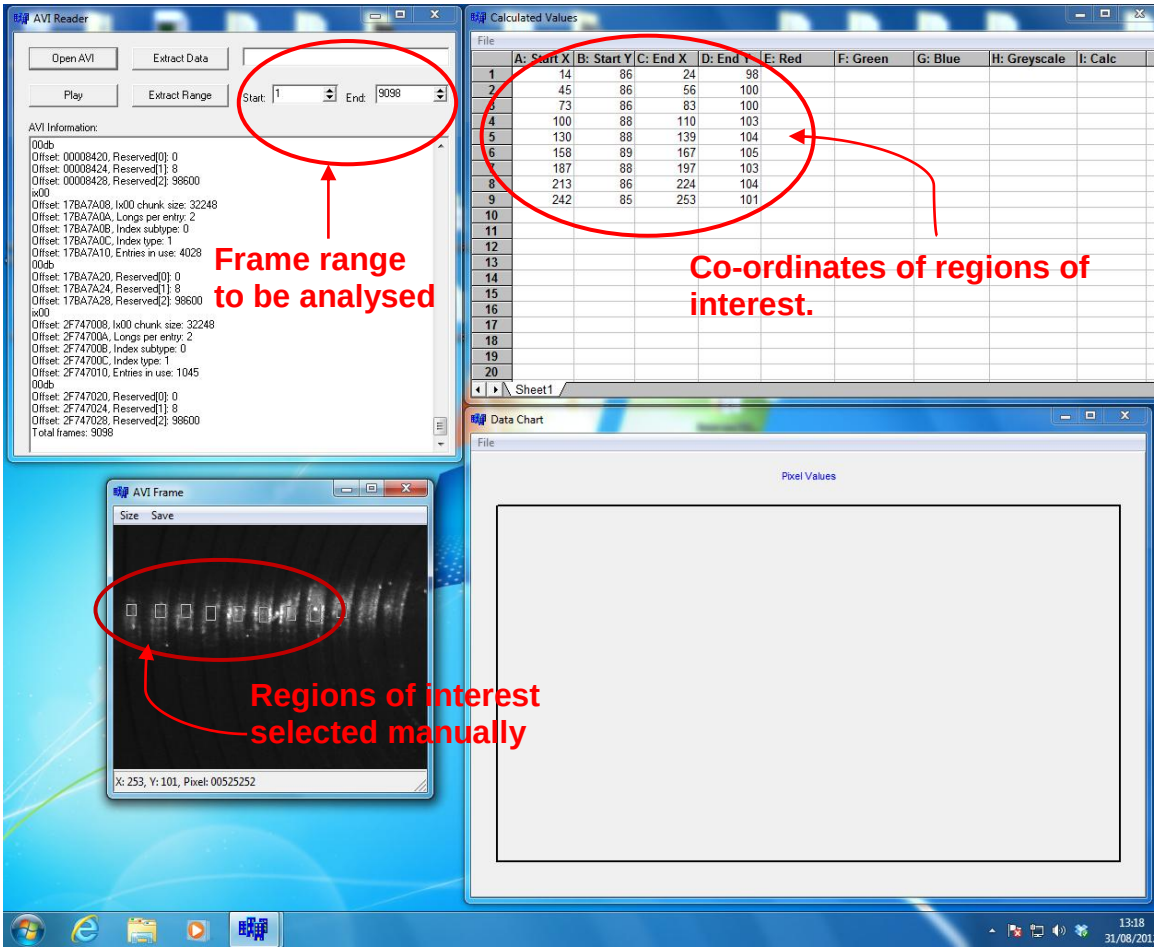


**Figure 3.14: The AVI reader program used to analyse videos. Top left, the AVI reader window allows videos to be opened and selection of the frame range to be analysed. When all other settings are determined the 'extract range' button will start the analysis and prompt the user to save the analysed data. Bottom left, regions of interest are selected manually in the AVI frame window. The intensity inside the selected regions will be determined for each frame of the extraction range selected. Top right, the calculated values window contains the co-ordinates of the regions of interest selected in the AVI frame window. These coordinates can be saved and reopened for subsequent videos. Bottom right, the data chart is a plot of the intensity as a function of frame number enabling the user to monitor the analysis.**

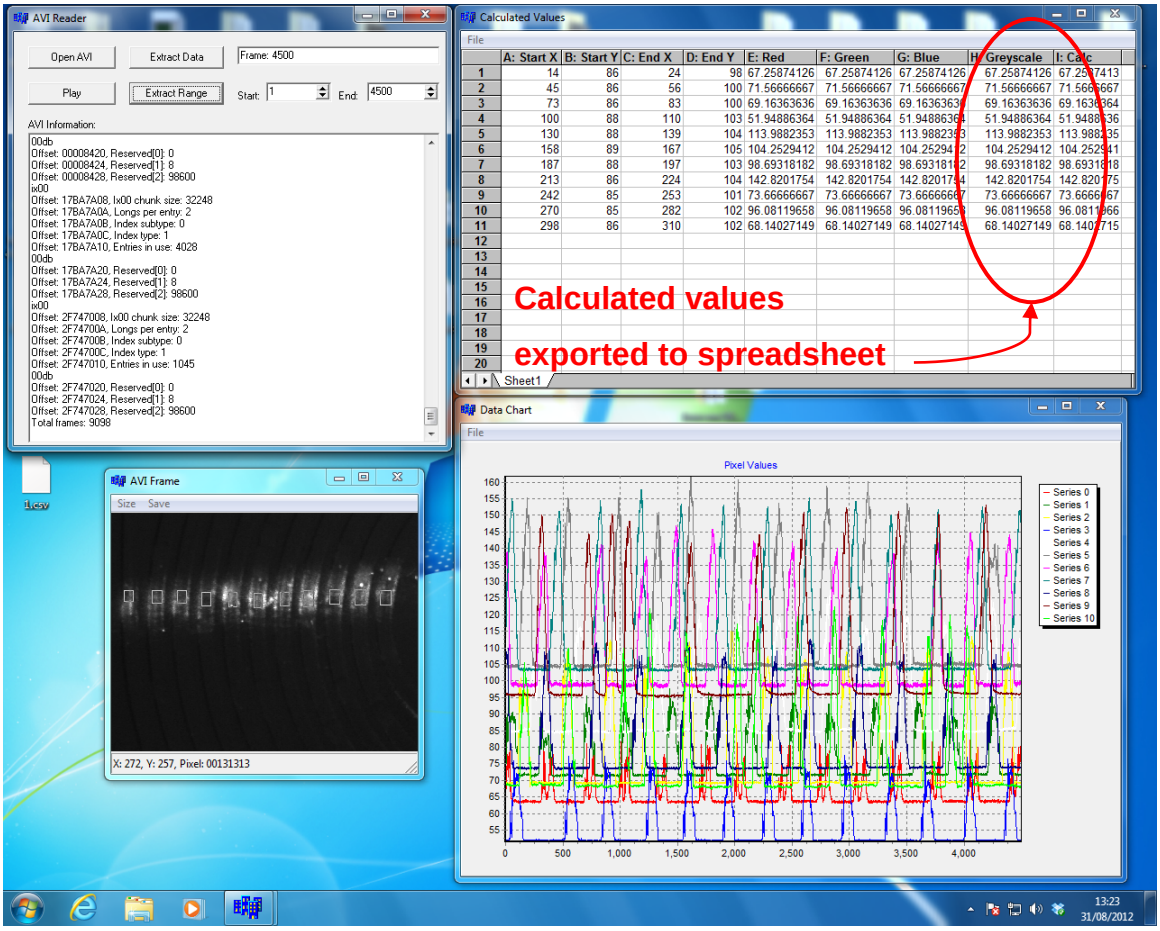


**Figure 3.15: The AVI reader at completion of a video analysis. The data chart shows the intensity determined for all the frames selected at each position on chip (each position is assigned a different colour). The intensity for each frame (column I of the calculated values chart) is imported into a spreadsheet for further analysis.**

A graph function built into the software allows the intensity to be monitored as the analysis is running (figure 3.15). The results are saved as a CVI file (figure 3.16) and then manually imported into an Excel template, where the intensities can be normalised using the normalisation constant obtained through the device calibration (section 3.4.2.7).

| | A | B | C | D | E | F | G | H | I | J | K | L |
|---|---|---|---|---|---|---|---|---|---|---|---|---|
| 1 | Frame | Position1 | Position2 | Position3 | Position4 | Position5 | Position6 | Position7 | Position8 | Position9 | Position10 | Position11 |
| 2 | 0 | 40.70238 | 72.3 | 43.58824 | 33.72 | 87.56471 | 52.64211 | 137.425 | 52.36667 | 38.13333 | 75.645833 | 52.684211 |
| 3 | 1 | 40.82143 | 68 | 43.37647 | 34.02667 | 88.94118 | 61.29474 | 143.6125 | 55.88889 | 38.07778 | 73.958333 | 52.578947 |
| 4 | 2 | 40.54762 | 66.5625 | 43.37647 | 34.10667 | 88.4 | 66.84211 | 146.2125 | 60.76667 | 37.98889 | 71.625 | 52.45614 |
| 5 | 3 | 40.89286 | 64.45 | 43.62353 | 33.81333 | 89.01177 | 66.04211 | 148.0875 | 65.24444 | 37.9 | 69.802083 | 52.5 |
| 6 | 4 | 40.90476 | 60.375 | 43.44706 | 33.84 | 91.22353 | 64.73684 | 150.9625 | 65.18889 | 38.06667 | 66.510417 | 53.008772 |
| 7 | 5 | 40.52381 | 58.025 | 43.51765 | 33.66667 | 98.15294 | 65.34737 | 156.75 | 65.88889 | 37.97778 | 64.364583 | 52.447368 |

**Figure 3.16: Data obtained from the AVI reader. Each position is given a separate column containing the intensity determined for each frame of the video analysed.**

### 3.4.2.7 Calibration of the microfluidic system

The device was calibrated with a phosphate buffer (blank solution) and a latex bead suspension to account for background scattering and uneven illumination of the microfluidic channels by the laser. A latex bead solution (384 nm diameter particles, $3.37 \times 10^8$ particles $mL^{-1}$) was infused into the chip through the aqueous inlets using Kloehn syringe pumps at a total flow rate of 20 µL $min^{-1}$. A video of the droplets as they travel through the spiral was recorded and the scattered intensity determined using the AVI reader. Figure 3.17a shows the scattering intensity measured from the latex bead suspension. The graph was obtained by plotting the intensity data obtained from the AVI reader as a function of frame number. Each peak represents a droplet, the intensity of which is determined by subtracting the minimum (background) intensity from the maximum intensity. The intensity of light scattered from blank droplets (those containing phosphate buffer) is obtained in the similar manner, however the profile of the intensity differs from that of droplets containing the latex bead suspension. Reflections from the front and back of the droplet are present (see figure 3.17b), therefore the maximum scattered light due to the phosphate buffer is given by the intensity between the two reflection peaks. The background intensity is subtracted from the maximum intensity to give the intensity of light scattered by the phosphate buffer. The normalisation constant is determined by subtracting the average scattered intensity obtained for the blank droplet from the average scattered intensity obtained from the droplet containing the latex bead solution. This process is repeated for each position on chip. Calibration was carried out before each run of experiments.

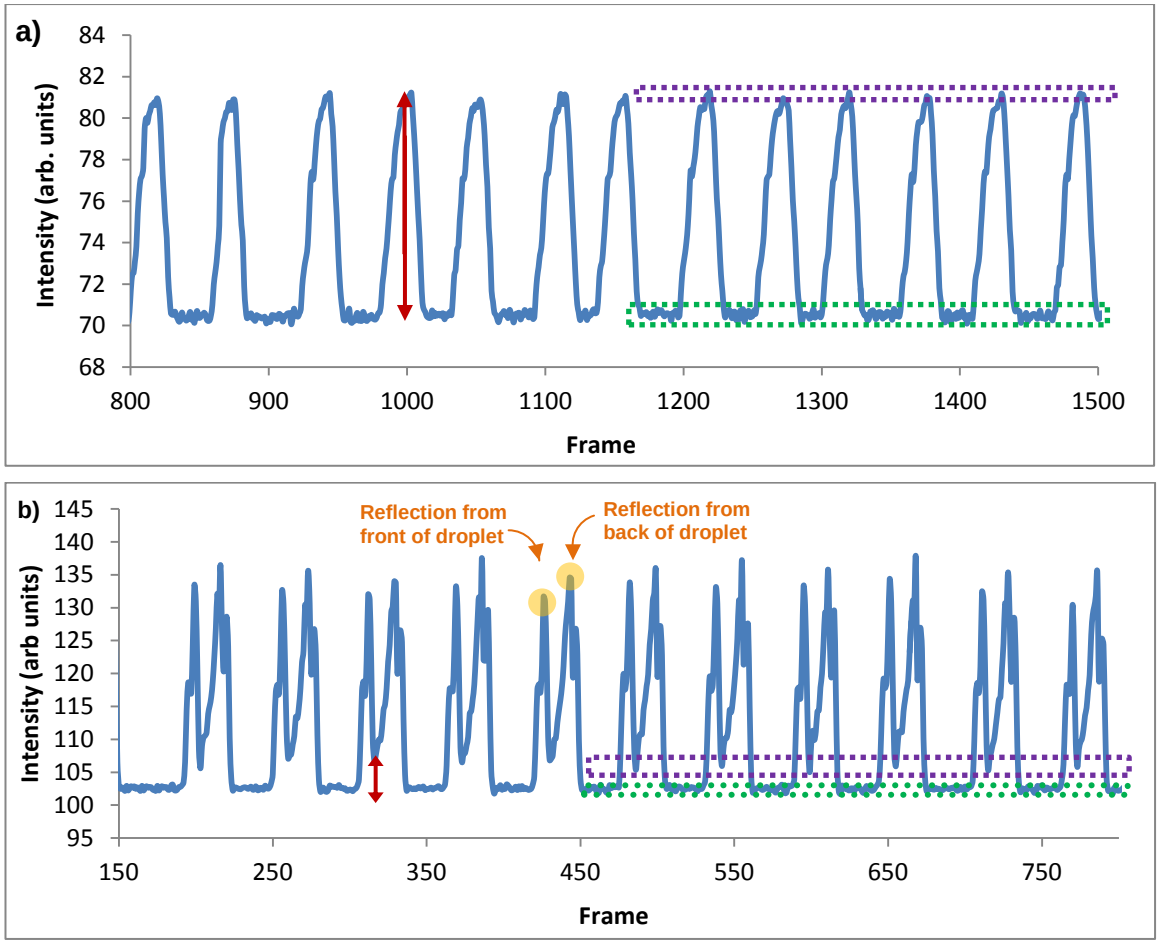


**Figure 3.17: Light scattering profiles of droplets containing a latex bead suspension (a) and a buffer solution (b). a) Each peak is a droplet containing latex beads (384 nm diameter particles, $3.37 \times 10^8$ particles $mL^{-1}$). The intensity of light scattered due to the beads (shown by the red arrow) is obtained by subtracting the minimum (background) intensity (green dashed box) from the maximum intensity (purple dashed box). The dashed boxes represent the range of intensities which are averaged to produce the minimum and maximum intensities. A range is used to account for slight variations observed in the maximum and minimum intensities. b) Each buffer droplet produces two peaks as it passes through the detection region due to light scattering from the surface of the droplet. The first peak is due to the reflection of light from the front of the droplet and the second peak is due to the reflection from the back of the droplet. The intensity of light scattered by the buffer (shown by the red arrow) is in between the two reflection peaks and is determined by subtracting the minimum intensity (green dashed box) from the maximum intensity (purple dashed box).**

### 3.4.2.8 Determination of scattering due to drug precipitation

The data from the analysed video are manually imported into a spreadsheet containing formulae required to determine the intensity (figure 3.18). Each page represents one position on chip. The intensity values are normalised using the normalisation constant obtained from the calibration, and a graph of the normalised intensity as a function of frame number is plotted (figure 3.19). The range of maximum and minimum intensity values are read from the graph and are inserted in cells D1 and E1 (high and low

maximum values respectively) and G1 and H1 (high and low minimum intensity values respectively) (figure 3.18). Formulae then average all the intensity values which fall within these ranges. The average minimum intensity is then subtracted from the average maximum intensity. This process is repeated for all the positions and a graph of intensity against time (time the droplet reaches each position after droplet generation) is plotted.

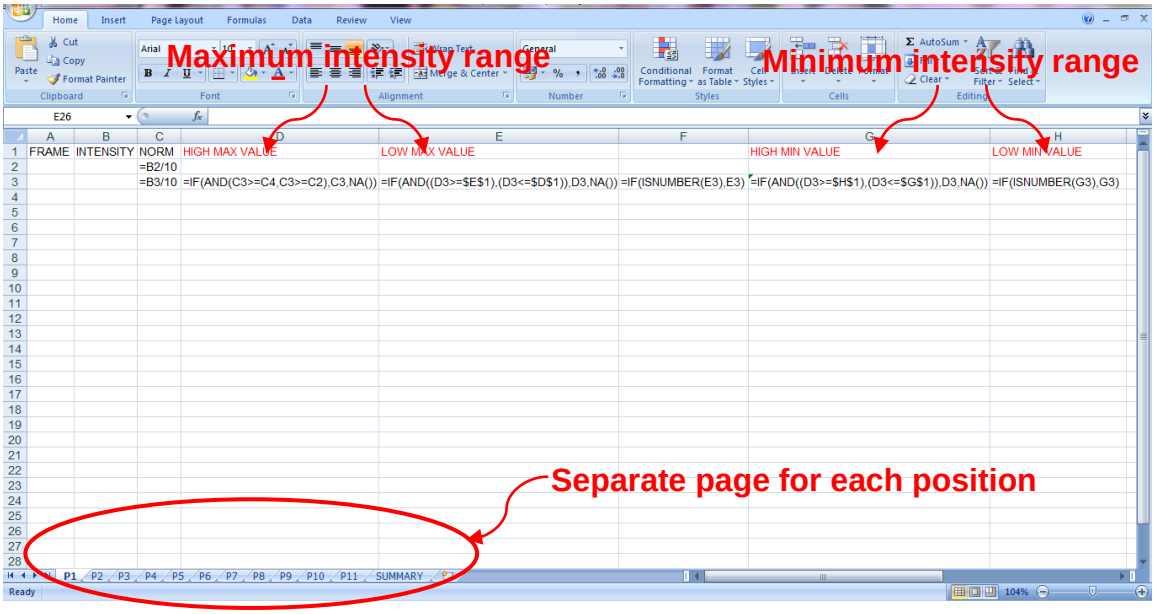


**Figure 3.18: Spreadsheet template used to analyse data obtained from the AVI reader. The intensity for each frame of the video, at each position, is manually imported into the template (column B). The intensity data are normalised using the normalisation constant (column C) and a graph of the normalised data as a function of frame number is plotted. High and low intensity values for the maximum and minimum intensities are read from the graph and the intensity values which fall into these ranges are averaged. The average minimum intensity is then subtracted from the average maximum intensity to give the scattering intensity due to drug precipitation within the droplet.**

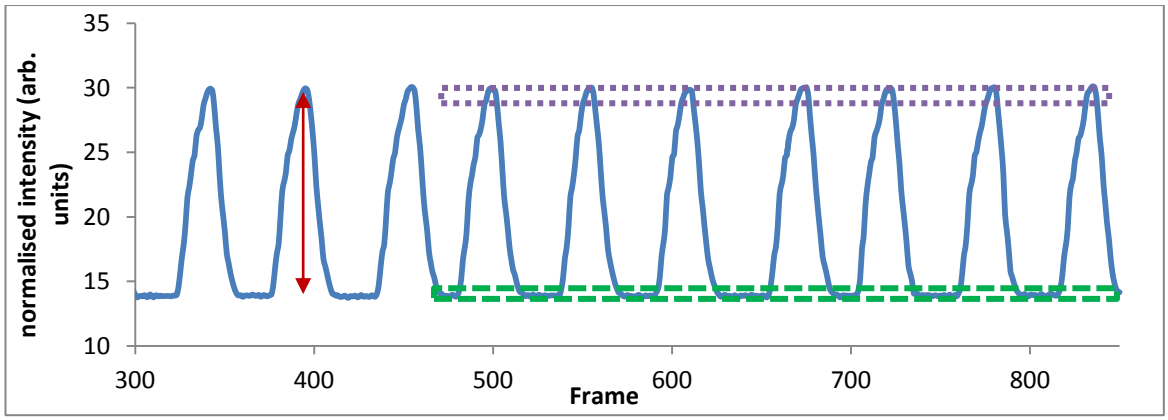


**Figure 3.19: A graph of the normalised intensity (arbitrary units) as a function of frame number. The intensity of light scattered by the precipitated solution (shown by the red arrow) is given by the difference between the average background scattering (minimum intensity) (shown by green dashed box) and the average maximum intensity (shown by purple dashed box).**

### 3.4.2.9 A latex bead study to determine the response of the system to different concentrations and particle sizes

The response of the system to different concentrations and different particle sizes was evaluated using latex bead suspensions with a range of particle diameters (384, 460, 600, 800, and 1000 nm). The solutions were made up to the desired concentration (0.0002 - 0.003 % w/w solutions corresponding to concentrations of between $5.73 \times 10^6$ - $1.01 \times 10^9$ particles $mL^{-1}$) and infused onto the chip through both aqueous inlets at a total flow rate of 20 µL $min^{-1}$. The scattering data were normalised with the normalisation constant determined from the calibration and the intensity determined as above (section 3.4.2.8).

### 3.4.2.10 On-chip supersaturation generation using a pH shift

Figure 3.20 shows a schematic of the droplet composition used in the on-chip pH shift experiment to monitor drug precipitation. To simulate gastric conditions, ketoconazole was dissolved in dilute phosphoric acid (0.1 M, pH 1.5). The acidic solution of ketoconazole is then mixed with sodium phosphate solution upon droplet formation, so the pH of the droplet reflects that of the small intestine (pH 6.5 and pH 7.0 are used in these experiments). The shift in pH results in the generation of a supersaturated solution. Kloehn syringe pumps were used to infuse the aqueous solutions at flow rates of 10 µL $min^{-1}$ and the organic phase at 40 µL $min^{-1}$. Monodisperse aqueous plugs, approximately 500 nL in volume, were generated in immiscible perfluorodecalin. The droplets contained 50 % of the solution of ketoconazole dissolved in 0.1 M phosphoric acid and 50 % sodium phosphate solution. A range of ketoconazole concentrations were used (x = 0.56, 0.75, 0.94, 1.13, 1.32, 1.51, 1.69, 1.88 mM, see Figure 3.19). The concentration of the sodium phosphate solution (yM, see Figure 3.20) was varied to generate a buffered solution of desired pH upon droplet formation. Ketoconazole precipitation at pH 6.5 (y = 0.19 M) and pH 7.0 (y = 0.62 M) was investigated in this study. The pH values of the mixed solutions were confirmed using a calibrated digital pH meter (model 211, Hanna Instruments, Leighton Buzzard, UK).

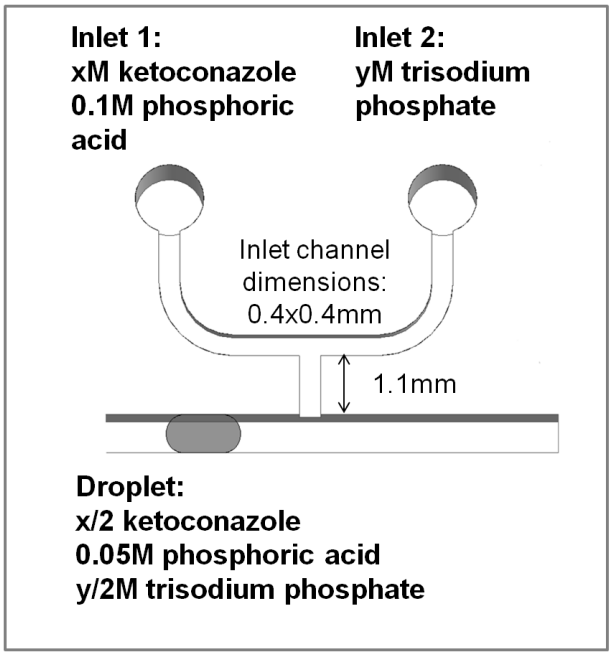


**Figure 3.20: Schematic of droplet composition for the pH shift experiment. The droplet contained 50% of the solution from inlet 1 (xM ketoconazole in 0.1 M phosphoric acid) and 50% of the solution from inlet 2 (yM trisodium phosphate). The concentration of trisodium phosphate from inlet 2 is varied to control the pH of the generated droplet (y=0.19 M for pH 6.5, y=0.62 M for pH 7.0).**

### 3.4.2.11 Dynamic light scattering (DLS) macroscale experiments to corroborate microscale results

Ketoconazole precipitates formed under similar conditions to the pH shift conditions listed above (section 3.4.2.10) but on the macroscale were examined using DLS. DLS measurements were performed using a BI-9000 instrument (Brookhaven Instruments, Holtsville, USA) operating in dynamic light scattering mode. Measurements were made at 25 ºC, using a detector slit width of 200 nm, a detection angle of 90°, and a wavelength of 514 nm. Equal quantities of the ketoconazole solution (0.56 mM) and the trisodium phosphate solution (0.19 and 0.62 M) were combined to generate a buffer solution with a ketoconazole concentration of 0.29 mM at pH 6.5 and 7.0, corresponding to supersaturations of 31.82 and 48.31 respectively (degree of supersaturation was calculated with equation 3.5, using solubility values of 4.714 µg $mL^{-1}$ for pH 6.5 and 3.105 µg $mL^{-1}$ for pH 7.0). The samples were then briefly vortexed and DLS measurements were taken over a 20 minute period. Particle sizes were calculated assuming a refractive index of 1.590 for ketoconazole.

### 3.4.2.12 Amaranth dye experiment to evaluate mixing in the T-junction prior to droplet formation

Mixing in the T-junction prior to droplet generation was investigated using amaranth dye as one of the aqueous flows. The flow rates used in this experiment reflect those used in the pH shift experiment. The amaranth dye solution and water were infused into the aqueous inlets at flow rates of 10 µL $min^{-1}$. Droplets were formed in perfluorodecalin, which was infused at a flow rate of 40 µL $min^{-1}$. Videos of the T-junction during droplet generation were recorded using a Lumenera LU125C camera (Lumenera Corporation, Ontario, Canada) and ViMicro Cam software (ViMicro Corporation).

### 3.4.2.13 Cresol red dye experiment to evaluate mixing in the T-junction prior to droplet formation

The presence of acid-base based mixing in the T-junction prior to droplet formation was investigated using a pH indicator (cresol red), which undergoes a colour change yellow to purple in the pH range 7.0 - 8.8. The acidic aqueous phase consisted of cresol red dye dissolved in 0.01 M hydrochloric acid, and the basic aqueous phase used was 0.04 M sodium hydroxide solution. Both aqueous phases were infused onto the chip at a flow rate of 10 µL $min^{-1}$, while the organic phase (perfluorodecalin) was infused at a flow rate of 40 µL $min^{-1}$. Videos of the T-junction during droplet generation were recorded using a Lumenera LU125C camera (Lumenera Corporation) and ViMicro Cam software (ViMicro Corporation).

## 3.4.3 Results and discussion

### 3.4.3.1 Research aims and chip design

The objective of this research was to develop a microfluidic based system which could be used to study drug precipitation in real time. Current techniques require off-line concentration measurement, which often does not reflect the concentration at the time of sampling. By incorporating detection on-chip, the extent of drug precipitation could be determined quickly and would reflect the precipitation in the droplet at the detection time, eliminating the need for sampling, filtration or centrifugation, and concentration determination. In order to measure the precipitation in the droplets after different incubation times a spiral based chip was devised. The spiral allows the droplets to be studied at multiple incubation times as detection can be carried out at the points at which the laser line generator intersects the microchannel. The spiral also allows a long channel

to fit on the microchip without the need for sharp bend which may affect the degree of precipitation as the fluid would undergo ‘stretching’ and ‘folding’ as it travels around the bend. Relatively large channels are used, 730 x 700 µm, in order to produce droplets large enough for precipitation to readily occur and allow the use of viscous liquids in the microchannels, such as the polymer solutions used in chapter four. The microfluidic setup presented in this thesis differs from other microfluidic devices used to study drug precipitation in that light scattering detection is used to determine the extent the drug has precipitation from the solution, and real-time measurement of precipitation is made possible as detection occurs as the droplet travel through a spiral channel. Current literature mainly concerns the optimisation of protein crystallisation conditions, whereas the microfluidic setup presented here is designed to study drug molecules under physiological conditions.

### 3.4.3.2 Solubility of ketoconazole

Figure 3.21 shows the measured solubility of ketoconazole as a function of pH. Ketoconazole solubility decreases with increasing pH; this is expected as it is a weakly basic drug and will have greater solubility in an acidic environment. The solubility of ketoconazole at pH 6.5 in FaSSIF was also determined. Ketoconazole solubility at pH 6.5 in FaSSIF (11.9 µg $mL^{-1}$) was found to be approximately 2.5 fold greater than its solubility in pH 6.5 aqueous buffer, which is 4.7 µg $mL^{-1}$ (figure 3.21). As ketoconazole is known to be administered as a 200 mg tablet, estimation of the minimum and maximum intraluminal concentration of the drug can be made. The minimum intraluminal concentration is likely to be around 121 µg $mL^{-1}$ (calculated by dividing the dose by the volume of the small intestine, 1650 mL[133]). The maximum intraluminal concentration, based on taking the drug with a 250 mL glass of water, will probably be around 800 µg $mL^{-1}$ (calculated by dividing the dose by the quantity of water, and ignoring any dilutions within the lumen). The estimated intraluminal concentrations can be translated to supersaturations using equation 3.5 (section 3.2.4.3). At the minimum intraluminal concentration of 121 µg $mL^{-1}$, supersaturations of 10 and 26 would be expected in FaSSIF and pH 6.5 buffer, respectively. At the maximum intraluminal concentration of 800 µg $mL^{-1}$, supersaturations of 67 and 170 would be expected in FaSSIF and pH 6.5 aqueous buffer, respectively.

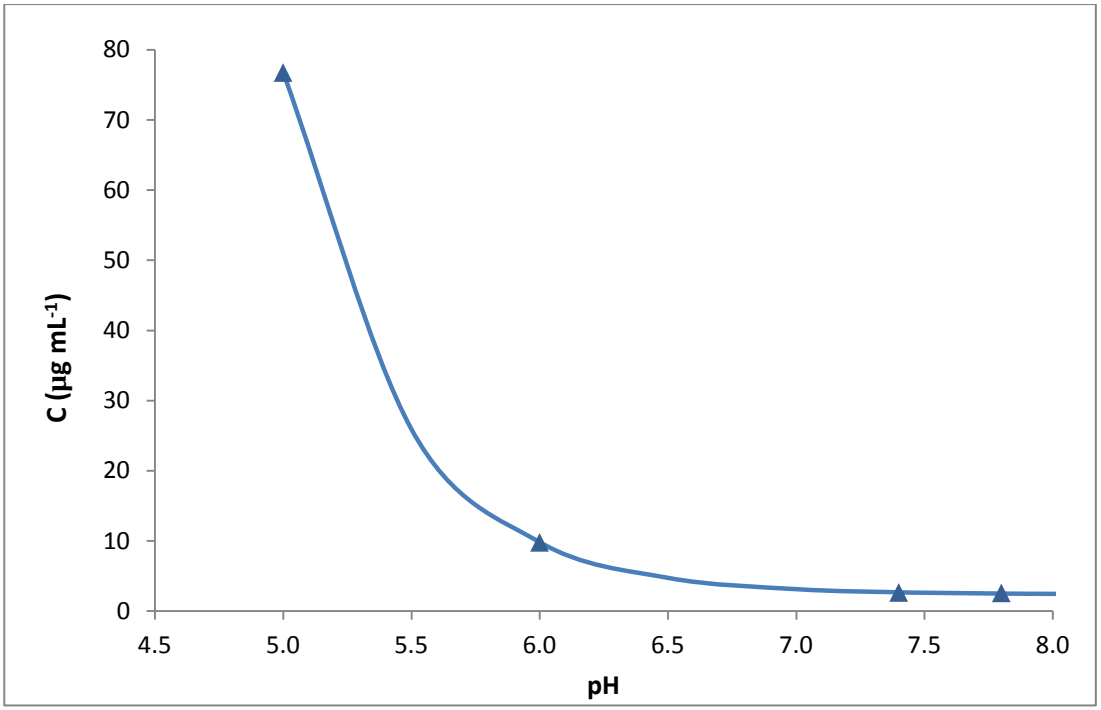


**Figure 3.21: Measured solubility (C) of ketoconazole as a function of pH. The line represents the calculated solubility profile:** $C = C_0(1+10^{(pK_a - pH)})$ **where C and $C_0$ represent the solubility and intrinsic solubility (2.4 µg $mL^{-1}$) respectively. Solubility data at pH 5.0, 6.0 and 7.8 were quoted from references 133 and 134.**

### 3.4.3.3 Characterisation of the microfluidic system using latex beads

The response of the laser scattering detection system was evaluated using latex bead suspensions. Figure 3.22 shows an image of the light scattered by a $6.75 \times 10^8$ particle $mL^{-1}$ latex bead (diameter 384 nm) suspension. The scattering intensity of different concentration latex bead suspensions containing 384 nm diameter beads was determined at ten positions on chip (positions 2-11, see figure 3.11). The results of this experiment are shown in figure 3.23. The scattering intensity measured for a latex bead concentration should be the similar across all positions that detection occurred, as the droplet should contain the same quantity of latex beads. This is observed at lower bead concentrations, however there is some deviation at higher bead concentrations. This may indicate limitations of the detector to measure scattering intensity accurately for solutions that are very concentrated.

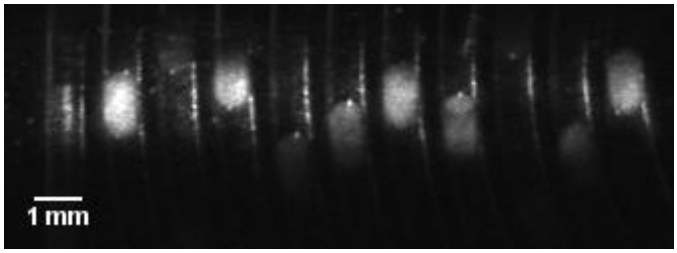


**Figure 3.22: An image of the illumination of the microfluidic chip using a laser light source, taken using a PixeLINK camera (PL-A741) and ViMicro Cam software. The droplets contain a 6.75 x $10^8$ particles $mL^{-1}$ latex bead (384 nm diameter) suspension.**

The values for each concentration were averaged across all positions and are shown in figure 3.24 with other results obtained using different diameter latex bead suspensions. Latex bead diameters of between 384 nm and 1000 nm were investigated, as these diameters are typical of the diameters of ketoconazole particles measured using DLS, which will be discussed later. Concentrations of between 5.73x$10^6$ – 1.01x$10^9$ particles $mL^{-1}$ which correspond to concentrations of 0.0002 - 0.003 % w/w were used. These concentrations are similar to the ketoconazole concentrations (0.0001 – 0.0005 % w/w) used in the pH shift experiments. The intensity of scattered light measured in these experiments show that this detection method is responsive to both changes in particle size and concentration.

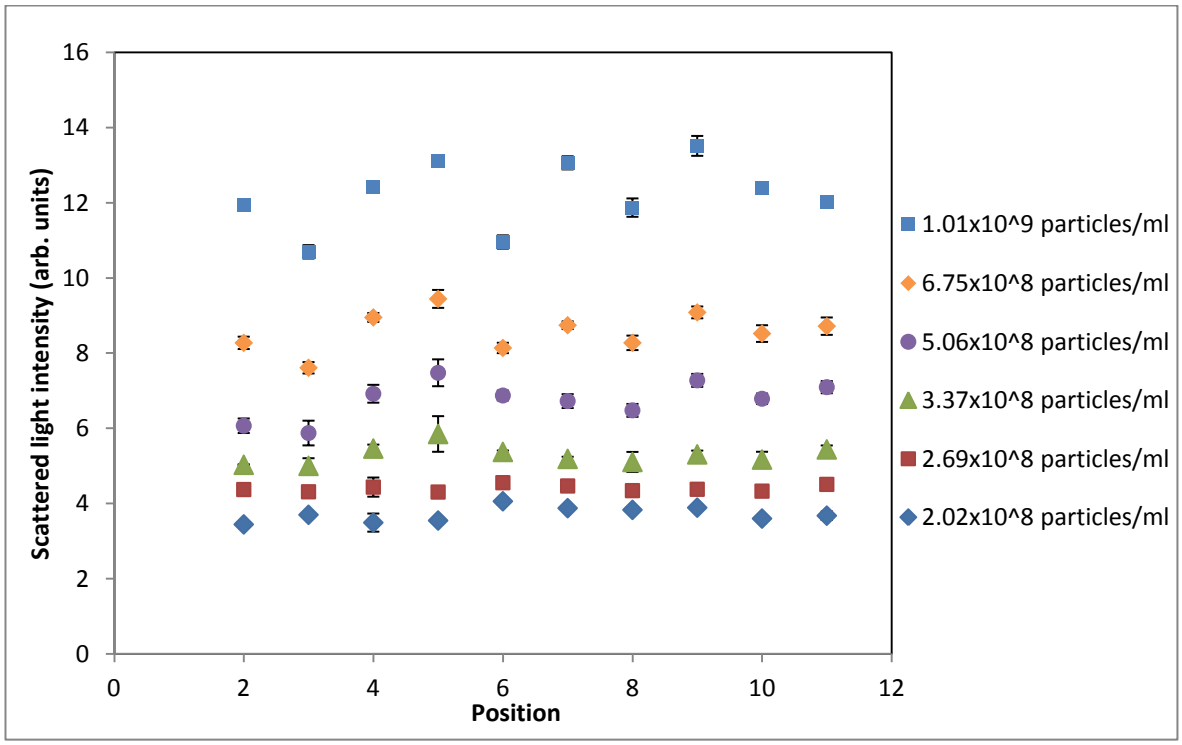


**Figure 3.23: Scattered light intensity (arbitrary units) of different concentrations of a latex bead suspension (bead diameter 384 nm) at positions 2-11 (see figure 3.11) on chip, using a laser light source. The error bars show the standard deviation (n=3).**

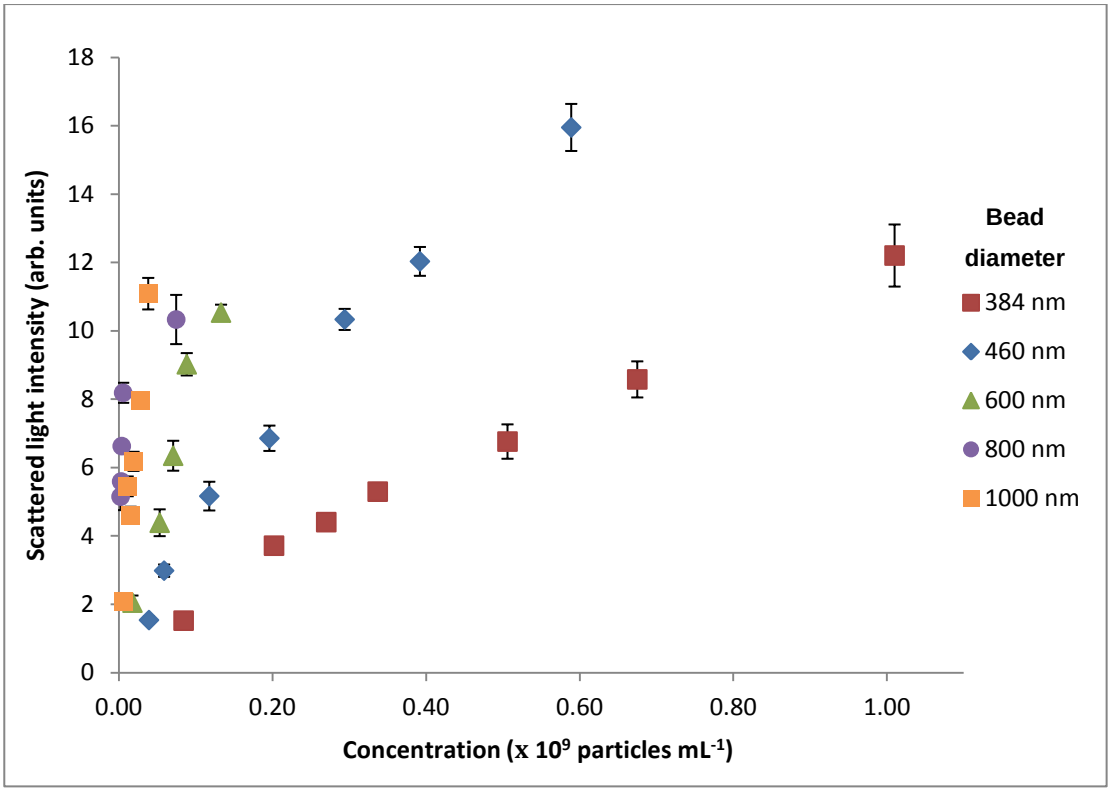


**Figure 3.24: Average scattered light intensity (average taken across positions 2-11 on chip) of different diameter latex beads as a function of concentration. The error bars show the standard deviation (n=3).**

### 3.4.3.4 The effect of supersaturation on ketoconazole precipitation

The precipitation was measured on-chip at pH 6.5 and 7.0 using various ketoconazole concentrations, which correspond to supersaturations of between 32 - 161, calculated using equation 3.5 (solubility values of 4.714 µg $mL^{-1}$ for pH 6.5 and 3.105 µg $mL^{-1}$ for pH 7.0 were used). Figures 3.25 and 3.26 show the precipitation curves obtained from low, intermediate and high supersaturations within the range investigated at pH 6.5 and pH 7.0. An increase in scattering intensity was observed as the supersaturation was increased. This was expected as supersaturation is the driving force for precipitation. The increase in scattering intensity is most likely due to a combination of increased drug precipitation and particle growth (figure 3.24). These results suggest that the on-chip light scattering detection method presented is sensitive to changes in supersaturation.

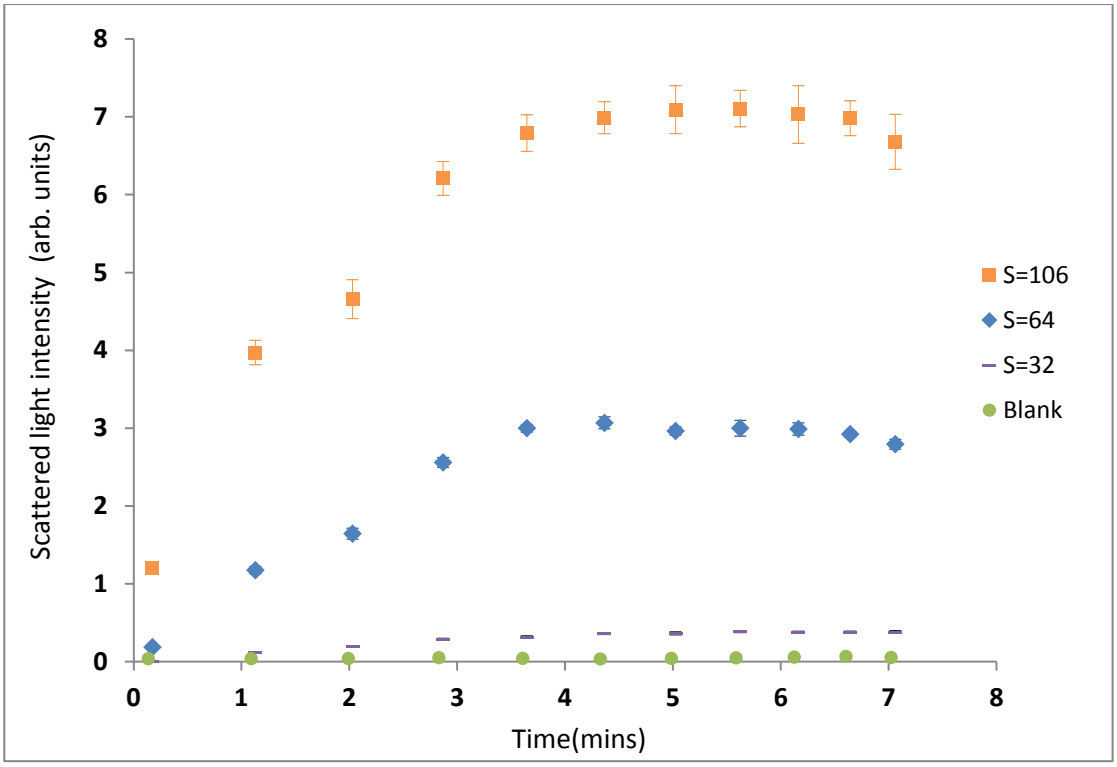


**Figure 3.25: Intensity of scattered light (arbitrary units) as a function of time obtained from droplets containing ketoconazole precipitate. Measurements were taken following a pH shift from pH 1.5 to pH 6.5 for different ketoconazole supersaturations (S). The blank droplets contain pH 6.5 buffer without ketoconazole. The error bars show the standard deviation (n=3).**

Figures 3.25 and 3.26 show the intensity of scattered light reaches a maximum after approximately five minutes on chip. This plateau in scattering intensity is most probably due to drug precipitating to the point where the solution is no longer supersaturated, i.e. all the supersaturated drug has precipitated. Another possible reason is that the ketoconazole precipitates are undergoing Oswald ripening resulting in the generation of fewer but larger particles at the expense of smaller nuclei, the greater scattering intensity of larger particles may be negated by the reduction in the number of precipitates within the droplet.

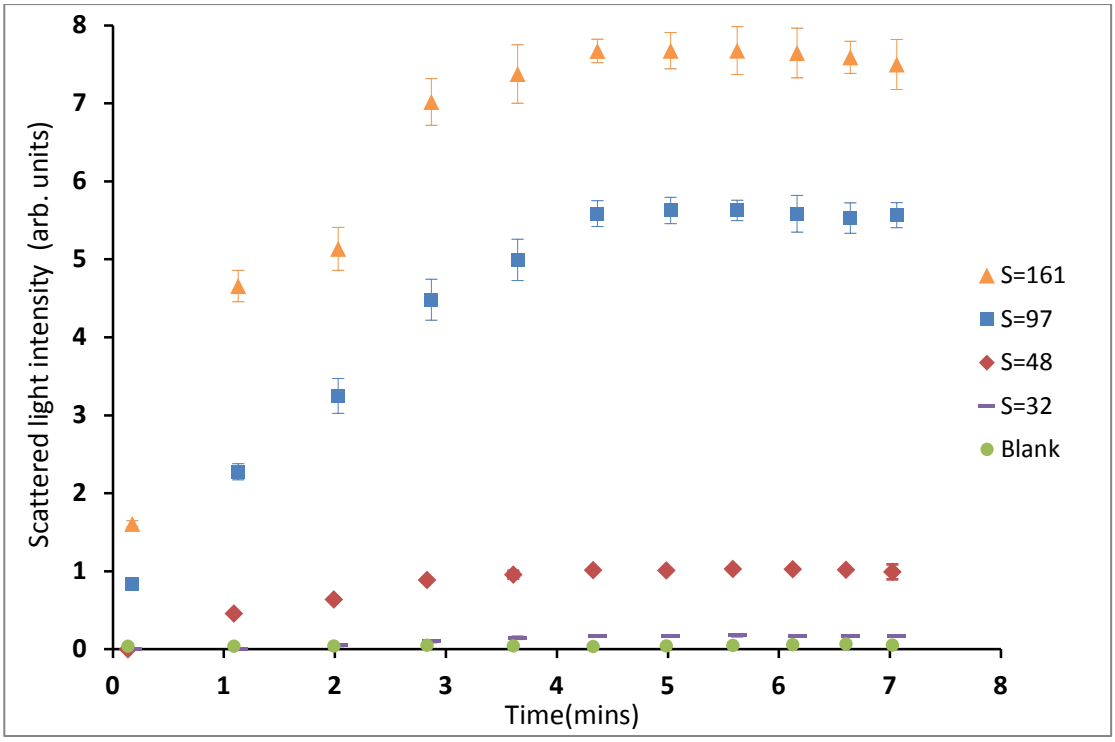


**Figure 3.26: Intensity of scattered light (arbitrary units) as a function of time obtained from droplets containing ketoconazole precipitate. Measurements were taken following a pH shift from pH 1.5 to pH 7.0 for different ketoconazole supersaturations (S). The blank droplets contain pH 7.0 buffer without ketoconazole. The error bars show the standard deviation (n=3).**

The plateau in scattering intensity allows the extent of precipitation for each supersaturation to be determined. The term 'average maximum intensity' will be used hereafter and is defined as the average scattered light intensities obtained between five and seven minutes on chip. The average maximum intensity as a function of supersaturation is given in figure 3.27. The figure indicates the pH conditions under which the supersaturations were generated, i.e. upon a pH shift from pH 1.5 to either pH 6.5 or pH 7.0, to emphasise the good correlation observed between results obtained at different pH. The average maximum intensity increases linearly with supersaturation up to a supersaturation of 110, suggesting that all the drug in the supersaturated state has precipitated. These results suggest that the average maximum intensity determined using the current microfluidic system can be used to study drug precipitation. At higher supersaturations the average maximum intensity deviates from linearity, indicating limitations of the device at high supersaturation. The corresponding supersaturations of the minimum intraluminal concentrations estimated previously (section 3.4.3.2) are well within the linear range of detection. The maximum intraluminal concentration estimated for pH 6.5 aqueous buffer corresponds to a supersaturation of 170, which is greater than the linear range, however the maximum intraluminal concentrations are likely to be inflated as dilution in the lumen was not taken into account in their estimation. The supersaturation

limit of 110 is still well above the estimated maximum intraluminal concentration at FaSSIF which corresponds to a supersaturation of 67. As FaSSIF represents a more physiologically relevant matrix than pH 6.5 buffer, it is suggested that the present device is capable of determining the extent of precipitation for physiologically relevant supersaturations.

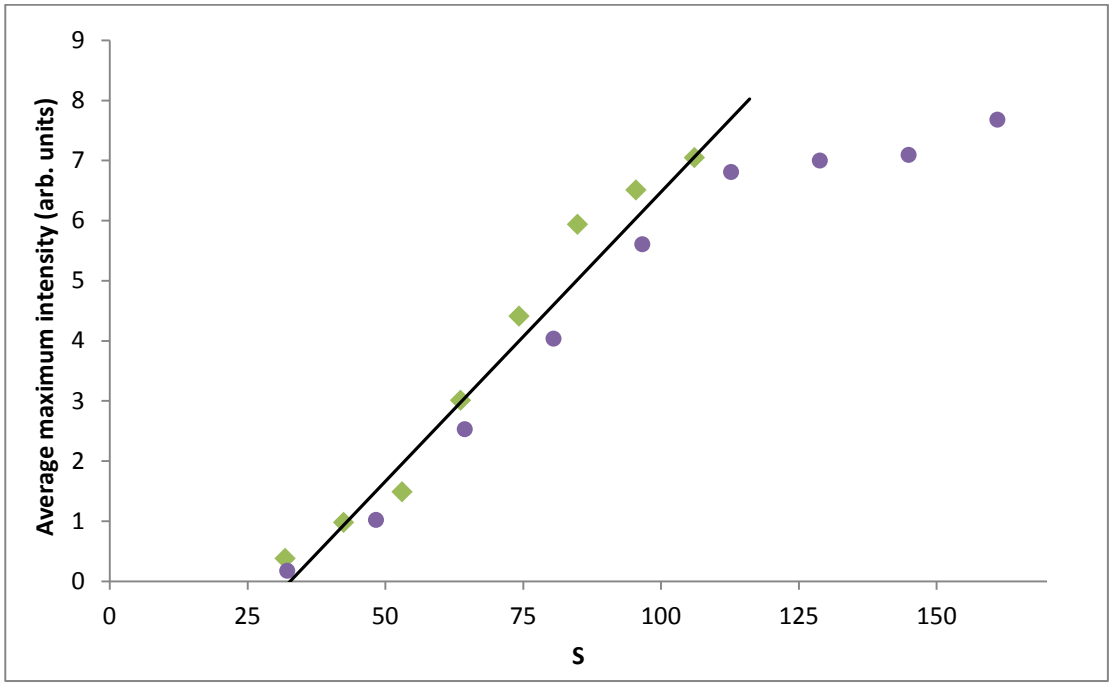


**Figure 3.27: The average maximum intensity (arbitrary units) as a function of supersaturation (S) taken at pH 6.5 (♦) and 7.0 (●). The line represents the linear regression line generated using data up to a supersaturation of 110 ($R^2$=0.96).**

### 3.4.3.5 Dynamic light scattering (DLS) macroscale experiments to corroborate microscale results

The pH shift experiments were replicated on the macroscale employing dynamic light scattering as the detection technique. The effect of supersaturation on particle size was investigated for two supersaturations corresponding to a ketoconazole concentration of 150 µg $mL^{-1}$ at pH 6.5 (S=31.82) and pH 7.0 (S=48.31). The results from these experiments are shown in figure 3.28. Decreasing the supersaturation of the ketoconazole solution resulted in a decrease in the average effective diameter of the precipitated particles. It is interesting that particle growth rates were found to be slower at lower supersaturation, resulting in the reduced particle diameters. Figure 3.28 shows that there was little change in particle diameter after approximately 14 minutes, which is consistent with the results obtained in the pH shift experiments, where the scattering intensity stopped increasing after five minutes on chip.

The diameters of ketoconazole observed in the dynamic light scattering experiments are between 200 – 1000 nm (see figure 3.28). The dimensions of the precipitates suggest that Mie scattering is occurring, as they correspond to size parameter ($x$) values of between 1.32 – 6.58 (calculated using equation 3.12 and 3.13, using a refractive index of 1.33 for the media[126]). As the relative refractive index of the system is 1.23 (calculated using equation 3.11 and refractive index values of 1.642[135] and 1.33[126] for ketoconazole and water respectively), it conforms to the requirement of Rayleigh light scattering that the refractive index of the particle must be close to 1. Therefore, Rayleigh scattering may be observed at the initial stages of ketoconazole precipitation when the diameters of the precipitates are less than 75 nm (where x < 0.5). A difference in scattering intensity may be observed upon switching from the Rayleigh scattering regime to the Mie scattering regime, however as the detector is placed at a approximately 45° scattering angle, the difference is not expected to be very pronounced (see figure 3.8 and 3.9 for the light scattering profiles due to Rayleigh scattering and Mie scattering respectively).

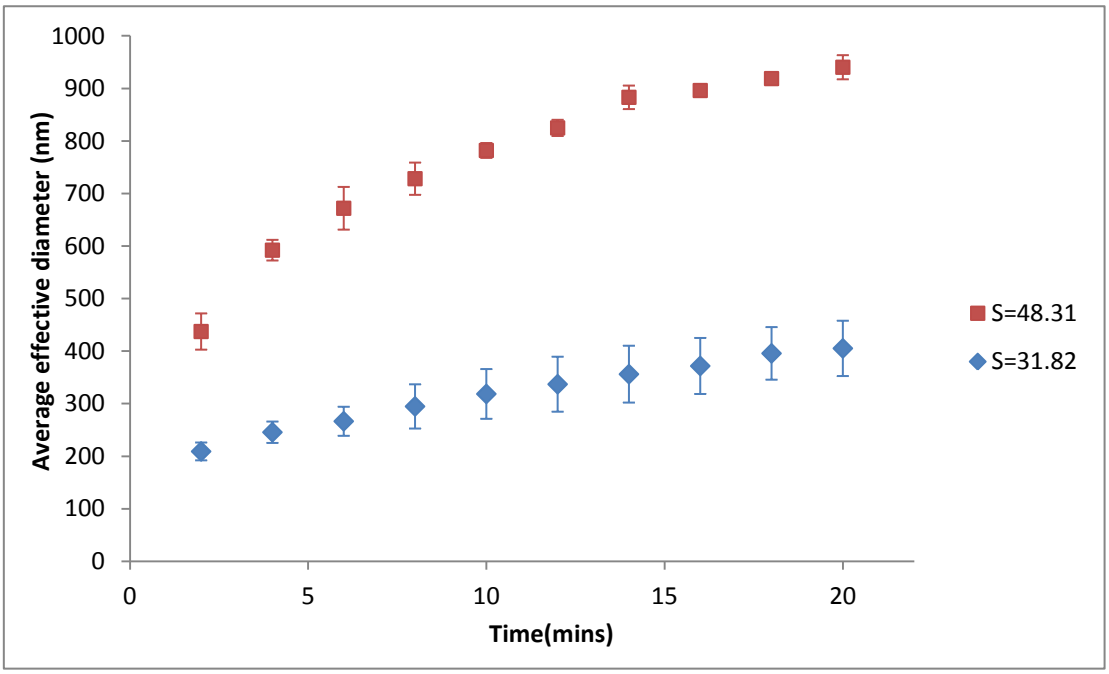


**Figure 3.28: DLS measurements to illustrate the effect of different supersaturations of ketoconazole solution on the effective diameter of ketoconazole precipitates over a twenty minute period. Measurements were taken for two ketoconazole supersaturations (S=31.82 and S=48.31) using a BI-9000 instrument (Brookhaven instruments) operating in dynamic light scattering mode, with a detector slit width of 200 nm, a detection angle of 90º, and a wavelength of 514 nm. The error bars show the standard deviation (n=3).**

Linear plots of the cubed effective diameter as a function of time of different supersaturations (figure 3.29) indicate Ostwald ripening of the particles. Ostwald ripening, discussed in section 3.2.4.4.2, it is thought to be a result of the solid phase in the system

achieving a minimum total surface energy and considered to be an important process, especially in solutions in which the primary precipitates are smaller than 1 µm in diameter, which is the case in the DLS experiments. These results may not directly relate to the droplet experiments as the number of ketoconazole molecules present in the droplet will be much less than the number of ketoconazole molecules in the vials used in the DLS measurements. Ostwald ripening in the droplet may explain the slight decrease observed in scattered intensity by the droplet at approximately seven minutes on chip. The scattered intensity may be decreasing as the number of ketoconazole precipitates is decreasing.

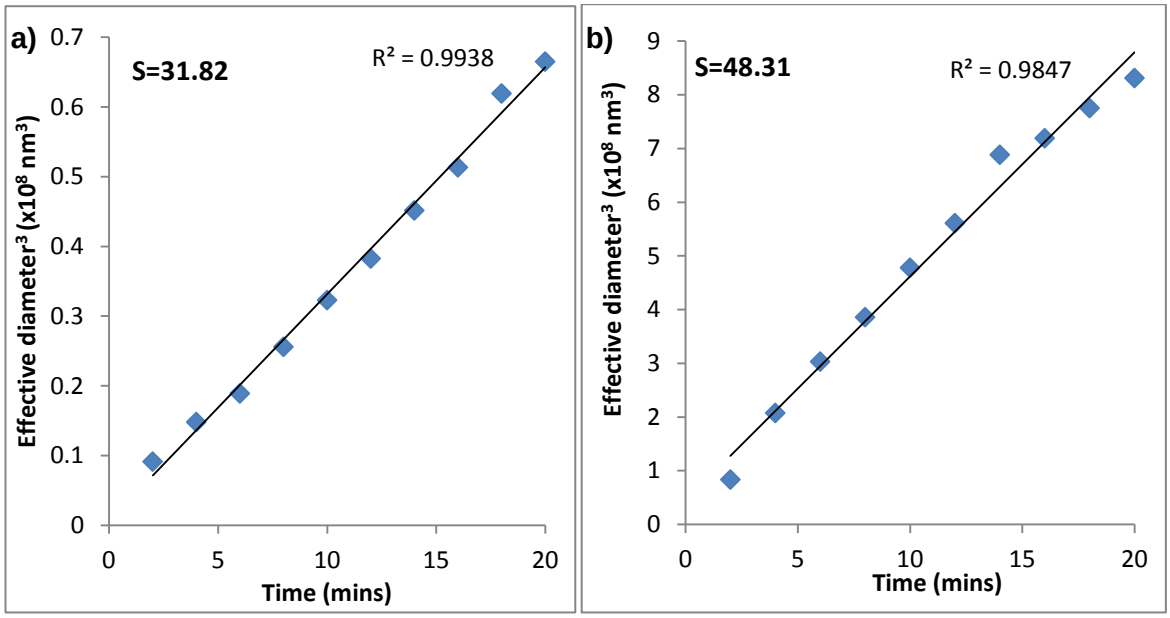


**Figure 3.29: The average effective diameter of ketoconazole precipitates measured by DLS cubed as a function of time to investigate Ostwald ripening of the particles. Measurements were taken at ketoconazole supersaturation of 31.82 (a) and 48.31 (b).**

### 3.4.3.6 Limitations of the microfluidic device and detection system

During the pH shift experiment certain limitations of the device and detection system were apparent. The inability to determine the average maximum intensity at high supersaturations has been described in section 3.4.3.4. Another limitation observed was the negative times determined for onset of precipitation. The onset time of precipitation can in theory be determined from the linear regression line generated for data at which precipitation is still occurring, i.e. before the scattering intensity begins to plateau. Figure 3.30 shows precipitation curves at three supersaturations: 48.31, 64.41 and 96.62. Linear regression lines have been generated for data obtained within the first three minutes on chip; the equations of these lines are also shown on the graph. The onset times of precipitation were determined from the linear regression lines i.e. time (x) when the

scattering intensity (y) is equal to zero. The onset time of precipitation at a supersaturation of 48.31 was + 8.78 seconds, however at higher supersaturations of 64.41 and 96.62 the onset of precipitation times were -8.85 and -29.3 seconds respectively. The negative onset time of precipitation suggests that there is precipitation present in the system before the time is started. As the time is started when the droplet begins to form, precipitation could be occurring before this time, i.e. in the T-junction. Although mixing in the T-junction may account for a negative onset time of precipitation, the magnitude of the negative onset time for a supersaturation of 96.62 suggests that there may be another factor, as the aqueous flows will not be in contact with each other for nearly 30 seconds while in the T-junction. It is possible that not enough data are collected at the initial stages of precipitation to accurately extrapolate the data.

As there is a complex relationship between the intensity of scattered light and the number and size of particles it is difficult to predict the response of the system. The above onset time determination was based on the assumption that there is a linear relationship between the intensity of scattered light and time until all the drug in the supersaturated state has precipitated, where the intensity plateaus. However, as the precipitation curves look almost logarithmic in nature, logarithmic regression lines were fitted to the data in figure 3.30 to determine whether the response of the system was in fact logarithmic. It is clear from figure 3.31 that although the logarithmic regression lines fit the data obtained at low supersaturation ($R^2$ = 0.9369), there is a lot of deviation of the data from the logarithmic regression line at higher supersaturations, which result in lower $R^2$ values for 64.41 and 96.62 (0.9142 and 0.9303 respectively), but what is more obvious, is the difference in shape of the data and the logarithmic regression line. Figures 3.30 and 3.31 suggest that the data obtained conforms more to the initial assumption of a linear dependence then a plateau once all the drug in the supersaturated state has precipitated, than a logarithmic dependence. Development of a more sophisticated detection system which includes multiple detectors at different light scattering angles would allow details on particle size to be obtained, providing a better understanding of the contribution to scattering intensity of different size particles.

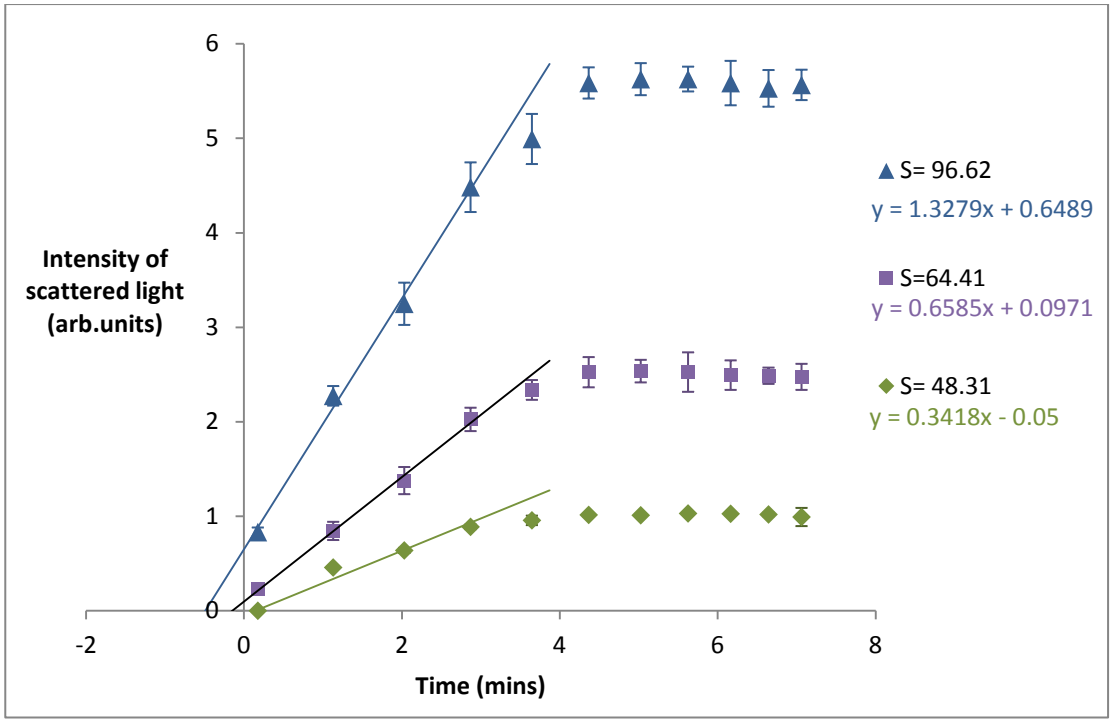


**Figure 3.30: Intensity of scattered light as a function of time, for supersaturations of 48.31, 64.41 and 96.62 to emphasize the negative onset time of precipitation issues present in the system. Linear regression lines ($R^2$ = 0.960, 0.997 and 0.996 for S = 48.31, 64.41 and 96.62, respectively) were generated using data obtained in the first three minutes. The error bars show the standard deviation (n=3).**

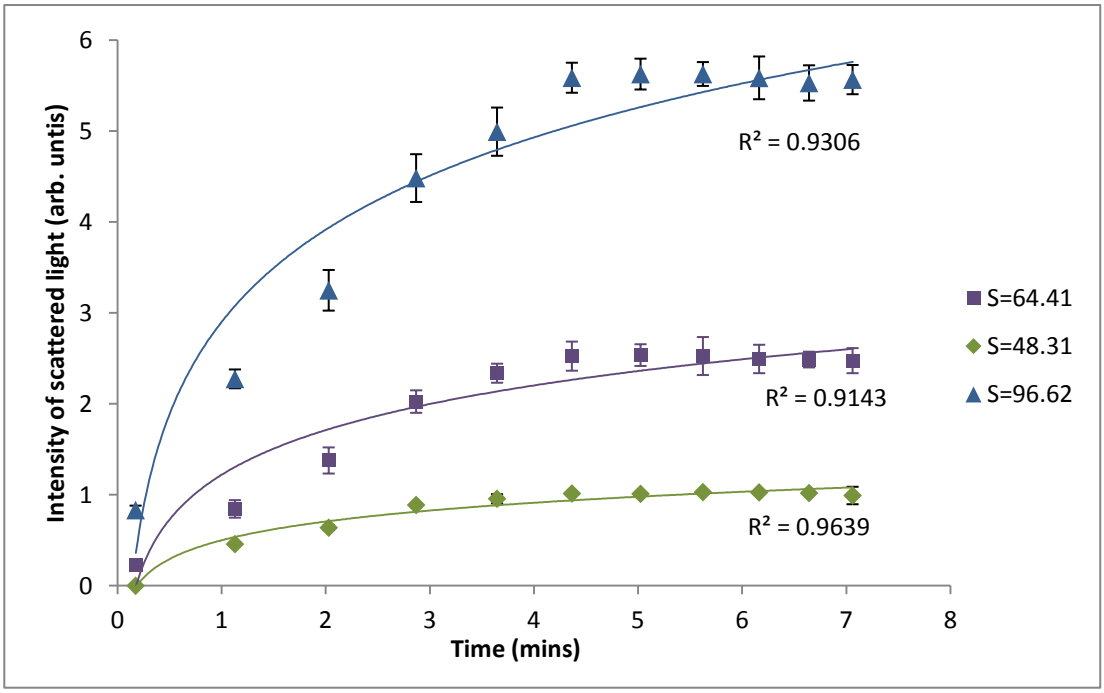


**Figure 3.31: Intensity of scattered light as a function of time, for supersaturations of 48.31, 64.41 and 96.62 to determine whether there is a logarithmic relationship between the intensity of scattered light and time. Logarithmic regression lines ($R^2$ = 0.963, 0.914 and 0.931 for S = 48.31, 64.41 and 96.62, respectively) were generated using data obtained in the first three minutes. The error bars show the standard deviation (n=3).**

The negative onset times of precipitation obtained from the pH-shift experiments were unexpected as on the dimensions of the chip the aqueous phase streams show laminar flow. Mixing between the two flows will be through diffusion, and given the short distance (1.52 mm) the two fluids are in contact before droplet generation, diffusive mixing is expected to be minimal. Dye experiments were carried out to confirm mixing in the T-junction. The presence of laminar flow in the T-junction was demonstrated by infusing a dye (amaranth) through one of the aqueous inlets while water is infused though the other. The images of this experiment are shown in figure 3.32. Laminar flow can be observed and there is no visible mixing in the T-junction.

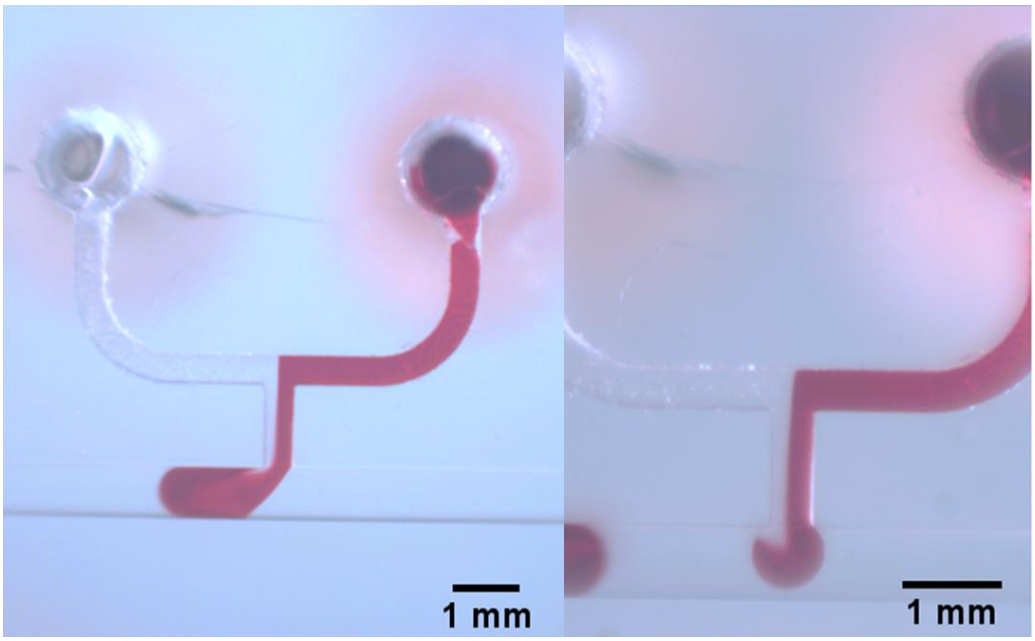


**Figure 3.32: Images of the T-junction taken for the water amaranth experiments to investigate mixing in the T-junction. Inlet 1 contained distilled water; inlet 2 contained an amaranth solution. Droplets were generated in perfluorodecalin using an aqueous flow rate of 10 µL $min^{-1}$ and an organic flow rate of 40 µL $min^{-1}$. Images were recorded using a camera (Lumenera LU125C) and ViMicro Cam software.**

As the pH shift experiment requires combining acidic and basic solutions, it is possible that acid-base reactions, which typically occur on a timescale of nanoseconds, might be responsible for mixing prior to droplet formation. An acid-base experiment was carried out to confirm this theory. Sodium hydroxide (0.04 M) and hydrochloric acid (0.01 M) were pumped onto the chip through the aqueous inlets. The solution of hydrochloric acid contained cresol red, which appears yellow/red under acidic conditions and purple under basic conditions, therefore any mixing in the T-junction should be discernible to the eye. A greater concentration of base was used so that mixing would result in a clear colour change, as cresol red undergoes a colour change from yellow to purple in the pH range

7.0 - 8.8. Figure 3.33 shows the images obtained during the acid-base experiments. There is a purple band visible between the acidic and basic solutions indicating that acid base mixing is occurring in the T-junction prior to droplet formation.

As the concentration of the solutions used for the pH shift experiments (0.1 M phosphoric acid, and 0.19 M sodium phosphate solution for pH 6.5 and 0.62 M sodium phosphate solution for pH 7.0) are greater than those used in this experiment the mixing in the pH shift experiment may be more pronounced.

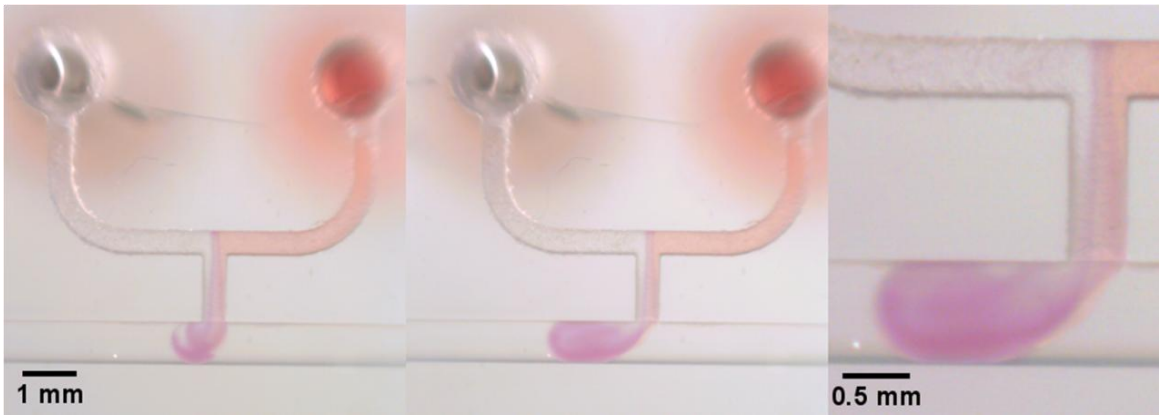


**Figure 3.33: Images taken to investigate acid-base mixing within the T-junction. Inlet 1 contained 0.04 M sodium hydroxide and inlet 2 contained 0.01 M hydrochloric acid and cresol red. Droplets were generated in perfluorodecalin using an aqueous flow rate of 10 µL $min^{-1}$ and an organic flow rate of 40 µL $min^{-1}$. Images were recorded using a camera (Lumenera LU125C) and ViMicro Cam software.**

## 3.5 Conclusions

The on-chip light scattering technique developed for this study was able to monitor drug precipitation upon a pH shift, simulating gastric emptying of the drug into the small intestine where precipitation is likely to occur. The spiral-based microfluidic design was shown to work well for real-time measurement of drug precipitation and allows supersaturation to be generated easily on-chip using the pH shift method, which is a more appropriate method of supersaturation generation than the use of temperature as reported in other microfluidic devices used to monitor precipitation as it mimics pH changes that the drug will encounter as it travels through the body.

The system responded well to changes in supersaturation, as the scattering intensity was found to have a linear correlation to supersaturation up to a supersaturation of 110. It was justified that the system could deal with physiologically relevant degrees of supersaturation, as the supersaturations calculated from the estimated minimum and

maximum intraluminal concentrations based on ketoconazole solubility in FaSSIF were well within the linear detection range of the system.

It is envisioned that the microfluidic device could be developed further, to not only monitor drug precipitation but also investigate conditions that could reduce or even prevent drug precipitation. Chapter four will discuss the role of precipitation inhibitors in drug formulations and the ability of the microfluidic device to evaluate the performance of precipitation inhibitors will be assessed. The limitations of the device with respect to the negative onset times of precipitation will be revisited in chapter five.

# Chapter 4: Microfluidics in drug formulation

## 4.1 Chapter overview

Chapter four concerns the use of microfluidics to evaluate the use of different additives which can affect the absorption of the drug *in vivo*. An overview of the drug formulation process will be given and the role of water soluble polymers as additives in drug formulations will be discussed. The microfluidic device presented in chapter three will be used to investigate two different water soluble polymers which are frequently used in drug formulation in the pharmaceutical industry. The effect of these polymers on ketoconazole precipitation will be determined and compared to results obtained from macroscale experiments and a similar study reported in the literature. A microfluidic device designed to increase the number of additives which can be examined in an experiment will be evaluated using different colour dyes and suggestions on how the design of the microfluidic device could be developed further will be discussed.

## 4.2 Introduction to drug formulation

When the lead compound reaches the formulation department, investigation into possible additives, or excipients, which improve drug dissolution, stability and absorption properties will be carried out. The drug can be formulated for topical, oral or parenteral administration. Due to the ease of administration and versatility of oral formulations, they are the most frequently used form of dosage. The oral dosage form can be designed to be easily administered, for example in the form of chewable tablets, lozenges or effervescent tablets. The drug delivery method of oral dosage forms can also be designed to elicit the optimum therapeutic response, for example allowing immediate release of the drug, controlled release over a period of time (extended release) and release of the drug as a result of *in vivo* conditions (delayed release) e.g. enteric coated tablets/capsules which are resistant to the acidic conditions of the stomach and will release the drug in the small intestine. This chapter will give an introduction into drug formulation and describe a drug-excipient screening method using the microfluidic system presented in chapter three.

### 4.2.1 Pharmaceutical excipients

Drug formulations typically contain excipients, which include diluents such as binders and compounds with good compaction properties to produce tablets with appropriate physical characteristics, e.g. hardness, as well as sweeteners to improve drug taste. Lubricants are typically added to solid dosage forms to reduce friction during tablet compression, and

colourants may also be added to improve the appearance of the drug. To improve drug dissolution, disintegrants which aid the breakdown of the tablet and wetting agents may be added. Excipients which are able to prevent precipitation *in vivo* may also be added to the formulation and will be discussed later. The excipients added must be inert, they should not have a detrimental effect on bioavailability, they should be compatible with the drug, and should conform to regulatory requirements.

### 4.2.2 Evaluation of formulations

*In vitro* dissolution studies will be conducted to investigate the effect of food and pH on drug dissolution and to determine the drug release mechanism of the formulation. *In vitro* studies will be followed by *in vivo* bioavailability studies to ensure the formulation has good dissolution and absorption properties; this will be done by monitoring drug plasma concentrations and the presence of drug and drug metabolites in the urine. Radioactive labelling can be used to image the formulation as it travels through the body, providing details on GI tract residence time, disintegration of solid formulations, and the relationship between the location of formulation and drug plasma concentration.

## 4.3 Formulation of poorly water soluble drugs

The absorption of poorly water soluble drugs is highly dependent on their formulation. The trend towards NCEs with low aqueous solubility and the challenging nature of their formulation has resulted in significant research being undertaken to alleviate the poor absorption properties associated with these compounds. Oral dosage formulations can be classified into three categories: crystalline solid formulations, amorphous solid formulations and lipid formulations. Crystalline solid formulations contain a stable form of the drug, which will remain stable upon dissolution in the lumen. Amorphous formulations contain the drug in a metastable state. Amorphous solids typically have faster dissolution rates than their crystalline counterparts. As a result, the use of amorphous solids can lead in improved drug absorption, however as the solid is in a metastable state, a supersaturated solution may be generated upon dissolution in the lumen, resulting in drug precipitation. Lipid based formulations are potentially metastable and often suffer from the same problems as amorphous solid formulations. If precipitation occurs soon after gastric emptying into the small intestine, drug absorption will be limited. Many amorphous solid and lipid formulations contain surfactants, cosolvents, and water soluble polymers. Surfactants and cosolvents can inhibit precipitation *in vivo* by solubilising the drug,

whereas water soluble polymers can inhibit nucleation and crystal growth through a number of mechanisms, which will be discussed later.

### 4.3.1 The 'spring and parachute' approach

The absorption of poorly water soluble drugs can be improved by achieving two things, (1) generation of a supersaturated state and (2) stabilisation of the supersaturated state for a long enough time for absorption to occur. This approach was referred to as a 'spring and parachute' by Guzmán *et al*. and is illustrated in figure 4.1.[136] The spring is the increase in aqueous drug concentration through the use of a higher energy drug form e.g. an amorphous solid. Profile two shows a dramatic increase in aqueous drug concentration of the spring form compared to that of the crystalline material; however, the aqueous drug concentration soon decreases to a similar concentration to that of the crystalline form. This is due to generation of a supersaturated solution and subsequent drug precipitation. Formulations can stabilise a supersaturation solution and inhibit precipitation, hence the parachute is provided by the precipitation inhibitors in the formulation (profile three). Precipitation inhibitors are typically water soluble polymers or cyclodextrins. These excipients can stabilise the supersaturated state in numerous ways. The mechanisms of supersaturation stabilisation are discussed in section 4.3.4.

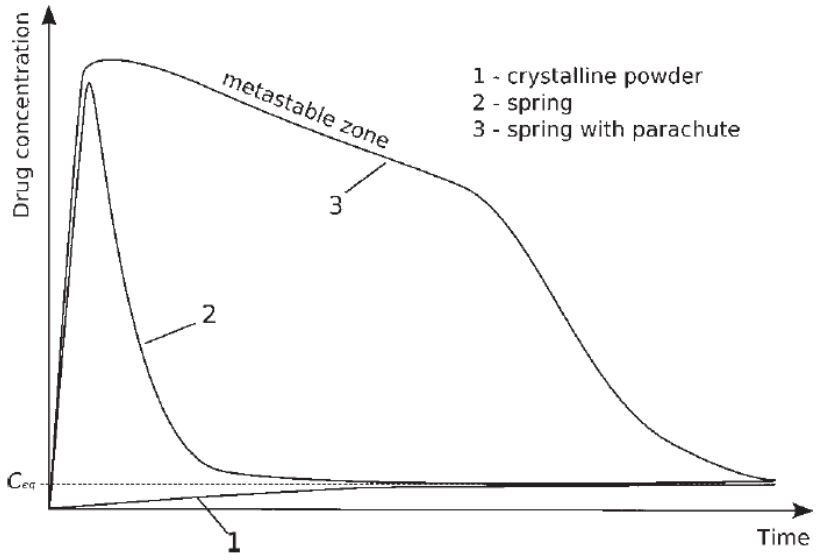


**Figure 4.1: Aqueous drug concentration as a function of time for three different drug forms to demonstrate the 'spring and parachute' approach. Profile one shows the dissolution of crystalline drug, profile two shows the dissolution of a high energy form of the drug, e.g. an amorphous drug, without any precipitation inhibitors present, and profile three shows the dissolution of a high energy form of the drug in the presence of a precipitation inhibitor. The 'spring', i.e. the increase in aqueous drug concentration, can be observed for the high energy forms of the drug (profiles two and three), while the 'parachute' is observed in the presence of a precipitation inhibitor (profile three). $C_{eq}$ is the equilibrium solubility of the drug.[137]**

### 4.3.2 Solid dispersion formulations

In the case of solid dispersion formulations, a supersaturated state is generated by administering the drug in a high energy or rapidly dissolving form i.e. an amorphous state or less stable polymorph. Solid dispersions typically contain a high energy form of the drug, a hydrophilic carrier, such as a water soluble polymer, and/or surfactant. The dissolution rate and apparent solubility of the drug can also be increased by decreasing the drug particle size. Reduced drug particle size can be achieved using milling techniques. It should be noted, however, that when using amorphous solids their unstable character can result in precipitation during storage.

### 4.3.3 Lipid based formulations

Lipid based formulations are an important type of solubilised formulation or self-emulsifying drug delivery system (SEDDS), they typically contain pure oils (glycerides) or a mixture of oils, cosolvents and/or surfactants. These formulations work by solubilising the drug *in vivo*, however, even if the solubilisation capacity is increased, bioavailability is not necessary improved. Absorption will only occur for free drug molecules not those solubilised within micelles and emulsified oil. SEDDS which are also capable of generating a supersaturated state are referred to as supersaturable SEDDS (S-SEDDS). These formulations use a smaller quantity of surfactant and a precipitation inhibitor, so that instead of solubilising the drug, a supersaturated solution is generated, creating a high aqueous free drug concentration for absorption. For further information, a review on the use of S-SEEDS for the formulation of poorly water soluble drugs has been published by Gao and Morozowich.[138]

### 4.3.4 Mechanism of supersaturation stabilisation

After dispersion of the formulation, polymeric excipients can stabilise the metastable supersaturated state, inhibit precipitation and improve drug absorption. Stabilisation of the supersaturated state is thought to occur through hydrophobic interactions and hydrogen bonding between the drug and excipient.[139] Steric hindrance of nucleation and crystal growth processes by the polymer is also believed to play an important role.[139] Although the mechanism of precipitation inhibition by polymers is complex and not fully understood, it is thought to occur through a number of mechanisms such as:[140]

- Changing the bulk properties of the system, for example increasing solubility which reduces the degree of saturation and likelihood of precipitation, and increasing viscosity which will hinder diffusion of the drug molecules.
- Altering the adsorption layer at the crystal-solution interface, hence impairing diffusion of drug molecules to the crystal.
- Adsorption onto the crystal growth sites and surface imperfections, disrupting growth across the crystal surface and causing rough surfaces to become smooth and therefore ill-disposed for crystal growth.

#### 4.3.4.1 Factors which affect drug-polymer interactions

As the mechanism of precipitation inhibition may rely on drug-polymer interactions, it is important to consider factors which influence these interactions, factors such as:

*Temperature*

As the temperature is increased the interactions between the polymer and the drug will be weakened. Higher temperatures will also increase the solubility of the drug, reducing the extent of supersaturation.

*Molecular weight*

Higher molecular weight polymers tend to exhibit greater interaction with the drug. This is possibly due to the increase in the number of functional groups on the polymer chains that are available for interaction with the drug.

*Viscosity*

Higher molecular weight polymers will also result in an increase in viscosity of the aqueous media. Precipitation may be inhibited by increases in viscosity, as transport of the drug molecules to the crystal surface will be impaired.

*Function groups on the polymer and drug*

The type of functional groups on the polymer chain and on the drug will have a significant impact on how the polymer and the drug interact. The presence of functional groups which are able to bond with the functional groups on the drug could result in bonding between the polymer and the drug. It should be noted, however, that the effect a polymer will have on a drug can not be predicted from its structure; a trial-and-error approach is typically required to evaluate potential precipitation inhibitors.

### 4.3.5 Water soluble polymers as precipitation inhibitors

Polymers that have been studied as precipitation inhibitors include vinyl polymers, cellulose based polymers and ethylene polymers[141]. However, the main focus has been on polyvinylpyrrolidone (PVP),[141-143] hydroxypropyl methylcellulose (HPMC)[141-144] and, more recently, hydroxypropyl methylcellulose acetate succinate (HPMCAS).[142, 143] A more extensive list of different polymers studied is available in a review on the use of polymeric precipitation inhibitors published by Warren *et al*.[145]

Yamashita *et al*. investigated the use of polymeric excipients to aid drug absorption, when they evaluated solid dispersion formulations containing PEG, PVP and HPMC on the sparsely water soluble immunosuppressant tacrolimus (figure 4.2a). PVP was found to out perform PEG 6000, while HPMC was by far the best inhibitor; HPMC was able to maintain the supersaturated concentration over a 24 hour period.[141] A study by Gao *et al*. compared SEDDS formulations of paclitaxel without and with HPMC present.[144] *In vitro* studies show that even after two hours paclitaxel concentration for the formulation containing 5% w/w HPMC was greater than the initial concentration observed for the HPMC free formulation. These results were echoed in *in vivo* experiments where a ten fold increase in bioavailability was observed for the formulation containing HPMC.

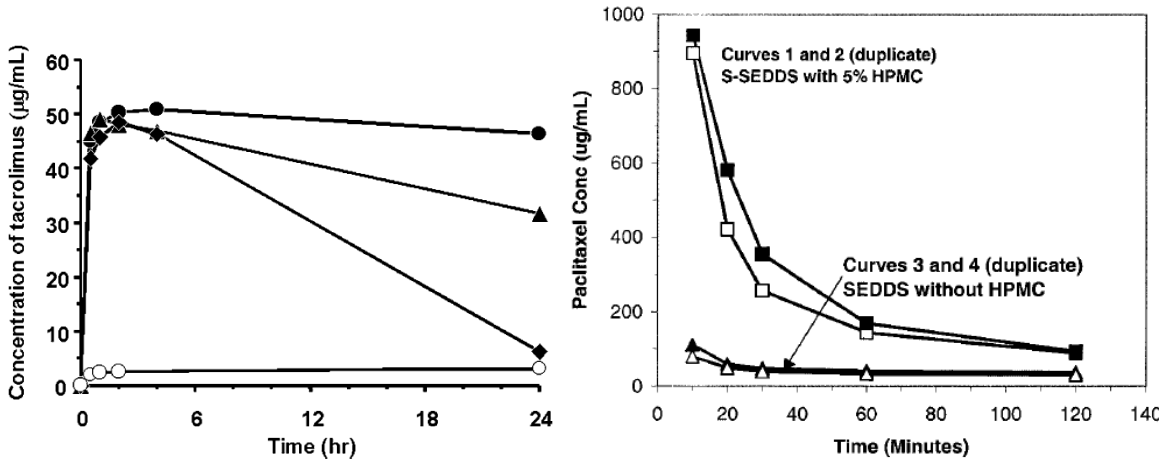


**Figure 4.2: a) Aqueous concentration of tacrolimus as a function of time for crystalline tacrolimus (○), and tacrolimus in solid dispersion formulations containing PEG 6000 (♦), PVP (▲) and HPMC (●).[141] b) Aqueous paclitaxel concentration as a function of time for SEDDS formulation without HPMC (▲,△) and a S-SEDDS formulation with HPMC (■,□).[144]**

#### 4.3.5.1 Current screening methods to evaluate precipitation inhibitors

Current *in vitro* methods to determine the effect of excipients typically involve monitoring drug concentration as a function of time during incubation with a possible precipitation

inhibitor. The concentration of the drug is determined at time intervals, which requires solution sampling, removal of solids by centrifugation or filtration and concentration determination using either HPLC or UV-Vis spectroscopy.[140, 146] However, centrifugation or filtration of the sample increases the time between sampling and detection, therefore the concentration determined may not be an accurate reflection of the *in situ* concentration at time of sampling.

## 4.4 Microfluidics devices developed for use in drug formulation

Development of microfluidic devices for use in drug formulation has been limited; so far the focus of these devices has been on reducing the particle size of the drug. For example, Panagiotou *et al*. produced 170 - 350 nm diameter drug particles using solvent-anitsolvent crystallisation in microfluidic channels,[147] and Thiele *et al*. synthesized nanosized (20 - 60 nm diameter) particles using a microfluidic spray dryer.[148] Commercial devices marketed as microfluidizer processors are available from Microfluidics Corporation.[149] Microfluidic devices which screen drug-excipient combinations have yet to be reported.

## 4.5 Evaluation of water soluble polymers as precipitation inhibitors using microfluidic technology

### 4.5.1 Overview

The effect of two water soluble polymers, HPMC and PVP, on ketoconazole precipitation was examined using the pH shift experiment presented in chapter three. The polymers were chosen due to their different hydrogen bonding properties. The carboxyl groups on the backbone of PVP make it a hydrogen bond acceptor, whereas the hydroxyl groups on HPMC make it a hydrogen bond donor (see figure 4.9 for polymer structures). It was anticipated that the interaction between each polymer and the drug would be very different.

## 4.5.2 Methods and materials

### 4.5.2.1 Materials

Ketoconazole was obtained from Fisher Scientific and trisodium phosphate from Acros Organics. Perfluorodecalin was obtained from Fluorochem. Hydroxypropyl methylcellulose ($\overline{M}_n$ ~ 10,000) and phosphoric acid were obtained from SigmaAldrich. Polyvinylpyrrolidone was obtained from BASF (Ludwigshafen, Germany) (Kollidon 30, $\overline{M}_n$ ~ 12,000). Amaranth, naphthol yellow, methylene blue, and brilliant green dyes were obtained from SigmaAldrich. All materials were used as received.

### 4.5.2.2 Microfabrication[4]

#### 4.5.2.2.1 Drug precipitation (DP) chip

The excipient experiments were carried out on the DP chip used in chapter three. Details of the fabrication of this chip are given in section 3.4.2.3.

#### 4.5.2.2.2 Multiple excipient (ME) chip

The ME chip design is shown in figure 4.3. A rectangular cross-section spiral channel 730 µm wide, 700 µm deep and 828.4 mm in length, including a T-junction containing five aqueous inlet channels, the configuration and dimensions of which are shown in figure 4.3b, was milled into a PMMA substrate using a CAT3D-M6 computer numerical control (CNC) milling machine (Datron Technologies Ltd.). Six inlet holes (one organic and five aqueous) and one outlet hole were drilled through the substrate, all holes drilled were 1.398 mm in diameter. The microfluidic device was sealed using a PCR seal (Corning Inc.) and a hydrophobic coating applied to the channels by infusing a surface modifying fluorinated polymer in a hydrofluoroether solvent (Certonal FC732, Acota Ltd.). The fluorinated polymer was left in the chip for an hour before being removed and the chip allowed to dry.

[4] Fabrication carried out by Dr Stephan Mohr (University of Manchester)

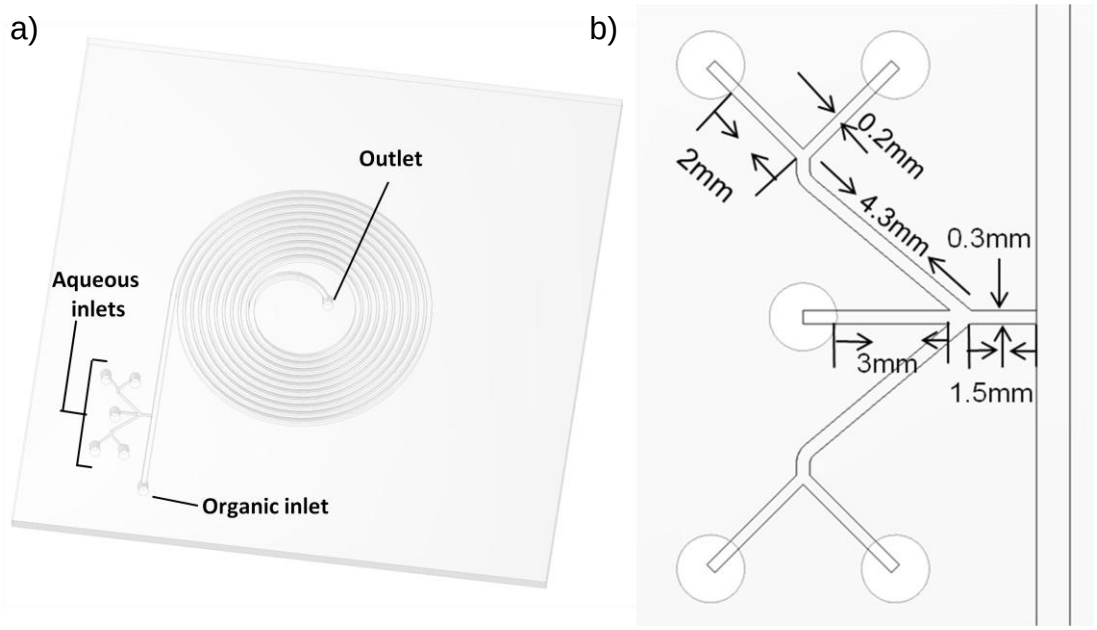


**Figure 4.3: a) A schematic of the multiple excipient (ME) chip. b) Dimensions of the aqueous inlet channels, the aqueous channels are square in cross-section.**

### 4.5.2.3 Experimental setup

The experimental setup used in the excipient experiments is identical to the setup used for the pH shift experiments (see section 3.4.2.4, figure 3.6), except videos were recorded using video capture software designed by Dr Bernard Treves Brown in LabVIEW.

### 4.5.2.4 Excipient effects on ketoconazole precipitation

The effect of two water soluble polymers, PVP and HPMC, on ketoconazole precipitation was evaluated. The polymers were dissolved in a sodium phosphate solution (0.62 M) in various concentrations (0.84, 1.68, 2.54, 3.40 mM of PVP, and 0.10, 0.20, 0.30 mM of HPMC). The droplet composition is illustrated in figure 4.4. The pH shift experiment (described in section 3.4.2.10) was repeated for each of the polymer concentrations using an initial ketoconazole concentration of 0.56 mM. Light scattering due to the presence of the polymer was investigated by infusing solutions of each polymer at concentrations greater that those used in the excipient experiments (5 mM PVP and 5 mM HPMC).

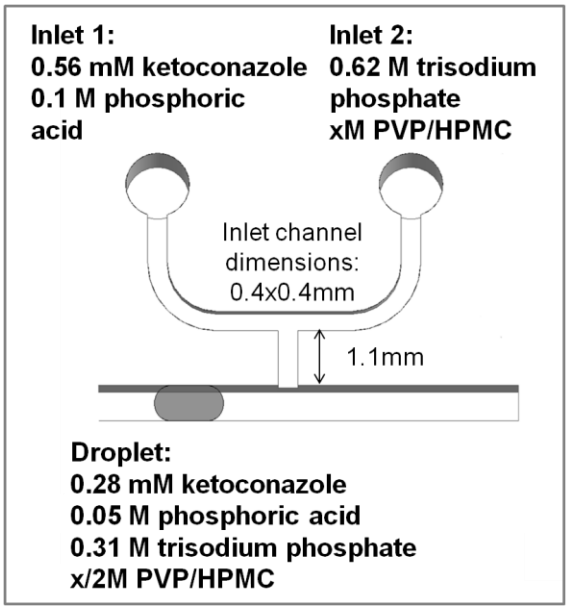


**Figure 4.4: Schematic of droplet composition for the excipient experiments. The droplet contained 50% of the solution from inlet one (0.56 mM ketoconazole in 0.1 M phosphoric acid) and 50% of the solution from inlet two (0.62 M trisodium phosphate containing xM PVP or HPMC).**

### 4.5.2.5 Macroscale dynamic light scattering experiments to corroborate results from microfluidic experiments

DLS studies of ketoconazole precipitates formed in the presence of PVP and HPMC were undertaken. DLS measurements were performed using a BI-9000 instrument (Brookhaven Instruments) operating in dynamic light scattering mode. Measurements were made at 25 ºC, using a detector slit width of 200 nm, a detection angle of 90°, and a wavelength of 514 nm. Equal quantities of the ketoconazole solution (0.56 mM) and the trisodium phosphate solution (0.62 M) containing the water soluble polymer were combined to generate a buffer solution with a ketoconazole concentration of 0.29 mM at pH 7.0, corresponding to supersaturation of 48.31 (calculated using equation 3.5). The trisodium phosphate solution contained different concentrations of PVP (1.6 mM and 4.2 mM) and HPMC (0.2 mM and 0.5 mM). The samples were briefly vortexed prior to DLS measurements, which were taken over a 20 minute period. Particle sizes were calculated assuming a refractive index of 1.590 for ketoconazole. DLS measurement of 'blank' solutions containing trisodium phosphate solution with 4.2 mM PVP and 0.5 mM HPMC were undertaken to ensure the effective diameters measured were for ketoconazole precipitates and not due to the presence of the polymers.

### 4.5.2.6 Evaluation of the ME chip – mixing experiments

Before excipients were introduced into the ME chip, mixing of the aqueous phases was evaluated using different colour dyes. Figure 4.5 shows which colour dyes were introduced into which inlets. It is envisioned that inlet three will contain the drug in phosphoric acid, while inlets one, two, four and five will each contain a different excipient dissolved in sodium phosphate solution. For this reason distilled water was infused into inlet three, while different colour dyes are infused into inlets one, two, four and five.

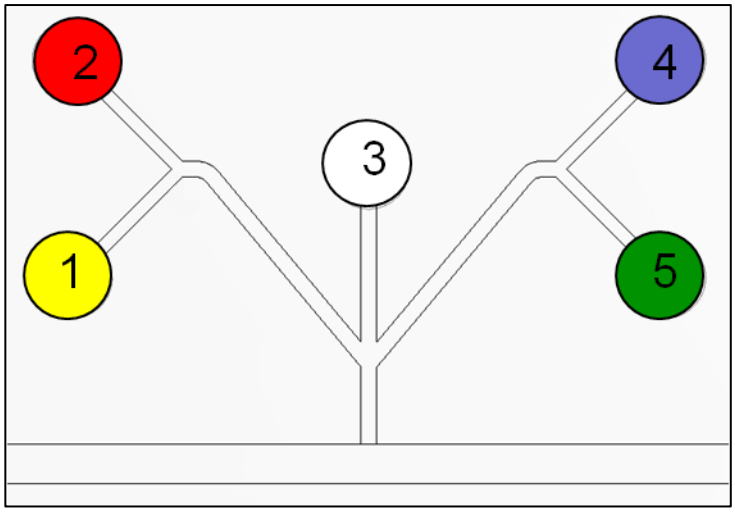


**Figure 4.5: Schematic illustrating the dyes used in the ME chip mixing experiments. Inlet one contains naphthol yellow, inlet two contains amaranth, inlet three contains distilled water, inlet four contains methylene blue and inlet five contains brilliant green dye.**

#### 4.5.2.6.1 Mixing different ratios of dyes

The mixing of different ratios of aqueous flows was investigated using naphthol yellow and amaranth dyes. The organic phase was infused at a flow rate of 48 µL $min^{-1}$, while the aqueous phases were infused at a total flow rate of was 12 µL $min^{-1}$; Distilled water was infused at a flow rate of 6 µL $min^{-1}$, while the dyes were infused at a total flow rate of 6 µL $min^{-1}$. The dye flow rates were varied so that the contribution of the dye to the droplet ranged from 100% naphthol yellow to 100% amaranth, with intermediate ratios of 1:2, 1:1 and 2:1 naphthol yellow to amaranth being used. Videos of the mixing in the aqueous channels and droplet generation were taken with a Lumenera camera (LG11059C) using video capture software designed by Dr Bernard Treves Brown in LabVIEW.

#### 4.5.2.6.2 Mixing of three dye streams

The mixing of three dye flows was investigated using distilled water, and naphthol yellow, amaranth, and methylene blue dyes. The organic phase was infused at a flow rate of 48 µL $min^{-1}$. Distilled water was infused at a flow rate of 6 µL $min^{-1}$, while naphthol yellow, amaranth and methylene blue were infused at flow rates of 2 µL $min^{-1}$. Videos of the mixing in the aqueous channels and droplet generation were taken with a Lumenera camera (LG11059C) using video capture software designed by Dr Bernard Treves Brown in LabVIEW.

#### 4.5.2.6.3 Number of droplets required for droplet composition stabilisation

A dye experiment was run to determine the number of droplets required for the droplet composition to change after different aqueous flows were introduced. It is important to know this before excipients are introduced, as droplets formed in the transition between different aqueous flows will need to be discounted as they may contain excipients from the previous experiment and give invalid results. The organic phase was infused onto the chip at a flow rate of 48 µL $min^{-1}$. Distilled water was infused at 6 µL $min^{-1}$ while the dyes were infused at a combined flow rate of 6 µL $min^{-1}$. Amaranth and naphthol yellow were infused onto the chip at 3 µL $min^{-1}$, followed by methylene blue and brilliant green at 3 µL $min^{-1}$. Videos were recorded of the switch between amaranth and naphthol yellow, and methylene blue and brilliant green dyes with a Lumenera camera (LG11059C) using video capture software designed by Dr Bernard Treves Brown in LabVIEW.

### 4.5.3 Results and Discussion

#### 4.5.3.1 Research aims

The objective of this research was to determine whether the microfluidic setup used in chapter three to study the precipitation of a poorly water soluble weakly basic drug could also be used to evaluate the effect of different excipients. A microfluidic setup which could be used to reliably and quickly evaluate different drug-excipient combinations would be invaluable to drug formulation as current methods to determine the effect an excipient will have on drug precipitation are time consuming and require large amounts of drug compared to microfluidic systems.

### 4.5.3.2 Effect of water soluble polymers on ketoconazole precipitation

The ability of two water soluble polymers, HPMC and PVP, to inhibit ketoconazole precipitation was evaluated using the pH shift experiment. Figures 4.6 and 4.7 show the scattering intensity as a function of time for ketoconazole precipitation in the presence of various concentrations of polymer. Measurements were taken at pH 7.0 using a ketoconazole supersaturation of 48. The figures show that both PVP and HPMC are capable of inhibiting ketoconazole precipitation, however, it is evident that the effect of HPMC is more pronounced than PVP. There is a gradual decrease in ketoconazole precipitation as the concentration of PVP is increased by increments of approximately 0.4 mM, whereas there is a significant decrease in intensity of light scattered after addition of just 0.05 mM of HPMC. When the concentration of HPMC was doubled and tripled to 0.1 and 0.15 mM, however, there was only a small decrease in the intensity of scattered light. The data obtained in the presence of 0.1 and 0.15 mM HPMC was almost indistinguishable from one another; a t-test performed on the data found that only data obtained after 5.5 mins on chip (last four data points on figure 4.7) were significantly different ($p<0.05$).

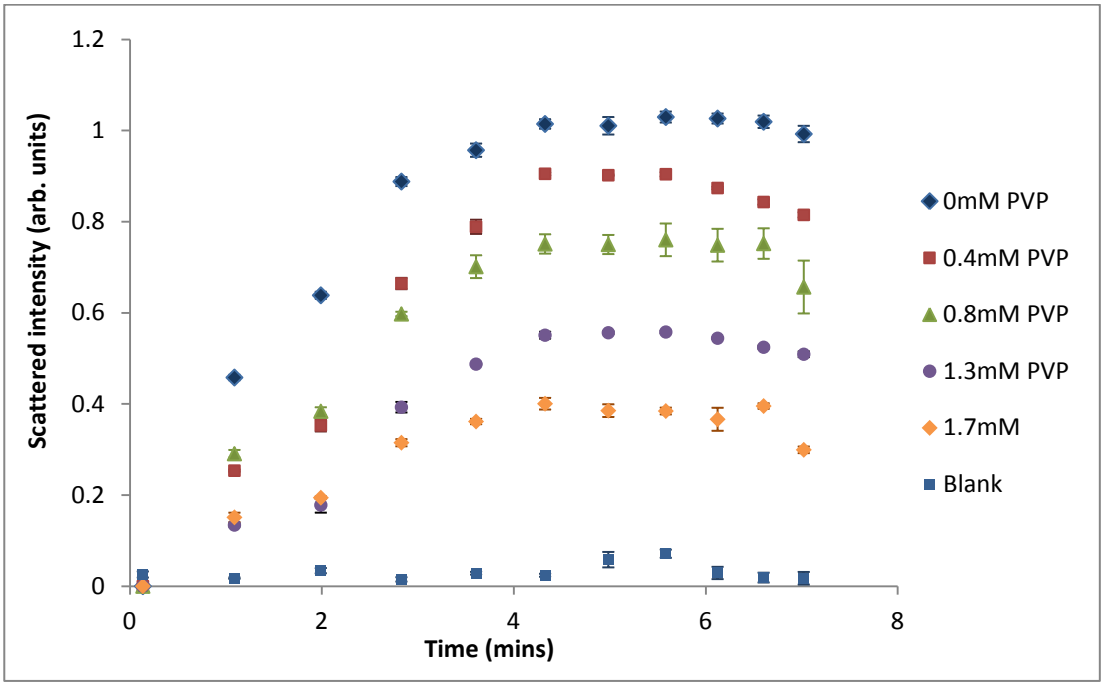


**Figure 4.6: Scattered intensity (arbitrary units) as a function of time for different concentrations of PVP taken at a ketoconazole supersaturation of 48. Blank droplets contained a concentrated solution of PVP (5 mM in distilled water). The error bars show the standard deviation (n=3).**

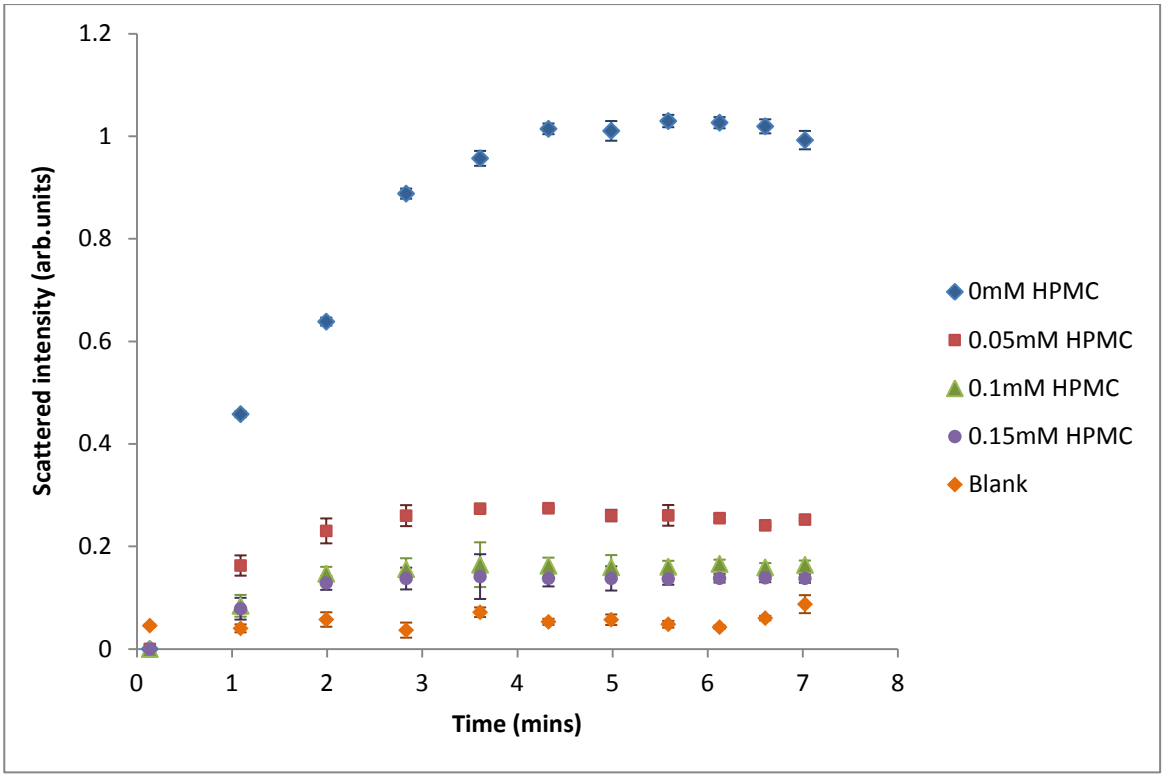


**Figure 4.7: Scattered intensity (arbitrary units) as a function of time for different concentrations of HPMC taken at a ketoconazole supersaturation of 48. Blank droplets contained a concentrated solution of HPMC (5 mM in distilled water). The error bars show the standard deviation (n=3).**

To rule out the possibility of light scattering due to the presence of the polymer, concentrated polymer solutions (5 mM PVP, 5 mM HPMC) were infused onto the chip. These concentrations are much greater than those used in the precipitation experiments. The light scattering profile of these solutions resembled that of the buffered solution used for device calibration (section 3.4.2.7) and a droplet which contains no detectible precipitates. The values obtained for the concentrated polymer solutions were less than 0.1 arbitrary units, much less than the intensities obtained for ketoconazole precipitation in the presence of PVP, but only slightly less than those obtained in the presence of HPMC. However, it should be noted that the shape of the scattering profiles for the concentrated polymers are indicative of background scattering from the solution and not from particles present, therefore it is assumed that the presence of the polymer does not contribute to the scattering intensities observed in figures 4.6 and 4.7.

Comparison of the polymers was achieved through averaging the maximum intensity values as done previously with the pH shift experiments (section 3.4.3.4). Figure 4.8 shows the average maximum intensities as a function of polymer concentration for PVP and HPMC.

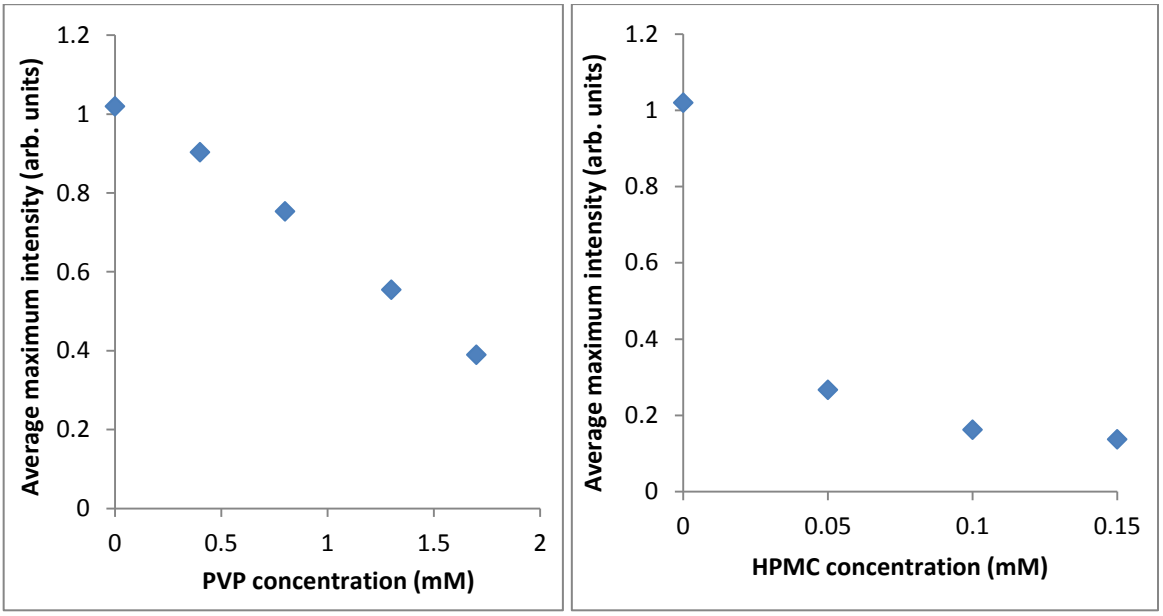


**Figure 4.8: a) Average maximum intensity of scattered light as a function of PVP concentration. b) Average maximum intensity of scattered light as a function of HPMC concentration. Measurements were taken at pH 7.0 using a ketoconazole supersaturation of 48.**

It is clear from figure 4.8 that HPMC is a more potent precipitation inhibitor than PVP. After addition of just 0.05 mM HPMC, the scattering intensity ,and hence extent of ketoconazole precipitation, decreased by nearly 75%, outperforming that of 1.7 mM PVP, which decreased the scattering intensity by approximately 60%. This was expected as ketoconazole has eight hydrogen bond acceptors and no hydrogen bond donors; therefore, it is expected to have greater interaction with polymers containing hydrogen bond donor sites than polymers containing hydrogen bond acceptor sites. HPMC contains 4 possible hydrogen bond donor sites whereas PVP has no hydrogen bond donors and is a hydrogen bond acceptor (figure 4.9).

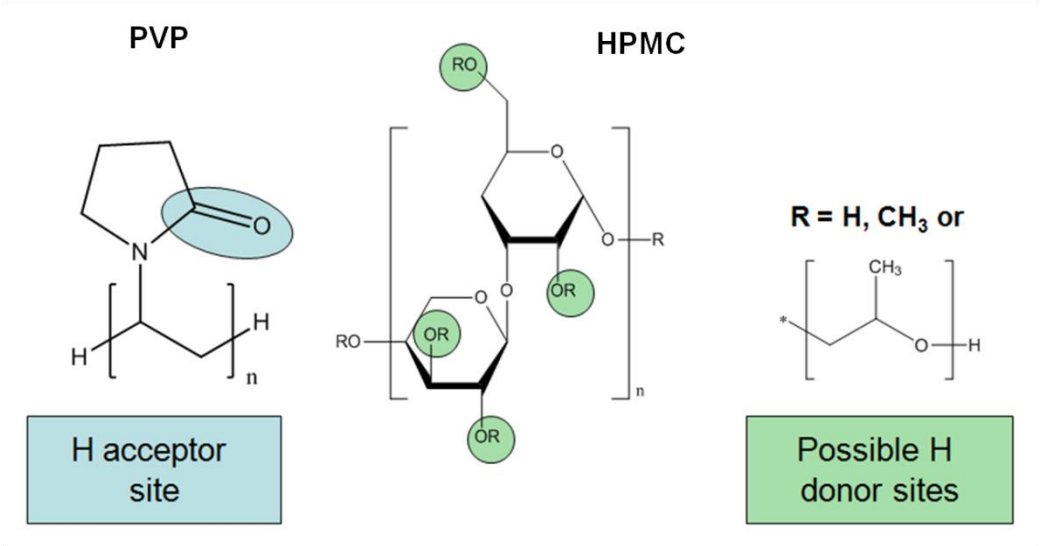


**Figure 4.9: Structure of PVP and HPMC to illustrate hydrogen bond donor (green) and hydrogen bond acceptor (blue) properties.**

Unfortunately no literature investigating the effect of PVP and HPMC on ketoconazole precipitation could be found. There are however, studies on the effect of these polymers on itraconazole, a chemical relative of ketoconazole. It is expected that the effect of the polymers should be similar for ketoconazole and itraconazole, as they are structurally alike (figure 4.10), although itraconazole is a larger molecule. Ketoconazole and itraconazole contain no hydrogen bond donors, and eight and twelve hydrogen bond acceptors respectively. Indeed, it is noteworthy that HPMC has been shown to be a effective precipitation inhibitor for ketoconazole in this study, and has also been used in the formulation of itraconazole, in the commercially marketed Sporanox.[150]

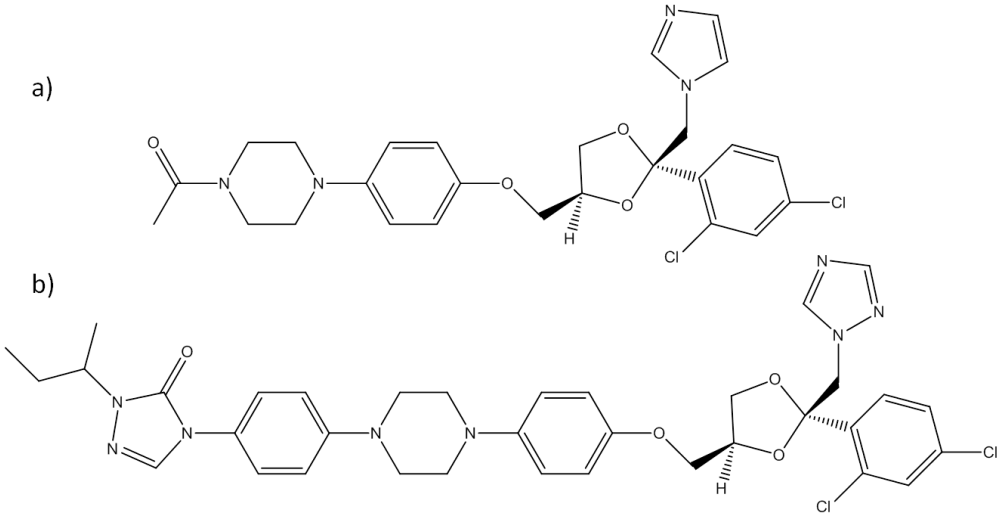


**Figure 4.10: Structures of ketoconazole (a) and itraconazole (b) for comparison.**

Miller *et al*. investigated the polymeric precipitation inhibitors Kollidon® 12PF and 90F, available from BASF, and Methocel™ E5 and E50, available from the Dow Chemical company (Midland, United States).[139] Kollidon® is the trade name of PVP and 12 and 90 represent number average molecular weights ($\overline{M}_n$) of 1,300 and 360,000 respectively.[151] Methocel™ is the trade name of HPMC and E5 and E50 represent $\overline{M}_n$ of 10,000 and 20,000 respectively.[152] Miller reported that the Methocel™ E50 formulation had the fastest dissolution rate, with approximately 68% itraconazole dissolved after thirty minutes in acidic media (0.1 M HCl), this was followed by Methocel™ E5, Kollidon® 90 and Kollidon® 12 formulations with 47%, 35% and 22% itraconazole in solution after the same time, respectively. After two hours in acidic media the Methocel™ formulations reached above 90% itraconazole in solution and the Kollidon® formulations approximately 57%. Following the pH shift to pH 6.8, Methocel™ E50 was found to be the most effective precipitation inhibitor with 62% itraconazole remaining in solution after ten minutes, whereas only 11% was left in solution for the E5 formulation. The Kollidon® formulations were not effective as precipitation inhibitors; only 0.17% of itraconazole remained in solution after ten minutes.

The results reported by Miller *et al*. are comparable with the results reported in this study concerning the precipitation of ketoconazole in the presence of HPMC and PVP. However, PVP appears to have a greater inhibitory effect in the microfluidic experiments when ketoconazole is used as the model drug. The results from the ketoconazole experiments and the results reported by miller *et al*. suggest that interactions between the drug and the water soluble polymer are playing a crucial role in precipitation inhibition. HPMC was significantly more effective as a precipitation inhibitor of ketoconazole and itraconazole than PVP, suggesting that the drug is interacting with the polymer and not just inhibiting nucleation and crystal growth through increasing the viscosity of the solution. The higher molecular weight polymer was shown to perform better in the study performed by Miller *et al*.; this may be due to an increase in functional groups available for bonding or an increase in viscosity or a combination of both. The polymers chosen for the ketoconazole experiments were of similar number average molecular weight (PVP, $\overline{M}_n$ ~12,000 and HPMC, $\overline{M}_n$ ~ 10,000). Different molecular weight polymers could be examined using the microfluidic setup up to a certain extent, however, if the polymer solutions were very viscous droplet generation could be affected.

### 4.5.3.3 Corroboration of results from microfluidic experiments using dynamic light scattering

The excipient experiments were replicated on the macroscale employing dynamic light scattering as the detection technique. Figures 4.11 and 4.12 show the effective diameter of ketoconazole precipitates in the presence of PVP and HPMC over a twenty minute period. It is clear that both PVP and HPMC inhibit particle growth. The presence of 0.8 mM and 2.1 mM PVP resulted in a decrease in particle diameter by approximately 225 nm and 350 nm respectively after twenty minutes, compared to ketoconazole particle diameters obtained where PVP was not present. The effect of HPMC is more pronounced, after twenty minutes the particle diameters decreased by approximately 430 nm and 540 nm for 0.1 mM and 0.25 mM HPMC respectively, compared to ketoconazole particle diameters obtained where HPMC was not present. Not only did HPMC result in reduced ketoconazole particle diameters, but the rate of particle growth was also diminished. Ketoconazole particles in the presence of 0.8 mM and 2.1 mM PVP increased by 387 nm and 268 nm over the twenty minute period, whereas in the presence of 0.1 mM and 0.25 mM HPMC the particles grew by only 150 nm and 111.7 nm respectively.

The presence 0.1 mM HPMC results in a large decrease (430 nm) in the average effective diameter, yet more than doubling the HPMC concentration to 0.25 mM (a concentration greater than those used in the microfluidic experiments) only decreased the effective diameter by approximately a further 100 nm. These macroscale experiments corroborate the results obtained using microfluidics where 0.05 mM HPMC resulted in a significant decrease in ketoconazole precipitation but doubling and tripling the concentration to 0.1 and 0.15 mM did not decrease ketoconazole precipitation by much more than 0.05 mM (figure 4.8b). No scattering signal was observed for the polymer solutions which did not contain ketoconazole suggesting the particle sizes obtained in the DLS measurements are due to ketoconazole precipitates.

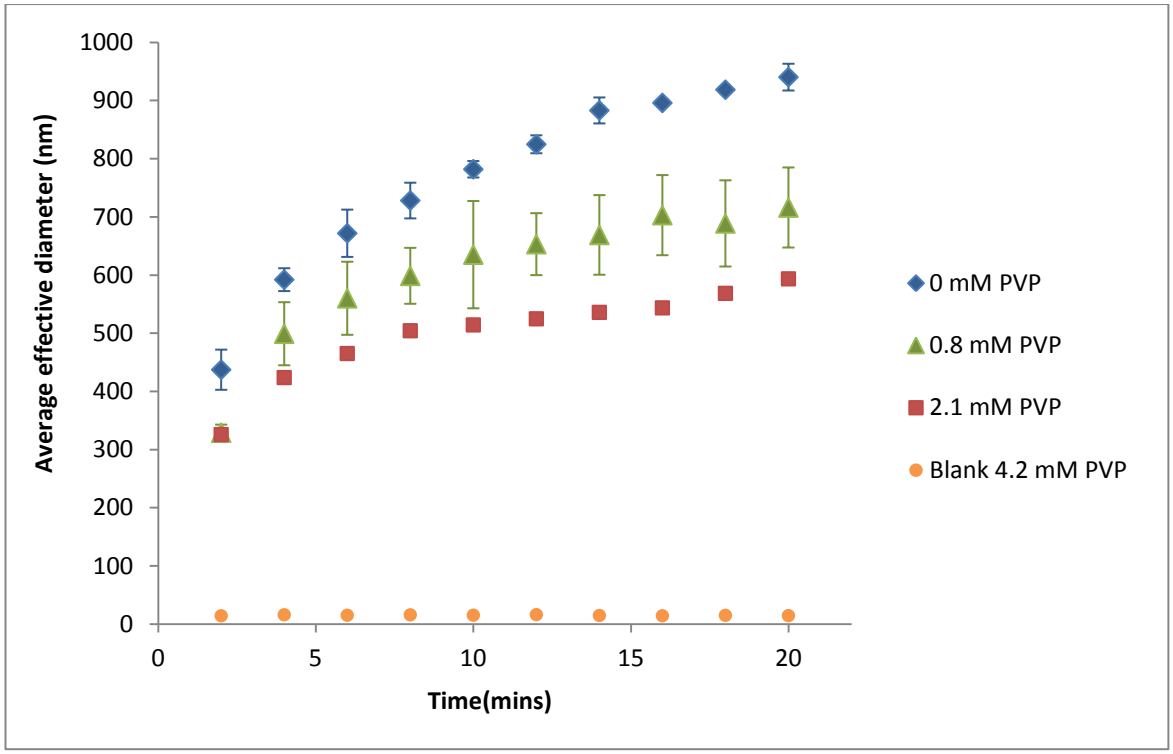


**Figure 4.11: DLS measurements to illustrate the effect of PVP on the effective diameter of ketoconazole precipitates over a twenty minute period. Measurements were taken at a ketoconazole supersaturation of 48. The blank solution contained 4.2 mM PVP in trisodium phosphate solution. The error bars show the standard deviation (n=3).**

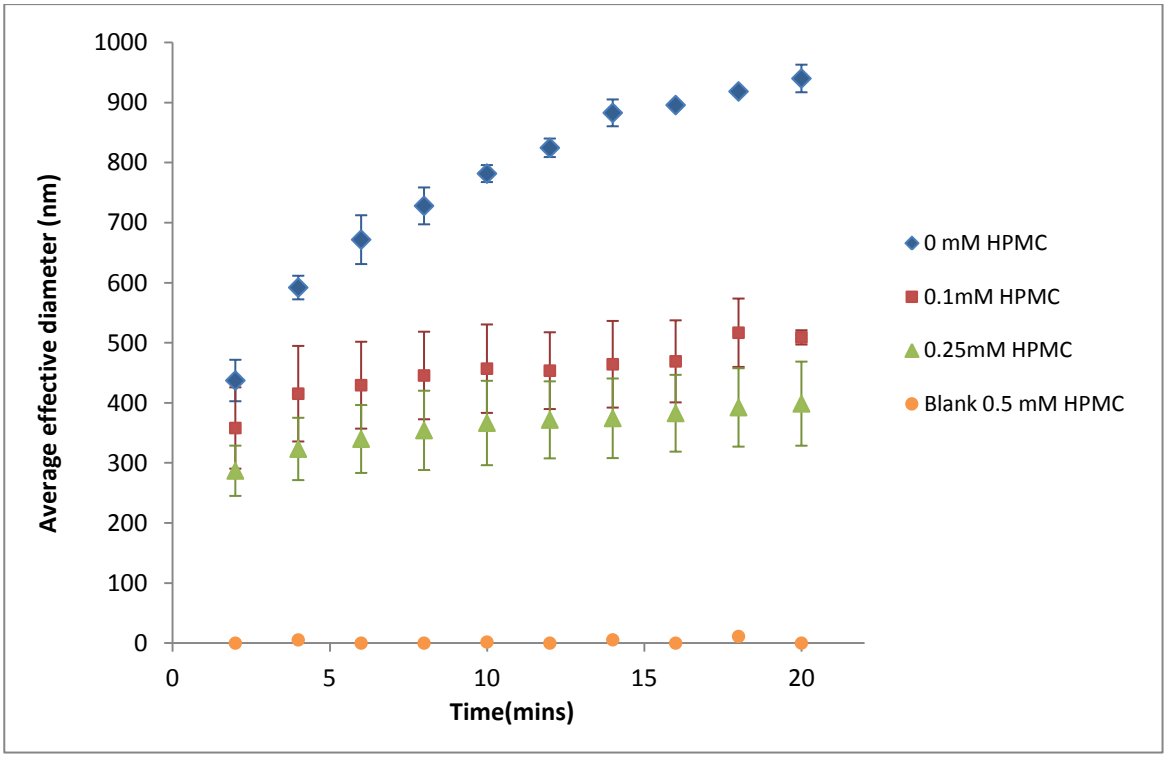


**Figure 4.12: DLS measurements to illustrate the effect of HPMC on the effective diameter of ketoconazole precipitates over a twenty minute period. Measurements were taken at a ketoconazole supersaturation of 48. The blank solution contained 0.5 mM HPMC in trisodium phosphate solution. The error bars show the standard deviation (n=3).**

Figure 4.13 shows the cubed effective diameters of ketoconazole in the presence of PVP and HPMC as a function of time. The linear response observed for the cubed effective diameter as a function of time for different supersaturations of ketoconazole (figure 3.29), was not observed for the DLS measurements in which water soluble polymers were present. This suggests that Oswald ripening of particles is not occurring when the water soluble polymers are present. This deviation from linearity is probably due to inhibition of crystal growth through interaction of the polymer with the crystal interface of the ketoconazole precipitates, and/or increase in viscosity slowing the diffusion of redissolved particles to the larger particles.

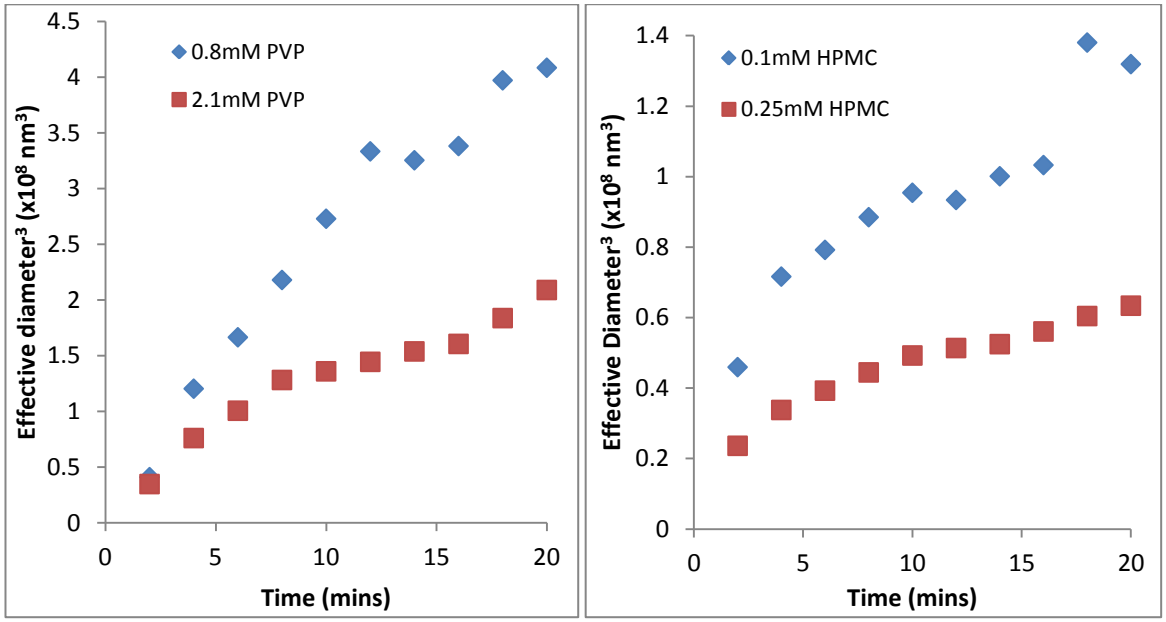


**Figure 4.13: The average effective diameter of ketoconazole precipitates measured by DLS cubed as a function of time to investigate Ostwald ripening of the particles. Measurements were taken at a ketoconazole supersaturation of 48 in the presence of a) 0.8 and 2.1 mM PVP, and b) 0.1 and 0.25 mM HPMC.**

### 4.5.3.4 Evaluation of the ME chip

The above results demonstrate that microfluidic technology can be used to screen precipitation inhibitors, however, as it is difficult to predict the effect an excipient will have on the drug, often multiple excipients and mixtures of different excipients must be screened. The DP chip allows only one drug excipient to be examined at a time as the chip has just two aqueous inlets; increasing the number of aqueous inlets will allow multiple excipients and excipient mixtures to be screened with the drug. A chip which contains five aqueous inlets was fabricated (chip design given in figure 4.3) to allow for screening of multiple excipients. Preliminary experiments were performed to investigate the mixing of the different aqueous flows, determine how long it takes the droplet

composition to stabilise after switching between excipient mixtures and generally flag up any problems before drugs and excipients are introduced into the chip. To do this, aqueous flows containing different colour dyes were infused into the chip. Naphthol yellow, amaranth, methylene blue and brilliant green dyes were infused into the inlets designed to contain excipient solutions (inlets one, two, four, and five, figure 4.5), while inlet three (designed to contain the drug solution) contained distilled water.

#### 4.5.3.4.1 Mixing aqueous flows in different ratios

Naphthol yellow and amaranth aqueous streams were mixed in different ratios using the method detailed in section 4.5.2.6.1. The distilled water was infused at a constant flow rate throughout the experiment, while the flow rates of naphthol yellow and amaranth were varied. Methylene blue and brilliant green dyes were not used in this experiment. Figure 4.14 shows the mixing of different ratios of naphthol yellow and amaranth. The first image shows droplet generation by infusing distilled water and naphthol yellow, it is obvious that the droplet contains no other dyes. In the second image the droplet should contain 50% distilled water and 50% 2:1 naphthol yellow to amaranth solution; however, amaranth has bled into the naphthol yellow stream making the two streams nearly indistinguishable from one another. In the third image the droplet should contain 50% distilled water and 50% 1:1 naphthol yellow to amaranth solution and the fourth image 50% distilled water and 50% 1:2 naphthol yellow to amaranth solution. It is difficult to make out the ratio of mixing in images two to four as the naphthol yellow appears red, however, there is a change in the colour of the droplets being generated in images two to four suggesting that the dye streams are mixing in different ratios. The final Image shows 1:1 mixing of the distilled water and amaranth streams.

Although these images are positive in that the composition of the droplet appears to be changing when the ratio of naphthol yellow to amaranth is altered, there appears to be some backflow occurring in image b which would explain the gradual reddening of the naphthol yellow stream. This backflow is probably due to back pressure in the channels at the flow rates used. The aqueous channels could be decreased in length to reduce this pressure.

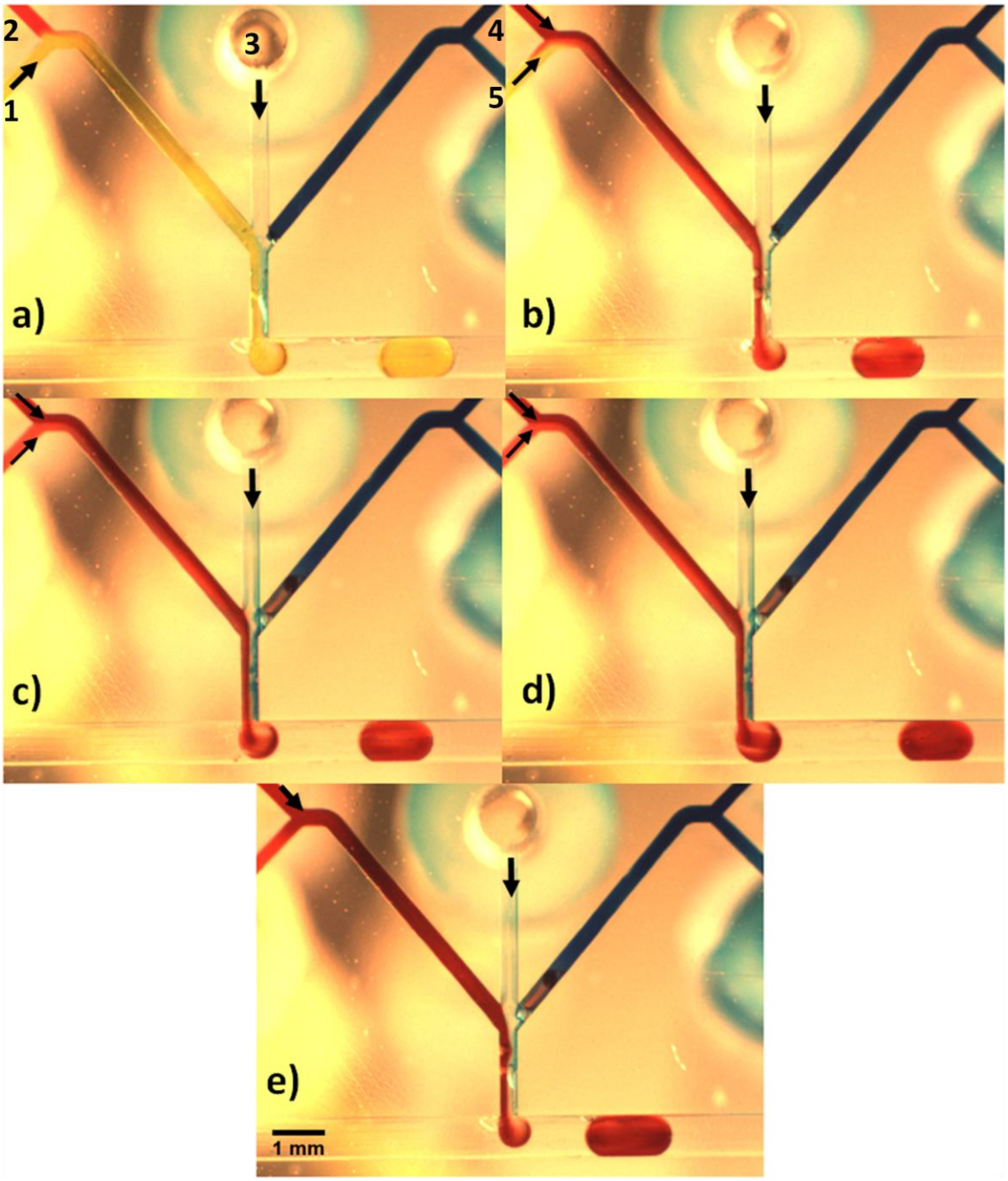


**Figure 4.14: Mixing aqueous flows in different ratios. The arrows indicate the aqueous flows used in the experiment. The organic phase (perfluorodecalin) was infused at a flow rate of 48 µL min$^{-1}$ and the total aqueous flow rate used was 12 µL min$^{-1}$. The aqueous flow rate from inlet three (distilled water) remained constant at 6 µL min$^{-1}$ throughout the experiment. a) shows naphthol yellow dye infused at 6 µL min$^{-1}$, b) shows naphthol yellow and amaranth infused at flow rates of 4 and 2 µL min$^{-1}$ respectively, c) shows naphthol yellow and amaranth infused at flow rates of 3 µL min$^{-1}$, d) shows naphthol yellow and amaranth infused at flow rates of 2 and 4 µL min$^{-1}$ respectively, and e) shows amaranth infused at a flow rate of 6 µL min$^{-1}$. Images were taken with a Lumenera camera (LG11059C) using video capture software design by Dr Bernard Treves Brown using LabVIEW.**

### 4.5.3.4.2 Mixing of three different dye streams

The mixing of three different dye streams with the distilled water stream was evaluated. Figure 4.15 shows an image of droplet generated when distilled water is infused from inlet three at a flow rate of 6 µL $min^{-1}$, and naphthol yellow, amaranth, and methylene blue were infused at a flow rates of 2 µL $min^{-1}$ from inlets one, two and four respectively; Inlet five was not used during this experiment. The distribution of dyes in the T-junction in figure 4.15, suggests that the methylene blue dye is infused at the same flow rate as the combined naphthol yellow and amaranth flow rates; however, all the flow rates are equal, hence the combined naphthol yellow and amaranth flow is twice that of methylene blue. This issue will need to be examined further, as it is crucial that the composition of the droplet reflects the relative flow rates of the aqueous phases. Another point of concern is the slow mixing of the dyes in the droplet after detachment, i.e. the droplet appears half blue and half red. As the intensity of scattered light is measured as a function of time, slow or incomplete mixing will lead to a delay in the system, as ketoconazole precipitation will be dependent on the mixing time of the droplet. This will not be a problem when determining the extent of ketoconazole precipitation, but will be an issue if the microfluidic device is used to investigate precipitation kinetics.

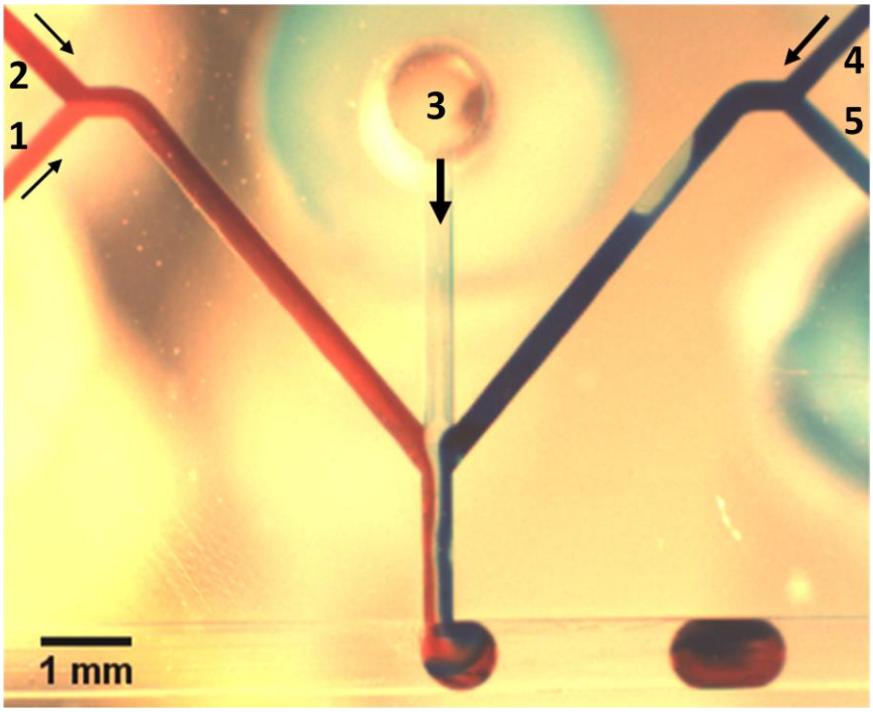


**Figure 4.15: Mixing of three different dye streams with the distilled water stream. The arrows indicate the aqueous flows used in the experiment. The organic phase was infused at a flow rate of 48 µL $min^{-1}$. Distilled water was infused at a flow rate of 6 µL $min^{-1}$ from inlet three. Naphthol yellow, amaranth, and methylene blue were infused at flow rates of 2 µL $min^{-1}$ from inlets one, two and four respectively. Images were taken with a Lumenera camera (LG11059C) using video capture software design by Dr Bernard Treves Brown using LabVIEW.**

#### 4.5.3.4.3 Number of droplets required for stabilisation of droplet composition

Switching between one aqueous feed and another will evidently involve a transition period where the droplet may contain a proportion of the previous aqueous feed. As a result, knowledge of how many droplets are required for the composition of the droplet to contain only the desired components is essential. Droplets formed in the transition period will need to be discounted as their contents will be unknown. Figure 4.16 shows the transition between infusing methylene blue and brilliant green dye from inlets four and five, to infusing naphthol yellow and amaranth dyes from inlets one and two. The first image shows formation of droplets which contain 50% distilled water, 25% methylene blue and 25% brilliant green dye. The brilliant green dye is difficult to see in these images as it is nearly indistinguishable from the methylene blue dye. The second image shows droplet generation when the pumps have stopped momentarily between pumping programs, this results in a larger droplet being produced which may be able to act as a marker during analysis, i.e. an indication of when the aqueous flows were changed. In image three, the pumps have started to infuse naphthol yellow and amaranth, the droplet generated is the same volume as droplet produced before the switch, but mostly contains residual methylene blue and brilliant green dye from the T-junction with only a small amount of red dye visible in the droplet. Image four shows the next droplet produced; no blue/green dye is visible within this droplet. These results suggest that upon switching from one branch of the aqueous inlet to another, the third droplet produced should contain the desired concentration. Further experiments will need to be undertaken to see if this number changes when mixing aqueous flows from different branches, i.e. naphthol yellow and methylene blue, followed by amaranth and brilliant green. First the different aqueous streams need to be more distinguishable from one another to be able determine droplet composition.

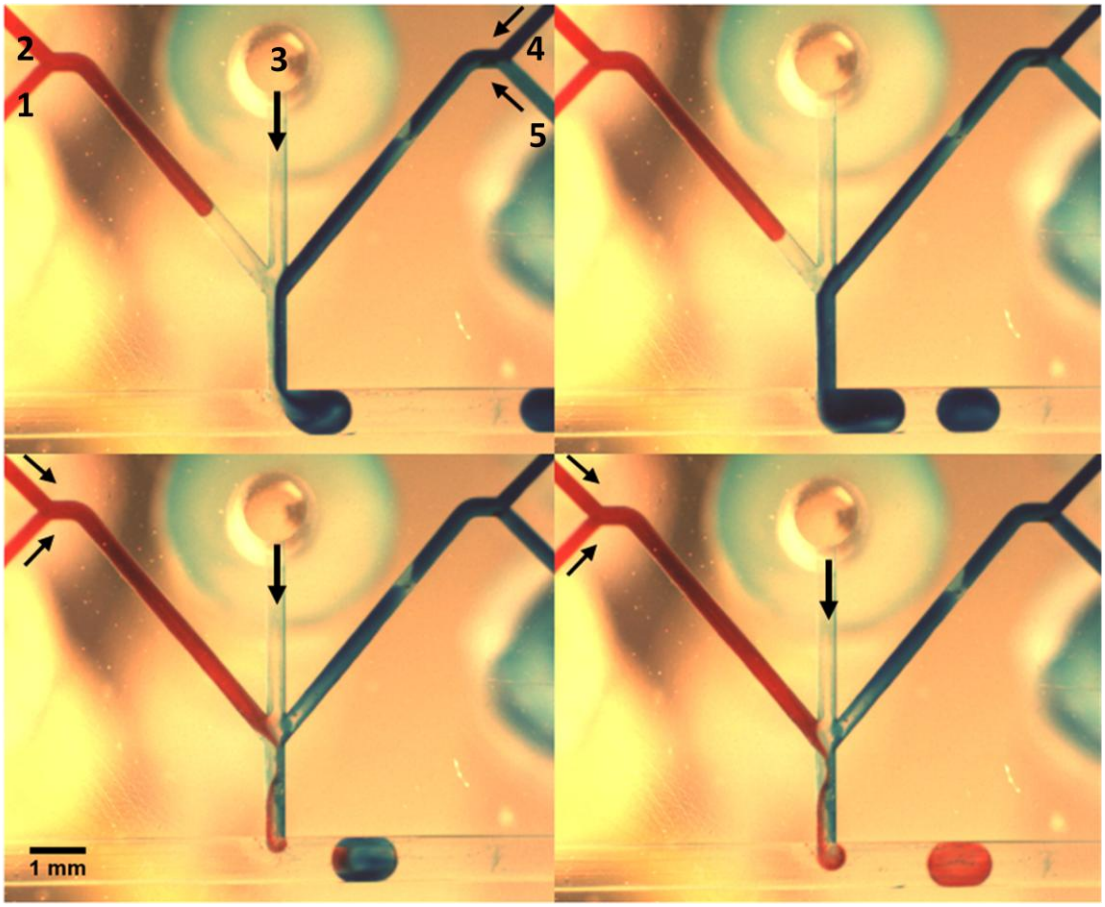


**Figure 4.16: Images to illustrate the number of droplets required for the droplet composition to stabilise after changing droplet composition. The arrows indicate the aqueous flows used in the experiment. The first image shows droplets containing 50% distilled water (inlet three), and 50% methylene blue (inlet four) and brilliant green dye (inlet five), with each contribute 25% of the total aqueous flow. The different dyes are difficult to distinguish in these images, as the brilliant green dye appears blue. Image two shows droplet formation when the flow is stopped, i.e. when the pumps have stopped momentarily between pumping steps, resulting in generation of a droplet of greater volume being produced. Image three shows the first droplet produced after the aqueous flow is switched from inlets three, four and five to inlets one, two and three. The droplet should contain 50% distilled water from inlet three and 50% amaranth and naphthol yellow, with each contributing 25% of the total aqueous flow rate. The droplet produced contains some residual methylene blue and brilliant green dye. Image four shows the subsequent droplet produced. The droplet appears to contain only distilled water, naphthol yellow and amaranth; there is no blue/green dye visible in the droplet. The blue colour observed in the T-junction is just where the dye has stained the chip. The organic flow was infused at 48 µL $min^{-1}$, the distilled water was infused at 6 µL $min^{-1}$, and the dyes were infused at flow rates of 3 µL $min^{-1}$. Images were taken using a Lumenera camera (LG11059C) using video capture software design by Dr Bernard Treves Brown using LabVIEW.**

## 4.6 Conclusions

The microfluidic system has been shown to be capable of evaluating precipitation inhibitors. The effect of two water soluble polymers, PVP and HPMC, on ketoconazole

precipitation was determined. HPMC was found to be a more potent precipitation inhibitor than PVP. This was suggested to be due to the hydrogen donor ability of the hydroxyl groups on the polymer and the hydrogen bond acceptor properties of ketoconazole. As PVP is a hydrogen bond acceptor, precipitation inhibition of ketoconazole in the presence of PVP was probably due to the increase in viscosity of the aqueous solution which would hinder diffusion of drug molecules to the crystal surface.

The next step would be the development of a microfluidic chip capable of screening multiple precipitation inhibitors. Preliminary experiments were performed on a microfluidic chip which contained five aqueous inlets to evaluate the mixing of different aqueous flows. A couple of issues were flagged up in these experiments, for example the distribution of dyes observed in the T-junction did not appear reflect the relative flow rates of the aqueous phases, raising concerns about the composition of the droplet. The backflow observed will also naturally affect the droplet composition; the dimensions of the aqueous inlets will need to altered to reduce this problem. Another issue is the slow mixing of the droplet after formation observed in figure 4.15, as the intensity of scattered light is measured as a function of time, slow or incomplete mixing may become an issue if the device is used to study precipitation kinetics. An experiment to determine how long it takes the droplet composition to stabilise after the aqueous flows are altered had positive results, however, the time taken for the aqueous solution to reach the T-junction is not taken into account as switching from inlet one to inlet two will also incur a delay in droplet stabilisation as the aqueous flow will need to replace the previous aqueous flow in the aqueous channel before the T-junction is reached.

Further experiments will need to undertaken to investigate these issues before drugs and excipients can be introduced into the system. Given the concerns regarding the droplet composition and slow mixing in the droplet after detachment, mixing of different aqueous flows may be better achieved through the use of droplet fusion. Droplet fusion will allow better control over droplet composition and the time of droplet fusion will be able to be accurately determined.

# Chapter 5: Nucleation kinetics

## 5.1 Chapter overview

Chapter five investigates the use of microfluidics to determine precipitation kinetics. A brief introduction to nucleation theory will be presented. The benefits of using droplet-based microfluidics to monitor precipitation kinetics will be considered and two microfluidic devices capable of determination of precipitation kinetics which have been reported in the literature will be discussed. A microfluidic device based on the spiral design reported in chapters three and four will be presented and used to determine the onset time of drug precipitation. Both the effectiveness and limitations of the device will be discussed in detail.

## 5.2 Importance of kinetic measurements for drug discovery and development

The quantity of drug absorbed will not only be dependent on the amount of the drug that precipitates out of solution but also the time at which precipitation occurs. If the drug precipitates immediately after gastric emptying into the small intestine then drug absorption is expected to be minimal. The longer the supersaturated state can be stabilised for, the greater the chance of adequate drug absorption to elicit the desired therapeutic response. The following chapter will give a brief introduction into nucleation theory and discuss the use of microfluidics to determine precipitation kinetics.

## 5.3 Brief nucleation theory

Nucleation concerns the generation of crystals or precipitates in a system. The critical size required for the clusters to grow into macroscopic particles and the activation energy of nucleation was discussed in chapter three. Another important aspect of nucleation is the nucleation rate, J, (expressed in $m^{-3}$ $s^{-1}$ or $m^{-2}$ $s^{-1}$). The nucleation rate is a measure of the number of supernuclei in the solution per unit time per unit volume. The supersaturation dependent nucleation rate can be determined using equation 5.1.[115]

$$\mathrm{J(S)} = \mathrm{AS\ e}^{\left(\frac{-\mathrm{B}}{\ln^2 \mathrm{S}}\right)} \qquad [5.1]$$

$$B = \frac{16\,\pi\,{\nu_0}^2\,{\gamma_{ef}}^3}{3\,(k_B T)^3} \qquad [5.2]$$

$$A = \left(\frac{k_B T}{{\nu_0}^2 \gamma}\right)^{\frac{1}{2}} D C_e \, lnS \qquad [5.3]$$

Where $B$ is a thermodynamic parameter given by equation 5.2, and $A$ is a supersaturation independent kinetic parameter ($m^{-3}$ $s^{-1}$) given by equation 5.3. $\nu_0$ is the volume occupied by a molecule in a cluster ($m^3$), $\gamma$ is the specific surface energy of the cluster/solution interface (J $m^{-2}$), $\gamma_{ef}$ is the effective specific surface energy (J $m^{-2}$), $k_B$ is the Boltzmann constant (J $K^{-1}$), $T$ is the temperature (K), D is the monomer diffusion coefficient ($m^2$ $s^{-1}$), $C_e$ is the solubility ($m^{-3}$), and $S$ is the supersaturation. Values of A for 3D or 2D heterogeneous nucleation are typically in the range of $10^{15}$-$10^{25}$ $m^{-3}$ $s^{-1}$, while for homogeneous nucleation values of A tend to be many orders of magnitude greater than this.

The nucleation rate can be determined experimentally by counting the number, *N*, of supernuclei formed in a system of volume, $V$, or on a surface with a surface area, $A_s$, over a time, *t*, (equations 5.4 and 5.5).[115]

$$N = J\, V\, t \qquad [5.4]$$

$$N = J\, A_s\, t \qquad [5.5]$$

The nucleation rate, at a given temperature and supersaturation, is given by the gradient of the linear dependence of N on time. Measurement of the nucleation rate at constant temperature but varying degrees of supersaturation will lead to determination of the supersaturation dependent nucleation rate, which can then be used to determine the parameters A and B. There is a linear dependence of ln(J/S) on $1/\ln^2 S$, the gradient of the straight line gives the thermodynamic parameter, B, while the supersaturation independent kinetic parameter, A, can be obtained from the intercept, which is equivalent to lnA.

### 5.3.1 Induction time

The induction time refers to the delay between supersaturation being reached and appearance of crystals/precipitates; it is dependent on a number of factors, such as the degree of supersaturation, presence of impurities and the degree of agitation, among others. The induction time ($t_{ind}$) is thought to be an accumulation of the time it takes to complete three processes: the time required for the system to reach a quasi-steady-state of molecular cluster distribution referred to as the relaxation time ($t_r$), the time necessary

for stable nucleus formation ($t_n$), and the time required for the stable nucleus to reach a detectible size ($t_g$) (equation 5.6).[113]

$$t_{ind} = t_r + t_n + t_g \qquad [5.6]$$

The induction time can be determined experimentally, however, it is dependent on the experimental technique employed. Different techniques will have different sensitivities, and therefore detect the presence of macroscopic clusters at different times. For this reason, the induction time must be determined using the $t_{ind}$ formula corresponding to the experimental technique used.

The appearance of the first supernucleus in the system can be determined using equation 5.4; when the number of supernuclei equals one and the time is the induction time, equation 5.4 becomes equation 5.7. Equation 5.7 shows that the induction time is inversely proportional to the nucleation rate.[115]

$$t_{ind} = \frac{1}{J\,V} \qquad [5.7]$$

In the case of formation of numerous supernuclei, the induction time can be determined using equation 5.8.[115]

$$t_{ind} = \left(\frac{3\,\alpha_v}{\pi\,G^3\,J}\right)^{\frac{1}{4}} \qquad [5.8]$$

Where $\alpha_v$ is the detectable volume or mass fraction of the particle and G is the growth rate of the particle, i.e. the change in particle radius as a function of time. The induction time due to either one or many supernuclei can be determined by combining equations 5.7 and 5.8 to give:[115]

$$t_{ind} = \left(\frac{1}{J\,V}\right) + \left(\frac{3\,\alpha_v}{\pi\,G^3\,J}\right)^{\frac{1}{4}} \qquad [5.9]$$

The induction time can also be determined from the change in the intensity of transmitted light through a nucleating solution and is given by equation 5.10,[115] if Rayleigh light scattering is occurring.

$$t_{ind} = \left(\frac{7\alpha_i}{2\,\pi\,a\,L\,G^6\,J}\right)^{\frac{1}{7}} \quad [5.10]$$

Where $\alpha_i$ is the detectable fraction of light scattered by the supernuclei, L is the length the light beam travels through the solution, and α is given by equation 5.11,[115] where $n$ is the refractive index of the particle and λ is the wavelength of the light.

$$a = \frac{64\,\pi^4\left(n^2-1\right)^2}{3(n^2-2)^2\lambda^4} \quad [5.11]$$

Determination of induction times becomes a problem when the induction time is less than five seconds, at this timescale the mixing time may be similar or greater than the induction time, therefore measurement of induction times requires fast mixing and a sensitive detection method.

### 5.3.2 The droplet method

The droplet method was proposed by Vonnegut in 1948; Vonnegut discovered that measurement of nucleation rate could be simplified by using a large number of small independent crystallisation volumes.[118] This technique reduced the difficulty of separating nucleation and crystal growth kinetics. If the crystallisation volumes were small enough to contain just one nucleus, the nucleation rate could be deduced from the fraction of droplets which contained a nucleus. The droplet method also allowed homogeneous nucleation to be observed, if the number of droplets exceeded the number of impurities present in the system. Vonnegut noted that the information that could be deduced from the droplets was dependent on how monodisperse the droplets were, as there is greater probability of finding a nucleus in a larger droplet than a smaller droplet.

## 5.4 Microfluidic devices which have been designed to determine precipitation kinetics

Gong *et al*. used microfluidic technology to determine the nucleation kinetics of the thermo-responsive polymer poly-*N*-isopropylacrylamide (PNIPAM).[153] The birefringent crystals produced were detected using an optical microscope with a pair of crossed polarisers. Between 3,000 and 4,000 droplets were used for a single experiment. The authors show that multiple nucleation events occurred in 500 μm diameter droplets, but when the droplet diameter was decreased to 100 μm mononucleation events were observed.

Salmon *et al*. presented a microfluidic device based on the classical droplet method, up to 300 droplets of small volumes (~100 nL) were stored for a few hours in a microfluidic channel.[120] The temperature was decreased from a temperature greater than the solubility temperature at a rate of 0.1 ºC $s^{-1}$, and the presence of a crystal in the droplet was determined using a stereomicroscope with a CCD camera under crossed polarisers. The authors attempted to determine the nucleation rate of potassium nitrate from the probability, P, of finding a crystal in a droplet of volume, V (equation 5.12). In this case, the authors were unable to determine a unique nucleation rate and suggest the reason for this is the presence of impurities in the droplets.

$$P(t) = e^{(-J\,V\,t)} \qquad [5.12]$$

## 5.5 Development of a microfluidic device to determine the onset time of precipitation

### 5.5.1 Overview

Chapter three demonstrated that the light scattering method presented in this study, can be used to monitor the precipitation process and determine the extent of drug precipitation; however, due to issues regarding the mixing of aqueous solutions in the T-junction prior to droplet formation, the DP chip was not suitable to determine the time at which precipitation occurred. This chapter will describe the development of a microfluidic chip that has been designed to monitor the initial stages of precipitation and give some insight into the time at which precipitation occurs. This time will be referred to as the onset time ($T_{onset}$) of precipitation. $T_{onset}$ is related to the induction time, however as no information is available on the growth rate or the detectible size of the particles, $T_{onset}$ will be used in the following results instead of $T_{ind}$.

### 5.5.2 Methods and Materials

#### 5.5.2.1 Chemicals

Latex bead solutions were obtained from SigmaAldrich (460, 600, 800 nm diameter), Varian (Agilent Technologies) (1000 nm) and Polysciences Inc. (384 nm). Ketoconazole was obtained from Fisher Scientific, and trisodium phosphate from Acros Organics (Fisher

Scientific). Perfluorodecalin was obtained from Fluorochem. Amaranth and cresol red were obtained from SigmaAldirch. All materials were used as received.

### 5.5.2.2 Microfabrication[5]

#### 5.5.2.2.1 The drug precipitation (DP) chip

The evaluation of the LED light source was carried out on the DP chip used in chapter three. Details of the fabrication of this chip are given in section 3.4.2.3.

#### 5.5.2.2.2 The centre inlet (CI) chip

The chip design is illustrated in figure 5.1. A rectangular cross-section spiral channel 730 µm wide, 700 µm deep and 828.4mm in length, was milled into a PMMA substrate using a CAT3D-M6 CNC milling machine (Datron Technologies Ltd.). In the centre of the spiral, three aqueous inlet channels 300 µm wide, 300 µm deep, and 7 mm in length, which merged into a T-junction 300 µm in cross-section and 400 µm in length were milled (figure 5.1b). One organic inlet, three aqueous inlets and an outlet were drilled through the substrate; all holes drilled were 1.398 mm in diameter. The microfluidic device was sealed using a PCR seal (Corning Inc, USA) and a hydrophobic coating applied to the channels by infusing a hydrofluoroether solvent containing a surface modifying fluorinated polymer (Certonal FC732, Acota Ltd.). The fluorinated polymer was left in the chip for an hour before being removed and the chip allowed to dry.

[5] Fabrication carried out by Dr Stephan Mohr (University of Manchester)

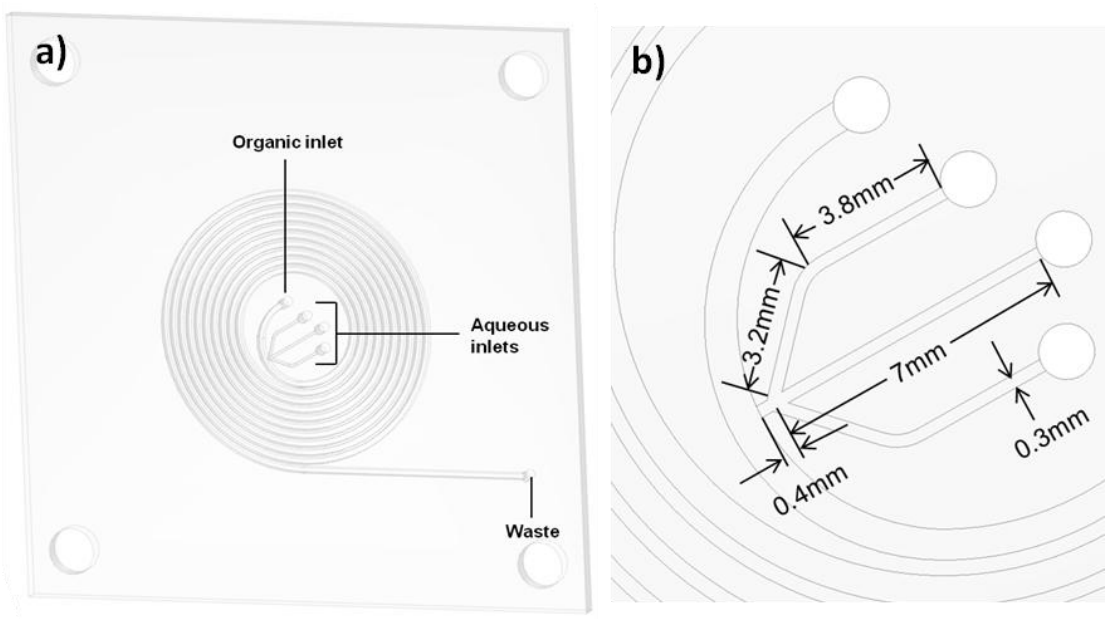


**Figure 5.1: a) The design of centre inlet (CI) chip. The organic and aqueous inlets are positioned in the centre of the chip to allow the intensity to be determined with greater frequency at the initial stages of drug precipitation. b) The dimensions of the aqueous inlet channels. The aqueous inlet channels merge close to the spiral channel (0.4 mm) to reduce the likelihood of mixing prior to droplet generation.**

### 5.5.2.3 Experimental setup

The experimental setup used in the following experiments is identical to the setup used for the pH shift experiments (see section 3.4.2.4, figure 3.6), except a blue LED (low dome lens, 1 W, 470 nm wavelength) (Philips Lumileds Lighting Company, San Jose, USA) is used as the light source instead of the laser, and the videos were captured using video capture software designed by Dr Bernard Treves Brown in LabVIEW.

### 5.5.2.4 Evaluation of the LED light source using latex beads

The latex bead study described in section 3.4.2.9 was repeated using an alternative light source. The entire chip was illuminated with a blue LED, and the response of the system to different concentrations and different particle sizes was evaluated using latex bead suspensions with a range of particle diameters (384, 460, 600, and 1000 nm). The solutions were made up to concentrations of 0.0003 - 0.005 % w/w, which correspond to concentrations of between $1.15 \times 10^{7}$ -$1.69 \times 10^{9}$ particles $mL^{-1}$. The intensity of scattered light was determined in the same way as for the laser light source. The same positions on the chip were selected; hence the time from droplet generation to detection remained the same for all the detection positions.

### 5.5.2.5 Determination of the flow rate and the time taken for the droplet to reach each detection point

The onset time of precipitation was determined at various total aqueous flow rates (120 - 800 µL $min^{-1}$, table 5.1) with a 0.94 mM (0.47 mM in the droplet) ketoconazole solution at pH 6.5, using the pH shift method described in section 3.4.2.10. As only two aqueous inlets were required for this experiment, the centre aqueous inlet was not used. The ratio of total aqueous flow rate to organic flow rate (1:2) was consistent throughout the experiment to ensure that droplet volume remained constant for each flow rate experiment. The time taken for the droplet to reach each detection point (labelled 1-11, figure 5.2) was calculated for total aqueous flow rates of 120 and 200 µL $min^{-1}$, as described in section 3.4.2.5; while the time taken for total aqueous flow rates of 400, 600 and 800 µL $min^{-1}$ was calculated from the droplet speed determined when using a flow rate of 200 µL $min^{-1}$, as the high flow rates made the determination of droplet speed more challenging. The calculated times for all the flow rates investigated are given in table 5.2. The intensity of light scattered by the droplet was detected at each detection point. The intensities were plotted as a function of time, and $T_{onset}$ of precipitation determined from the x intercept of the linear regression line fitted to the data. Mixing prior to droplet formation was considered insignificant, when increasing the flow rate further resulted in minimal change in the $T_{onset}$ value obtained.

| Inlet 1: ketoconazole dissolved in phosphoric acid (µL $min^{-1}$) | Inlet 3: trisodium phosphate solution (µL $min^{-1}$) | Inlet 4: perfluorodecalin (µL $min^{-1}$) | Total flow rate (µL $min^{-1}$) | Total time on chip (s) |
|---|---|---|---|---|
| 60 | 60 | 240 | 360 | 72.15 |
| 100 | 100 | 400 | 600 | 43.65 |
| 200 | 200 | 800 | 1200 | 21.83 |
| 300 | 300 | 1200 | 1800 | 14.55 |
| 400 | 400 | 1600 | 2400 | 10.91 |

**Table 5.1: Flow rates used to determine the adequate flow rate required to eliminate mixing in the T-junction.**

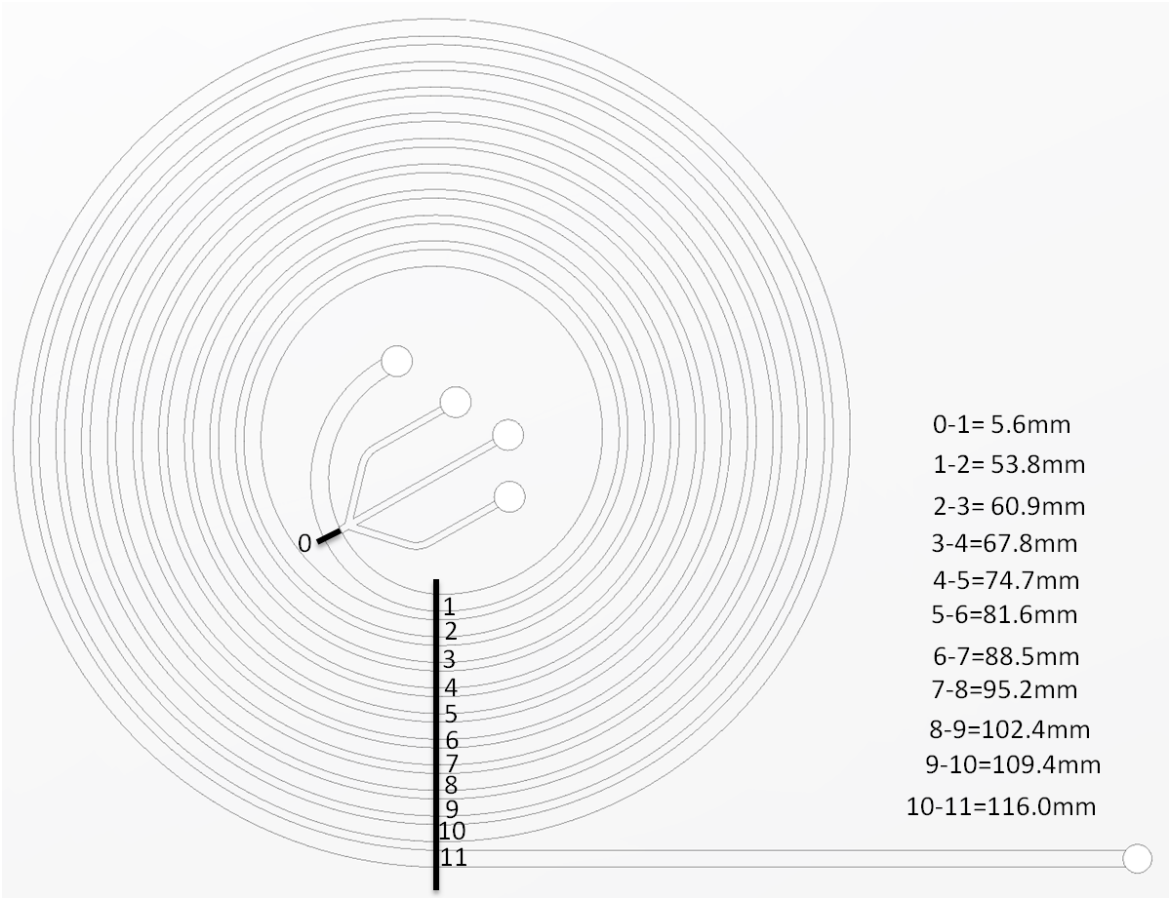


**Figure 5.2: Schematic of the CI chip. The eleven positions at which the intensity of scattered light was measured are denoted 1-11, the distances between the positions are given to the right of the spiral.**

| | Time taken for droplet to reach each position (seconds) | | | | |
|---|---|---|---|---|---|
| | Total aqueous flow rate (μL $min^{-1}$) | | | | |
| **Position** | **120** | **200** | **400** | **600** | **800** |
| **1** | 0.47 | 0.29 | 0.14 | 0.10 | 0.07 |
| **2** | 5.01 | 3.03 | 1.51 | 1.01 | 0.76 |
| **3** | 10.14 | 6.14 | 3.07 | 2.05 | 1.53 |
| **4** | 15.86 | 9.59 | 4.80 | 3.20 | 2.40 |
| **5** | 22.15 | 13.40 | 6.70 | 4.47 | 3.35 |
| **6** | 29.033 | 17.56 | 8.78 | 5.85 | 4.39 |
| **7** | 36.49 | 22.08 | 11.04 | 7.36 | 5.52 |
| **8** | 44.52 | 26.93 | 13.47 | 8.98 | 6.73 |
| **9** | 53.15 | 32.16 | 16.08 | 10.72 | 8.04 |
| **10** | 62.37 | 37.73 | 18.87 | 12.58 | 9.43 |
| **11** | 72.15 | 43.65 | 21.83 | 14.55 | 10.91 |

**Table 5.2: Time taken for the droplet to reach each detection point on chip, for various total aqueous flow rates.**

### 5.5.2.6 Investigation into mixing in the T-junction prior to droplet formation

The presence of acid-base based mixing in the T-junction prior to droplet formation was investigated using a similar method to that used for the DP chip in section 3.4.2.13. The acidic aqueous phase consisted of 0.01 M hydrochloric acid and cresol red, a pH indicator, which undergoes a colour change from yellow to purple in the pH range 7.0 – 8.8. The basic aqueous phase used was 0.04 M sodium hydroxide solution. The acidic aqueous phase were infused through the outer aqueous inlets, while the basic aqueous phase was infused through the centre aqueous inlet. The ratio of the aqueous phase to the organic phase remained constant throughout the experiment, however, the flow rate was varied to investigated the extent of mixing at the flow rates used in section 5.5.2.5. The individual flow rates used for each experiment are given in table 5.3. Videos of the T-junction during droplet generation were recorded using a Lumenera LG11059 camera (Lumenera Corporation) and video capture software designed by Dr Bernard Treves Brown in LabVIEW.

| **Inlet 1: cresol red in 0.01 M hydrochloric acid (µL min$^{-1}$)** | **Inlet 2: 0.04 M sodium hydroxide (µL min$^{-1}$)** | **Inlet 3: cresol red in 0.01 M hydrochloric acid (µL min$^{-1}$)** | **Inlet 4: perfluorodecalin (µL min$^{-1}$)** |
|---|---|---|---|
| **40** | 40 | 40 | 240 |
| **66.67** | 66.67 | 66.67 | 400 |
| **133.33** | 133.33 | 133.33 | 800 |
| **200** | 200 | 200 | 1200 |

**Table 5.3: Flow rates used to investigate mixing in the T-junction prior to droplet generation using a pH indicator (cresol red).**

### 5.5.2.7 Determination of the onset time of precipitation

The onset time of precipitation was determined using the CI chip for various ketoconazole supersaturations. Inlet one contained ketoconazole in 0.1 M phosphoric acid, inlet two contained 0.1 M phosphoric acid and inlet three contained trisodium phosphate solution (0.19 and 0.62 M, for pH 6.5 and pH 7.0 respectively). Monodisperse plugs approximately 500 nL in volume were generated in immiscible perfluorodecalin. 50% of the droplet consisted of the trisodium phosphate solution, and the other 50%, was a combination of ketoconazole in 0.1 M phosphoric acid and 0.1M phosphoric acid. Initial solutions of ketoconazole in 0.1 M phosphoric acid were made up to concentrations of 0.75, 0.85, 0.94 and 1.02 mM. These solutions of ketoconazole were mixed with 0.1 M phosphoric acid, in

ratios of 2:1, 1:1 and 1:2, to generate different concentrations of ketoconazole within the droplet. Perfluorodecalin was infused at a flow rate of 800 µL $min^{-1}$; trisodium phosphate was infused at a flow rate of 200 µL $min^{-1}$, and the combined flow rate of the ketoconazole solution and the phosphoric acid solution was 200 µL $min^{-1}$.

## 5.5.3 Results and Discussion

### 5.5.3.1 Research aims

The objective of this study was to determine whether the microfluidic device coupled with light scattering detection could be used to obtain information on the kinetics of the precipitation process. Alterations to the chip design were made in an attempt to overcome problems associated with the DP chip (chapter three) and are discussed below. Determination of the kinetics of drug precipitation would be particularly useful in drug formulation, where it is not only important to determine the extent the drug precipitate out of the solutions but also when the drug begins to precipitate, as this will have a significant impact on whether the drug is absorbed.

### 5.5.3.2 CI chip design

It was suggested in chapter three, that negative onset times of precipitation determined using the DP chip could be a result of mixing in the T-junction prior to droplet formation, and inaccurate extrapolation due to the limited number of data points used to generate the linear regression lines. For these reasons, a new chip was designed which had the organic and aqueous inlets in the centre of the spiral; it was envisioned that this chip would allow more frequent measurements to be taken at the initial stages of drug precipitation, as the detection points will be closer together, therefore allowing more accurate measurement of the onset time. The length of the T-junction was also shortened from 1.1 mm to 0.4 mm, reducing the distance the aqueous streams are in contact before droplet generation, and hence decreasing the possibility of mixing. All other dimensions of the chip remained the same as the channel dimensions used for the DP chip, as the DP was shown to be able to successfully determine the extent of drug precipitation. The throughput capabilities of the chip were increased slightly through the addition of a third aqueous inlet, which enabled the concentration of the ketoconazole solution to be varied on chip.

### 5.5.3.3 Evaluation of the LED light source

An alternative light source was evaluated, as it was hoped that a more stable signal would be generated from a LED, as the speckle pattern which is often observed when using lasers would not be present. The evaluation of the LED light source was carried out on the DP chip to allow direct comparison with the response obtained from the laser. The LED illuminated the whole microfluidic chip (figure 5.3), as apposed to just a section of the chip which was illuminated by the laser (figure 3.20). The reflection of light from the surface of the droplets is more visible in figure 5.3 as a greater proportion of the chip is illuminated. The detection points used were the same as those used for the laser; the LED was positioned to reduce scattering from the droplet surface in these areas. The response of the system was evaluated using latex bead suspensions. Figure 5.4 shows the response at each position on chip using different concentrations of latex suspensions (bead diameter 384 nm). The scattered intensity of these suspensions were averaged across all eleven detection points allowing comparison of the intensity of scattered light detected from the different concentrations.

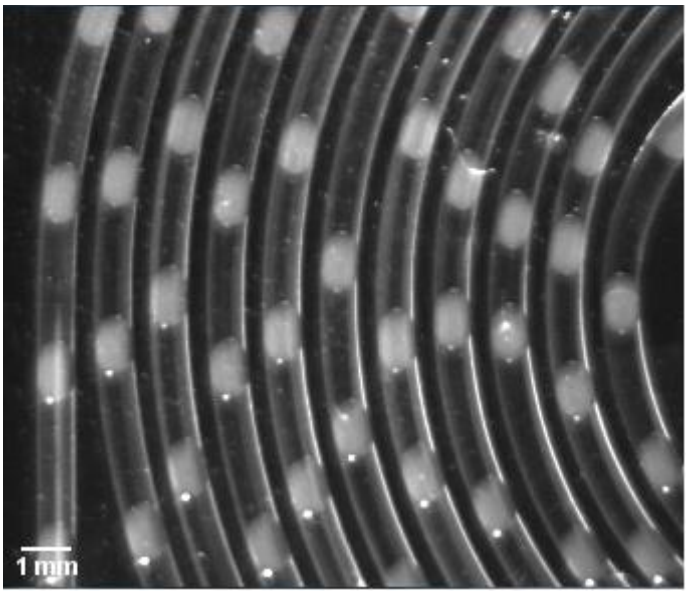


**Figure 5.3: Illumination of the microfluidic chip using the LED light source. The droplets contain a 6.75 x $10^8$ particles $mL^{-1}$ latex bead (384 nm diameter) suspension. Image taken using a PixeLINK camera (PL-A741) and video capture designed by Dr Bernard Treves Brown in LabVIEW.**

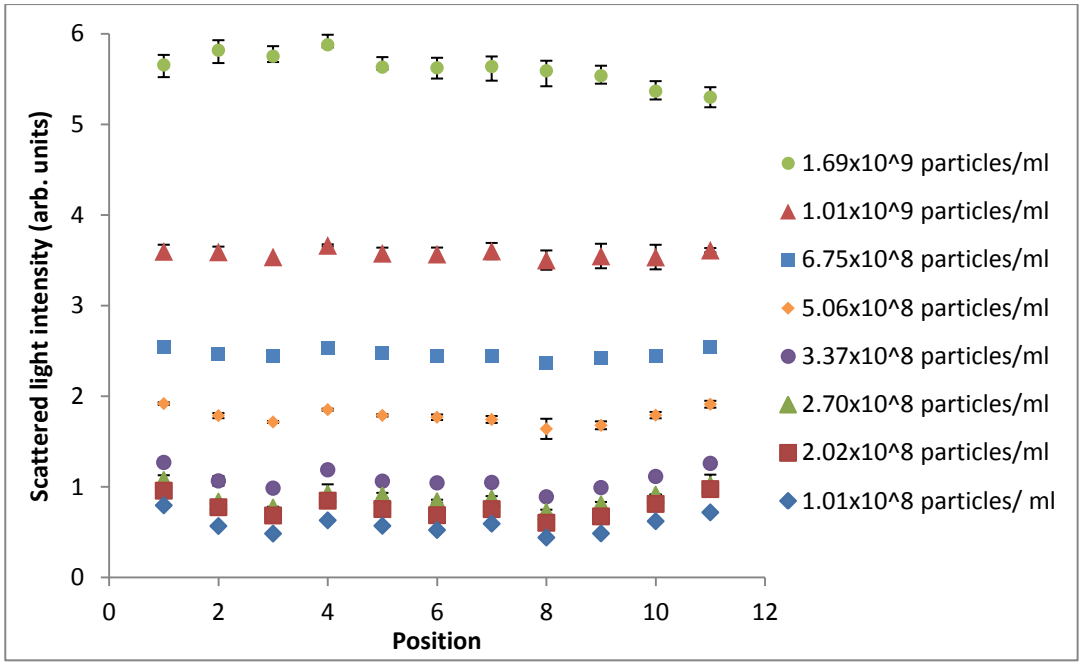


**Figure 5.4: Scattered intensity of different concentrations of a latex suspension (bead diameter 384 nm) at each position on chip, using a LED light source. The error bars show the standard deviation (n=3).**

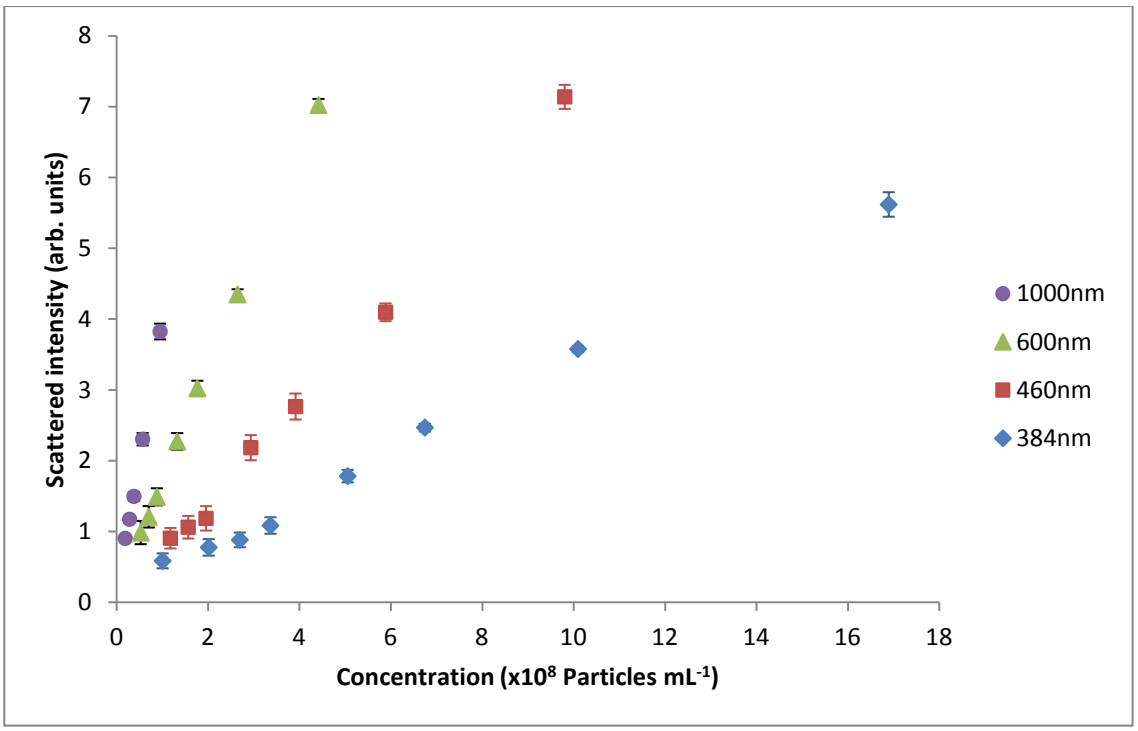


**Figure 5.5: Average scattered intensity (determined across all positions on chip) of different diameter latex beads as a function of concentration, taken using a LED light source. The error bars show the standard deviation (n=3).**

Figure 5.5 shows the average intensity determined across each position on chip as a function of concentration for different diameter latex beads (384, 460, 600 and 1000 nm);

the latex bead diameters used are within the same range as the ketoconazole diameters measured in the DLS experiments (section 3.4.3.5, figure 3.26). The latex bead concentrations (particles $mL^{-1}$) used correspond to concentrations of 0.0003 - 0.005 % w/w, similar to the concentrations (0.0002 - 0.003 % w/w) detected using the laser. The scattered light was found to respond to both changes in particle diameter and concentration. When compared to the results obtained from the laser, the sensitivity of the LED light source was slightly reduced, while the stability of the different light sources was comparable. A benefit of the LED light source is that the whole chip is illuminated; hence, it would be possible to determine the intensity at other positions on chip, not just the eleven positions used for this study, as long as the reflections from the droplet surface in these extra positions are not significant.

### 5.5.3.4 Flow rate determination for the onset of precipitation experiments

Negative onset times of precipitation determined using the DP chip suggested that precipitation was occurring before the droplet had been generated; this was thought to a consequence of aqueous phase mixing in the T-junction, which was confirmed using a pH indicator (cresol red). Although the T-junction has been shortened to reduce the possibility of mixing, $T_{onset}$ was determined for a range of flow rates using a ketoconazole supersaturation of 35.35 to determine whether negative $T_{onset}$ values were still being obtained using the CI chip.

Figure 5.6 shows the scattered intensity as a function of time for various flow rates (120 – 800 µL $min^{-1}$ total aqueous flow rates). It is obvious that total aqueous flow rates of 120 and 200 µL $min^{-1}$ gave negative values for $T_{onset}$, while $T_{onset}$ of precipitation was not altered significantly upon doubling the total aqueous flow rate from 400 µL $min^{-1}$ to 800 µL $min^{-1}$. $T_{onset}$ values determined for flow rates of 400, 600 and 800 µL $min^{-1}$ were 1.68, 1.49 and 0.98 seconds respectively. The times determined for flow rates of 400 and 600 are similar, while the value for 800 is a little lower than expected, however, it should be noted that this experiment was not repeated, and values obtained are only used to indicate the flow rate at which $T_{onset}$ does not change greatly with increases in flow rate. As the onset time should be dependent on the degree of supersaturation of ketoconazole and independent of the flow rate used, when the flow rate used no longer had an impact on $T_{onset}$ then mixing in the T-junction could be considered insignificant. As the flow rate of 400 µL $min^{-1}$ is the lowest flow rate within this range, this flow rate will be used to determine $T_{onset}$ for various supersaturations.

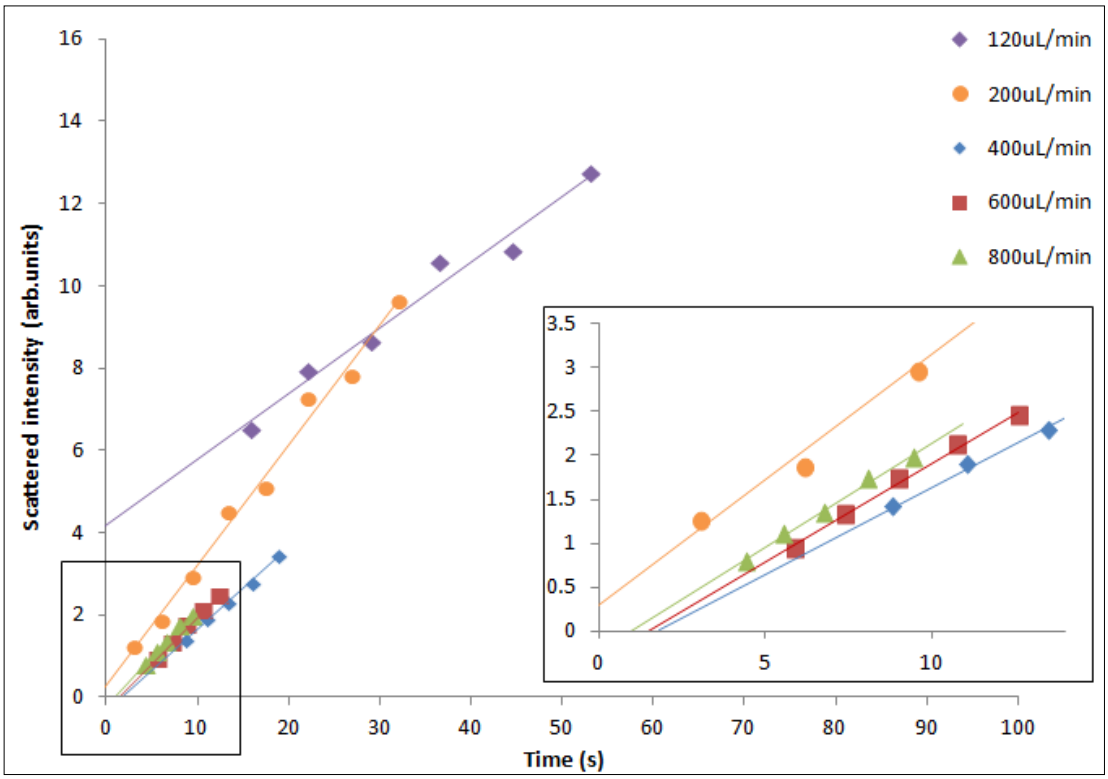


**Figure 5.6: Scattered intensity (arbitrary units) as a function of time (seconds) for different total aqueous flow rates (120 – 800 µL $min^{-1}$) to illustrate the dependence of onset time on flow rate. Measurements were taken using the pH shift method and a ketoconazole supersaturation of 35.35.**

### 5.5.3.5 Investigation of mixing in the T-junction at different flow rates using cresol red

The cresol red experiments used to investigate mixing in the DP chip were repeated for the CI chip, using some of the flow rates investigated in section 5.5.2.5. Figure 5.7 shows the images obtained from these experiments. A 0.01 M hydrochloric acid solution containing cresol red is being infused into the outer aqueous inlets (solution appears yellow in figure 5.7), while 0.04 M sodium hydroxide is being infused into the centre aqueous inlet. It is difficult to tell whether there is any mixing in the T-junction from these images; image a) appears to have a pinkish interface between the different aqueous phases indicating mixing, this mixing seems to be slightly reduced in image b), while images c) and d) are indistinguishable from one another.

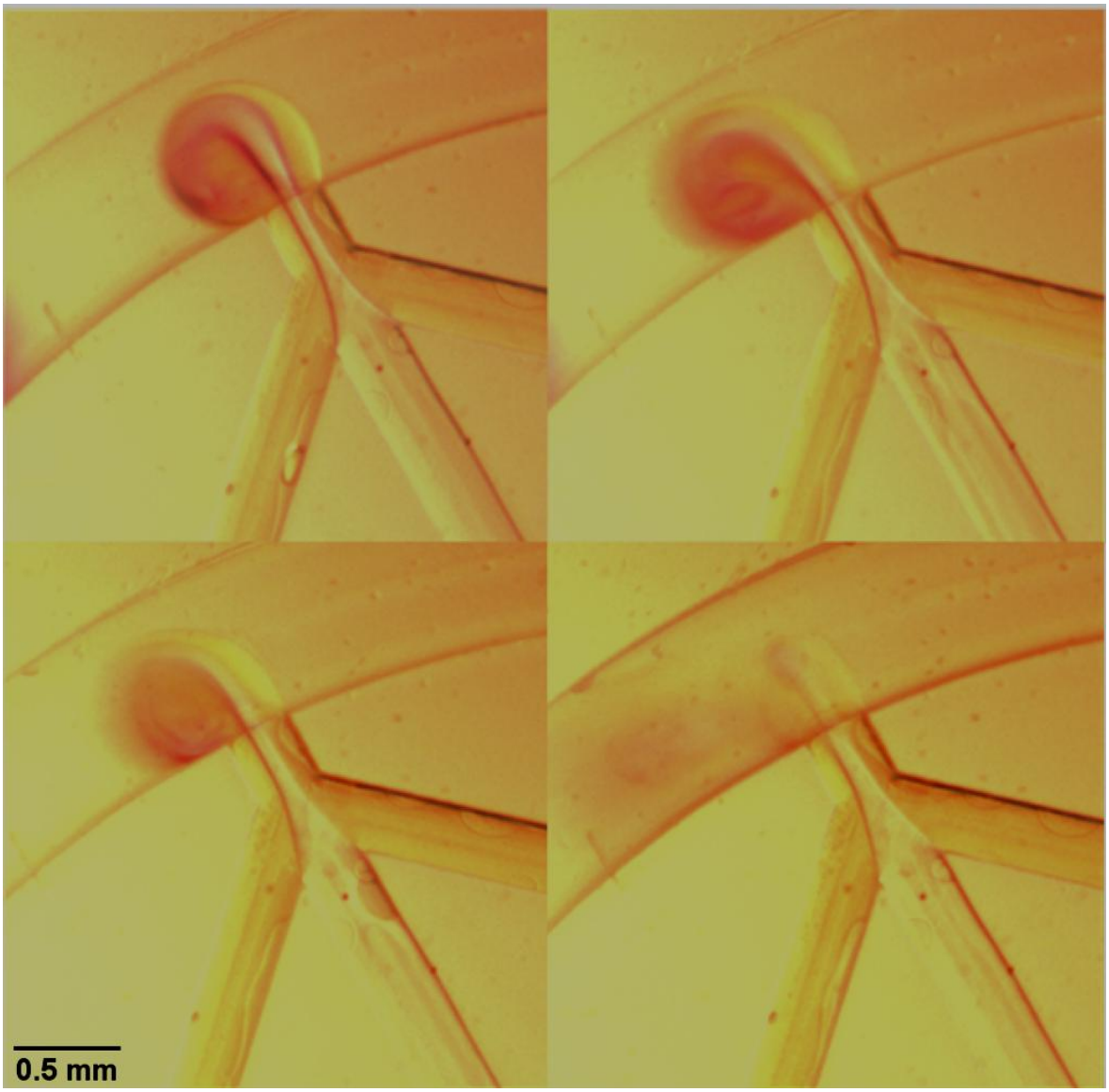


**Figure 5.7: Images taken to investigate acid-base mixing in the CI chip for different flow rates. The centre aqueous inlet contains 0.04 M NaOH, while the outer aqueous inlets contain 0.01 M HCl and cresol red. The individual flow rates used are given in table 5.3; a) was taken using an organic flow rate of 240 µL $min^{-1}$ and a total aqueous flow rate of 120 µL $min^{-1}$, b) was taken using an organic flow rate of 400 µL $min^{-1}$ and a total aqueous flow rate of 200 µL $min^{-1}$, c) was taken using an organic flow rate of 800 µL $min^{-1}$ and a total aqueous flow rate of 400 µL $min^{-1}$, and d) was taken using an organic flow rate of 1200 µL $min^{-1}$ and a total aqueous flow rate of 600 µL $min^{-1}$. Images were taken with a Lumenera camera (LG11059C) using video capture software designed by Dr Bernard Treves Brown in LabVIEW.**

### 5.5.3.6 Onset time determination

The onset time of precipitation was determined for a range of ketoconazole supersaturations at intestinally relevant pH (pH 6.5, 7.0). Figure 5.8 shows the scattered intensity recorded as a function of time for four ketoconazole supersaturations. $T_{onset}$ is obtained from the x-axis intercept of the linear regression line. It is evident from figure 5.8

that higher supersaturations resulted in an increased rate of precipitation and shorter onset of precipitation times.

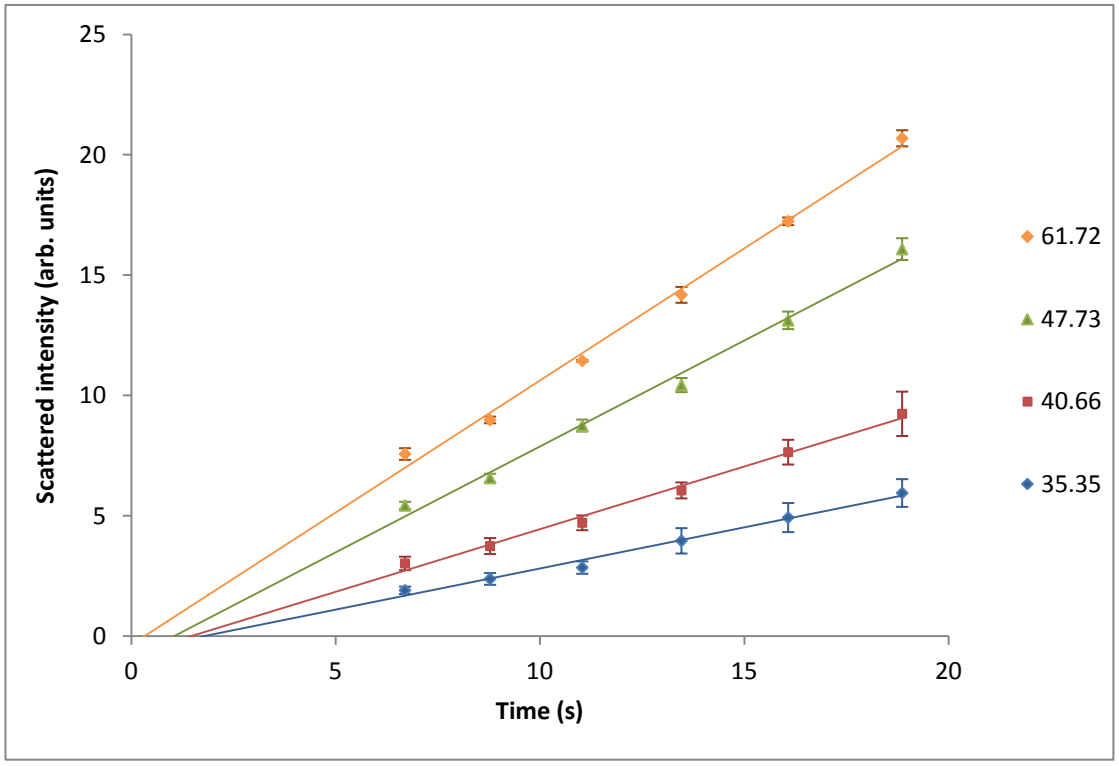


**Figure 5.8: Scattered intensity as a function of time for different supersaturations of ketoconazole. Linear regression lines were fitted to the data to emphasise the different $T_{onset}$ values obtained for the supersaturations. The error bars show the standard deviation (n=3).**

Only scattered light intensities obtained between six and twenty seconds were used to determine the onset times, as the intensities prior to six seconds on chip were variable. Figure 5.9a shows the intensity as a function of frame number at 3.07 seconds on chip using a ketoconazole supersaturation of 47.73. It is evident that the signal obtained is variable, as there is a broad range of maximum intensities for the nineteen droplets shown in figure 5.9a (peak height RSD 10.53). As the maximum intensity range is broad, using the intensities determined at these times may lead to inaccurate determination of $T_{onset}$. Figure 5.9b shows the intensity as a function of frame number using the same supersaturation at 8.78 seconds on chip. It is clear that the intensity is more stable, with a RSD in peak height of 5.29, it is nearly half that associated with the peak heights obtained at 3.07 seconds. It is for this reason that intensities obtained at positions one to four (0 - 4.8 seconds) have been omitted from the $T_{onset}$ determination.

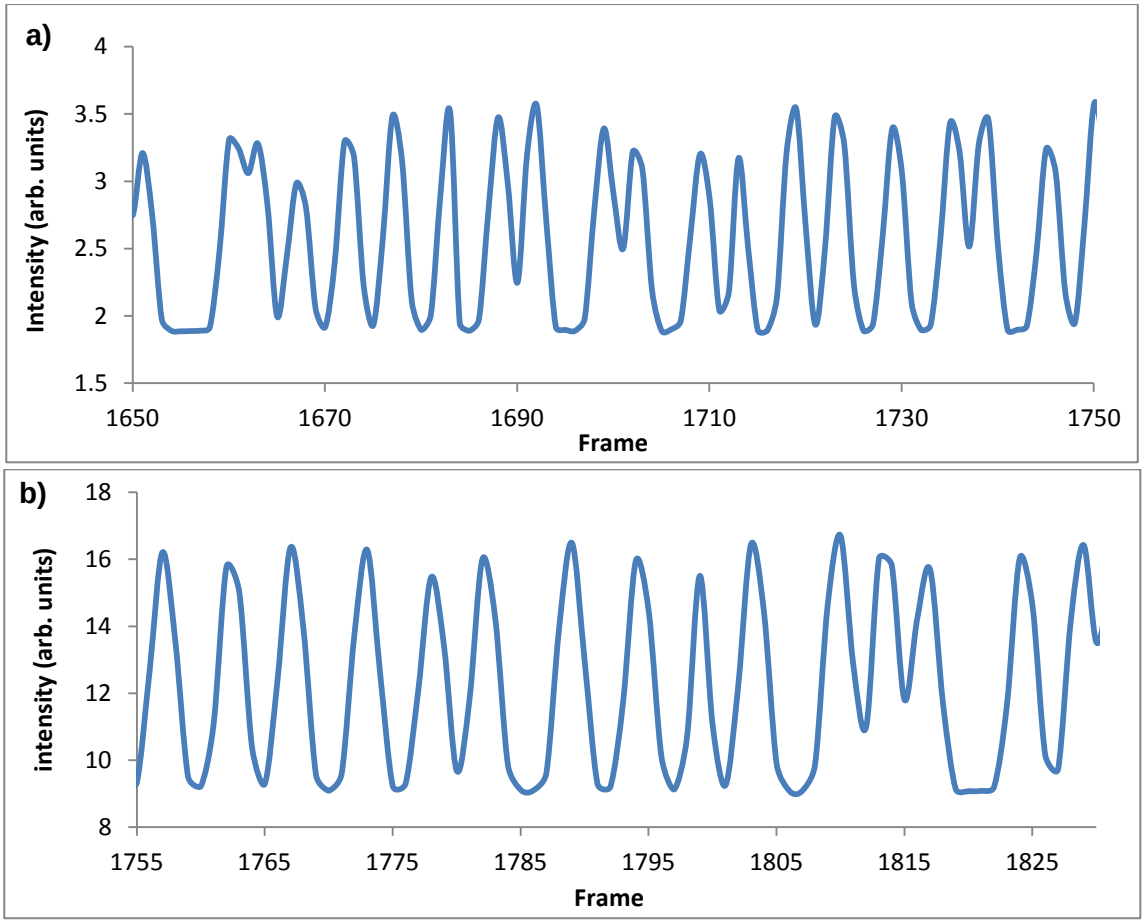


**Figure 5.9: Intensity as a function of frame number for a ketoconazole supersaturation of 47.73, obtained at different times on chip, a) was obtained after 3.07 seconds on chip, while b) was obtained after 8.78 seconds on chip.**

Figure 5.10 shows the $T_{onset}$ of precipitation values obtained for a range of supersaturations. $T_{onset}$ decreases rapidly upon increasing the supersaturation from 32 to approximately 45, where the decrease in $T_{onset}$ becomes less pronounced with increasing supersaturation. This response is similar to the dependence of induction time on supersaturation typically observed experimentally.[154-156] The onset times of precipitation determined in this study are small (<2.5 seconds). On this timescale $T_{onset}$ values are likely to be inaccurate as the mixing time of the droplets will probably exceed the $T_{onset}$ values obtained, i.e. $T_{onset}$ is less than 0.26 seconds for supersaturations greater than sixty, while mixing of the contents of the droplet will most likely take much longer than this. As the initial intensity measurements were not used due to their inconsistency, $T_{onset}$ was determined by extrapolating back 6.7 seconds. Extrapolating this far back is probably the cause of the large error associated with $T_{onset}$ values obtained at supersaturations less than 50.

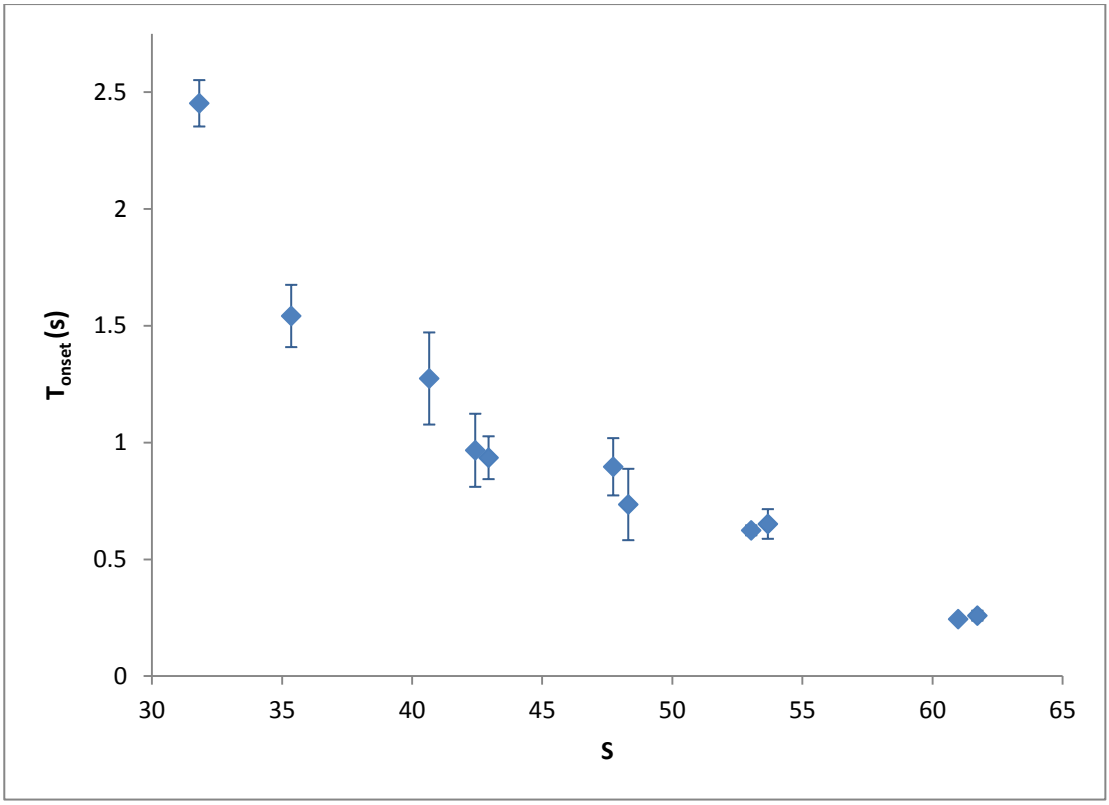


**Figure 5.10: $T_{onset}$ as a function of supersaturation (S). The error bars show the standard deviation (n=3).**

### 5.5.3.7 Limitations of the CI chip based detection system

Supersaturations greater than 62 were investigated in the above experiment, however, it was not possible to determine $T_{onset}$ for these supersaturations due to limitations of the current setup. Figure 5.11 shows the intensity measured as a function of frame number for a supersaturation of 121.98. The maximum intensities obtained are nearly identical across the 2000 frames of video that were analysed, suggesting that the limit of detection of the system has been reached. $T_{onset}$ could not be obtained for supersaturations greater than 65 as the intensities determined for different positions on chip started to plateau, and therefore a linear regression line could no longer be fitted to the data.

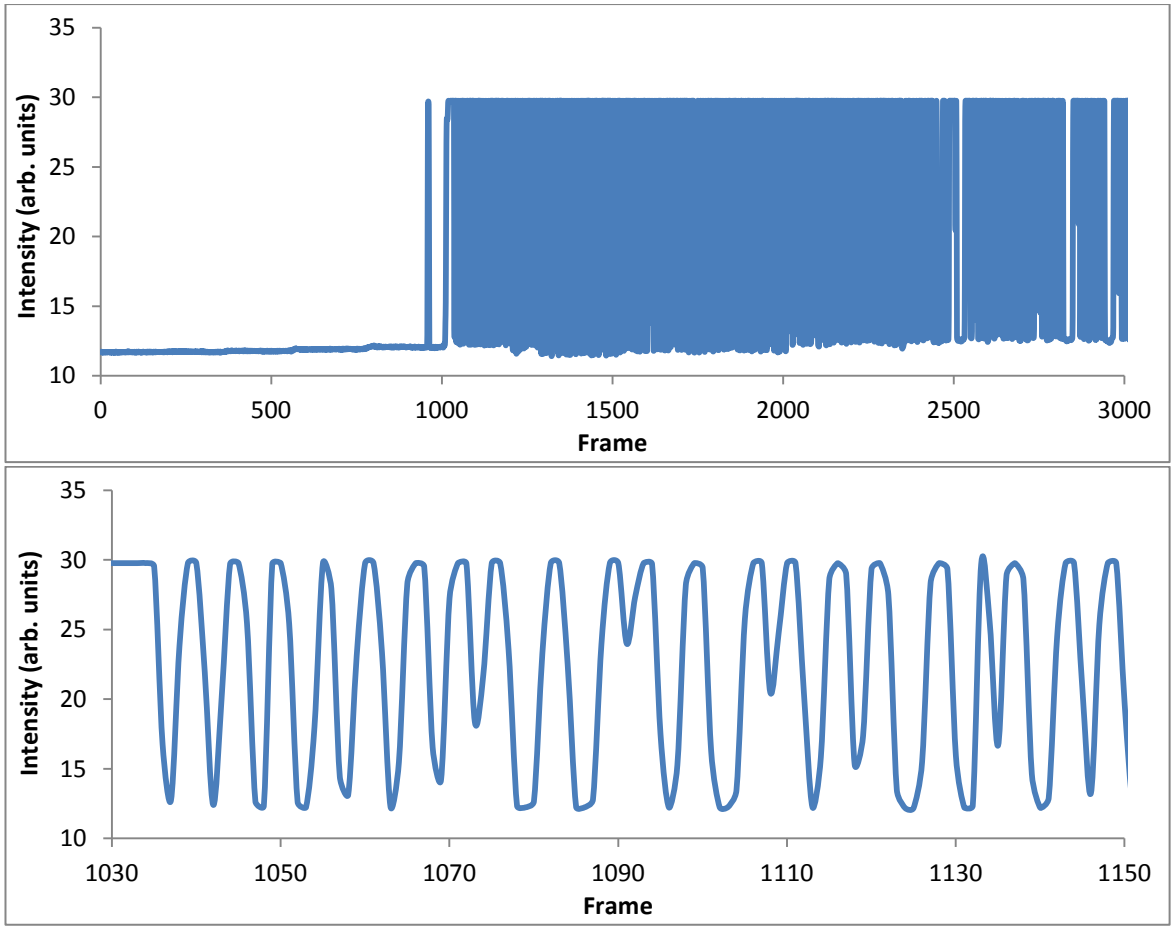


**Figure 5.11: Intensity as a function of frame rate observed at high supersaturations to emphasise the limitations of the microfluidic setup at these supersaturations. The intensity was determined at a supersaturation of 121.98, 11.04 seconds after droplet generation. The top graph shows the intensity recorded for the whole experiment, hardly any scattering is observed before 1500 frames as the droplets had not reached the detection point then. The graph below is a close up of the intensity measured between frames 1030 and 1150. The maximum intensities observed for the droplets are nearly identical.**

This system may be more appropriate for studying lower supersaturations over a longer period of time; the longer timescales would make the experiments more physiologically relevant, as the residence time in the GI Tract is approximately 1-3 hours.[112] Although droplets have been stored in microfluidic chips for this amount of time, the present method will need to be adapted as the aqueous phase begins to stick to the channel after a short period of use, affecting droplet generation and causing droplet merging as the droplets travel around the spiral. Figure 5.12 shows the aqueous phase sticking which was observed when investigating mixing in the T-junction using cresol red (section 5.5.2.6). Image a) shows a small quantity of aqueous phase stuck to the side of the channel despite flushing perfluorodecalin through the channels previously, image b) shows that there is still aqueous phase stuck to the side of the channel even after droplet generation, the aqueous phase has changed colour from yellow to purple suggesting there is some

mixing occurring between the stuck phase and the droplets being formed hence the stuck aqueous phase may alter the composition of the droplets being produced. Images c) and d) show the detrimental effect aqueous phase sticking can have on droplet generation. The droplet detachment point has moved further down the channel and typically droplets of greater volume are produced, although the latter effect can not be seen in these images.

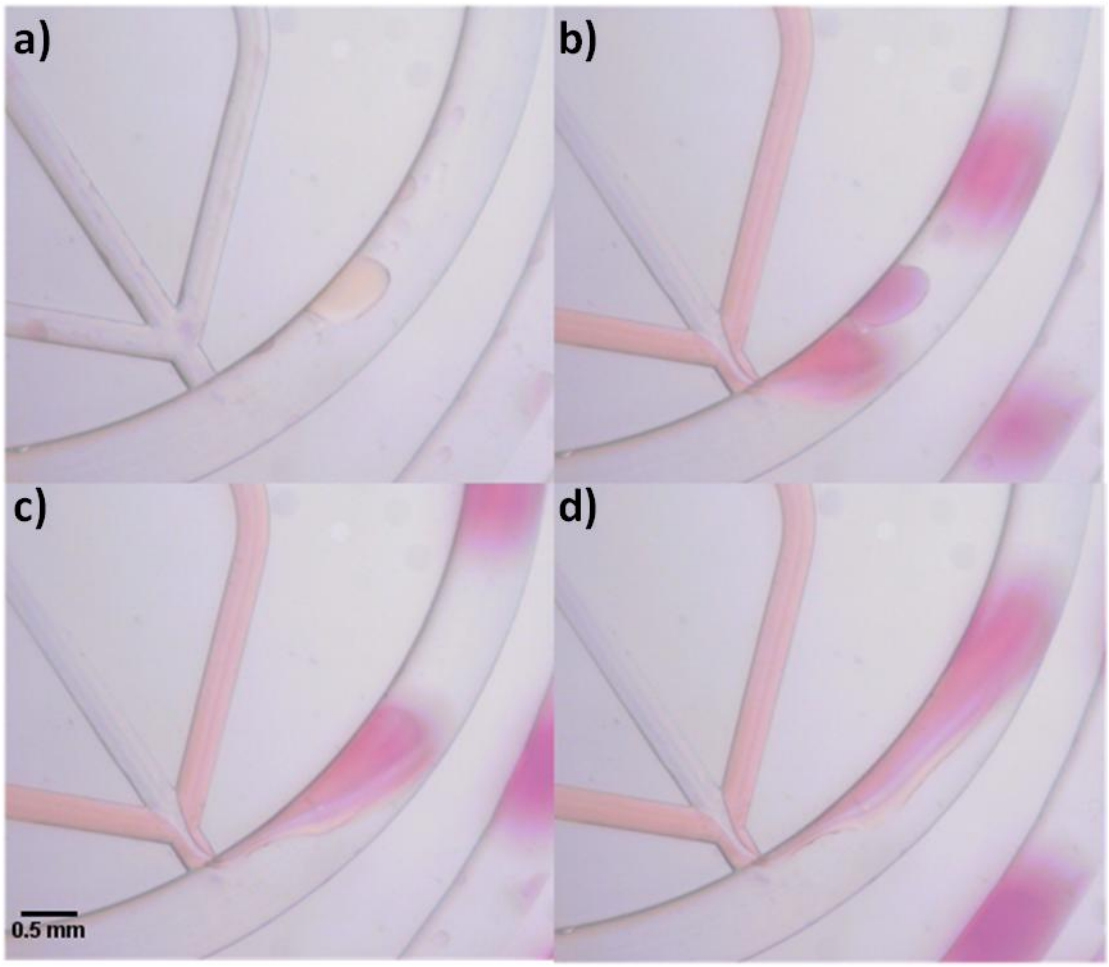


**Figure 5.12: Images of the aqueous phase sticking to the microfluidic channels when investigating mixing of aqueous phases in the T-junction using cresol red. The organic phase (perfluorodecalin) was infused at a flow rate of 400 µL $min^{-1}$, while the aqueous phases (0.01 M HCl and cresol red outer aqueous channels and 0.04 M NaOH central aqueous channel) were infused at approximately 67 µL $min^{-1}$. Image a) shows the HCl and cresol red aqueous phase sticking to the channel just past the aqueous inlets, after the chip has been flushed through with perfluorodecalin, image b) shows the aqueous phase is still sticking even after droplets are being generated, there has been some mixing with the other aqueous phase (NaOH) as the aqueous phase sticking to the channel now appears purple. Images c) and d) show the deterioration of droplet generation as the channel become more hydrophilic. Larger droplets are produced and the site of droplet detachment moves further down the channel. Images were taken with a Lumenera camera (LG11059C) using video capture software designed by Dr Bernard Treves Brown in LabVIEW.**

Decreasing the supersaturation and increasing the time the droplet is on chip may lead to generation of more reliable $T_{onset}$ determination. In the current system the initial intensity measurements were not used as the intensity observed was variable, therefore $T_{onset}$ was determined by extrapolating back 6.7 seconds. Extrapolating this far back is most likely the cause of the large error associated with $T_{onset}$ values obtained at supersaturations less than 50. A more accurate $T_{onset}$ determination could be made if a greater number of measurements were carried out. Increasing the time would also allow a more accurate determination of the time taken for the droplet to reach each detection point, however this would mean that the system would be limited to lower supersaturations. The time the droplet takes to reach each detection point was based on the times determined for a total aqueous flow rate of 200 µL $min^{-1}$ and an organic flow rate of 400 µL $min^{-1}$; a flow rate which is still quite fast to be able to determine droplet speed accurately, hence the error associated with this measurement may have been magnified when calculating the times for the flow rate used for the $T_{onset}$ experiments.

## 5.6 Conclusions

The microfluidic setup was able to determine $T_{onset}$ of precipitation for a supersaturation range of 32.81 – 64.41. $T_{onset}$ for supersaturations greater than 65 were unobtainable due to limitations in the light scattering detection system. Variability of intensity generated before ten seconds on the chip suggest that the precipitation in droplets should have been monitored for a greater period of time, however, negative $T_{onset}$ values were obtained when a total aqueous flow rate of 200 µL $min^{-1}$ and an organic flow rate of 400 µL $min^{-1}$ were investigated, making this challenging. Mixing in the T-junction could be eliminated if mixing of different aqueous phases was achieved by droplet fusion, however this would add another level of complexity to the chip design. To achieve monitoring of precipitation on physiologically relevant timescales, a more hydrophobic chip substrate or resistant hydrophobic coating will be required. This would allow lower supersaturations to be investigated and determination of $T_{onset}$ on timescales greater than the mixing time of the droplet, i.e. more accurate $T_{onset}$ determination.

# Chapter 6: Conclusions and future work

This thesis focuses on the development of microfluidic devices for application within the pharmaceutical industry. Two possible applications were investigated: a microfluidic mass spectrometry interface and a microfluidic-based light scattering detection system to monitor drug precipitation and evaluate pharmaceutical excipients in drug formulation. It is anticipated that microfluidics will have a major impact in the pharmaceutical industry in the future due to its high throughput capabilities and low sample volume requirements, however, at present considerable research still needs to be undertaken to develop reliable and user friendly microfluidic technology. The development of the mass spectrometry interface will be examined initially and suggestions made for future work in this area. Secondly, the findings from the development of the drug precipitation light scattering detection system, its limitations and possible future work to improve the system further will be discussed.

## 6.1 The microfluidic-based mass spectrometry interface

Chapter two concerns the development of a microfluidic electrospray ionisation mass spectrometry interface. Electrospray ionisation mass spectrometry is regularly used in the pharmaceutical industry and therefore development of a device which increases the throughput of mass spectrometric analysis could have a significant impact in drug discovery and development.

A continuous flow microfluidic device capable of electrospray ionisation was developed in this study. The response from the microfluidic device was compared to the response from the commercial probe operating under typical desolvation gas flow rates and desolvation temperature. On average the microchip resulted in a 38% improvement in signal intensity across a capillary voltage range of 4 – 4.75 kV when compared to the commercial probe operating with a desolvation gas flow rate of 120 L $hr^{-1}$ across the same capillary voltage range. When operating at a typical desolvation temperature of 350 ºC, the commercial probe outperformed the microchip operating at a desolvation temperature of 60 ºC. It should be noted, however, that increasing the desolvation temperature by 290 ºC only increased the signal intensity by 18%. Use of an alternative microchip substrate which has higher resistance to temperature, such as PEEK, will allow the microchip to take advantage of the benefits of operating at a higher desolvation temperature. Although comparable results were obtained for both systems, it should be noted that desolvation temperature and gas flow rate parameters were evaluated independently, and will need to

be investigated simultaneously if a proper comparison is to be made, nevertheless, the results obtained from these experiments are encouraging.

Further development of the platform will need to be undertaken to determine optimum electrospray conditions. Literature in this area suggests that capillaries with both reduced internal and external diameters could lead to improved sensitivity, both the dimensions and the material of the capillary should be investigated further to determine whether improvements to signal intensity could be achieved by altering the capillary. The capillary used in ESI chip 3 was chosen because it was identical to the capillary used in the commercial probe, hence allowing a direct comparison of the microchip and the probe to be made. The dimensions of this capillary (100 µm i.d) are on the large end of the scale of capillaries used for other mass spectrometry microfluidic interfaces reported in the literature (typically 10-100 µm i.d), therefore it stands to reason that further improvement to the mass spectrometric response could be made by reducing the dimensions of the capillary.

In order for microfluidic mass spectrometry interfaces to be taken up by the pharmaceutical industry, three important requirements must be met: the interface must provide comparable or greater sensitivity and reliability than the current system, it must be user friendly, and it must be compatible with the mass spectrometer without requiring much modification. Ideally, the microfluidic interface should also have high throughput capabilities, which could be achieved by incorporating a droplet based extraction system into the chip design. For this reason, it is envisioned that the interface will only be capable of droplet extraction and electrospray ionisation. Microfluidic devices with different functionalities could then be connected to the interface chip, increasing the versatility of the setup. To make the interface compatible with the mass spectrometer, it could be developed into an alternative probe format, which could be effortlessly slotted into place when required. The probe format will require the dimensions of the chip to be small, however, as the chip will contain only droplet extraction and electrospray capabilities, it is not anticipated that this will be a problem.

It is evident that significant work is still required to develop a microfluidic mass spectrometry interface. Although the interface developed in this study is only comparable to the current system in intensity of signal and throughput capabilities, it has resulted in consideration of not only how the mass spectrometry interface can be improved but also

how these interfaces may be introduced into drug discovery and development in a manner which compliments the mass spectrometers currently in use.

## 6.2 Development of microfluidic devices to monitor drug precipitation and evaluate pharmaceutical excipients.

Chapters three to five concern the development of microfluidic devices to monitor drug precipitation and screen pharmaceutical excipients. It is envisioned that the devices developed in these chapters would be applicable to drug formulation. Current pharmaceutical methods to determine drug solubility/precipitation typically requires solid separation and off-line sample quantification. Microfluidics offers the possibility of *in situ* monitoring of drug precipitation, reducing the time required to carry out the experiment and eliminating the time delay between sampling and measurement.

Drug precipitation of a weakly basic drug, ketoconazole, was monitored using a novel microfluidic-based light scattering detection system. A pH shift method was employed to generate a supersaturated state and simulate gastric emptying conditions of the drug into the small intestine. The system was found to be sensitive to changes in ketoconazole supersaturation and was able to detect precipitation for the wide range of supersaturations studied (32-161). It was observed that the scattered intensity obtained for different supersaturations of ketoconazole began to plateau after five minutes on chip, suggesting that all the drug in the supersaturated state had precipitated. This allowed determination of the extent of precipitation, which is referred to as the ‘average maximum intensity’ in this study. The average maximum intensity allowed a comparison to be made between the different supersaturations, and showed that there was a good correlation between results obtained at different pH (pH 6.5 and pH 7.0). The relationship between the average maximum intensity and supersaturation was shown to be linear for supersaturations up to 110. There was a deviation from linearity at higher supersaturations indicating limitations in the light scattering detection system; however, the estimated maximum intraluminal concentration based on taking a 200 mg tablet of ketoconazole with a 250 mL glass of water, corresponds to a supersaturation of 67 (calculated based on the solubility of ketoconazole at pH 6.5 in FaSSIF), which is well within the linear detection range. For this reason, it is suggested that the microfluidic-based light scattering detection system presented in this thesis is capable of determining the extent of precipitation at physiologically relevant supersaturations.

The first example of using microfluidic technology to screen the effect of pharmaceutical excipients was presented in this thesis. The effect of polymeric precipitation inhibitors on ketoconazole precipitation was evaluated using the same microfluidic light scattering detection system. Two water soluble polymers were investigated, polyvinylpyrrolidone (PVP) and hydroxypropyl methylcellulose (HPMC). The results obtained suggest both polymers were capable of inhibiting ketoconazole precipitation, however, HPMC was found to be a more potent precipitation inhibitor that PVP. The presence of just 0.05 mM of HPMC decreased the scattering intensity, and hence ketoconazole precipitation by 75%, outperforming 1.7 mM PVP, which only decreased ketoconazole precipitation by 60%. The effect of PVP concentration on the average maximum intensity was found to be linear, while the average maximum intensity decreased significantly in the presence of 0.05 mM HPMC, but there was not a significant decrease upon doubling or even tripling the HPMC concentration. These results corroborate the findings obtained using dynamic light scattering and are comparable to results reported in the literature for itraconazole, which is structurally similar to ketoconazole. The greater inhibitory effect of HPMC is attributed to its hydrogen bonding capabilities, which would be expected to result in greater interaction with ketoconazole which is a proton acceptor, than PVP which is also a proton acceptor. It was suggested that the inhibition of ketoconazole precipitation observed for PVP was due to an increase in solution viscosity and not through interaction with ketoconazole. Although it was anticipated that HPMC would be a more effective precipitation inhibitor in the case of ketoconazole, it is difficult to predict the effect an excipient will have on drug precipitation. For this reason, multiple excipients and mixtures of excipients typically need to be screened against the drug. A microfluidic chip was fabricated to allow screening of four different excipients and their mixtures. Preliminary experiments were undertaken to assess the mixing of the different aqueous flows and to evaluate the chip design prior to introduction of the drug and excipients. The results from the mixing experiments suggested that the design of the chip should be modified before it could be used to evaluate drug-excipient combinations. Backflow of the aqueous phases resulted in mixing of the aqueous streams prior to droplet formation, and hence concerns regarding the contents of the droplet formed. It is suggested that the aqueous inlet channels could be shortened or widened to reduce the pressure created in the channels at the flow rates used, modelling could be employed to deduce the optimum channel dimensions and aqueous flow rates prior to fabrication and evaluation of the next microchip.

The determination of the onset time ($T_{onset}$) of precipitation for a range of ketoconazole supersaturations using microfluidic technology was discussed in chapter five. A LED light source was used for this study; a comparison of the LED with the laser light source indicated that they exhibited similar stability, but the LED was slightly less sensitive, however, the LED benefits from illumination of the whole chip, hence additional detection positions could be selected, as the LED is not limited to the eleven detection positions used for the laser light source. Mixing of the aqueous streams prior to droplet formation was an issue with the CI chip used to conduct these experiments; a flow rate experiment led to the conclusion that at a total aqueous flow rate of 400 µL $min^{-1}$ and an organic flow rate of 800 µL $min^{-1}$ the mixing in the T-junction could be considered insignificant as increasing the flow rate further did not significantly alter the $T_{onset}$ value obtained. The high flow rates used equated to a droplet resident time on chip of approximately 22 seconds, however the intensity observed prior to 6.7 seconds was variable and could not be used in the $T_{onset}$ determination. The $T_{onset}$ values obtained for ketoconazole supersaturations of between 30 - 65 were small (< 2.5 seconds), and were determined by extrapolating back 6.7 seconds, due to the variable intensity observed. For these reasons, the $T_{onset}$ values obtained may be questionable as the mixing time of the droplet may be comparable or even exceed the $T_{onset}$ value determined, especially at higher supersaturations, such as at supersaturations between 60 – 65, where $T_{onset}$ was found to be less than 0.26 seconds. The low $T_{onset}$ values obtained are probably due to the high degree of supersaturation used, as both the rates of nucleation and crystal growth are expected to be large at these supersaturations. Determination of $T_{onset}$ of precipitation for higher supersaturations (greater than 65) was not possible due to limitations in the light scattering detection system The results obtained for these experiments suggest that the light scattering detection system was not ideal for determination of $T_{onset}$ of precipitation; the sensitivity of the system was not sufficient to detect small quantities of precipitation, which is the reason why a large proportion of data had to be discarded at the early stages of the experiment.

The above work is based on weakly basic drugs which are more soluble in the acidic conditions of the stomach than the intestine, therefore a pH shift can be used to simulate gastric empty into the small intestine and generate a supersaturated state. Wells estimated that weakly basic drugs account for 75% of drugs produced,[28] therefore the method presented in this thesis is applicable to many NCEs, however a microfluidic method will need to be developed to study drugs which are not basic. This could be achieved using the antisolvent method, in which the drug is dissolved in a solvent in which

it is soluble; this solution is then mixed with a solvent in which the drug is less soluble (the antisolvent), resulting in generation of a supersaturated state. This could be easily achieved in the microfluidic setup described in this study, for example, one aqueous stream could contain the drug solution and another aqueous stream could contain the antisolvent.

Development of a more sophisticated detection system could allow information to be generated on particle sizes; however, this would require detectors to be placed at different angles, and due to the reflections observed from the surface of the droplet, the angles at which the detector could be placed is rather limited. Refection of light from the droplet surface at different angles will need to be investigated to assess whether multi-angle light scattering detection would be viable.

Although much research is still required to enable these devices to be suitable for use in the pharmaceutical industry, the devices developed in this thesis emphasise the potential impact of microfluidic technology in drug formulation. Information concerning the extent of drug precipitation and excipients which inhibit drug precipitation is crucial to ensure the drug is formulated to enhance its therapeutic effect. If the throughput capabilities of the chip were increased to allow screening of multiple drugs and excipients then the microfluidic setup would be a valuable asset to drug formulation, however this would require significant development of the system and automation of the data analysis, otherwise the throughput capabilities of the system would be limited by the time taken to process the data.

## Chapter 7: References


1. A. Manz, J. C. Fettinger, E. Verpoorte, H. Ludi, H. M. Widmer and D. J. Harrison, *Trac-Trends in Analytical Chemistry*, 1991, **10**, 144-149.
2. Y. J. Wang, W. Y. Lin, K. Liu, R. J. Lin, M. Selke, H. C. Kolb, N. G. Zhang, X. Z. Zhao, M. E. Phelps, C. K. F. Shen, K. F. Faull and H. R. Tseng, *Lab on a Chip*, 2009, **9**, 2281-2285.
3. K. H. Chung, S. H. Park and Y. H. Choi, *Lab on a Chip*, 2010, **10**, 202-210.
4. S. Joo, K. H. Kim, H. C. Kim and T. D. Chung, *Biosens Bioelectron*, 2010, **25**, 1509-1515.
5. P. Tabeling, *Introduction to microfluidics*, 1st edn., Oxford University Press, Oxford, 2005.
6. H. Song, J. D. Tice and R. F. Ismagilov, *Angewandte Chemie-International Edition*, 2003, **42**, 768-772.
7. R. M. Lorenz, J. S. Edgar, G. D. M. Jeffries and D. T. Chiu, *Analytical Chemistry*, 2006, **78**, 6433-6439.
8. E. Quevedo, J. Steinbacher and D. T. McQuade, *Journal of the American Chemical Society*, 2005, **127**, 10498-10499.
9. O. Ozen, N. Aubry, D. T. Papageorgiou and P. G. Petropoulos, *Physical Review Letters*, 2006, **96**, 144501.
10. T. Thorsen, R. W. Roberts, F. H. Arnold and S. R. Quake, *Physical Review Letters*, 2001, **86**, 4163-4166.
11. T. Nisisako, T. Torii and T. Higuchi, *Lab on a Chip*, 2002, **2**, 24-26.
12. Y. C. Zhao, G. W. Chen and Q. Yuan, *Aiche Journal*, 2006, **52**, 4052-4060.
13. S. L. Anna, N. Bontoux and H. A. Stone, *Applied Physics Letters*, 2003, **82**, 364-366.
14. T. Ward, M. Faivre, M. Abkarian and H. A. Stone, *Electrophoresis*, 2005, **26**, 3716-3724.
15. T. Nisisako and T. Torii, *Lab on a Chip*, 2008, **8**, 287-293.
16. D. R. Link, E. Grasland-Mongrain, A. Duri, F. Sarrazin, Z. D. Cheng, G. Cristobal, M. Marquez and D. A. Weitz, *Angewandte Chemie-International Edition*, 2006, **45**, 2556-2560.
17. L. M. Fidalgo, C. Abell and W. T. S. Huck, *Lab on a Chip*, 2007, **7**, 984-986.
18. N. Bremond, A. R. Thiam and J. Bibette, *Physical Review Letters*, 2008, **100**, 024501.
19. L. H. Hung, K. M. Choi, W. Y. Tseng, Y. C. Tan, K. J. Shea and A. P. Lee, *Lab on a Chip*, 2006, **6**, 174-178.
20. D. N. Adamson, D. Mustafi, J. X. J. Zhang, B. Zheng and R. F. Ismagilov, *Lab on a Chip*, 2006, **6**, 1178-1186.
21. D. R. Link, S. L. Anna, D. A. Weitz and H. A. Stone, *Physical Review Letters*, 2004, **92**, 054503.
22. T. H. Ting, Y. F. Yap, N. T. Nguyen, T. N. Wong, J. C. K. Chai and L. Yobas, *Applied Physics Letters*, 2006, **89**, 234101.
23. Y. C. Tan and A. P. Lee, *Lab on a Chip*, 2005, **5**, 1178-1183.
24. A. Y. Fu, C. Spence, A. Scherer, F. H. Arnold and S. R. Quake, *Nature Biotechnology*, 1999, **17**, 1109-1111.
25. K. Bernath, M. T. Hai, E. Mastrobattista, A. D. Griffiths, S. Magdassi and D. S. Tawfik, *Analytical Biochemistry*, 2004, **325**, 151-157.

26. L. Kang, B. G. Chung, R. Langer and A. Khademhosseini, *Drug Discovery Today*, 2008, **13**, 1-13.
27. R. A. Prentis, Y. Lis and S. R. Walker, *British Journal of Clinical Pharmacology*, 1988, **25**, 387-396.
28. J. I. Wells, *Pharmaceutical Preformulation: The Physicochemical Properties of Drug Substances*, 1st edn., Ellis Horwood, London, 1988.
29. S. Babic, A. J. M. Horvat, D. M. Pavlovic and M. Kastelan-Macan, *Trac-Trends in Analytical Chemistry*, 2007, **26**, 1041-1061.
30. C. A. Lipinski, F. Lombardo, B. W. Dominy and P. J. Feeney, *Advanced Drug Delivery Reviews*, 1997, **23**, 3-25.
31. J. S. Lee, J. Ryu and C. B. Park, *Analytical Chemistry*, 2009, **81**, 2751-2759.
32. E. Garcia-Egido, V. Spikmans, S. Y. F. Wong and B. H. Warrington, *Lab on a Chip*, 2003, **3**, 73-76.
33. D. Lombardi and P. S. Dittrich, *Analytical and Bioanalytical Chemistry*, 2011, **399**, 347-352.
34. K. Carlsson and B. Karlberg, *Analytica Chimica Acta*, 2000, **423**, 137-144.
35. M. Alimuddin, D. Grant, D. Bulloch, N. Lee, M. Peacock and R. Dahl, *Journal of Medicinal Chemistry*, 2008, **51**, 5140-5142.
36. OECD, *Test No. 107: Partition Coefficient (n-octanol/water): Shake Flask Method*, OECD Publishing.
37. E. Brouzes, M. Medkova, N. Savenelli, D. Marran, M. Twardowski, J. B. Hutchison, J. M. Rothberg, D. R. Link, N. Perrimon and M. L. Samuels, *Proceedings of the National Academy of Sciences of the United States of America*, 2009, **106**, 14195-14200.
38. D. Huh, B. D. Matthews, A. Mammoto, M. Montoya-Zavala, H. Y. Hsin and D. E. Ingber, *Science*, 2010, **328**, 1662-1668.
39. J. H. Sung, C. Kam and M. L. Shuler, *Lab on a Chip*, 2010, **10**, 446-455.
40. D. I. Papac and Z. Shahrokh, *Pharmaceutical Research*, 2001, **18**, 131-145.
41. J. Zeleny, *Physical Review*, 1914, **3**, 69-91.
42. B. N. Pramanik, A. K. Ganguly and M. L. Gross, *Applied Electrospray Mass Spectrometry*, Marcell Dekker, New York, 2002.
43. P. Kebarle and U. H. Verkerk, *Mass Spectrometry Reviews*, 2009, **28**, 898-917.
44. D. P. H. Smith, *Ieee Transactions on Industry Applications*, 1986, **22**, 527-535.
45. G. Taylor, *Proceedings of the Royal Society of London Series a-Mathematical and Physical Sciences*, 1964, **280**, 383-397.
46. J. W. S. Rayleigh, *The Theory of Sound*, 2nd edn., Macmillian and Co. Ltd., London, 1896.
47. A. T. Blades, M. G. Ikonomou and P. Kebarle, *Analytical Chemistry*, 1991, **63**, 2109-2114.
48. M. Dole, L. L. Mack and R. L. Hines, *Journal of Chemical Physics*, 1968, **49**, 2240-2249.
49. A. Gomez and K. Q. Tang, *Physics of Fluids*, 1994, **6**, 404-414.
50. J. V. Iribarne and B. A. Thomson, *Journal of Chemical Physics*, 1976, **64**, 2287-2294.
51. M. Yamashita and J. B. Fenn, *Journal of Physical Chemistry*, 1984, **88**, 4451-4459.
52. M. Peschke, U. H. Verkerk and P. Kebarle, *Journal of the American Society for Mass Spectrometry*, 2004, **15**, 1424-1434.
53. M. Yamashita and J. B. Fenn, *Journal of Physical Chemistry*, 1984, **88**, 4671-4675.
54. M. G. Ikonomou, A. T. Blades and P. Kebarle, *Journal of the American Society for Mass Spectrometry*, 1991, **2**, 497-505.

55. A. P. Bruins, T. R. Covey and J. D. Henion, *Analytical Chemistry*, 1987, **59**, 2642-2646.
56. M. R. Emmett and R. M. Caprioli, *Journal of the American Society for Mass Spectrometry*, 1994, **5**, 605-613.
57. M. S. Wilm and M. Mann, *International Journal of Mass Spectrometry*, 1994, **136**, 167-180.
58. M. Wilm and M. Mann, *Analytical Chemistry*, 1996, **68**, 1-8.
59. G. A. Valaskovic, N. L. Kelleher, D. P. Little, D. J. Aaserud and F. W. McLafferty, *Analytical Chemistry*, 1995, **67**, 3802-3805.
60. R. S. Ramsey and J. M. Ramsey, *Analytical Chemistry*, 1997, **69**, 1174-1178.
61. Q. F. Xue, F. Foret, Y. M. Dunayevskiy, P. M. Zavracky, N. E. McGruer and B. L. Karger, *Analytical Chemistry*, 1997, **69**, 426-430.
62. Y. X. Wang, J. W. Cooper, C. S. Lee and D. L. DeVoe, *Lab on a Chip*, 2004, **4**, 363-367.
63. B. Zhang, H. Liu, B. L. Karger and F. Foret, *Analytical Chemistry*, 1999, **71**, 3258-3264.
64. D. Figeys, Y. B. Ning and R. Aebersold, *Analytical Chemistry*, 1997, **69**, 3153-3160.
65. N. H. Bings, C. Wang, C. D. Skinner, C. L. Colyer, P. Thibault and D. J. Harrison, *Analytical Chemistry*, 1999, **71**, 3292-3296.
66. Y. Tachibana, K. Otsuka, S. Terabe, A. Arai, K. Suzuki and S. Nakamura, *Journal of Chromatography A*, 2003, **1011**, 181-192.
67. H. H. Liu, C. Felten, Q. F. Xue, B. L. Zhang, P. Jedrzejewski, B. L. Karger and F. Foret, *Analytical Chemistry*, 2000, **72**, 3303-3310.
68. P. Liuni, T. Rob and D. J. Wilson, *Rapid Communications in Mass Spectrometry*, 2010, **24**, 315-320.
69. J. Svobodova, S. Mathur, A. Muck, T. Letzel and A. Svatos, *Electrophoresis*, 2010, **31**, 2680-2685.
70. C. Wang, A. B. Jemere and D. J. Harrison, *Electrophoresis*, 2010, **31**, 3703-3710.
71. J.-L. Huang, F.-A. Li and G.-R. Her, *Electrophoresis*, 2011, **32**, 3385-3391.
72. N. J. Petersen, S. T. Foss, H. Jensen, S. H. Hansen, C. Skonberg, D. Snakenborg, J. P. Kutter and S. Pedersen-Bjergaard, *Analytical Chemistry*, 2011, **83**, 44-51.
73. Q. Chen, J. Wu, Y. Zhang and J.-M. Lin, *Analytical Chemistry*, 2012, **84**, 1695-1701.
74. G. A. Schultz, T. N. Corso, S. J. Prosser and S. Zhang, *Analytical Chemistry*, 2000, **72**, 4058-4063.
75. M. Svedberg, A. Pettersson, S. Nilsson, J. Bergquist, L. Nyholm, F. Nikolajeff and K. Markides, *Analytical Chemistry*, 2003, **75**, 3934-3940.
76. X. Sun, R. T. Kelly, K. Tang and R. D. Smith, *Analytical Chemistry*, 2011, **83**, 5797-5803.
77. X. Sun, R. T. Kelly, K. Tang and R. D. Smith, *Analyst*, 2010, **135**, 2296-2302.
78. M. Dijkstra, J. W. Berenschot, M. J. de Boer, H. J. van der Linden, T. Hankemeier, T. S. J. Lammerink, R. J. Wiegerink, M. Elwenspoek and N. R. Tas, *Microfluidics and Nanofluidics*, 2012, **13**, 29-35.
79. S. Arscott and D. Troadec, *Nanotechnology*, 2005, **16**, 2295-2302.
80. L. M. Fidalgo, G. Whyte, B. T. Ruotolo, J. L. P. Benesch, F. Stengel, C. Abell, C. V. Robinson and W. T. S. Huck, *Angewandte Chemie-International Edition*, 2009, **48**, 3665-3668.
81. R. T. Kelly, J. S. Page, I. Marginean, K. Q. Tang and R. D. Smith, *Angewandte Chemie-International Edition*, 2009, **48**, 6832-6835.

82. Y. Zhu and Q. Fang, *Analytical Chemistry*, 2010, **82**, 8361-8366.
83. S. Sun, T. R. Slaney and R. T. Kennedy, *Analytical Chemistry*, 2012, **84**, 5794-5800.
84. D. Figeys, S. P. Gygi, G. McKinnon and R. Aebersold, *Analytical Chemistry*, 1998, **70**, 3728-3734.
85. V. de Biasi, N. Haskins, A. Organ, R. Bateman, K. Giles and S. Jarvis, *Rapid Communications in Mass Spectrometry*, 1999, **13**, 1165-1168.
86. A. M. Tan, S. Benetton and J. D. Henion, *Analytical Chemistry*, 2003, **75**, 5504-5511.
87. J. J. Li, T. L. Tremblay, C. Wang, S. Attiya, D. J. Harrison and P. Thibault, *Proteomics*, 2001, **1**, 975-986.
88. B. L. Zhang, F. Foret and B. L. Karger, *Analytical Chemistry*, 2001, **73**, 2675-2681.
89. P. Mao, H.-T. Wang, P. Yang and D. Wang, *Analytical Chemistry*, 2011, **83**, 6082-6089.
90. K. Q. Tang, Y. H. Lin, D. W. Matson, T. Kim and R. D. Smith, *Analytical Chemistry*, 2001, **73**, 1658-1663.
91. L. Sainiemi, T. Nissila, R. Kostiainen, R. A. Ketola and S. Franssila, *Lab on a Chip*, 2011, **11**, 3011-3014.
92. S. Zhang, C. K. Van Pelt and J. D. Henion, *Electrophoresis*, 2003, **24**, 3620-3632.
93. A. D. Zamfir, L. Bindila, N. Lion, M. Allen, H. H. Girault and J. Peter-Katalinic, *Electrophoresis*, 2005, **26**, 3650-3673.
94. V. Kertesz and G. J. Van Berkel, *Journal of Mass Spectrometry*, 2010, **45**, 252-260.
95. A. Hawkins and H. Schmidt, *Handbook of Optofluidics*, CRC Press, Boca Raton, 2010.
96. R. P. Schneider, M. J. Lynch, J. F. Ericson and H. G. Fouda, *Analytical Chemistry*, 1991, **63**, 1789-1794.
97. S. L. Zhou and M. Hamburger, *Rapid Communications in Mass Spectrometry*, 1995, **9**, 1516-1521.
98. W. Jolly, *Modern Inorganic Chemistry*, 2nd edn., McGraw-Hill, New York, 1991.
99. I. Marginean, R. T. Kelly, D. C. Prior, B. L. LaMarche, K. Q. Tang and R. D. Smith, *Analytical Chemistry*, 2008, **80**, 6573-6579.
100. Y. Kazakevich and R. Lobrutto, *HPLC for Pharmaceutical Scientists*, 1st edn., John Wiley & Sons, New Jersey, 2007.
101. J. M. Oreilly, H. E. Bair and F. E. Karasz, *Macromolecules*, 1982, **15**, 1083-1088.
102. M. Brivio, R. E. Oosterbroek, W. Verboom, A. van den Berg and D. N. Reinhoudt, *Lab on a Chip*, 2005, **5**, 1111-1122.
103. A. K. Sen, J. Darabi and D. R. Knapp, *Sensors and Actuators B-Chemical*, 2009, **137**, 789-796.
104. G. L. Amidon, H. Lennernas, V. P. Shah and J. R. Crison, *Pharmaceutical Research*, 1995, **12**, 413-420.
105. CDER/FDA, Center for Drug Evaluation and Research, 2000.
106. M. S. Ku, *Aaps Journal*, 2008, **10**, 208-212.
107. C. A. Lipinski, F. Lombardo, B. W. Dominy and P. J. Feeney, *Advanced Drug Delivery Reviews*, 2001, **46**, 3-26.
108. L. Pan, Q. Ho, K. Tsutsui and L. Takahashi, *Journal of Pharmaceutical Sciences*, 2001, **90**, 521-529.
109. S. N. Bhattachar, J. A. Wesley and C. Seadeek, *Journal of Pharmaceutical and Biomedical Analysis*, 2006, **41**, 152-157.

110. C. Seadeek, H. Ando, S. N. Bhattachar, T. Heimbach, J. L. Sonnenberg and A. C. Blackburn, *Journal of Pharmaceutical and Biomedical Analysis*, 2007, **43**, 1660-1666.
111. A. M. Persson, A. Sokolowski and C. Pettersson, *Drug discoveries & therapeutics*, 2009, **3**, 104-113.
112. J. B. Dressman, G. L. Amidon, C. Reppas and V. P. Shah, *Pharmaceutical Research*, 1998, **15**, 11-22.
113. J. Mullin, *Crystallization*, 4th edn., Butterworth-Heinemann, 2001.
114. H. A. Miers and F. Isaac, *Proceedings of the Royal Society of London Series a-Containing Papers of a Mathematical and Physical Character*, 1907, **79**, 322-351.
115. D. Kashchiev and G. M. van Rosmalen, *Crystal Research and Technology*, 2003, **38**, 555-574.
116. R. Boistelle and J. P. Astier, *Journal of Crystal Growth*, 1988, **90**, 14-30.
117. P. Hartman and W. G. Perdok, *Acta Crystallographica*, 1955, **8**, 49-52.
118. B. Vonnegut, *Journal of Colloid Science*, 1948, **3**, 563-569.
119. D. Kashchiev, N. Kaneko and K. Sato, *Journal of Colloid and Interface Science*, 1998, **208**, 167-177.
120. P. Laval, A. Crombez and J.-B. Salmon, *Langmuir*, 2009, **25**, 1836-1841.
121. P. Laval, C. Giroux, J. Leng and J.-B. Salmon, *Journal of Crystal Growth*, 2008, **310**, 3121-3124.
122. P. Laval, N. Lisai, J.-B. Salmon and M. Joanicot, *Lab on a Chip*, 2007, **7**, 829-834.
123. J.-u. Shim, G. Cristobal, D. R. Link, T. Thorsen and S. Fraden, *Crystal Growth & Design*, 2007, **7**, 2192-2194.
124. B. Zheng, L. S. Roach and R. F. Ismagilov, *Journal of the American Chemical Society*, 2003, **125**, 11170-11171.
125. C. L. Hansen, E. Skordalakes, J. M. Berger and S. R. Quake, *Proceedings of the National Academy of Sciences of the United States of America*, 2002, **99**, 16531-16536.
126. M. Jonasz and G. Fournier, *Light Scattering by Particles in Water: Theorectical and Experimental Foundations*, 1st edn., Elsevier Inc., Burlington, 2007.
127. N. Sergienko, D. Godovsky, B. Zavin, M. Lee and M. Ko, *Nanoscale research letters*, 2012, **7**, 181-181.
128. H. C. van de Hulst, *Light Scattering by Small Particles*, 1st edn., John Wiley & Sons Inc., New York, 1957.
129. M. Kerker, *The Scattering of Light, and other Electromagnetic Radiation* 1st edn., Academic Press, New York, 1969.
130. *Physician's Desk Reference*, PDR Network LLC, 2009.
131. K. Walter and H. Kurz, *Journal of Pharmacy and Pharmacology*, 1988, **40**, 689-693.
132. J. G. Baxter, C. Brass, J. J. Schentag and R. L. Slaughter, *Journal of Pharmaceutical Sciences*, 1986, **75**, 443-447.
133. A. Diakidou, M. Vertzoni, J. Dressman and C. Reppas, *Biopharmaceutics & Drug Disposition*, 2009, **30**, 318-325.
134. M. Vertzoni, A. Diakidou, M. Chatzilias, E. Soderlind, B. Abrahamsson, J. B. Dressman and C. Reppas, *Pharmaceutical Research*, 2010, **27**, 2187-2196.
135. http://www.chemspider.com/Chemical-Structure.401695.html (accessed 19:01, Mar 24 2013).
136. H. R. Guzman, M. Tawa, Z. Zhang, P. Ratanabanangkoon, P. Shaw, C. R. Gardner, H. Chen, J.-P. Moreau, O. Almarsson and J. F. Remenar, *Journal of Pharmaceutical Sciences*, 2007, **96**, 2686-2702.

137. J. Brouwers, M. E. Brewster and P. Augustijns, *Journal of Pharmaceutical Sciences*, 2009, **98**, 2549-2572.
138. P. Gao and W. Morozowich, *Expert opinion on drug delivery*, 2006, **3**, 97-110.
139. D. A. Miller, J. C. DiNunzio, W. Yang, J. W. McGinity and R. O. Williams, *Drug Development and Industrial Pharmacy*, 2008, **34**, 890-902.
140. R. Vandecruys, J. Peeters, G. Verreck and M. E. Brewster, *International Journal of Pharmaceutics*, 2007, **342**, 168-175.
141. K. Yamashita, T. Nakate, K. Okimoto, A. Ohike, Y. Tokunaga, R. Ibuki, K. Higaki and T. Kimura, *International Journal of Pharmaceutics*, 2003, **267**, 79-91.
142. H. Konno, T. Handa, D. E. Alonzo and L. S. Taylor, *European Journal of Pharmaceutics and Biopharmaceutics*, 2008, **70**, 493-499.
143. D. E. Alonzo, G. G. Z. Zhang, D. Zhou, Y. Gao and L. S. Taylor, *Pharmaceutical Research*, 2010, **27**, 608-618.
144. P. Gao, B. D. Rush, W. P. Pfund, T. H. Huang, J. M. Bauer, W. Morozowich, M. S. Kuo and M. J. Hageman, *Journal of Pharmaceutical Sciences*, 2003, **92**, 2386-2398.
145. D. B. Warren, H. Benameur, C. J. H. Porter and C. W. Pouton, *Journal of Drug Targeting*, 2010, **18**, 704-731.
146. W.-G. Dai, L. C. Dong, X. Shi, J. Nguyen, J. Evans, Y. Xu and A. A. Creasey, *Journal of Pharmaceutical Sciences*, 2007, **96**, 2957-2969.
147. T. Panagiotou, S. V. Mesite and R. J. Fisher, *Industrial & Engineering Chemistry Research*, 2009, **48**, 1761-1771.
148. J. Thiele, M. Windbergs, A. R. Abate, M. Trebbin, H. C. Shum, S. Foerster and D. A. Weitz, *Lab on a Chip*, 2011, **11**, 2362-2368.
149. http://microfluidicscorp.com. (accessed 13:24, Mar 12, 2013)
150. US Pat., US20040081696-A1, 2004
151. *www.pharma-ingredients.basf.com*. (accessed 11:44, Mar 16, 2013)
152. www.dow.com. (accessed 12:13, Mar 16, 2013)
153. T. Gong, J. Shen, Z. Hu, M. Marquez and Z. Cheng, *Langmuir*, 2007, **23**, 2919-2923.
154. K. V. R. Prasad, R. I. Ristic, D. B. Sheen and J. N. Sherwood, *International Journal of Pharmaceutics*, 2001, **215**, 29-44.
155. J. Liu, Z. Chang, Y. He, M. Yang and J. Dang, *Journal of Crystal Growth*, 2007, **307**, 131-136.
156. W. Cheng and Z. Li, *Journal of Crystal Growth*, 2010, **312**, 1563-1571.